Determination of material parameters by comparison of 3D simulations and 3D experiments

Zhang, Jin

Publication date:
2018

Document Version
Publisher's PDF, also known as Version of record

Determination of material parameters by comparison of 3D simulations and 3D experiments

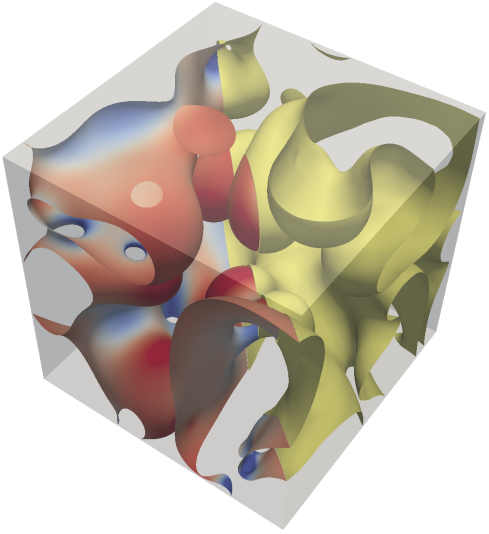

Jin Zhang

DTU Physics
Department of Physics

Determination of material parameters by comparison of 3D simulations and 3D experiments

Jin Zhang

Kongens Lyngby 2018

Supervisors and assessment committe:

Supervisors:	prof. Henning Friis Poulsen, DTU Physics
	prof. Peter W. Voorhees, Northwestern University
Chairman:	prof. Karsten Wedel Jacobsen, DTU Physics
Examiners:	assoc.prof. Nele Moelans, KU Leuven
	prof. Anthony D. Rollett, Carnegie Mellon University

Cover image:
Comparison of simulated and experimental Al-Cu coarsening microstructures
left: simulated microstructure using the best fitted parameters.
right: experimentally measured microstructure.
The mean curvature of the simulated interface is shown.

Technical University of Denmark
Department of Physics
Fysikvej, building 307,
2800 Kongens Lyngby, Denmark
www.fysik.dtu.dk

Abstract

Computer-based materials design plays an essential role in the development of new materials. Accurate prediction of the materials behavior during manufacturing and applications relies on accurate and complete materials databases. Traditional ways of material parameters measurements typically use idealized samples and sample environments, which may not be representative of the engineering processing and real-life usage. Moreover, material parameters are typically measured one at a time; thus it is time-consuming and costly to measure material parameters with large spectrum.

In this thesis, a fitting methodology is proposed to determine material parameters by comparison between 4D x-ray experiments and phase-field simulations. The evolution of material microstructures is measured at a condition that mimics realistic engineering manufacturing and applications with 3D non-destructive *in situ* x-ray techniques. Starting from one snapshot of the experimental microstructure, the evolution of the 3D material microstructure is simulated using a phase-field model. An iterative optimization technique is used to find the values of material parameters that yield the best match between the simulated microstructure and the measured microstructure in a global manner.

The proposed method is demonstrated on a simple case to fit two material parameters: the liquid diffusion coefficient and the capillary length of a hypoeutectic Al-Cu alloy, and a complicated case to fit hundreds of material parameters: the reduced grain boundary mobilities of pure iron. Results show that the proposed method is capable of providing reliable measurements of material parameters that are difficult to measure in traditional ways and can determine many - possibly all relevant - values of material parameters simultaneously. Moreover, the method developed is broadly applicable to many materials systems and experiments that provide 3D microstructure evolution.

Resumé

Computerbaseret design af materialer spiller en essentiel rolle inden for udviklingen af nye materialer. Præcise forudsigelser af materialers opførsel under fremstillingsprocesser og anvendelse er afhængig af præcisionen og kompletheden af materialedatabaser. Traditionelt bliver materialeparametre typisk målet ved brug af idealiserede prøver og prøvemiljøer, hvilke ikke altid er repræsentative for de virkelige påvirkninger under behandling og anvendelse. Derudover måles materialeparametre oftest en af gangen, hvilket går det tidskrævende og dyrt at måle et bredt spektrum af parametre.
I denne afhandling fremsættes en tilpasningsmetodik til at bestemme materialeparametre ud fra sammenligning mellem 4D røntgeneksperimenter og fasefeltssimuleringer. Udviklingen af et materiales mikrostruktur bliver målt under realistiske forhold for behandling og anvendelse ved brug af 3D ikke-destruktive *in situ* røntgenteknikker. Materialets 3D mikrostruktur og dens udvikling bliver simuleret med en fasefeltsmodel ud fra et øjebliksbillede af den målte mikrostruktur. En iterativ optimeringsteknik benyttes til at finde de materialeparametre, der globalt set giver den bedste overensstemmelse mellem den simulerede og målte mikrostruktur.
Den foreslåede metode bliver demonstreret ved to forskellige eksempler. Først et simpelt eksempel med to materialeparametre – den flydende diffusionskoefficient og den kapillære længde af hypoeutektisk Al-Cu. Dernæst et mere komplekst eksempel med tilpasning af hundrede materialeparametre – den reducerede korngrænsemobilitet af rent jern. Resultaterne viser at den foreslåede metode er i stand til at finde pålidelige målinger af materialeparametre, der er svære at måle på traditionelt vis. Ydermere kan den bestemme mange af – muligvis alle – de relevante materialeparametre samtidig. Derudover er den udviklede metode bredt anvendelig for mange materialesystemer og eksperimenter, der har en udvikling af en 3D mikrostruktur.

Abstract (chinese)

为了加快新材料的研发和应用，基于计算机仿真的材料设计方法吸引了广泛关注。准确地对材料加工过程进行模拟需要完备和准确的材料参数数据库。本文提出了一种材料参数测量新方法。通过比较四维X射线实验结果和材料相场计算结果，对相场计算的输入材料参数进行拟合。材料本征的材料参数应当使相场模拟结果同实验结果达到最佳吻合。而通过优化拟合得到的最优材料参数值即被认为是材料的本征材料参数值。同传统基于理想试样与理想测试环境的材料参数测量方法不同，本文提出的方法使用更贴近真实工程材料加工过程的样品以及加工环境，从而使得所测得的材料参数更具工程指导意义。为了验证这一材料参数拟合方法，本文对铝铜合金的液态扩散系数以及纯铁的各向异性缩减界面迁移率进行了测量。结果表明，材料参数拟合方法可以用来测量传统方法难以测量的材料参数并且可以在一次测量中得到较大范围材料参数空间的参数。

Acknowledgements

I would like to thank my supervisor, Henning F. Poulsen, for providing me this opportunity and an extraordinary platform. Your deep insight and good guide are very important for my PhD. Along the way, your patience and toleration give me much strength to go ahead. I would also like to thank my co-supervisor, Peter W. Voorhees, for teaching me the phase-field method and providing me the opportunity to visit Northwestern and CHiMaD. Your extraordinary insight on everything in materials science continuously inspires me. I am very lucky to work with both of you.

I would like to thank Stefan O. Poulsen. Your participation in my supervisor meeting is a great plus for my PhD. I learned a lot from you, not only phase-field but also your attitude on research. I would like to thank Yubin Zhang for your help during the day-and-night beamtimes as well as the sample preparation and data analysis. Without you, the experiments cannot be such successful. I would also like to thank Wolfgang Ludwig, who taught me so much about DCT. Your tireless help during the DCT beamtime and in the data analysis make this work possible. During a beamtime at APS, I got much help from Bob Suter, Yufeng Shen, and He Liu. I really had an enjoyable beamtime with you. I also want to thank Allan Lyckegaard for your Laguerre tessellation code. It helped a lot in the APS beamtime. I am grateful to Dave Rowenhorst for the fruitful collaboration on grain growth analysis.

I am very fortunate to work in Henning's group with all past and present group members: Søren, Wolfgang, Hugh, Jette, Tato, Sonja, Anders and Anders, Phil, Jack, Peter, Nicolai, Annika, Jeppe, Hanne, and Nanna. Your passion for science and always trying to push the measurement to the limit continuously inspire me.

I still remember when I saw you finding a diffraction spot on a tiny detector located meters away, I was shocked. At here I learned x-rays and 3D materials science, and it opened a new world for me. I also want to thank Hanne Sørensen for helping me with my questions and the administrative matters.

During my external research stay, I was fortunate to visit the Voorhees group and the CHiMaD center. I had very fruitful discussions with many of the group members. Special thanks go to: Yue Sun for the great discussion on the tomography reconstruction, TomoPy, and phase-field; Peisheng Wang at CHiMaD/NIST for discussion on the materials database; Matthew Peters for the CALPHAD free energy of Al-Cu; Ashwin Shahani for the discussion on imaging processing; and John Gibbs for the Al-Cu dataset.

I would like to take this opportunity to thank people who helped me on phase-field before this PhD. These experiences are always part of my PhD. It is the lecture given by Kris van der Zee at Eindhoven, which fascinated me by the beauty of the phase-field method. Special thanks to Xunxun Wu for very helpful discussion on phase-field and math. I am grateful to Paul van der Schoot for teaching me non-equilibrium thermodynamics. It will continuously influence my view of physics and the world.

In the past years, I experienced a lot, and it is good to remember. I sincerely thank all my friends, colleagues and office mates. You are always part of my life.

Finally, I would like to thank parents. Your endless support means a lot to me. I love you. 爸妈，谢谢！Above all I want to thank my wife Xuhui. Without your continued support and encouragement, I won't go this far.

The work has been carried out from February 2015 to January 2018 at the section for Neutrons and X-rays for Materials Physics (NEXMAP) at the Department of Physics of the Technical University of Denmark (DTU). I thank DTU Physics and NEXMAP for providing a pleasant working environment. The financial support from CINEMA project, the travel grant from Danscatt and the MAXIVESSFUN project are kindly acknowledged.

Publication list

Paper I

Determining material parameters using phase-field simulations and experiments
Jin Zhang, Stefan O. Poulsen, John W. Gibbs, Peter W. Voorhees, Henning F. Poulsen
Acta Materialia, Volume 129, 2017, Pages 229-238, `https://doi.org/10.1016/j.actamat.2017.02.056`.

Paper II

Three-dimensional grain growth in pure iron. part I: statistics on the grain level
Jin Zhang, Yubin Zhang, Wolfgang Ludwig, David J. Rowenhorst, Peter W. Voorhees, Henning F. Poulsen
Acta Materialia, *Submitted*.

Nomenclature

X-ray experiment

μ	linear attenuation coefficient
λ	wavelength of an x-ray beam
$\mathbf{Q}$	diffraction vector $\mathbf{Q} = \mathbf{k}_{\text{out}} - \mathbf{k}_{\text{in}}$, where $\mathbf{k}_{\text{in}}$ and $\mathbf{k}_{\text{out}}$ are the incoming and diffracted wavevectors, respectively.
ω	angle of rotation stage
$\mathbf{G}_{hkl}$	reciprocal lattice vector of (hkl) lattice planes
d_{hkl}	distance between adjacent (hkl) lattice planes
θ	scattering angle

Solidification

D^{L}, D^{S}	liquid and solid diffusion coefficients
l^{L}, l^{S}	liquid and solid capillary lengths
M^{L}, M^{S}	liquid and solid diffusion mobilities
f^{L}, f^{S}	bulk free energy density in the liquid and solid phases
$c^{\text{L,eq}}$, $c^{\text{S,eq}}$	common tangent compositions
σ	solid-liquid interfacial energy
$\mathcal{H}$	mean curvature $2\mathcal{H} = \kappa_1 + \kappa_2$, where κ_i are the principal curvatures

Grain growth

$\Delta\mathbf{g}$	misorientation matrix
$\hat{n}$	grain boundary plane normal
$M_{\mathrm{gb}}(\Delta\mathbf{g}, \hat{n})$	grain boundary mobilities
$\sigma_{\mathrm{gb}}(\Delta\mathbf{g}, \hat{n})$	grain boundary energies
m_{gb}	reduced grain boundary mobilities $m_{\mathrm{gb}} = M_{\mathrm{gb}}\sigma_{\mathrm{gb}}$

Phase-field method

Ω_α	the space spanned by one phase/domain
$\mathcal{D}$	the microstructure domain $\mathcal{D} \subset \mathbb{R}^n$, where n is the dimension of real space. For a microstructure composed of p phases or domains, the microstructure domain is $\mathcal{D} = \bigcup_{\alpha=1}^{p} \Omega_\alpha$
$\mathbb{R}^p$	the phase space. p is the number of phase-field variables
$\mathbf{u}$	phase-field variables $\mathbf{u} = \{u_\alpha\} : \mathbb{R}^n \times \mathbb{R}^+ \to \mathbb{R}^p$
c	composition/diffusion field $c : \mathbb{R}^n \times \mathbb{R}^+ \to \mathbb{R}$
$W(\mathbf{u})$	potential function: $W(\mathbf{u}) : \mathbb{R}^p \to \mathbb{R}$
F	free energy of the system
h^α	interpolation function
l, l_{gb}	diffuse-interface width

Fitting

ϕ	signed distance function
$f_{\mathrm{cost}}^{\mathrm{corr}}$	corr-cost function. Defined using the correlation function
$f_{\mathrm{cost}}^{\mathrm{norm}}$	norm-cost function. Defined using q-norms
$f_{\mathrm{cost}}^{\alpha\beta}$	local cost function of interface $\Gamma^{\alpha\beta} = \Omega_\alpha \cap \Omega_\beta$
$\|f\|_q$	q-norm: $\|f\|_q = \int f^q \, \mathrm{d}V$

Abbreviations

3DXRD	Three-Dimensional X-Ray Diffraction
APS	Advanced Photon Source
ART	Algebraic Reconstruction Technique
CALPHAD	CALculation of PHAse Diagrams
CT	Computed Tomography
DCT	Diffraction Contrast Tomography
DFXRM	Dark-Field X-Ray Microscopy
EBSD	Electron BackScatter Diffraction
ESRF	European Synchrotron Radiation Facility
FBP	Filtered Back Projection
GBE	Grain Boundary Energy
GBM	Grain Boundary Mobility
ICME	Integrated Computational Materials Engineering
IPF	Inverse Pole Figure
LabDCT	Laboratory-based Diffraction Contrast Tomography
MGI	Materials Genome Initiative
MPI	Message Passing Interface
PCT	Phase Contrast Tomography

Contents

Chapter 1

Introduction

The time frame for materials from discovery to deployment typically is 10 to 20 years [1, 2]. Application of new materials is hindered by the high cost of the traditional experience-driven design approach due to its trial-and-error nature. These disadvantages in time and cost make changing materials in an established technology rare even when the material in use is not optimal. To speed up the development of new materials and to reduce costs, computational model-based design and screening are essential to overcome these disadvantages. Recently, there have been many success stories of applying a computational-model based design approach. For example, the design of a Ferrium M54 steel for aircraft-arresting tailhooks took only eight years from the initial design to the completion of deployment [3]. High-throughput materials screening based on atomic-scale calculations was successfully applied in the design of various new materials [4, 5, 6].

Most materials have hierarchical structures [8]; thus the design of materials needs materials models and databases at various length scales. This thesis will focus on phenomena at the so-called mesoscale [9], a scale that is large enough compared to the atom size so the continuous assumption is valid, while small enough that the rich features of materials microstructures are not lost. Fig. 1.1 is an example of the approach frequently used for materials design, especially in research related to the so-called Materials Genome. It shows the hierarchical structure and key components of the data/knowledge-driven materials design

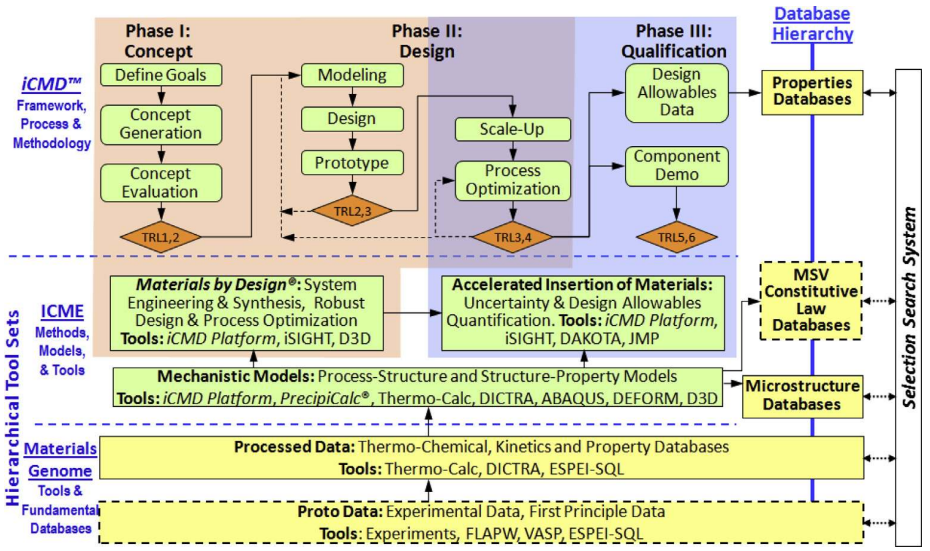

Figure 1.1: Key components of materials design approach: materials methods, tools and databases [7].

approach. Materials databases, such as thermodynamic and kinetic databases, play a fundamental role in the materials design. On top of the databases, a series of materials models provide links among process, structure, and properties. Given the databases and materials models, data mining or machine learning tools can be applied to identify materials with the required properties. In this process, a large database of material parameters and precise models are essential.

The material parameters in real life materials systems can be many, have a broad spectrum and can be difficult to measure. For example, accurate prediction of grain growth requires the knowledge of grain boundary energies (GBE) and mobilities (GBM) for all boundaries. Both GBE and GBM are functions of a five-dimensional (5D) space, including three parameters for misorientation and two parameters for inclination [10]. Suppose each dimension is loosely binned with a 10 degree interval, a huge number (15 million) of data points are needed for both GBE and GBM, not to mention that these parameters also depend on various thermodynamic variables, *e.g.*, temperature, pressure, and composition. Symmetry could help to reduce the size of the parameter space, but still, a significant amount of data points (6561 for cubic symmetry) are required. Traditionally, the material parameters are measured experimentally using specifically designed samples, *e.g.*, using bi-crystals [11] to measure GBE or GBM. This approach is very time-consuming, and only limited number of values can be determined at a time. Therefore, it is difficult to access even a

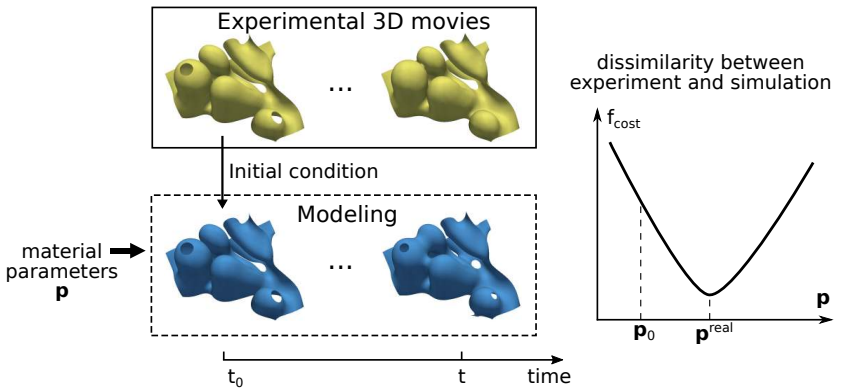

Figure 1.2: Schematic diagram of the fitting approach. A simulated microstructure evolution with given input of material parameter vector $\mathbf{p}$ is compared with an experimentally measured evolution. $\mathbf{p}$ is varied iteratively to identify a minimum $\mathbf{p}^{\text{real}}$ of a cost function f_{cost}.

reasonably large portion of the 5D parameter space. Moreover, in the traditional approach, samples and sample environments used are typically idealized, and the experiment may not represent the real engineering process. For example, in a liquid diffusivity measurement, a cylindrical shaped sample with a planar interface at directional solidification condition is often used. However, solid-liquid interfaces are mostly curved in the engineering process, and the characteristic length scale is typically much smaller than the sample size. Thus the applicability of measured values of material parameters in real engineering applications needs further verification. In recent years, researchers start using atomic-scale calculations to provide values of material parameters, *e.g.*, the free energy [12], diffusion coefficients [13, 14, 15, 16], surface energies [17], and grain boundary properties [18, 19, 20, 21]. However, experimental verification of the quality of the calculated parameters is required. In summary, a new way allowing fast measurements of large amount of values of material parameters using samples and sample environments close to real engineering conditions is highly demanded.

To ensure that the measured values of material parameters apply to the design of engineering materials, a straightforward way is to mimic the real manufacturing process, *i.e.*, to use realistic samples and sample environments, in the measurement. Thus experiments need to be non-destructive and *in situ*. It is also essential to investigate materials in bulk to ensure the relevant length scales are representative and the results are not influenced by artificial boundaries. With the recent development of advanced x-ray imaging techniques, three-

dimensional *in situ* measurements of microstructure evolution become available with synchrotron and laboratory sources [22, 23]. In parallel, the continuous development of materials models and high-performance computing allows fast and detailed simulation of the 3D microstructure evolution of large datasets. Usually, material parameters used in the model are assumed to be known and are treated as input parameters. In this thesis, a new fitting approach, which combines 3D experiments and modeling, is proposed to extract a large number of material parameters' values. As shown in Fig. 1.2, in this approach, the experimental results are treated as input and solution of the model. By fitting the simulated 3D microstructure to the 3D experimental results, the values of material parameters are optimized. The optimal value of the material parameter should correspond to the physical one. This fitting approach has several advantages over traditional methods:

- With this approach, material parameters and an empirically-verified model are obtained simultaneously.
- As the measurements are performed with realistic samples under conditions similar to the engineering processing, the measured material parameters are more representative than those measured in a separate idealized experiment.
- The fitting approach can access the portion of the material parameter space that is most frequently observed in realistic engineering condition.
- Hundreds or even thousands of material parameters' values can be determined simultaneously in one experiment.
- The fitting approach can be applied to a wide variety of materials and processing methods.

The thesis is organized as follows: experiments and simulation techniques used are presented in Chapter 2. In Chapter 3, the theory of the fitting approach is given in detail. Previous measurements of material parameters related to this work are reviewed. In Chapter 4, the fitting approach is firstly tested on a hypoeutectic Al-Cu alloy to determine two important material parameters in coarsening: the liquid diffusion coefficient and the capillary length. In Chapter 5, the fitting approach is applied to a more challenging problem – fitting reduced grain boundary mobilities in pure iron. Conclusions and outlook are given in Chapter 6.
Two journal papers are attached to this thesis. In Paper I, the fitting methodology was proposed and was applied to a simple case of Al-Cu to fit two material parameters. In Paper II, the grain growth experiment of pure iron was presented, and statistical analysis of the material system was carried out to serve as a basis for fitting.

Chapter 2

Background

In this chapter, experimental techniques and materials models are introduced. In Section 2.1, a brief description of non-destructive 3D experiments and related data analysis are given. In Section 2.2, the thermodynamic foundation of materials models are introduced and two kinds of materials models - the sharp interface model and the phase-field model - are presented. Previous measurements of material parameters studied in this thesis are reviewed in Section 2.3.

2.1 Non-destructive 3D experiments

Optical microscopes (OM) and scanning electron microscopes (SEM) are widely used in examining materials microstructures in 2D sections. However, 2D sections only provide part of the information of materials behaviors because materials microstructures are generally 3D. Moreover, these 2D techniques cannot be used to investigate internal stress, as stress tends to be relieved on surfaces. Combined with serial sectioning, OM and SEM can be used to study 3D microstructures [24, 25]. However, serial sectioning is a destructive characterization method; thus cannot be used to examine the dynamics of microstructures. To study the evolution of 3D materials microstructures, non-destructive measurement is essential. The most widely used non-destructive techniques rely on

x-rays because x-rays can penetrate a substantial distance in matter. Moreover, synchrotron sources can provide high intensity and brilliance x-rays, which is essential for fast and precise measurements.

2.1.1 Interaction of x-rays with matter

In the typical range of x-ray energy used in materials science, x-rays interact with matter in three ways: absorption, diffraction, and Compton scattering. For imaging, the former two are the most relevant. These two interactions will be briefly introduced in the following subsections.

2.1.1.1 Absorption

When an x-ray beam with intensity I_0 passes through a homogeneous slab of matter of thickness z, it is partly absorbed. The transmitted intensity I is determined according to Beer-Lambert law [22]

$$I = I_0 e^{-\mu z}, \tag{2.1}$$

where μ is the linear attenuation coefficient. Different elements have different abilities to absorb x-rays, and the attenuation coefficient μ can be related to the absorption cross-section σ_a by

$$\mu = \rho_{\mathrm{at}} \sigma_a = \frac{\rho_m N_A}{M} \sigma_a, \tag{2.2}$$

where ρ_{at} is the atomic density, ρ_m is the mass density, N_A is the Avogadro's number, and M is the molar mass. For materials composed of N elements, the attenuation coefficient can be calculated from the element absorption cross-section σ_a^i and the atomic density ρ_{at}^i by

$$\mu = \sum_i^N \rho_{\mathrm{at}}^i \sigma_a^i. \tag{2.3}$$

2.1.1.2 Diffraction

As shown in Fig. 2.1, an x-ray beam with wavelength $\lambda = 2\pi / |\mathbf{k}|$ is diffracted by a crystalline material if and only if the Bragg condition is fulfilled [22], *i.e.*

$$n\lambda = 2 d_{hkl} \sin\theta, \tag{2.4}$$

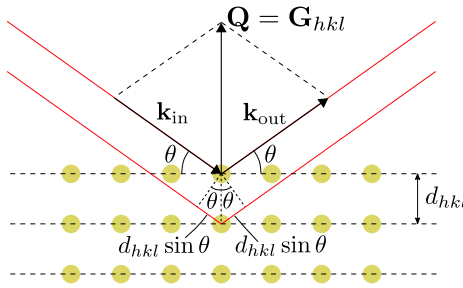

Figure 2.1: Schematic diagram of diffraction in Bragg geometry. The incoming wave vector $\mathbf{k}_{\text{in}}$ with incident angle θ is diffracted to generate the outgoing beam with wave vector $\mathbf{k}_{\text{out}}$. The diffraction vector is $\mathbf{Q} = \mathbf{k}_{\text{out}} - \mathbf{k}_{\text{in}}$ and the reciprocal lattice vector associated with the (hkl) lattice plane is $\mathbf{G}_{hkl}$. $d_{hkl} = 2\pi / |\mathbf{G}_{hkl}|$ is the lattice plane distance.

where n is a positive integer, d_{hkl} is the distance between adjacent (hkl) lattice planes, and the incident and the diffracted angles both equal θ. An alternative way to express the diffraction condition is the Laue condition [22]

$$\mathbf{Q} = \mathbf{G}_{hkl}, \tag{2.5}$$

where $\mathbf{Q}$ is the diffraction vector and $\mathbf{G}_{hkl} = h\mathbf{a}_1^* + k\mathbf{a}_2^* + l\mathbf{a}_3^*$ is the reciprocal lattice vector ($\mathbf{a}_i^*$ are the reciprocal lattice basis).

Far from absorption edges, the observed diffraction intensity I has an important property given by Friedel's law [22]

$$I(\mathbf{Q}) = I(-\mathbf{Q}). \tag{2.6}$$

Eq. 2.6 means the diffracted intensity $I(\mathbf{Q})$ from the (hkl) lattice plane and $I(-\mathbf{Q})$ from the $(\bar{h}\bar{k}\bar{l})$ lattice plane are the same. In other words, in a typical diffraction experiment where a monochromatic beam is applied and the sample is rotated by 360° around an ω-axis perpendicular to the incoming beam, the same intensity can be observed four times: at $\omega = \alpha$, $\omega = \pi - \alpha$, $\omega = \alpha + \pi$, and $\omega = 2\pi - \alpha$.

2.1.2 X-ray imaging techniques

Imaging techniques are used to provide 3D images of an object in real space. Two techniques corresponding to interactions mentioned in Section 2.1.1 are presented, including the absorption contrast tomography and the diffraction-based tomography.

2.1.2.1 Absorption contrast tomography

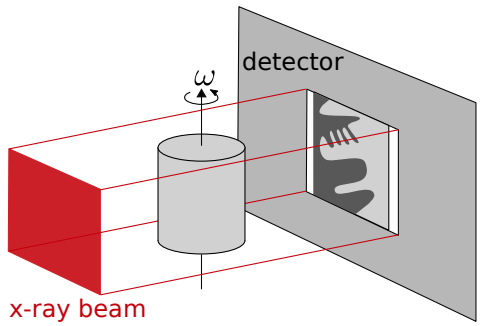

Figure 2.2: Schematic diagram of absorption contrast tomography. The sample rotates continuously on a rotation stage ω. A parallel x-ray beam illuminates the sample, and the transmitted beam is recorded on a detector.

Data acquisition A typical geometry for absorption contrast tomography with a parallel beam (typical of synchrotron setups) is shown in Fig. 2.2. An x-ray beam confined by certain slits illuminates the sample. The intensity of the transmitted beam is measured by a 2D detector while the sample rotates continuously around an axis perpendicular to the beam. According to Eq. 2.3, images captured by the detector reflect regions with different attenuation coefficients μ, *i.e.*, different phases/domains in the sample. When these phases/domains in the sample show a weak contrast difference, *i.e.*, having a similar linear attenuation coefficient μ, the technique of phase contrast tomography (PCT) can be used to gain better contrast [26].

Data analysis: reconstruction According to Eq. 2.1, the images on the detector reflect the integrated attenuation coefficient along the x-ray trajectory:

$$\ln\left(\frac{I}{I_0}\right) = -\int \mu(z)\,\mathrm{d}z. \tag{2.7}$$

Eq. 2.7 means each image reflects a projection of μ at a given rotation angle ω of the sample. The 3D distribution of $\mu(\mathbf{x})$, *i.e.*, the internal microstructure of the sample can be reconstructed from a series of projections. The most common used reconstruction techniques are filtered back projection (FBP) [27] and algebraic reconstruction technique (ART) [28]. The output of reconstruction is usually a voxelized volume with intensity values, which will be further segmented. For details on the reconstruction techniques, the reader can refer to, *e.g.* [29].

Data analysis: segmentation The segmentation process refers to the partition of the reconstructed volume into multiple regions to identify different phases/domains in the sample. There are two commonly used techniques: the threshold methods (*e.g.*, Otsu thresholding [30] and k-means clustering [31, 32]) and the variational methods (*e.g.*, level-set based methods [33, 34] and phase-field based methods [35, 36]). In this thesis, the threshold method and the level-set based segmentation are used.

Resolution The spatial resolution of the absorption contrast tomography is typically in a micrometer range with millimeter-sized samples. The temporal resolution can be as low as ten milliseconds [37].

2.1.2.2 Diffraction-based tomography

Since the development of three-dimensional x-ray diffraction (3DXRD) [38, 39], the tomographic principles are applied to the diffracted beam instead of the transmitted beam. In this way, the grains within polycrystals are visualized in 3D, and their crystallographic properties (orientation and stress) are determined [40, 41, 42, 43]. Based on this principle, various generalizations have been developed, such as diffraction contrast tomography (DCT) [44, 45, 46] and dark-field x-ray microscopy (DFXRM) [47]. As DCT is used in this thesis, it is briefly introduced below.

Data acquisition in DCT A typical DCT geometry with a parallel beam is shown in Fig. 2.3. The x-ray beam confined by slits illuminates a polycrystalline sample. Once the Bragg condition (Eq. 2.4) is fulfilled for a given grain, a diffraction spot will be observed on the detector. The spot on the detector is a 2D projection of the 3D grain shape. As the sample rotates continuously for 360°, different lattice planes of a grain come into the diffraction condition, and various spots from the same grain are recorded on the detector. In the middle of the detector is the transmitted beam, which is used to reconstruct the sample shape based on the principles described in Section 2.1.2.1. In most cases, the transmitted beam is much stronger than the diffracted beam, so either a detector with large dynamic range is used, or a beamstop is put between the sample and the detector to block a majority of the transmitted beam and to reduce image background noises in this area.

Data analysis in DCT The data analysis in the DCT includes the following key steps:

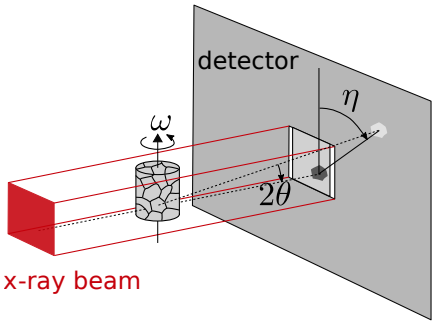

Figure 2.3: Schematic diagram of diffraction contrast tomography (DCT). A parallel x-ray beam illuminates a continuously rotating polycrystalline sample. Whenever the Bragg condition (Eq. 2.4) is fulfilled, a diffraction spot will be observed on the detector. The angle between the diffracted beam and the incident beam is 2θ. ω is the rotation angle, and η is the azimuthal angle. Extinction spots from the grains may be observed as dark spots in the transmitted beam, which is recorded in the middle of the detector.

1. Segmentation of diffraction spots from raw images,
2. Indexing diffraction spots,
3. Reconstruction of grain volumes individually,
4. Segmentation of the reconstructed grain volumes,
5. Assembly of individual grain volumes into the sample volume.

The segmentation (steps 1 and 4) and reconstruction (step 3) used in DCT are similar to those used in the absorption contrast tomography (see Section 2.1.2.1). The main differences between DCT and absorption contrast tomography are the indexing (step 2) and the assembly (step 5).
The indexing process groups the diffraction spots originating from the same grain into sets. Based on the DCT geometry in Fig. 2.3 and Friedel's law in Eq. 2.6, the Friedel pair for each reflection is found. Friedel pairs associated with a grain are used to determine the crystallographic orientation and the center-of-mass position of the grain inside the sample. Some spots cannot be detected as Friedel pairs because of the finite-sized detector. These individual spots are added to the group of spots associated with a grain afterward. Typically, several few up to a hundred spots can be detected for each grain. For details on the indexing procedure, please refer to [45, 46].
Given the diffraction spots associated with a grain, reconstruction and segmentation algorithms are applied to get the 3D grain volume. This process is

repeated for each grain. The grain volumes are then assembled into the sample volume. The reconstruction of the transmitted beam is used to confine the sample volume. As each grain is reconstructed individually, there may be gaps or overlaps between grains in the sample volume. These ambiguities can be removed by a 3D morphological dilation process [44].

Resolution The resolution of DCT is around 1 μm with millimeter-sized samples. The pixel size of current setup at ID11 ESRF is 1.54 μm. Using 2× and 2.5× eyepieces, the pixel size can be reduced to 0.77 μm and 0.62 μm, respectively. The scanning time is typically $1 \sim 3$ hours. DCT in its original form (one average orientation per grain) works best for non-deformed materials (intragranular orientation spread below 0.5 degrees). Higher values of orientation spread can be addressed using a recent extension of the reconstruction algorithm to a 6-D framework [48, 49].

2.2 Materials theory

In this section, I will start from the thermodynamics of materials, which is essential for building materials models. Then two sharp interface models are presented and discussed. The solution of the sharp interface model is used to verify the phase-field model. The fundamental principle of the phase-field model is presented, and details are given. In particular, two phase-field models used in the fitting are given.

2.2.1 Thermodynamics of materials

A majority of materials models at mesoscale are constructed based on thermodynamic principles. A brief introduction to an essential part is given here. For further details, the reader can refer to, *e.g.* [50, 51, 52, 53].

The second law of thermodynamics (the maximum entropy principle) can provide physical constraints or formulate equations. This law states the entropy S of an isolated system does not decrease spontaneously:

$$\frac{\mathrm{d}S}{\mathrm{d}t} \geq 0. \tag{2.8}$$

For systems that interact with surroundings, *e.g.*, exchanging energy or matter, the maximum entropy principle can be reformulated into the following minimum

energy principle using Legendre transforms.

$$\frac{\mathrm{d}F}{\mathrm{d}t} \leq 0, \tag{2.9}$$

where F can be the Helmholtz free energy, enthalpy, Gibbs' free energy, or grand potential, depending on the type of interactions the system has with its surroundings.

The thermodynamics can be extended to non-uniform systems under the local equilibrium assumption: *locally the intensive thermodynamic variables acquire equilibrium so fast that we can define the local version of the intensive variables* [54]. Let's denote $\boldsymbol{\rho} = \{\rho_1, \rho_2, \cdots\}$ as a generalized density vector. Examples of ρ_k are the energy density, mass density, momentum density, *etc.* For quantities that are globally conserved, *e.g.*, energy and mass, corresponding densities ρ_k must satisfy the continuity equation

$$\frac{\mathrm{d}\rho_k}{\mathrm{d}t} + \nabla \cdot \mathbf{J}^k = \sigma^k, \tag{2.10}$$

where $\mathbf{J}^k$ and σ^k are the corresponding flux and source terms of ρ_k, respectively.

To gain insight into the second law of thermodynamics, the change of entropy density ($s = \mathrm{d}S/\mathrm{d}V$) is formulated using the entropy flux $\mathbf{J}^s$ and the entropy production σ^s based on Eq. 2.10 [50]

$$\frac{\mathrm{d}s}{\mathrm{d}t} = -\nabla \cdot \mathbf{J}^s + \sigma^s. \tag{2.11}$$

Based on non-equilibrium thermodynamics, the local entropy production σ^s can be described as the sum of the product of a generalized flux J^k and a generalized force X^k [50]

$$\sigma^s = \sum_k J^k X^k. \tag{2.12}$$

The generalized forces X^k can be temperature gradient or chemical potential gradient. The generalized flux J^k can be heat or mass fluxes. Notice that the product operation between J^k and X^k depends on their tensor order. It can be shown from non-equilibrium thermodynamics that the local version of the second law of thermodynamics (Eq. 2.8) is

$$\sigma^s \geq 0. \tag{2.13}$$

Compared to Eq. 2.8, the local version of second law Eq. 2.13 is a strong statement, which means even locally entropy does not spontaneously decrease.

If the system is not far from equilibrium, the flux J^k can be Taylor expanded around zero forces ($X^l = 0$) to the first order, which leads to the famous Onsager's flux equation [50]

$$J^k = L_{kl} X^l, \tag{2.14}$$

where L_{kl} are the Onsager's kinetic coefficients.

The continuity equation (Eq. 2.10), the local form of second law (Eq. 2.13), the entropy production (Eq. 2.12), and the relation between generalized forces and fluxes (Eq. 2.14) are the basis to formulate many materials models at the mesoscale. For example, Fick's first law of diffusion is a special case of Eq. 2.14 and Fick's second law of diffusion is a special case of Eq. 2.10.

2.2.1.1 Thermodynamics of interfaces - Gibbs model

Interfaces are common in many material microstructures, appearing as solid-liquid interfaces, grain boundaries, ferroelectric domain walls, *etc.* The presence of interfaces contributes to thermodynamic quantities. A well-known model to formulate the thermodynamics of interfaces is the Gibbs' interfacial excess model [55]. Suppose an extensive thermodynamic quantity of the system is X, the excess term of X is defined as

$$X^{\text{interface}} := X - X^{\text{bulk}}, \tag{2.15}$$

where X^{bulk} is the contribution from the bulk phases. The total free energy can be split into the bulk part and the interface part

$$F = F^{\text{bulk}} + F^{\text{interface}} = \int_{\mathcal{D}} f^{\text{bulk}} \,\mathrm{d}V + \int_{\Gamma} f^{\text{interface}} \,\mathrm{d}A, \tag{2.16}$$

where f^{bulk} is the bulk free energy density and $f^{\text{interface}}$ is the interfacial/surface energy, $\mathcal{D}$ is the domain of the bulk structure, and Γ is the interface.

An important type of interface is the grain boundary. Grain boundaries play a central role in many properties of polycrystalline materials [56, 57, 58, 59]. Characterization of a grain boundary requires the misorientation between adjacent grains and the inclination of the grain boundary plane [60, 10, 61], as illustrated in Fig. 2.4. Orientation matrices of grain 1 and grain 2 are denoted as $\mathbf{g}_1$ and $\mathbf{g}_2$, respectively. For details on the grain orientation and its representations, the reader can refer to textbooks on texture, *e.g.* [62, 63]. The misorientation of the grain boundary between two grains is defined as

$$\Delta\mathbf{g} = \mathbf{g}_2\mathbf{g}_1^{-1} = \mathbf{g}_1\mathbf{g}_2^{-1}.$$

Notice that the symmetry of crystalline materials should be taken into account when calculating the misorientation. For grain boundaries with the same misorientation, atoms may arrange differently for boundary planes with different inclinations $\hat{n}$, as shown in Fig. 2.4 (right). Thus, both the misorientation $\Delta\mathbf{g}$ and the boundary plane inclination $\hat{n}$ are needed to get a full picture of the grain

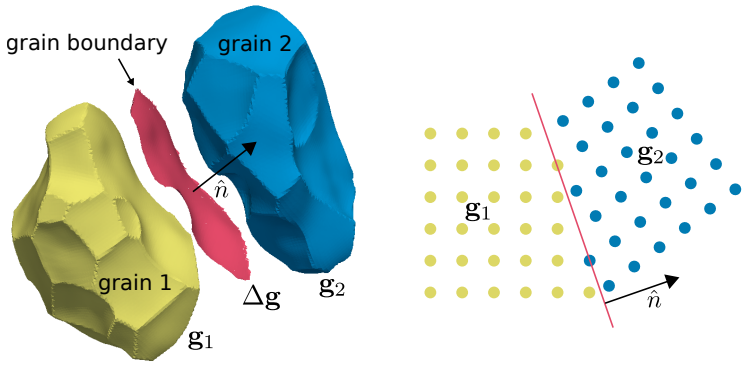

Figure 2.4: Grain boundary characteristics. The two adjacent grains share the grain boundary shown in red. The grains are separated for visualization purpose. The right figure is a zoom-in view in the vicinity of one point at the grain boundary, where atoms are shown by circles in the corresponding color. The grain orientation $\mathbf{g}_\alpha$ represents the orientation of the crystal lattice in grain α. The inclination $\hat{n}$ represents the orientation of the boundary plane. The grain boundary at each grain boundary point is characterized by the misorientation between two grains $\Delta\mathbf{g} = \mathbf{g}_2\mathbf{g}_1^{-1}$ and the inclination $\hat{n}$.

boundary characteristics. In summary, the grain boundary can be characterized by five parameters: three parameters in misorientation $\Delta\mathbf{g}$ and two in inclination $\hat{n}$. The grain boundary energies σ_{gb} and mobilities M_{gb} are functions of the 5D parameter space.

$$m_{\text{gb}}(\Delta\mathbf{g}, \hat{n}) = M_{\text{gb}}(\Delta\mathbf{g}, \hat{n})\sigma_{\text{gb}}(\Delta\mathbf{g}, \hat{n}), \tag{2.17}$$

where m_{gb} is called the reduced mobility.

2.2.1.2 Thermodynamics of interfaces - Gibbs-Thomson equation

The presence of a curved interface can alter thermodynamic quantities. The Gibbs-Thomson equations describe the difference between thermodynamic quantities of a curved interface with mean curvature $\mathcal{H}$ and those of a planar interface.

Isotropic materials The Gibbs-Thomson equation can be derived based on the Gibbs model given in Section 2.2.1.1 and thermodynamic equilibrium conditions at the interface [64].

Let's denote $\cdot|_{\mathcal{H}}$ as the quantity of a curved interface with mean curvature $\mathcal{H}$ and $\cdot|_{\text{planar}}$ as the quantity of a planar interface. For isotropic materials, the change of melting temperature T_M of a curved interface as compared to a planar one ($\Delta T_M = T_M|_{\mathcal{H}} - T_M|_{\text{planar}}$) can be described by the Gibbs-Thomson equation [64]:

$$\Delta T_M = -2\Gamma\mathcal{H}, \tag{2.18}$$

where Γ is the Gibbs-Thomson coefficient. In a similar fashion, the change of composition of a curved interface as compared to a planar one ($\Delta c = c|_{\mathcal{H}} - c|_{\text{planar}}$) is [64]:

$$\Delta c = l\mathcal{H}, \tag{2.19}$$

where l is the capillary length. Similarly, the change in chemical potential difference between a curved interface and a planar interface is

$$\Delta\mu = 2\sigma\mathcal{H}. \tag{2.20}$$

Here σ is the interfacial energy, μ is the chemical potential and $\Delta\mu = \Delta\mu|_{\mathcal{H}} - \Delta\mu|_{\text{planar}}$ (Δ on the right of the equal sign refers to the difference of chemical potential between two phases on each side of the interface).

Anisotropic materials For anisotropic materials, the energy depends on misorientation $\Delta\mathbf{g}$ and inclination $\hat{n}$: $\sigma(\Delta\mathbf{g}, \hat{n})$, as shown in Section 2.2.1.1. The change in chemical potential difference is [65, 66]

$$\Delta\mu = \left(\sigma + \frac{\partial^2\sigma}{\partial {n_1}^2}\right)\kappa_1 + \left(\sigma + \frac{\partial^2\sigma}{\partial {n_2}^2}\right)\kappa_2 = \nabla_\Gamma \cdot \boldsymbol{\xi}, \tag{2.21}$$

where κ_i are the principal curvatures, n_i are components of the norm along the principal coordinate directions, $\nabla_\Gamma \cdot (\cdot)$ is the surface divergence operator (see Eq. A.2), and $\boldsymbol{\xi}$ is the Cahn-Hoffman vector [67]. Notice that Eq. 2.21 reduces to the isotropic equation (Eq. 2.20) if the inclination dependence of the energy is ignored.

2.2.1.3 Thermodynamics of triple-junctions

The triple-junction line is the line where three grains meet, as shown in Fig. 2.5. Triple-junctions are frequently observed in materials with more than two grains or domains. According to the minimum energy principle (Eq. 2.9), a force balance at the triple-junction can be derived. This force balance is described by the Herring's relation [65]:

$$\sum_{i=1}^{3}\left(\sigma_i\hat{t}_i + \frac{\partial\sigma_i}{\partial\hat{n}_i}\right) = \mathbf{0}, \tag{2.22}$$

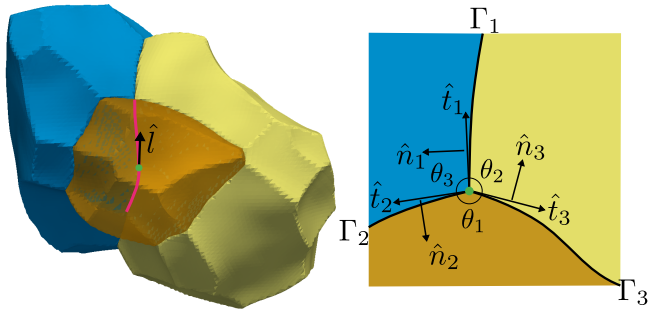

Figure 2.5: Illustration of triple-junction line (red line) shared by three grain boundaries Γ_i. The right figure is a section plot at the triple-junction point (green dot) perpendicular to $\hat{l}$ viewed from the top.

where σ_i is the energy of the ith grain boundary Γ_i, $\hat{t}_i$ is the vector in the plane of Γ_i and normal to the triple-junction line, and $\hat{n}_i$ is the normal vector of Γ_i. See Fig. 2.5 for an illustration of the symbols. Eq. 2.22 can be formulated in a compact form using the Cahn-Hoffman vector [67]:

$$\sum_{i}^{3} \boldsymbol{\xi}_i \times \hat{l} = \mathbf{0}, \tag{2.23}$$

where $\boldsymbol{\xi}_i$ is the Cahn-Hoffman vectors of the ith grain boundary, and $\hat{l}$ is the tangent vector of the triple-junction line, *c.f.*, Fig. 2.5. For details on the Cahn-Hoffman vector $\boldsymbol{\xi}$, please refer to [66, 67].
If the inclination dependence of the energy is neglected, Herring's relation (Eq. 2.22 or Eq. 2.23) reduces to Young's law:

$$\frac{\sigma_1}{\sin\theta_1} = \frac{\sigma_2}{\sin\theta_2} = \frac{\sigma_3}{\sin\theta_3}. \tag{2.24}$$

For the case that all boundaries inside a sample have the same interfacial energy (*e.g.*, in soap bubbles), all triple-junction angles are 120° (Plateau's law).

2.2.2 Sharp interface materials models

Based on the theory of thermodynamics, such as those given in Section 2.2.1, we can formulate partial differential equations (PDEs) to describe the behavior of materials at mesoscale. Depending on whether an interface is treated as a sharp interface with zero width or a diffuse interface with a finite width, the materials models can be categorized into two types [68]: the sharp interface

model and the diffuse interface model. A brief overview of the sharp interface models for material processes: isothermal solidification and grain growth are presented. These two processes will be used in the fitting later. Analytical solutions for the sharp interface model with ideal geometries and boundary conditions are presented and will serve as the basis for verifying the phase-field models presented in Section 2.2.3. Difficulties faced by the sharp interface models are also discussed.

2.2.2.1 Sharp interface model for isothermal solidification

In this part, a sharp interface model for the case of isothermal solidification is presented. Consider a domain $\mathcal{D} = \Omega^{\mathrm{S}} \cup \Omega^{\mathrm{L}}$ composed of a solid region Ω^{S} and a liquid region Ω^{L}. The interface between Ω^{S} and Ω^{L} is denoted by Γ ($\Gamma = \Omega^{\mathrm{S}} \cap \Omega^{\mathrm{L}}$). The general equations for isothermal solidification are given in Eq. 2.25: (a1-2) the diffusion equations in the bulk region (Fick's law of diffusion); (b1-2) the Gibbs-Thomson equations at the curved interface (Eq. 2.19); (c) the mass conservation equation at the interface; (d) the initial condition.

$$
\begin{cases}
\partial_t c(\mathbf{x},t) = \nabla \cdot (D^{\mathrm{S}} \nabla c(\mathbf{x},t)) & \mathbf{x} \in \Omega^{\mathrm{S}} \quad (a1) \\
\partial_t c(\mathbf{x},t) = \nabla \cdot (D^{\mathrm{L}} \nabla c(\mathbf{x},t)) & \mathbf{x} \in \Omega^{\mathrm{L}} \quad (a2) \\
c(\mathbf{x},t) = c^{\mathrm{S,eq}} - l^{\mathrm{S}} \mathcal{H} & \mathbf{x} \in \Gamma^{-} \quad (b1) \\
c(\mathbf{x},t) = c^{\mathrm{L,eq}} - l^{\mathrm{L}} \mathcal{H} & \mathbf{x} \in \Gamma^{+} \quad (b2) \\
(c|^{+} - c|^{-})V = -D^{\mathrm{L}} \partial_n c|^{+} + D^{\mathrm{S}} \partial_n c|^{-} & \mathbf{x} \in \Gamma \quad (c) \\
c(\mathbf{x},0) = c^{\mathrm{m}}(\mathbf{x}) & \mathbf{x} \in \mathcal{D} \quad (d)
\end{cases}
\tag{2.25}
$$

where D^{S} and D^{L} are the solid and liquid diffusion coefficient, respectively; l^{S} and l^{L} are solid and liquid capillary lengths, respectively; $c^{\mathrm{S,eq}}$ and $c^{\mathrm{L,eq}}$ are equilibrium compositions and $c^{m}(\mathbf{x})$ represents an initial composition field. There is no general solution for Eq. 2.25. However, for special cases, as shown in Fig. 2.6, analytical solutions can be obtained.

For the case shown in Fig. 2.6a - isothermal solidification of precipitate growth inside an infinite initially uniform media with composition c^{m} - an analytical solution can be derived under assumptions of negligible solid diffusivity $D^{\mathrm{S}} = 0$ and insignificant capillary effect ($l^{\mathrm{S}}\mathcal{H} = 0$ and $l^{\mathrm{L}}\mathcal{H} = 0$). The analytical solution

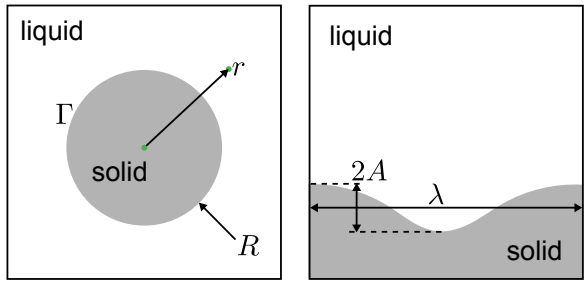

(a) Spherical particle **(b)** Sinusoidal interface

Figure 2.6: Test problems for the isothermal solidification. (a) Spherical precipitate growth inside an infinitely large liquid phase. (b) The decay of a sinusoidal interface in 2D.

for the composition field is [69]:

$$c(r,t) = c^m + (c^{\mathrm{L,eq}} - c^m)\frac{\phi_d\left(\frac{r}{\sqrt{D^{\mathrm{L}}t}}\right)}{\phi_d\left(\frac{R(t)}{\sqrt{D^{\mathrm{L}}t}}\right)}, \tag{2.26}$$

where $d = 1, 2$, and 3 represent dimension 1D, 2D, and 3D, respectively. The radius is

$$R(t) = k_d\sqrt{D^{\mathrm{L}}t}, \tag{2.27}$$

and the function $\phi_d(\cdot)$ is expressed as

$$\phi_d(x) = \int_x^{+\infty} \frac{1}{\xi^{d-1}} e^{-\frac{\xi^2}{4}}\,\mathrm{d}\xi.$$

The parameter k_d is the solution of the following equation:

$$(k_d)^d = \frac{c^{\mathrm{m}} - c^{\mathrm{L,eq}}}{c^{\mathrm{S,eq}} - c^{\mathrm{L,eq}}}\frac{2e^{-\frac{k_d^2}{4}}}{\phi_d(k_d)}.$$

For the case of the sinusoidal interface shown in Fig. 2.6b, the solution of the composition field for an infinitely large liquid phase is [70]

$$c^{\mathrm{L}} = c^{\mathrm{L,eq}} - A_0 l^{\mathrm{L}} k^2 \exp\left(-\sqrt{\frac{\zeta + D^{\mathrm{L}}k^2}{D^{\mathrm{L}}}}z\right) e^{i\mathbf{k}\cdot\mathbf{r}+\zeta t}, \tag{2.28}$$

where $k = 2\pi/\lambda$ is the wavenumber of the perturbed interface, A_0 is the initial amplitude of the interface, and the decay coefficient ζ is

$$\zeta = \frac{D^{\mathrm{L}}d_0^2k^4}{2}\left(1 - \sqrt{1 + \frac{4}{d_0^2k^2}}\right), \tag{2.29}$$

where $d_0 = l^{\mathrm{L}}/[2(c^{\mathrm{L,eq}} - c^{\mathrm{S,eq}})]$. The amplitude of the sinusoidal interface is

$$A(t) = A_0 e^{\zeta t}. \tag{2.30}$$

These analytical solutions are used to verify the phase-field model, as will be shown in Chapter 4.

2.2.2.2 Sharp interface model for grain growth

The underlying assumption in many grain growth models is that the normal velocity $v_n = \mathbf{v} \cdot \hat{n}$ is linearly proportional to the driving force $\Delta\mu$:

$$v_n = -M_{\mathrm{gb}} \Delta\mu, \tag{2.31}$$

where M_{gb} is the grain boundary mobility. If the inclination dependence is neglected, general equations for grain growth are obtained by substituting the Gibbs-Thomson equation (Eq. 2.20) into Eq. 2.31:

$$\begin{cases} v_n = -M_{\mathrm{gb}} \sigma_{\mathrm{gb}} 2\mathcal{H} \quad \mathbf{x} \in \Gamma_{\mathrm{GB}} & (a) \\ \mathcal{G}(\mathbf{x}, t=0) = \mathcal{G}_0 & (b) \end{cases} \tag{2.32}$$

where σ_{gb} is the grain boundary energy and $\mathcal{G}$ represents the geometry of the microstructure. Eq. 2.32(b) is the initial condition. In the most general case, there is no analytical solution for this equation. However, for an individual grain α, the exact integral of the normal velocity, *i.e.*, the growth rate

$$\frac{\mathrm{d}V_\alpha}{\mathrm{d}t} = \int_{\partial\Omega_\alpha} v_n \, \mathrm{d}A,$$

can be derived for 2D (von Neumann-Mullins law) [71, 72] and, more recently, for 3D isotropic case, *i.e.*, uniform grain boundary energy and mobility, (MacPherson-Srolovitz theory) [73]:

$$\frac{\mathrm{d}V}{\mathrm{d}t} = -2\pi M_{\mathrm{gb}} \sigma_{\mathrm{gb}} \left(\mathcal{L}_{\mathrm{grain}} - \frac{1}{6}\mathcal{M} \right), \tag{2.33}$$

where $\mathcal{L}_{\mathrm{grain}}$ is the mean width of the grain [73], and $\mathcal{M}$ is the total length of all triple-lines of the grain.

The analytical solution of Eq. 2.32 can be found for cases with idealized geometries shown in Fig. 2.7.
For the case of a spherical grain inside another (see Fig. 2.7a), the mean width and the total triple-junction line length of grain 1 are $\mathcal{L}_{\mathrm{grain}} = 4R$ and $\mathcal{M} = 0$, respectively. Substituting them into Eq. 2.33, we have the radius of grain 1

$$R(t)^2 = R_0^2 - 4M_{\mathrm{gb}} \sigma_{\mathrm{gb}} t. \tag{2.34}$$

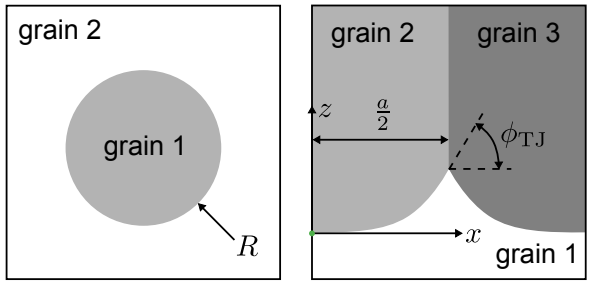

(a) Spherical grain **(b)** three grains

Figure 2.7: Test problems for grain growth. (a) A spherical grain inside another grain. (b) The growth of three grains with one triple-junction.

For the case of 2D, *i.e.*, the growth of a circular grain in another, the radius R is

$$R(t)^2 = R_0^2 - 2M_{\mathrm{gb}}\sigma_{\mathrm{gb}}t. \tag{2.35}$$

Considering the case with three grains shown in Fig. 2.7b, the function of the curved interface between grains 1 and 2 is [72]

$$z(x) = -\frac{1}{\alpha}\ln\cos\alpha x, \tag{2.36}$$

where

$$\alpha = \frac{2\phi_{\mathrm{TJ}}}{a}.$$

See Fig. 2.7b for the definition of symbols. The normal velocity of the interface is

$$v_n = 2\frac{M_{\mathrm{gb}}\sigma_{\mathrm{gb}}}{a}\phi_{\mathrm{TJ}}. \tag{2.37}$$

These analytical solutions are used to verify the phase-field model, as will be shown in Chapter 5.

2.2.2.3 Difficulties in sharp interface models

Most of the problems encountered with the sharp interface model fall into the category of free boundary problems. In other words, the boundary condition is applied on the free boundary, which depends on the solution of the problem, see, *e.g.*, Eqs. 2.25(b1-2,c) and 2.32(a). This makes the sharp interface models very difficult to solve. Only very few cases with simple geometries and boundary

conditions enable analytical solutions. For most cases, the PDE has to be solved numerically. The interface then needs to be tracked explicitly. The explicit tracking of interface causes difficulties in numerical techniques, such as (a) the time-consuming remeshing process in a mesh-based solver and (b) the difficulty of handling topological changes of the microstructure. The level-set models [74, 34, 75] can be used to address these issues with an implicit representation of the interface. However, it is not straightforward to be extended to include other physical phenomena with the level-set method. To overcome these difficulties, the diffuse interface model was introduced. The diffuse interface model is also called the phase-field model for historical reasons, and it will be discussed in the next section. As will be shown later, the phase-field method not only is a mathematical tool but also has clear physical meaning. Another type of model that can avoid explicit tracking of the interface is the Potts model (used mostly in the simulation of grain growth) [76, 77]. The Potts model will not be discussed in this thesis.

2.2.3 Phase-field method

Instead of explicitly tracking the microstructure, a field variable is used to describe the microstructure in the phase-field method [78, 79]. The problem of tracking the interface is transformed to updating the field variable [80]. The diffuse interface model can be mathematically viewed as a regularization of the sharp interface model [81]. It can be shown that the diffuse interface model converges to the corresponding sharp interface model as the interface width tends to zero [82, 83, 84, 85, 86]. In addition, topological changes and singularities can be handled easily [81].

2.2.3.1 Free energy functional

As shown in Eq. 2.16, the total free energy of a system includes the contribution from the bulk region $\mathcal{D}$ and the interface Γ:

$$F = \int_{\mathcal{D}} f^{\text{bulk}} \, \mathrm{d}V + \int_{\Gamma} f_0^{\text{interface}} \, \mathrm{d}A. \tag{2.38}$$

The subscript 0 in $f_0^{\text{interface}}$ is used to denote that it is the sharp interface quantity. The bulk free energy f^{bulk} can be directly measured, *e.g.*, using CALPHAD [87] for the chemical free energy.
In the phase-field method, the interface is treated as a diffused one with finite width instead of a sharp interface. Thus, the surface integral in Eq. 2.38 can be

written as a volume integral (see Appendix A.2)

$$\int_\Gamma f \,\mathrm{d}A = \int_\mathcal{D} f\delta(\phi(\mathbf{x}))\,\mathrm{d}V = \int_\mathcal{D} f\delta^\epsilon(\phi(\mathbf{x}))\,\mathrm{d}V, \tag{2.39}$$

where ϕ is the signed distance function of the interface Γ, and $\delta(\cdot)$ is the delta-function. A regularized delta-function $\delta^\epsilon(\cdot)$ is used to introduce the diffuse interface. With the regularization given in Eq. 2.39, the free energy functional in Eq. 2.38 can be written as

$$F = \int_\mathcal{D} \left(f^{\text{bulk}} + f^{\text{interface}}\right)\,\mathrm{d}V. \tag{2.40}$$

The above argument is purely from a mathematical viewpoint. Physically, based on the Ginzburg-Landau theory, the interfacial energy can be written as [88]

$$f^{\text{interface}} = f(u, \nabla u, \Delta u, \cdots), \tag{2.41}$$

where u is the phase-field. According to symmetry arguments [89], f is a function of even terms, like u^2, u^4, u^6, $|\nabla u|^2$, $(\Delta u)^2$, *etc.* It turns out that only a few terms are enough for practical applications. The most commonly used form is

$$f^{\text{interface}} = W(u) + \frac{1}{2}\kappa|\nabla u|^2, \tag{2.42}$$

where W is a potential energy and the second term has a similar form as the kinetic energy. κ is a positive constant called the gradient energy coefficient. Notice that the $|\nabla u|^2$ term produces the diffuse interface.

2.2.3.2 Evolution equations

Evolution equations can be derived from the second law of thermodynamics. Considering a system described by the composition field c and the phase-field u, its free energy is a functional $F(u, c)$. From Eq. 2.40, the change of the total free energy of the system can be calculated by

$$\begin{aligned}\frac{\mathrm{d}F}{\mathrm{d}t} &= \int_\mathcal{D}\left(\frac{\delta F}{\delta u}\frac{\partial u}{\partial t} + \frac{\delta F}{\delta c}\frac{\partial c}{\partial t}\right)\mathrm{d}V \\ &= \int_\mathcal{D}\left(\frac{\delta F}{\delta u}\frac{\partial u}{\partial t} + \nabla\left(\frac{\delta F}{\delta c}\right)\cdot\mathbf{J}^c\right)\mathrm{d}V.\end{aligned} \tag{2.43}$$

Here the continuity equation (Eq. 2.10) and integral by parts are used (see Appendix A.1). According to the minimum energy principle (Eq. 2.9) and the fact that all possible evolution of the system should make $\mathrm{d}F/\mathrm{d}t \le 0$, we must have

$$\frac{\partial u}{\partial t} = -L\frac{\delta F}{\delta u}, \tag{2.44}$$

and

$$\mathbf{J}^c = -M\nabla\left(\frac{\delta F}{\delta c}\right). \tag{2.45}$$

Substituting Eq. 2.45 into the continuity equation (Eq. 2.10), we get

$$\frac{\partial c}{\partial t} = \nabla \cdot \left[M\nabla\left(\frac{\delta F}{\delta c}\right)\right]. \tag{2.46}$$

Here L and M are positive constants. Eq. 2.44 is the so-called Allen-Cahn equation [90] and Eq. 2.46 is the so-called Cahn-Hilliard equation [89].

2.2.3.3 Sharp interface limit

Here the convergence of the phase-field model to the corresponding sharp interface model is shown by a system of two phases. Suppose the domain of the system is $\mathcal{D}$, and the domain of one phase is Ω. If only interfacial energy is significant ($f^{\text{interface}} \gg f^{\text{bulk}}$), the free energy functional can be obtained from Eqs. 2.40 and 2.42:

$$F_\epsilon(u) = \int_{\mathcal{D}} \left(W(u) + \frac{\epsilon^2}{2}|\nabla u|^2\right) \mathrm{d}V. \tag{2.47}$$

Here ϵ can be viewed as a measure of the diffuse interface width. Based on Eq. 2.44 and the functional derivative given in Appendix A.3, the evolution equation for the free energy function F_ϵ in Eq. 2.47 is

$$\frac{\partial u}{\partial t} = \epsilon^2 \Delta u - W'(u). \tag{2.48}$$

According to the Γ-convergence theory proposed by De Giorgi, the free energy functional $F_\epsilon(u)/\epsilon$ can be shown to converge to the sharp counterpart as ϵ tends to zero [91]:

$$\frac{F_\epsilon(u)}{\epsilon} \xrightarrow{\epsilon \to 0} \sigma \int_{\partial\Omega} \mathrm{d}A, \tag{2.49}$$

where σ is the interfacial energy. Eq. 2.49 indicates that minimizing F_ϵ in Eq. 2.47 is equivalent to minimizing the system's total interfacial energy/interface area at the limit $\epsilon = 0$.

From the asymptotic analysis of Eq. 2.48 (Appendix A.5), the phase-field solution can be approximated from the steady-state solution q as

$$u(\mathbf{x}, t) = q\left(\frac{\phi(\mathbf{x}, t)}{\epsilon}\right) + \mathcal{O}(\epsilon^2). \tag{2.50}$$

where ϕ is the signed distance to $\partial\Omega$. For the case $W(u) = 2u^2(u-1)^2$, the steady-state solution has the form

$$q(x) = \frac{1}{2}\left(1 - \tanh\frac{x}{\epsilon}\right). \tag{2.51}$$

Moreover, the interfacial velocity is shown to recover the sharp condition as

$$v = 2\sigma\mathcal{H} + \mathcal{O}(\epsilon^2), \tag{2.52}$$

where σ is related to the steady-state solution q as

$$\sigma = \int_{-\infty}^{+\infty}\left(W(q(s)) + \frac{\epsilon^2}{2}(q'(s))^2\right)\mathrm{d}s = \int_0^1 \epsilon\sqrt{2W(q)}\,\mathrm{d}q = \frac{\epsilon}{3}. \tag{2.53}$$

With this, the physical parameter σ is linked with the model parameter ϵ. Notice that it is straightforward to extend the convergence study of the two-phase isotropic system presented here to more complex cases (involve more physics and anisotropy), such as those given in Sections 2.2.3.4 and 2.2.3.5.

2.2.3.4 Phase-field model for solidification

The phase-field model for solidification is formulated with two kinds of variables: the phase-field variable $\mathbf{u}(\mathbf{x},t) = \{u_\mathrm{S}(\mathbf{x},t), u_\mathrm{L}(\mathbf{x},t)\} : \Omega \times \mathbb{R}^+ \to \mathbb{R}^2$ and the composition variable $c(\mathbf{x},t) : \Omega \times \mathbb{R}^+ \to \mathbb{R}$. The phase-field variables are used to describe the microstructure: u_S has value one in the solid phase, zero in the liquid phase, and an intermediate value between zero and one near the solid-liquid interface, and vice versa for u_L. In this work, the phase-field model proposed by Moelans [92] is used in the fitting and is presented below.

The interfacial free energy functional $f^{\text{interface}} : \mathbb{R}^2 \to \mathbb{R}$ is

$$f^{\text{interface}}(\mathbf{u}) = W(\mathbf{u}) + \frac{\kappa}{2}\left((\nabla u_\mathrm{S})^2 + (\nabla u_\mathrm{L})^2\right), \tag{2.54}$$

where the potential $W : \mathbb{R}^2 \to \mathbb{R}$ is [93]

$$W(\mathbf{u}) = m\left(\frac{u_\mathrm{S}^4}{4} - \frac{u_\mathrm{S}^2}{2} + \frac{u_\mathrm{L}^4}{4} - \frac{u_\mathrm{L}^2}{2} + \gamma u_\mathrm{S}^2 u_\mathrm{L}^2 + \frac{1}{4}\right). \tag{2.55}$$

Here m and γ are model parameters. Both the chemical bulk free energy functional $f^{\text{bulk}} : \mathbb{R}^2 \times \mathbb{R} \to \mathbb{R}$ and the total composition field c follow the mixture law [94]

$$f^{\text{bulk}}(\mathbf{u}, c) = h^\mathrm{S}(\mathbf{u}) f^\mathrm{S}(c_\mathrm{S}) + h^\mathrm{L}(\mathbf{u}) f^\mathrm{L}(c_\mathrm{L}),$$
$$c = h^\mathrm{S}(\mathbf{u}) c_\mathrm{S} + h^\mathrm{L}(\mathbf{u}) c_\mathrm{L},$$

where the interpolation functions are given by [95]

$$h^{\alpha}(\mathbf{u}) = \frac{u_{\alpha}^2}{\sum_{\beta=\mathrm{L,S}} u_{\beta}^2}, \quad \alpha = \mathrm{L,S}. \tag{2.56}$$

Using a similar procedure as in Section 2.2.3.2, the phase-field equations can be derived as

$$\begin{aligned}
\frac{\partial u_{\mathrm{S}}(\mathbf{x},t)}{\partial t} &= -L\left(m\left[u_{\mathrm{S}}^3 - u_{\mathrm{S}} + 2\gamma u_{\mathrm{S}} u_{\mathrm{L}}^2\right] - \kappa\Delta u_{\mathrm{S}} + \frac{\partial h^{\mathrm{S}}}{\partial u_{\mathrm{S}}}\left[f^{\mathrm{S}} - f^{\mathrm{L}} - (c_{\mathrm{S}} - c_{\mathrm{L}})\tilde{\mu}\right]\right) \\
\frac{\partial u_{\mathrm{L}}(\mathbf{x},t)}{\partial t} &= -L\left(m\left[u_{\mathrm{L}}^3 - u_{\mathrm{L}} + 2\gamma u_{\mathrm{L}} u_{\mathrm{S}}^2\right] - \kappa\Delta u_{\mathrm{L}} + \frac{\partial h^{\mathrm{S}}}{\partial u_{\mathrm{L}}}\left[f^{\mathrm{S}} - f^{\mathrm{L}} - (c_{\mathrm{S}} - c_{\mathrm{L}})\tilde{\mu}\right]\right) \\
\frac{\partial c(\mathbf{x},t)}{\partial t} &= \nabla\cdot\left(\left[h^{\mathrm{S}}(u_{\mathrm{S}},u_{\mathrm{L}})M^{\mathrm{S}}(c) + h^{\mathrm{L}}(u_{\mathrm{S}},u_{\mathrm{L}})M^{\mathrm{L}}(c)\right]\nabla\tilde{\mu} + \mathbf{j}_{\mathrm{at}}\right).
\end{aligned} \tag{2.57}$$

where $\mathbf{j}_{\mathrm{at}}$ is the anti-trapping current [96, 94, 97] and the chemical potential $\tilde{\mu}$ is

$$\tilde{\mu} = \frac{\partial f^{\mathrm{S}}}{\partial c^{\mathrm{S}}} = \frac{\partial f^{\mathrm{L}}}{\partial c^{\mathrm{L}}}. \tag{2.58}$$

In this thesis, $\mathbf{j}_{\mathrm{at}}$ is neglected because the solute trapping effect of the problem studied is negligible (see details in Paper I).

Connection between physical parameters and model parameters The phase-field parameters can be connected with material parameters from the asymptotic analysis of the phase-field equation with a similar process as shown in Section 2.2.3.3. The parameter $\gamma = 1.5$ is used to get a symmetric profile, as proposed in [95]. The model parameters can be related to the surface energy σ, mobilities M^{S} and M^{L}, and the interface thickness l by [92]

$$\begin{aligned}
m &= \frac{6\sigma}{l}, \\
\kappa &= \frac{3}{4}\sigma l, \\
L &= \frac{2}{3}\frac{m(M^{\mathrm{S}} + M^{\mathrm{L}})}{\kappa(c^{\mathrm{S,eq}} - c^{\mathrm{L,eq}})^2}.
\end{aligned} \tag{2.59}$$

The mobilities M^{S} and M^{L} can be related to the diffusion coefficients D^{S} and D^{L} by [98]

$$\begin{aligned}
D^{\mathrm{S}} &= M^{\mathrm{S}}\frac{\partial^2 f^{\mathrm{S}}(c_{\mathrm{S}})}{\partial c_{\mathrm{S}}^2}, \\
D^{\mathrm{L}} &= M^{\mathrm{L}}\frac{\partial^2 f^{\mathrm{L}}(c_{\mathrm{L}})}{\partial c_{\mathrm{L}}^2}.
\end{aligned} \tag{2.60}$$

2.2.3.5 Phase-field model for grain growth

Phase-field models for grain growth can be categorized into three kinds depending on the degree of anisotropy considered [99]. (a) If grain boundary energies and mobilities are assumed isotropic, the phase-field model is called *isotropic* [93, 100]. (b) If grain boundary energies and mobilities are assumed to be dependent on the misorientation (3D parameter space, see Section 2.2.1.1), the phase-field model is called *asymmetric* [101, 102, 99] by Tóth *et al.* [99]. (c) If a phase-field model incorporates both the inclination and misorientation dependence of grain boundary energies and mobilities (5D parameter space), it is called *anisotropic* model [86, 103, 95, 104, 20, 99]. Notice that sometimes the model parameters need to be calibrated to correctly capture the triple-junction condition (Eq. 2.22) [105, 106, 107]. In this thesis, as a first step, inclination dependence of grain boundary energies and mobilities are neglected. Thus the model used is categorized as the asymmetric grain growth model [99]. One type of the asymmetric grain growth model is described by the vector-valued Allen-Cahn equation:

$$\partial_t \mathbf{u} = L\left(\kappa \Delta \mathbf{u} - \nabla_{\mathbf{u}} W(\mathbf{u})\right), \tag{2.61}$$

where $\mathbf{u} : \Omega \times \mathbb{R}^+ \rightarrow \mathbb{R}^p, \Omega \subset \mathbb{R}^n$ is the phase-field variable ($n = 2$ for 2D, $n = 3$ for 3D, and p is the total number of grains). The potential used here is a multi-well potential $W : \mathbb{R}^p \rightarrow \mathbb{R}$ [93]:

$$W(\mathbf{u}) = m\left[\sum_{\alpha=1}^{p}\left(\frac{u_\alpha^4}{4} - \frac{u_\alpha^2}{2}\right) + 2\sum_{\alpha=1}^{p}\sum_{\beta\neq\alpha}^{p}\gamma_{\alpha\beta}u_\alpha^2 u_\beta^2 + \frac{1}{4}\right]. \tag{2.62}$$

where $\gamma_{\alpha\beta}$ controls the barrier height between wells. The energy anisotropy is taken into account in $\gamma_{\alpha\beta}$. In this thesis, the grain boundary energy anisotropy is neglected, and $\gamma_{\alpha\beta} = 1.5, \forall \alpha\text{-}\beta$ is used to have a symmetric profile [95]. The gradient of W in phase space is

$$(\nabla_u W(\mathbf{u}))_\alpha = m\left(u_\alpha^3 - u_\alpha + 2u_\alpha \sum_{\beta\neq\alpha}^{p}\gamma_{\alpha\beta}u_\beta^2\right) \quad \alpha = 1, \cdots, p. \tag{2.63}$$

The mobility anisotropy is taken into account in L [95]

$$L(\mathbf{u}) = \frac{\sum_{\alpha,\beta} L_{\alpha\beta}u_\alpha^2 u_\beta^2}{\sum_{\alpha,\beta} u_\alpha^2 u_\beta^2}, \tag{2.64}$$

where $L_{\alpha\beta}$ is related to the boundary between grains α and β.

Connection between physical parameters and model parameters The model parameters $L_{\alpha\beta}$ are linked to the grain boundary mobility M_{gb} by [95]

$$L_{\alpha\beta} = \frac{4M_{\mathrm{gb}}}{3l_{\mathrm{gb}}}, \tag{2.65}$$

where l_{gb} is the grain boundary width, which is controlled by κ and m by

$$l_{\mathrm{gb}} = \sqrt{\frac{8\kappa}{m}}, \tag{2.66}$$

For the case of $\gamma = 1.5$, the grain boundary energies are related to the model parameters by

$$\sigma_{\mathrm{gb}} = \frac{\sqrt{2\kappa m}}{3}. \tag{2.67}$$

The parameter study of McKenna [104] shows that l_{gb} should be greater than 4 grid size and the majority of the grains in the system should have a size larger than $3l_{\mathrm{gb}}$.

2.2.3.6 Boundary conditions

With the aid of the phase-field method, boundary conditions at the free boundary (*e.g.*, Eqs. 2.25(b1, b2, and c) and 2.32(a)) are not needed. However, boundary conditions at the exterior of the simulation domain $\mathcal{D}$ are still required. Two types of boundary conditions are used in this thesis:
(a) the no-flux boundary condition

$$\nabla u \cdot \hat{n} = 0 \quad \mathbf{x} \in \partial\mathcal{D}, \tag{2.68}$$

and (b) the periodic boundary condition

$$u(\mathbf{x} + \mathbf{a}, t) = u(\mathbf{x}, t) \quad \mathbf{x} \in \partial\mathcal{D}, \tag{2.69}$$

where $\hat{n}$ is the outward normal of the exterior boundary of the simulation domain and $\mathbf{a}$ is the period of the microstructure.

2.2.3.7 Efficient phase-field algorithm for grain growth

In most cases, a grain only spans a small space in a simulation domain. In other words, phase-field variables u_α have zero value in most of the simulation domain. Based on this observation, computational- and memory-efficient algorithms can be built. Krill and Chen [100] proposed a dynamic grain reassignment algorithm

to compress the total number of phase-field variables. However, coalescence cannot be fully eliminated. To eliminate the coalescence, Gruber *et al.* [108] built a sparse data structure to store only phase-field variables larger than a tolerance value. As shown in this work, the memory cost and the computational time reduced significantly. However, the disadvantage is that it is difficult to build an efficient data structure for parallelization. Another approach is the so-called bounding box algorithm proposed by Vanherpe *et al.* [109, 110]. Only phase-field variables within a bounding box are stored. The bounding box algorithm has a larger memory cost than the sparse algorithm but can apply the compiler vectorization easily. However, the prescription of periodic boundary condition is not straightforward with the bounding box algorithm.

2.3 Difficult-to-measure material parameters

The fitting approach applies to a wide variety of materials and applications. In this thesis, I choose to verify the fitting approach through measurements of a set of difficult-to-measure parameters in two materials systems:
(a) Al-Cu alloy with 1-2 free parameters (the liquid diffusion coefficient and the capillary length/surface energy),
(b) Pure polycrystalline iron with hundreds and thousands of parameters (reduced grain boundary mobilities).
In this part, traditional measurements of the liquid diffusion coefficient and grain boundary properties are reviewed and, in particular, their difficulties are highlighted.

2.3.1 Liquid diffusion coefficient in Al-Cu alloy

The liquid diffusion coefficient in an alloy is a well-known difficult-to-measure material parameter. Here the Al-Cu alloy is chosen as an example for illustration, as it is a simple case to demonstrate the fitting approach. Moreover, Al-Cu is a well-studied system, and its liquid diffusion coefficient has been measured by several authors using different techniques. As listed in Table 2.1, measured values show more than one order of magnitude difference. This scatter is believed to be caused by convection in the measurement [111]. The thermal Rayleigh number Ra_T characterizes the importance of natural convection as compared to diffusion [111]:

$$\mathrm{Ra}_T = \frac{g\beta_T G_H d^4}{\nu\alpha},$$

Table 2.1: Literature values of the liquid diffusion coefficient of Al-Cu. The most popular methods rely on measuring the composition profile either by rapid quenching in the capillary tube method [111] or by x-ray radiography [112]. The droplet method measures the movement of a liquid droplet placed in a temperature gradient [113]. In the neutron scattering method, the diffusivity is determined from the quasielastic peak widths [114]. The coarsening method is based on a heuristic comparison between a 3D coarsening experiment and a phase-field simulation [115].

Year	Authors	Values $\times 10^{-9}$ m^2/s	Method
1968	Edwards *et al.* [116]	7.2	review article
1969	Sharp and Hellawell [117]	3	capillary tube
1971	Jordan and Hunt [118]	3.26	capillary tube
1975	Bhat [119]	3.57	capillary tube
1977	Sato and Ohira [120]	5.19∼5.55	capillary tube
1977	Watson and Hunt [113]	3.5	droplet
1980	Froschhammer *et al.*[121]	0.5	capillary tube
2004	Lee *et al.* [111]	2.4	capillary tube
2007	Dahlborg *et al.* [114]	3	neutron scattering
2010	Zhang *et al.* [112]	1.8	x-ray radiography
2011	Aagesen *et al.* [115]	0.83	coarsening

where g is the acceleration due to gravity, G_H is the temperature gradient, d is the characteristic length, and material parameters β_T, ν, and α are the thermal expansion coefficient, kinematic viscosity and thermal diffusivity, respectively. In a liquid diffusion coefficient measurement, the Rayleigh number should be minimized to make convection negligible compared to diffusion. As material parameters β_T, ν, and α are fixed for a given material, the only parameters that can be tailored are G_H, g, and d. The temperature gradient G_H cannot be too small; otherwise, the change in composition field will be too weak to be measured accurately. The gravitational acceleration g can be reduced by performing the experiment in space, *i.e.*, under microgravity environment [122]. However, only a very limited number of experiments can be performed in space. Therefore, the only practical way of lowering Ra_T is reducing the characteristic length d. In capillary tube experiments, the typical range of d is 0.8∼5 mm [117, 118, 119, 120, 121, 111]. In the work of Lee *et al.* [111], the capillary tube diameter was chosen to be small (< 0.8 mm) to minimize the effect of convection. However, it is not clear that convection had been eliminated as a source of bias in these studies. Aagesen *et al.* [115] measured the liquid diffusivity by matching a calculated velocity histogram to the measured one. This measurement was considered to be most accurate as the diffusivity is determined from a 3D coarsening experiment which mimics the condition in the engineering

process and the characteristic length of the microstructure is small ($\sim$100 μm [123]) such that convection is believed to be negligible.

2.3.2 Grain boundary energies and mobilities

In early times, the absolute grain boundary energy was determined by measuring the dihedral angle at triple-junctions during the grain boundary grooving process [124]. With this method, only a few energy values can be measured. With the development of electron backscatter diffraction (EBSD) and serial sectioning techniques, a 3D orientation map can be generated. Based on this orientation map, relative grain boundary energies can be determined from the triple-junction geometry [125, 126, 127], assuming the microstructure is approximately in equilibrium near the triple-junction. Adams *et al.* [125] proposed an algorithm to measure misorientation dependent relative grain boundary energies, which was successfully applied for aluminum [128]. Morawiec [126] proposed an algorithm to measure the 5D relative grain boundary energies. This algorithm was extensively used in Rohrer's group to measure the relative grain boundary energies in MgO [129], Ni [130], yttria [25], and ferritic steel [131]. A grain boundary energy database can also be built with the help of atomic-scale simulations [132, 133, 18, 134, 135, 136, 137]. Barmak *et al.* [132] compared the measured grain boundary energy in aluminum with the calculated energy by molecular dynamics, and a large variation was observed. Rohrer *et al.* [134] compared measured grain boundary energies in nickel with calculated ones. In this work, it was shown that experimentally obtained energies for the high populated grain boundaries showed correlation with calculated energies. However, it should be noticed that all measurements were done on the surface using a destructive method. To summarize, either the experimental data available is inadequate or the quality is not sufficient for the use of materials design.

Experimental measurements of grain boundary mobilities are extremely limited. The most popular approach is the bi-crystal method [11, 138]. In this method, a bi-crystal sample with a specific grain boundary type is manufactured, and the movement of the grain boundary is followed during annealing, from which the grain boundary mobility of this particular grain boundary type is measured. There are two issues of this method: (a) the measurement is only surface measurement, and (b) it is difficult to access a larger portion of the 5D parameter space. With the development of EBSD, grain boundary mobilities can be determined from the measured velocity of the recrystallization front as well as the driving pressure [139, 140]. However, the mobilities of store energy-driven boundaries may be different from that of curvature-driven boundaries. Current grain boundary mobility databases are mainly provided by molecular dynamics simulations [141, 142, 19, 143, 144, 145], but the experimental validation is still

Table 2.2: Review of 3D non-destructive grain growth measurements. The voxel size, the number of time-steps(TS) measured and the total number of grains (No.Gr) in the dataset are listed.

Year	Authors	Technique	Voxel size	TS	No.Gr
2008	Schmidt *et al.* [146]	3DXRD	5∼8 μm	6	480
2011	Li [147]	3DXRD	1.47∼4 μm	6	2000
2014	Syha [148]	DCT	0.7 μm	2	849
2014	McKenna *et al.* [149]	PCT	0.7 μm	2	1200
2015	Lin *et al.* [150]	3DXRD	2∼4 μm	3	2000
2017	Sun *et al.* [151]	LabDCT	5 μm	3	300

lacking.

Inspired by the idea of fitting given in the introduction (Chapter 1), the measurement of grain boundary properties can be performed with a dataset of grain growth. This kind of fitting is impossible before due to lack of experimental methods that can provide time-resolved 3D measurements of grain growth with high temporal and spatial resolution. The development of non-destructive 3D grain mapping techniques such as three-dimensional x-ray diffraction (3DXRD) [39] and diffraction contrast tomography (DCT) [152, 44], provides a possible remedy to the situation. In Table 2.2, a list of previous measurements of grain growth is given. The first 3DXRD results on the growth of 480 Al-Mn grains by Schmidt *et al.* [146], involved six time-steps and a resolution of about 5∼8 μm. Li [147] later used 3DXRD to measure the growth of about 2000 pure nickel grains with a slightly improved resolution (pixel size of 1.47 μm and 4 μm spacing between layers). Lin *et al.* [150] measured the growth of more than 2000 nickel grains with 3DXRD (pixel size of 2 μm and 4 μm layer spacing). Concerning DCT, Syha [148] measured two steps of grain growth in strontium titanate sample with 849 grains and with a voxel size of 0.7 μm. Recently, Sun *et al.* [151] studied three steps of grain growth of more than 300 grains using a laboratory-based DCT [153, 154] with a voxel size of 5 μm. It can be seen that, in all cases, experimental settings were not ideal for a detailed study of grain boundary mobilities and energies. Phase contrast tomography (PCT) using decoration of grain boundaries as the contrast is an alternative method exhibiting a superior spatial resolution [149]. However, the process is not representative of classical grain growth, and PCT does not provide crystallographic information. In this thesis, a DCT dataset with a high spatial resolution (1.54 μm) and 15 annealing time-steps is measured and applied to fit the reduced grain boundary mobilities, as will be shown in Chapter 5.

Chapter 3

Optimization

In this chapter, a fitting approach is introduced to determine material parameters, with an emphasis on the theoretical development. The fitting methodology and related key concepts are first introduced and discussed in Section 3.1. A detailed analysis of specific aspects related to coarsening and grain growth is provided in Sections 3.2 and 3.3, respectively. Applications of the fitting approach to real material systems are given in the following chapters.

3.1 The fitting methodology

To overcome difficulties encountered in traditional material parameters measurements, a fitting approach is proposed to extract material parameters by bridging 3D experiments and 3D simulations. As shown in Fig. 1.2, the fitting approach includes three key components:

1. A 3D experimental movie of evolving material microstructures measured under realistic engineering processing conditions,
2. A simulated movie with one frame of the experimental movie as initial condition and guessed values of material parameters $\mathbf{p}$ as input,

3. Comparison between experiment and simulation and optimization of the value of input material parameters.

Techniques that can provide the experimental movie (point 1) and the simulated movie (point 2) are presented in Sections 2.1 and 2.2, respectively. In this chapter, the focus is on the comparison between two movies, and the optimization of material parameters (point 3), *i.e.*, the fitting process. The fitting process can be described formally by the following optimization problem

$$\begin{aligned} \text{find} \quad & \mathbf{p} \\ \text{minimize} \quad & f_{\text{cost}}(t, \mathbf{p}) = f_{\text{cost}}\left(\mathcal{G}^{\text{exp}}(t), \mathcal{G}^{\text{sim}}(t, \mathbf{p})\right) \\ \text{such that} \quad & \mathcal{G}^{\text{sim}}(t_0, \mathbf{p}) = \mathcal{G}^{\text{exp}}(t_0) \\ & \mathcal{G}^{\text{sim}}(t, \mathbf{p}) \text{ is solution of the materials model.} \end{aligned} \tag{3.1}$$

where $\mathcal{G}^{\text{exp}}(t)$ represents the measured experimental movie, $\mathcal{G}^{\text{sim}}(t, \mathbf{p})$ represents the simulated movie with input values of material parameters $\mathbf{p}$ (*i.e.*, *the design variables*). f_{cost} is a cost function which measures the dissimilarity between the experiment and the simulation, and needs to be minimized (*i.e.*, *the objective function*). There are two kinds of *constraints*: (1) the initial microstructure for the simulation is input from the experiment, and (2) the evolution of the simulated microstructure is described by specific materials model, depending on the studied problem. Examples of materials models can be found in Section 2.2.

3.1.1 The cost function

The cost function plays a central role in the fitting approach. It characterizes the dissimilarity between the simulated microstructure $\mathcal{G}^{\text{sim}}$ and the experimental microstructure $\mathcal{G}^{\text{exp}}$, defined as $f_{\text{cost}} : \mathcal{G}_{\text{sim}} \times \mathcal{G}_{\text{exp}} \to \mathbb{R}$. It takes two microstructural geometries as input and returns a scalar. For the case that the microstructure geometry is implicitly represented by signed distance functions ($\mathcal{G}_{\text{sim}} = \phi_{\text{sim}}$, $\mathcal{G}_{\text{exp}} = \phi_{\text{exp}}$), the cost function can be defined with the q-norm as

$$f_{\text{cost}}(t, \mathbf{p}) = f_{\text{cost}}^{\text{norm}}(\phi_{\text{sim}}, \phi_{\text{exp}}) = \|\phi_{\text{sim}} - \phi_{\text{exp}}\|_q^2 . \tag{3.2}$$

The norm is calculated in the fitting domain Ω_{fit}. For the case that the microstructure geometry is represented by voxelized images ($\mathcal{G}_{\text{exp}} = \text{Img}^{\text{exp}}$, $\mathcal{G}_{\text{sim}} = \text{Img}^{\text{sim}}$), the cost function can be defined with the correlation function as

$$f_{\text{cost}}(t, \mathbf{p}) = f_{\text{cost}}^{\text{corr}}(\text{Img}^{\text{sim}}, \text{Img}^{\text{exp}}) = 1 - \operatorname*{corr}_{\Omega_{\text{fit}}}\left(\text{Img}^{\text{exp}}(t), \text{Img}^{\text{sim}}(t, \mathbf{p})\right). \tag{3.3}$$

The fitting domain Ω_{fit} is not necessarily the whole structure. It can be localized, such as a domain restricted to a region near a specific interface.

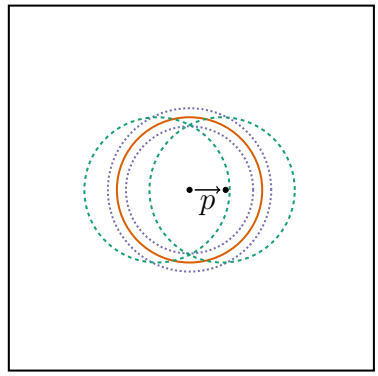

Figure 3.1: Illustration of the synthetic geometry (in 2D direct space) to study properties of the cost function. The solid red line represents the experimental microstructure $\mathcal{G}^{\text{exp}}$. The dashed green lines represent simulated microstructures $\mathcal{G}^{\text{sim}}(p)$ with given material parameter p. The dotted blue lines represent the boundary of the interfacial domain $\Omega_{\text{interface}}$.

Properties of the norm-cost function (Eq. 3.2) and the corr-cost function (Eq. 3.3) are illustrated with an artificial test case (moving circle). As shown in Fig. 3.1, the experimental microstructure $\mathcal{G}^{\text{exp}}$ is the red circle in the middle. Varying p results in a series of simulated microstructures $\mathcal{G}^{\text{sim}}$ (dashed green circles) with their centers shifted a distance p to the right. Cost functions given in Eq. 3.2 and Eq. 3.3 are calculated from $\mathcal{G}^{\text{exp}}$ and $\mathcal{G}^{\text{sim}}(p)$ and are plotted against p in Fig. 3.2. It is seen that all cost functions have a unique minimum at $p = 0$, *i.e.*, a complete match of two microstructures. The corr-cost function (Eq. 3.3) is easy to calculate, but the discretized representation of the microstructure causes the discontinuity in the cost function (see Figs. 3.2 and 3.3), especially when the geometry is represented by a limited number of voxels. The issue caused by discontinuity is not so severe when Ω_{fit} refers to a 3D domain. The norm-cost function (Eq. 3.2) is continuous, but an extra computational effect is needed to get the signed distance functions. As shown in Fig. 3.2, q in the q-norm-cost function only influences the shape of the cost function without changing the minimum. Because the minimum is the only thing concerned in the fitting, q is set to two ($q = 2$) in the following of this thesis.

As only the interface is used in the comparison, the fitting domain Ω_{fit} is limited to the interfacial region $\Omega_{\text{interface}=w}$ with a bandwidth w (see the dotted blue lines in Fig. 3.1). Please refer to Eq. 4 in Paper I for a formal definition of $\Omega_{\text{interface}=w}$. Cost function curves with various bandwidth values w are shown in Fig. 3.3. It is observed that w influences the shape of the corr-cost functions while has an invisible influence on the norm-cost functions. Moreover, all

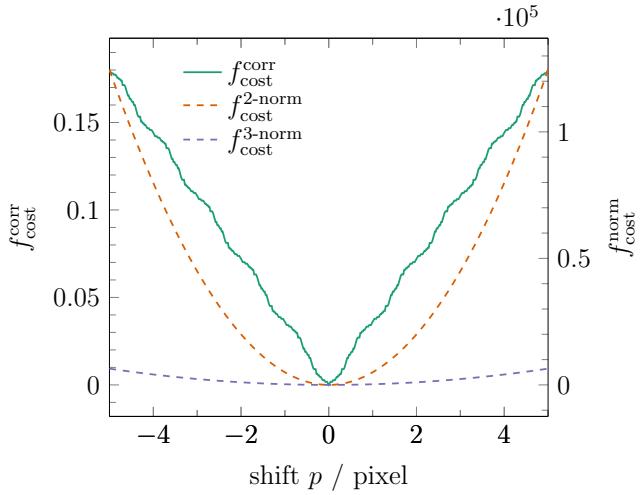

Figure 3.2: The cost functions are plotted against the distance p between the center of $\mathcal{G}^{\text{exp}}$ and the center of $\mathcal{G}^{\text{sim}}$. The fitting domain is the full 2D square of Fig. 3.1.

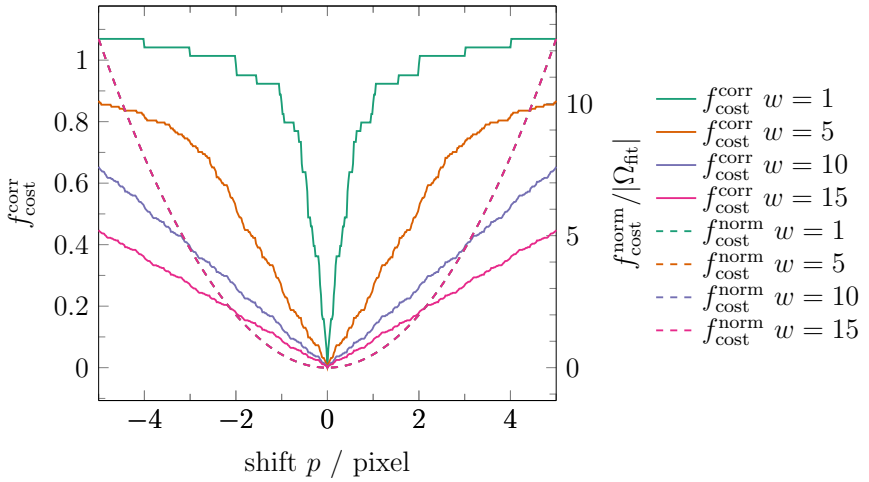

Figure 3.3: Cost functions with different interface bandwidth for the moving circle problem. The fitting domain is restricted to a narrow band with width w near the interface: $\Omega_{\text{fit}} = \Omega_{\text{interface}=w}$. The unit of w is the grid size. The norm-cost function is normalized by the fitting domain size $|\Omega_{\text{fit}}|$. Notice that the influence of w on norm-cost functions (2-norm) are not distinguishable from the plot.

cost functions give the right minimum point where the simulated circle and the experimental circle overlap entirely ($p = 0$).

For a detailed description and discussion of the fitting domain Ω_{fit}, please refer to Section 2.3 in the attached Paper I.

3.1.2 Modeling techniques

In this thesis, the phase-field method is employed as the modeling technique. However, it should be emphasized that there is no limitation in the fitting approach to using any relevant modeling techniques for the studied problem.

The accuracy of the model influences the accuracy of the fitting result; therefore, it is essential to choose a model which is suitable for the materials system and the studied problem. Moreover, it is essential to verify the phase-field model before using it in the fitting. Detailed verification of phase-field models will be given in Chapters 4 and 5.

3.1.3 Reducing computational cost

It can be seen from Eq. 3.1 that phase-field equations need to be solved in each optimization iteration. This makes the fitting time-consuming as 3D phase-field simulations are usually computationally expensive. However, in practice, many properties of the phase-field equation can be used to reduce the computational cost. An example is a scaling property

$$\mathcal{G}^{\text{sim}}(t, k\mathbf{p}) = \mathcal{G}^{\text{sim}}(kt, \mathbf{p}). \tag{3.4}$$

It means the simulated microstructure at time t with material parameter $k\mathbf{p}$ is the same as the simulated microstructure at kt with material parameter $\mathbf{p}$. In other words, many trials of material parameters can be performed with only one simulation. A detailed discussion on the scaling property related to coarsening and grain growth is given in Sections 3.2 and 3.3, respectively.
Moreover, some parameters may not live on the entire domain so local optimization may be applied. For example, the grain boundary property of a specific boundary is only defined on this boundary. Thus fitting could only be applied on this boundary. However, there may be coupling between boundaries, which will be analyzed in detail in Section 3.3.3.

3.1.4 Initial guess of material parameters

An initial guess of material parameters must be provided for the fitting algorithm. A good initial guess can help the optimization converge with less iteration. Therefore, estimating a good initial guess is needed. The initial guess of material parameters can originate from several sources:

1. Traditional experimental measurements.
2. Statistical analysis based on analytical models. For example, an estimation of the grain boundary mobility can be found from the grain growth theory as shown in the attached Paper II.
3. A rough fitting using simulations with a large grid size or a simplified model.

It should be noticed that if the scaling property (Eq. 3.4) can be applied to the fitting, the initial guess is not so critical.

3.2 Case study: coarsening

3.2.1 The cost function

X-ray tomography measurements can provide a signed distance function ϕ_{exp} of the 3D microstructure in coarsening [155]. Phase-field simulation (Section 2.2.3.4) can provide the phase-field variable u_{sim}. The cost function is then defined with the 2-norm

$$f_{\text{cost}}(u_{\text{sim}}, \phi_{\text{exp}}) = \|\phi(u_{\text{sim}}) - \phi_{\text{exp}}\|_2^2 , \tag{3.5}$$

or the correlation function

$$f_{\text{cost}}(u_{\text{sim}}, \phi_{\text{exp}}) = 1 - \text{corr}(\Omega(u_{\text{sim}} \geq 0.5), \Omega(\phi_{\text{exp}} \leq 0)). \tag{3.6}$$

Here $\Omega(\cdot)$ is the voxelized domain where its argument is true. According to the asymptotic analysis of the phase-field equation (Eq. 2.57), the signed distance function $\phi(u_{\text{sim}})$ can be approximated from the phase-field u_{sim} as (Eq. 2.50)

$$\phi(u_{\text{sim}}) \approx \frac{l}{2} \tanh^{-1}(1 - 2u_{\text{sim}}) . \tag{3.7}$$

3.2.2 The scaling property

If the diffusion mobility in the solid and the diffusion mobility in the liquid is related: $M^{\mathrm{S}} = \epsilon M^{\mathrm{L}}$ (ϵ is a small positive number), and f^{S} and f^{L} can be locally approximated by parabolic functions, the scaling property of D^{L} can be derived from Eqs. 2.57, 2.59, and 2.60. The phase-field variable of the liquid phase is

$$\begin{aligned} u^{\mathrm{L}}(\mathbf{x}, t; kD^{\mathrm{L}}) &= \int_0^t -kL\frac{\delta F}{\delta u^{\mathrm{L}}}\,\mathrm{d}t \\ &= \int_0^{kt} -L\frac{\delta F}{\delta u^{\mathrm{L}}}\,\mathrm{d}(kt) \\ &= u^{\mathrm{L}}\left(\mathbf{x}, kt; D^{\mathrm{L}}\right). \end{aligned} \tag{3.8}$$

Similarly, the scaling properties of the phase-field variable of the solid phase u^{S} and the composition field c are

$$u^{\mathrm{S}}\left(\mathbf{x}, t; kD^{\mathrm{L}}\right) = u^{\mathrm{S}}\left(\mathbf{x}, kt; D^{\mathrm{L}}\right), \tag{3.9}$$

$$c\left(\mathbf{x}, t; kD^{\mathrm{L}}\right) = c\left(\mathbf{x}, kt; D^{\mathrm{L}}\right). \tag{3.10}$$

Eqs. 3.8, 3.9, and 3.10 describe the scaling property of the liquid diffusion coefficient D^{L} for the coarsening problem.

By examining the phase-field equations in Eq. 2.57, there is no scaling property for the surface energy/capillary length. However, for the case of coarsening, an approximated scaling property of the surface energy/capillary length can be derived. As the surface energy σ is a linear function of the capillary length l^{L} (if f^{S} and f^{S} are locally approximated by parabolic functions), the scaling properties of the surface energy and the capillary length are the same. In the following, only the scaling property of the surface energy is derived. According to Eq. 2.59, model parameters m and κ are linear functions of σ. In coarsening, the interface velocity is very small, so $\partial u^{\mathrm{L}}/\partial t \approx 0$. Under this assumption, the two terms in Eq. 2.57 must have approximately the same order, *i.e.*,

$$m\left(u_{\mathrm{S}}^3 - u_{\mathrm{S}} + 2\gamma u_{\mathrm{S}} u_{\mathrm{L}}^2\right) - \kappa\Delta u_{\mathrm{S}} \approx -\frac{\partial h^{\mathrm{S}}}{\partial u_{\mathrm{S}}}\left[f^{\mathrm{S}} - f^{\mathrm{L}} - (c_{\mathrm{S}} - c_{\mathrm{L}})\tilde{\mu}\right].$$

Thus if $k\sigma$ is used in the simulation, the only way to reach the same order is to scale f^{S}, f^{L} and $\tilde{\mu}$, *i.e.*

$$km\left(u_{\mathrm{S}}^3 - u_{\mathrm{S}} + 2\gamma u_{\mathrm{S}} u_{\mathrm{L}}^2\right) - k\kappa\Delta u_{\mathrm{S}} \approx -\frac{\partial h^{\mathrm{S}}}{\partial u_{\mathrm{S}}}\left[kf^{\mathrm{S}} - kf^{\mathrm{L}} - (c_{\mathrm{S}} - c_{\mathrm{L}})k\tilde{\mu}\right].$$

Notice that $c_{\mathrm{S}} - c_{\mathrm{L}} \approx c^{\mathrm{S,eq}} - c^{\mathrm{L,eq}}$ for coarsening. With this, the following approximated scaling property of σ can be derived as

$$\begin{aligned} u^{\mathrm{L}}(\mathbf{x}, t; k\sigma) &\approx \int_0^t -L\left(k\frac{\delta F}{\delta u^{\mathrm{L}}}\right) \mathrm{d}t \\ &= u^{\mathrm{L}}\left(\mathbf{x}, kt; \sigma\right). \end{aligned} \tag{3.11}$$

Similarly, we have

$$u^{\mathrm{S}}(\mathbf{x}, t; k\sigma) \approx u^{\mathrm{S}}\left(\mathbf{x}, kt; \sigma\right), \tag{3.12}$$

$$\begin{aligned} c(\mathbf{x}, t; k\sigma) &\approx \int_0^t \nabla \cdot [M\nabla(k\tilde{\mu})] \, \mathrm{d}t \\ &= c\left(\mathbf{x}, kt; \sigma\right). \end{aligned} \tag{3.13}$$

Eqs. 3.11, 3.12, and 3.13 provide the approximated scaling property of the surface energy σ for the case of coarsening.
As will be shown in Section 4.4.2, the approximated scaling property of the surface energy is verified for the case of coarsening. Therefore, it is impossible to distinguish whether the scaling of the microstructure evolution is caused by the diffusion coefficient or the surface energy. In other words, these two parameters are not separable in the coarsening experiment: $D^{\mathrm{L}}\sigma = \text{constant}$, but could be with more experiments.

3.2.3 Algorithm for fitting the liquid diffusion coefficient

The fitting algorithm for the liquid diffusion coefficient is summarized in Algorithm 1. The fitting algorithm requires the experimental microstructure (described by a signed distance function) and an initial guess of D^{L} as input. On line 1, the phase-field simulation is performed with one frame of the experimental movie (at t_0) as the initial microstructure and the initial guess D_0^{L} as the material parameter. According to the scaling property derived in Section 3.2.2, phase-field simulations only need to be performed once throughout the whole fitting process. The loop on line 2 is used for the case when there are more candidates of the fitting domain Ω_{fit}. The cost functions of various candidates D^{L} at different t are calculated according to lines 3-7. The loop on line 3 is used for fitting more experimental time-steps t. On lines 8-11, the cost functions are used to search for the minimum. Data points at different candidate values of D^{L} are interpolated by a spline, and a standard nonlinear optimization algorithm is used to find the optimal D^{L}.

Algorithm 1 Fitting liquid diffusion coefficient D^{L}

Require: experimental microstructure $\phi_{\mathrm{exp}}(t)$
Require: initial guess D_0^{L}
get simulated microstructure $u_{\mathrm{sim}}(t; D_0^{\mathrm{L}}) = \text{phase-field}(\phi_{\mathrm{exp}}(t_0), D_0^{\mathrm{L}})$
for Ω_{fit} **do** ▷ loop different fitting domain
  for $t \in [t_1, t_2]$ **do** ▷ loop experimental time-steps
    for $D^{\mathrm{L}} \in [a, b]$ **do** ▷ loop candidate D^{L} values
      calculate cost function $f_{\mathrm{cost}}\left(u_{\mathrm{sim}}\left(\frac{D^{\mathrm{L}}}{D_0^{\mathrm{L}}} t; D_0^{\mathrm{L}}\right), \phi_{\mathrm{exp}}(t)\right)$
    end for
  end for
  for $t \in [t_1, t_2]$ **do**
    interpolate $f_{\mathrm{cost}}(D^{\mathrm{L}}; t)$
    find the minimum of the cost function f_{cost}: $D_{\mathrm{fit}}^{\mathrm{L}}$
  end for
end for

3.3 Case study: grain growth

3.3.1 The cost function

DCT presented in Section 2.1.2.2 can provide a grain map. Here the shape of each experimentally measured grain δ is described by a signed distance function $\phi_{\mathrm{exp}}^{\delta}$. Phase-field simulation based on the model presented in Section 2.2.3.5 is used to provide the phase-field variable of each grain $u_{\mathrm{sim}}^{\delta}$. The cost function is then defined using the 2-norm as

$$f_{\mathrm{cost}}(\mathbf{u}_{\mathrm{sim}}, \boldsymbol{\phi}_{\mathrm{exp}}) = \sum_{\delta} f_{\mathrm{cost}}^{\delta}(u_{\mathrm{sim}}^{\delta}, \phi_{\mathrm{exp}}^{\delta}) = \sum_{\delta} \left\| \phi(u_{\mathrm{sim}}^{\delta}) - \phi_{\mathrm{exp}}^{\delta} \right\|_2^2, \tag{3.14}$$

where the $\sum_{\delta}$ is summation over all grains and ϕ is the signed distance function (negative inside grain). Eq. 3.14 can be reformulated as a summation over all grain boundaries

$$f_{\mathrm{cost}}(\mathbf{u}_{\mathrm{sim}}, \boldsymbol{\phi}_{\mathrm{exp}}) = \sum_{\alpha\beta} f_{\mathrm{cost}}^{\alpha\beta}(u_{\mathrm{sim}}^{\alpha}, u_{\mathrm{sim}}^{\beta}, \phi_{\mathrm{exp}}^{\alpha}, \phi_{\mathrm{exp}}^{\beta}), \tag{3.15}$$

where

$$f_{\mathrm{cost}}^{\alpha\beta}(u_{\mathrm{sim}}^{\alpha}, u_{\mathrm{sim}}^{\beta}, \phi_{\mathrm{exp}}^{\alpha}, \phi_{\mathrm{exp}}^{\beta}) = \left\| \phi(u_{\mathrm{sim}}^{\alpha}) - \phi_{\mathrm{exp}}^{\alpha} \right\|_2^2 + \left\| \phi(u_{\mathrm{sim}}^{\beta}) - \phi_{\mathrm{exp}}^{\beta} \right\|_2^2. \tag{3.16}$$

Notice that the 2-norm only needs to be calculated at the grain boundary region. The signed distance ϕ can be calculated from the phase-field variable

u_{sim} according to Eq. 3.7. ϕ_{exp} can be got from a phase-field dilation process described in Section 5.2.6.

3.3.2 Optimization problem

The reduced grain boundary mobilities m_{gb} (Eq. 2.17) depend on the grain boundary mobilities M_{gb} and energies σ_{gb}. The grain boundary energies affect the dihedral angles, which in turn affect the evolution of the grain boundary network [156, 59]. The grain boundary mobilities affect the velocity of grain boundaries. In this thesis, as a first step, it is assumed that the effect of grain boundary energies on the change of the grain boundary network is small during two adjacent experimental time-steps. This assumption will cause an error in the fitted value of the reduced mobilities. In the future, the fitting of grain boundary energies or even simultaneous fitting of the energies and mobilities can be used to improve the fitting result. Thus, in the current work, the grain boundary energies σ_{gb} are set to be one, and only the mobilities M_{gb} are fitted. Based on this setting, the fitted mobility M_{gb} has the same value as the physical reduced mobility m_{gb}. The mobility variable of grain boundary Γ_i is written as M_i. The fitting of grain boundary mobilities can be formulated as the following optimization problem

$$\begin{aligned} \text{find} \quad & \mathbf{M} = \{M_i\},\ i \in \mathcal{S}^{\text{fit}} \\ \text{minimize} \quad & f_{\text{cost}}(t, \mathbf{M}) = \textstyle\sum_{\delta} f_{\text{cost}}^{\delta} = \sum_{\alpha\beta} f_{\text{cost}}^{\alpha\beta} \\ \text{such that} \quad & \mathbf{u}_{\text{sim}}(t_0, \mathbf{M}) = \mathbf{u}_{\text{exp}}(t_0) \\ & \mathbf{u}_{\text{sim}}(t, \mathbf{M}) \text{ follows Eq. 2.61.} \end{aligned} \tag{3.17}$$

Here $\mathbf{M}$ contains all fitted mobilities ($\mathcal{S}^{\text{fit}}$ is the set of all fitted boundaries). The cost function is calculated in two ways: summation over all grains (Eq. 3.14) or summation over all grain boundaries (Eq. 3.15).

3.3.3 Sensitivity analysis

The sensitivity, *i.e.*, $\partial f_{\text{cost}}/\partial M_i$, is carried out to derive an independence approximation that is used to simplify the optimization problem in Eq. 3.17.

Suppose M_i is the mobility of the grain boundary $\Gamma_{\alpha\beta}$ between grains α and β. According to Eq. 2.65, the sensitivity can be calculated as

$$\frac{\partial f_{\text{cost}}}{\partial M_i} = \frac{4}{3 l_{\text{gb}}} \frac{\partial f_{\text{cost}}}{\partial L_{\alpha\beta}}.$$

As grain boundary width l_{gb} is constant in the phase-field model used, the sensitivity to M_i only differs from the sensitivity to $L_{\alpha\beta}$ by a constant scaling. In the following, I will focus on the sensitivity to $L_{\alpha\beta}$.

The cost function in Eq. 3.14 can be explicitly written as

$$f_{\mathrm{cost}}(\mathbf{u}_{\mathrm{sim}}) = \sum_{\delta=1}^{p} \left(\int_{\Gamma_w^\delta} (\phi(u^\delta) - \phi_{\mathrm{exp}}^\delta)^2 \, \mathrm{d}V \right), \tag{3.18}$$

where Γ_w^δ is the domain of a narrow band near grain boundaries of grain δ: $\Gamma_w^\delta = \{\mathbf{x} : |\phi^\delta(\mathbf{x})| < w\}$ and $u^\delta = u_{\mathrm{sim}}^\delta$. For convenience, two quantities are defined as

$$g^\delta := 2\left(\phi(u^\delta) - \phi_{\mathrm{exp}}^\delta\right) \frac{\partial \phi(u^\delta)}{\partial u^\delta}, \tag{3.19}$$

$$A_{\alpha\beta} := \frac{u_\alpha^2 u_\beta^2}{\sum_{\alpha,\beta} u_\alpha^2 u_\beta^2}. \tag{3.20}$$

The sensitivity of the cost function (Eq. 3.18) is calculated as

$$\frac{\partial f_{\mathrm{cost}}}{\partial L_{\alpha\beta}} = \sum_{\delta=1}^{p} \left[\int_{\Gamma_w^\delta} \left(g^\delta \frac{\partial u^\delta}{\partial L_{\alpha\beta}} \right) \mathrm{d}V \right], \tag{3.21}$$

where the derivatives of phase-field variables u^δ with respect to $L_{\alpha\beta}$ are calculated from Eq. 2.61

$$\frac{\partial u^\delta}{\partial L_{\alpha\beta}} = \frac{\partial u^\delta(t_0)}{\partial L_{\alpha\beta}} + \int_{t_0}^{t} \frac{\partial(\partial_t u^\delta)}{\partial L_{\alpha\beta}} \, \mathrm{d}t. \tag{3.22}$$

The initial phase-field variables do not depend on the input material parameters; thus

$$\frac{\partial u^\delta(t_0, \mathbf{M})}{\partial L_{\alpha\beta}} = \frac{\partial u_{\mathrm{exp}}^\delta(t_0)}{\partial L_{\alpha\beta}} = 0. \tag{3.23}$$

From Eq. 2.61 and Eq. 2.64, we have

$$\begin{aligned} \frac{\partial(\partial_t u^\delta)}{\partial L_{\alpha\beta}} &= \frac{\partial(\partial_t u^\delta)}{\partial L} \frac{\partial L}{\partial L_{\alpha\beta}} \\ &= A_{\alpha\beta} \left(\kappa \Delta u^\delta - \nabla_u W(\mathbf{u}) \right). \end{aligned} \tag{3.24}$$

Considering that $A_{\alpha\beta}$ only has non-zero values near the α-β boundary $\Gamma_{\alpha\beta}$ and using Eqs. 3.22 and 3.23, the derivative of phase-field variables with respect to $L_{\alpha\beta}$ can be approximated as

$$\frac{\partial u_\delta}{\partial L_{\alpha\beta}} \approx \begin{cases} \displaystyle\int_{t_0}^{t} \frac{\partial(\partial_t u^\delta)}{\partial L_{\alpha\beta}} \, \mathrm{d}t & \Gamma_w^{\alpha\beta} \subset \Gamma_w^\delta \\ 0 & \Gamma_w^{\alpha\beta} \not\subset \Gamma_w^\delta, \end{cases} \tag{3.25}$$

where $\Gamma_w^{\alpha\beta}$ is a domain of a narrow band near grain boundary $\Gamma_{\alpha\beta}$: $\Gamma_w^{\alpha\beta} = \Gamma_w^{\alpha} \cap \Gamma_w^{\beta}$. Eq. 3.25 is the independence approximation, which means varying $L_{\alpha\beta}$ only influence the evolution of grain boundary $\Gamma_{\alpha\beta}$. Substituting Eq. 3.25 into Eq. 3.21, we get an approximation of the sensitivity

$$\frac{\partial f_{\text{cost}}}{\partial L_{\alpha\beta}} \approx \sum_{\delta=\alpha,\beta} \left[\int_{\Gamma_w^{\alpha\beta}} \left(g^{\delta} \frac{\partial u^{\delta}}{\partial L_{\alpha\beta}} \right) \mathrm{d}V \right] = \frac{\partial f_{\text{cost}}^{\alpha\beta}}{\partial L_{\alpha\beta}}, \tag{3.26}$$

which means $L_{\alpha\beta}$ only influences the local cost function $f_{\text{cost}}^{\alpha\beta}$ (Eq. 3.16). With the independence approximation (Eq. 3.25) and the sensitivity (Eq. 3.26), the original optimization problem Eq. 3.17 can be approximated by several sub-problems. For each fitted grain boundary α-β, the sub-problem is defined as

$$\begin{aligned} \text{find} \quad & L_{\alpha\beta} \\ \text{minimize} \quad & f_{\text{cost}}^{\alpha\beta}(t, L_{\alpha\beta}) \\ \text{such that} \quad & \mathbf{u}^{\text{sim}}(t_0, \mathbf{M}) = \mathbf{u}^{\text{exp}}(t_0) \\ & \mathbf{u}^{\text{sim}}(t, \mathbf{M}) \text{ follows Eq. 2.61.} \end{aligned} \tag{3.27}$$

In summary, the strategy to solve the original optimization problem (Eq. 3.17) is

1. Approximation of Eq. 3.17 by a sequence of sub-problems (Eq. 3.27).
2. Solving sub-problems (Eq. 3.27).
3. Approximation of the original optimization problem again based on the solution of all sub-problems.
4. Iterating over 2-3 until convergence.

3.3.4 The scaling property

Based on the independence approximation in Eq. 3.25, and following the same procedure as in Section 3.2.2, the approximated scaling property can be derived as

$$u^{\delta}(\mathbf{x}, t; kM_i) \approx u^{\delta}(\mathbf{x}, kt; M_i). \tag{3.28}$$

This property plays a significant role in reducing the computational cost of the fitting.

3.3.5 Algorithm for fitting reduced mobilities

The fitting algorithm for the reduced grain boundary mobilities is summarized in Algorithm 2. The fitting algorithm requires the experimentally measured grain shape (signed distance functions) and an initial guess of fitted mobilities. On line 2, the phase-field simulation is performed with one frame of the experimental data as an initial condition and a guess of material parameters $\mathbf{M}_0$. For each fitted grain boundaries $\Gamma_{\alpha\beta} \in \mathcal{S}^{\text{fit}}$ (line 3), the sub-problem in Eq. 3.27 is solved (lines 4-10). The fitting domain of $\Gamma_{\alpha\beta}$ is got by subtracting the triple-junction region Ω_{tj} from the interfacial domain: $\Omega_{\text{fit}}^{\alpha\beta} = \Gamma_w^{\alpha\beta} \setminus \Omega_{\text{tj}}$ (lines 4-5). The reason why Ω_{tj} needs to be removed from the fitting domain is that both the evaluation of signed distance function (Eq. 3.7) and the independence approximation (Eq. 3.25) fail near triple-junctions. The cost function is calculated with the help of the scaling property (lines 6-8), and its minimum is found using standard nonlinear optimization algorithm. On line 12, the convergence of values of material parameters is checked, and the mobility variables are updated (line 13).

Algorithm 2 Fitting reduced grain boundary mobilities

Require: experimental microstructure $\boldsymbol{\phi}_{\text{exp}}(t)$
Require: Initial guess $\mathbf{M}_0$
1: **for** iteration **do** ▷ fitting iteration
2: get simulated microstructure $\mathbf{u}_{\text{sim}}(t; \mathbf{M}_0) = \text{phase-field}(\phi_{\text{exp}}(t_0), \mathbf{M}_0)$
3: **for** α,β **do** ▷ loop all fitted grain boundaries
4: get interfacial domain $\Gamma_w^{\alpha\beta}$
5: get $\Omega_{\text{fit}}^{\alpha\beta}$ by subtracting triple-junction regions
6: **for** $M_{\alpha\beta} \in [a, b]$ **do** ▷ loop candidate $M_{\alpha\beta}$ values
7: calculate cost function $f_{\text{cost}}^{\alpha\beta}(M_{\alpha\beta})$ ▷ use scaling in Eq. 3.28
8: **end for**
9: find the minimum of the cost function $f_{\text{cost}}^{\alpha\beta}$: $M_{\alpha\beta}^{\text{fit}}$
10: save the result $M_{\alpha\beta}^{\text{fit}} \rightarrow \mathbf{M}$
11: **end for**
12: check convergence $|\mathbf{M} - \mathbf{M}_0| \leq \epsilon$
13: update material parameters $\mathbf{M}_0 = \mathbf{M}$
14: **end for**

Chapter 4

Application I: coarsening

In this chapter, the fitting approach proposed in Chapter 3 is applied to fit two parameters - the liquid diffusion coefficient and the capillary length in a hypoeutectic Al-Cu alloy. A brief introduction to the coarsening process and the Al-Cu material system is presented in Section 4.1. The coarsening experiment is briefly summarized in Section 4.2. Various aspects related to the phase-field model are addressed in Section 4.3. Results of the fitting are presented and discussed in Section 4.4. Part of the result is published in the attached Paper I.

4.1 Coarsening of hypoeutectic Al-Cu alloy

Coarsening is the late stage of solidification. During coarsening, the particle size or the inverse of surface area per unit volume S_v^{-1} increase with time at a constant annealing temperature under the curvature driving force.

In this thesis, an Al-Cu alloy with a composition of 20 wt%Cu and a solid fraction of 48 vol% is annealed at a temperature just above the eutectic temperature. As shown by the phase diagram in Fig. 4.1, at this stage, the system contains a Cu-rich liquid phase and an Al-rich solid phase. Details on material parameters of the Al-Cu system are provided below.

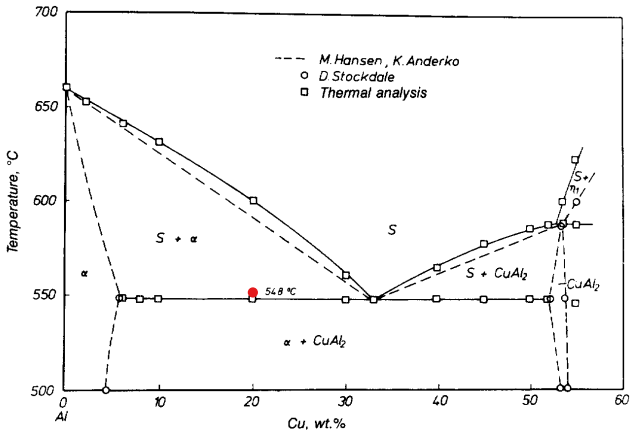

Figure 4.1: Phase diagram of the Al-Cu alloy at the Al-rich end, reproduced from [157]. S and α denote liquid and solid (fcc-A1) phases, respectively. The state at which the coarsening experiment is performed is shown by the red dot.

4.1.1 Material parameters

Free energy density The chemical bulk free energy density is provided by the CALculation of PHAse Diagrams (CALPHAD) method. The molar Gibbs energy of the liquid phase of Al-Cu is expressed in the following form [158]

$$\begin{aligned} G_m^{\text{liquid}}(T,c) &= (1-c)H_{\text{Al}}^{\text{SER}} + cH_{\text{Cu}}^{\text{SER}} \\ &+(1-c)G_{\text{Al}}^{\circ,\text{liquid}} + cG_{\text{Cu}}^{\circ,\text{liquid}} \\ &+RT(c\ln c + (1-c)\ln(1-c)) \\ &+c(1-c)\left(L_{\text{Al,Cu}}^{0,\text{liquid}} + L_{\text{Al,Cu}}^{1,\text{liquid}}(1-2c) + L_{\text{Al,Cu}}^{2,\text{liquid}}(1-2c)^2\right), \end{aligned} \tag{4.1}$$

and the molar Gibbs energy for the solid (fcc-A1) phase is expressed as [158]

$$\begin{aligned} G_m^{\text{fcc-A1}}(T,c) &= (1-c)H_{\text{Al}}^{\text{SER}} + xH_{\text{Cu}}^{\text{SER}} \\ &+(1-c)G_{\text{Al}}^{\circ,\text{fcc-A1}} + cG_{\text{Cu}}^{\circ,\text{fcc-A1}} \\ &+RT(c\ln c + (1-c)\ln(1-c)) \\ &+c(1-c)\left(L_{\text{Al,Cu:}\square}^{0,\text{fcc-A1}} + L_{\text{Al,Cu:}\square}^{1,\text{fcc-A1}}(1-2c) + L_{\text{Al,Cu:}\square}^{2,\text{fcc-A1}}(1-2c)^2\right), \end{aligned} \tag{4.2}$$

where T is the temperature and c is the composition (molar fraction). For the meaning of the other parameters, please refer to [158]. In this work, a parabolic approximation [92] of the CALPHAD free energy is used to avoid iteratively solving Eq. 2.58. The parabolic free energies have the following form:

$$V_m f^{\mathrm{L}}(c^{\mathrm{L}}) = \frac{A^{\mathrm{L}}}{2}\left(c^{\mathrm{L}} - c^{\mathrm{L},0}\right)^2 + C^{\mathrm{L}} \approx G_m^{\text{liquid}}, \tag{4.3}$$

$$V_m f^{\mathrm{S}}(c^{\mathrm{S}}) = \frac{A^{\mathrm{S}}}{2}\left(c^{\mathrm{S}} - c^{\mathrm{S},0}\right)^2 + C^{\mathrm{S}} \approx G_m^{\text{fcc-A1}}, \tag{4.4}$$

where A^{L}, A^{S}, $c^{\mathrm{L},0}$, $c^{\mathrm{L},0}$, C^{L}, and C^{S} are fitting parameters, and V_m is the molar volume, which is used to transfer from the molar free energy ($J \cdot \mathrm{mol}^{-1}$) to the volume density ($J \cdot m^{-3}$). The molar volume of Al-Cu is measured as $V_m = 11.1182\ \mathrm{cm}^3 \cdot \mathrm{mol}^{-1}$ [159]. As shown in Fig. 4.2, CALPHAD free energies in Eqs. 4.1 and 4.2 are fitted by parabolic functions in Eqs. 4.3 and 4.4 while keeping common tangent compositions close to the CALPHAD ones ($c^{\mathrm{S,eq}} = 1.99$ at% and $c^{\mathrm{L,eq}} = 15.5$ at%) with a penalty optimization method. Fitted parameters in Eqs. 4.3 and 4.4 are

$$\begin{aligned}
A^{\mathrm{L}} &= 1.1337 \times 10^5\ J \cdot \mathrm{mol}^{-1},\\
A^{\mathrm{S}} &= 6.1839 \times 10^4\ J \cdot \mathrm{mol}^{-1},\\
c^{\mathrm{L},0} &= 0.5703,\\
c^{\mathrm{S},0} &= 0.7822,\\
C^{\mathrm{L}} &= -4.9457 \times 10^4\ J \cdot \mathrm{mol}^{-1},\\
C^{\mathrm{S}} &= -5.1278 \times 10^4\ J \cdot \mathrm{mol}^{-1}.
\end{aligned}$$

Relative errors between CALPHAD free energies and corresponding parabolic fits are less than 1 %.

Capillary length The capillary length is derived from a measurement of the Gibbs-Thomson coefficient Γ (Eq. 2.18). Hunt measured the Gibbs-Thomson coefficient to be $\Gamma = 2.41 \times 10^{-7}\ mK$ [160]. The capillary length is then

$$l^{\mathrm{L}} = \frac{2\Gamma}{m} = 0.63\ nm, \tag{4.5}$$

where the liquidus slope m is measured to be $m = -763.79\ K$ from the CALPHAD free energy in Eq. 4.1. In the phase-field model given in Section 2.2.3.4, the solid-liquid surface energy is needed to calculate model parameters. The solid-liquid surface energy σ^{SL} is derived from the capillary length by

$$\sigma^{\mathrm{SL}} = \frac{l^{\mathrm{L}} G_m^{\text{liquid}''}(c^{\mathrm{L,eq}} - c^{\mathrm{S,eq}})}{2V_m^s}, \tag{4.6}$$

where V_m^s is the molar volume of the solid phase. In this work, it is assumed to be the same as V_m.

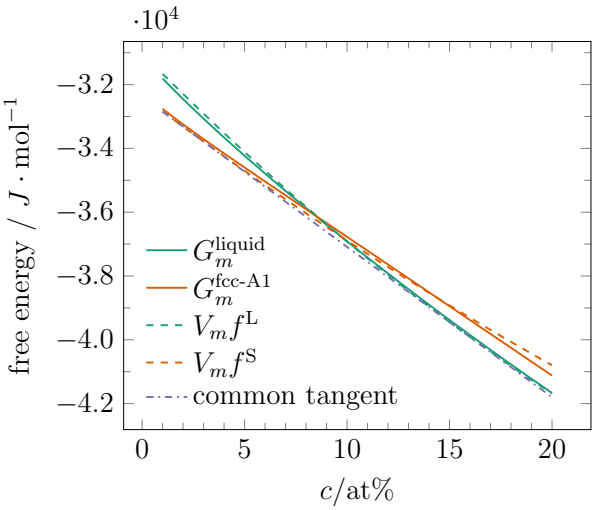

Figure 4.2: Parabolic fit of the molar Gibbs free energy. Solid green and red lines are CALPHAD free energies in Eqs. 4.1 and 4.2. Dashed lines are the parabolic fits in Eqs. 4.3 and 4.4. The dash-dotted line shows the common tangent of the parabolic free energies.

4.2 Coarsening experiment

Absorption contrast tomography (Section 2.1.2.1) is applied in the coarsening experiment with a 25 keV x-ray beam and exposure time of 250 ms. An *in situ* isothermal coarsening experiment is performed for 462 minutes at a temperature just above the eutectic temperature. Spatial and temporal resolutions are $\Delta x = 1.44$ μm and 231 s, respectively. An example of the coarsening dataset is shown in Fig. 4.3. The coarsening experiment was conducted by Juliet Fife and collaborators on beamline TOMCAT at the Swiss Light Source (SLS). The reconstruction and segmentation were conducted by John Gibbs. For details on the experiment and related data analysis, please refer to the work of Fife [161] and Gibbs [162, 155]. The 4D coarsening dataset is available at the Materials Data Facility[1] [163].

[1] `https://publish.globus.org/jspui/handle/ITEM/41`

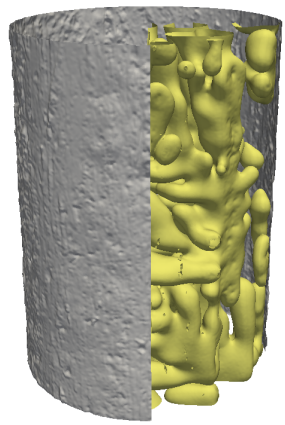

Figure 4.3: Illustration of the coarsening dataset used in this thesis.

4.3 Phase-field simulation of coarsening

4.3.1 Implementation of the phase-field model

The phase-field model presented in Section 2.2.3.4 is implemented to simulate the coarsening process. In this thesis, finite difference method is applied to discretize phase-field equations (Eq. 2.57), and the domain decomposition algorithm is used for parallelization.

4.3.1.1 Finite difference method

The simulation domain is discretized by cells of size $h_x \times h_y \times h_z = (\Delta x)^3$. The Laplacian operator is approximated by the 7-points stencil

$$\begin{aligned} \Delta^h f \quad &= \frac{f^{i+1,j,k} - 2f^{i,j,k} + f^{i-1,j,k}}{h_x^2} + \frac{f^{i,j+1,k} - 2f^{i,j,k} + f^{i,j-1,k}}{h_y^2} \\ &+ \frac{f^{i,j,k+1} - 2f^{i,j,k} + f^{i,j,k-1}}{h_z^2} + \mathcal{O}(h^2), \end{aligned} \tag{4.7}$$

where $f^{i,j,k} = f(ih_x, jh_y, kh_z)$. The term in Eq. 2.57 is discretized by a forward-backward scheme as

$$\begin{aligned}[\nabla \cdot (M\nabla\mu)]^h &= \frac{M^{i+1,j,k}(\mu^{i+1,j,k} - \mu^{i,j,k}) - M^{i-1,j,k}(\mu^{i,j,k} - \mu^{i-1,j,k})}{2h_x^2} \\ &+ \frac{M^{i,j+1,k}(\mu^{i,j+1,k} - \mu^{i,j,k}) - M^{i,j-1,k}(\mu^{i,j,k} - \mu^{i,j-1,k})}{2h_y^2} \\ &+ \frac{M^{i,j,k+1}(\mu^{i,j,k+1} - \mu^{i,j,k}) - M^{i,j,k-1}(\mu^{i,j,k} - \mu^{i,j,k-1})}{2h_z^2} \\ &+ \frac{1}{2} M^{i,j,k} \Delta^h \mu + \mathcal{O}(h^2).\end{aligned} \tag{4.8}$$

where $h = \max\{h_x, h_y, h_z\}$. In this work, the grid has equal size along all directions: $\Delta x = h = h_x = h_y = h_z$. Both discretization schemes (Eqs. 4.7 and 4.8) are accurate to the second-order. The forward Euler method (first-order accuracy) is used for temporal discretization, and the time-step is chosen to be $\Delta t \leq \Delta x^2/(2dD^{\mathrm{L}})$ for stability consideration, where d is the dimension.

4.3.1.2 Parallelization

To reduce the computational time, parallel programming is used in the phase-field implementation. The domain decomposition algorithm [164] is used to parallelize over multiple nodes with the Message Passing Interface (MPI) library. The code is written in C and is available on GitHub[2].

4.3.2 Verification of the phase-field model

The phase-field model and its implementation need to be verified before applied in the fitting. The analytical solutions given in Section 2.2.2.1 are taken as the ground truth for verifying the phase-field simulation results.

Test case 1: 1D precipitate particle growth in infinitely large media. The purpose of this test is to check the diffusion behavior of the phase-field model. The analytical solution derived by Zener [69] (Eqs. 2.26 and 2.27) is based on two assumptions: (1) the capillary effect is negligible and (2) the domain is infinite. In this test case, the above assumptions are validated. The domain size is chosen to be 400 μm, much larger than the precipitation size ($2 \sim 3.5$ μm), to mimic the infinite media (Zener's second assumption). The initial

[2]Parallel coarsening phase-field code: `https://github.com/jijn/phasefield_coarsening`

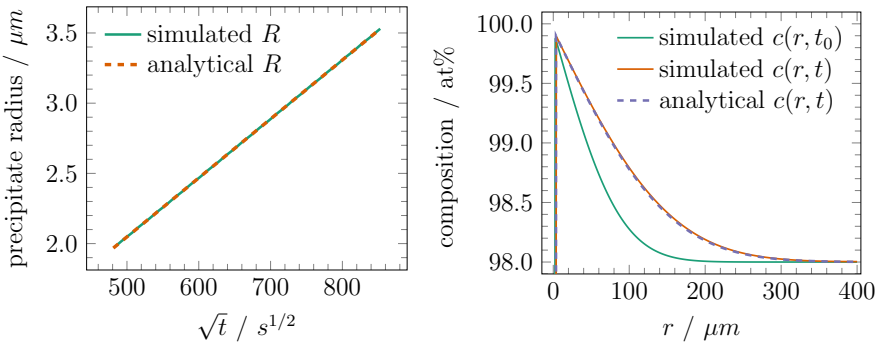

(a) Precipitate radius **(b)** Composition profile

Figure 4.4: Test case 1: 1D precipitation growth inside a uniform field. (a) The simulated precipitate radius is compared with the analytical solution (Eq. 2.27)). (b) The simulated composition profile is compared with the analytical solution (Eq. 2.26). The initial composition $c(r, t_0)$ is also shown. Notice that anti-trapping current is not used in the simulation results shown here.

precipitate radius is 2 μm. The material parameters used in the phase-field simulation are from Moelans' paper [92], including diffusion coefficients $D^{\mathrm{L}} = 1 \times 10^{-14}$ and $D^{\mathrm{S}} = 0$, interfacial energy $\sigma = 2$, common tangent compositions $c^{\mathrm{L,eq}} = 0.999$ and $c^{\mathrm{S,eq}} = 0.476$, and the initial homogeneous composition $c^m = 0.98$. The composition change due to capillary $2l^{\mathrm{L}}/R = 0.19\%$ is small compared with the difference in composition field $c^{\mathrm{L,eq}} - c^m = 1.9\%$; thus Zener's first assumption is approximately fulfilled. The grid size is $\Delta x = 0.1$ μm, and the interface width is $l = 7\Delta x$. The initial condition of phase-field variables is determined by the initial precipitate radius and the steady-state planar profile (Eq. 2.51). The initial condition of the composition field is determined from the analytical solution in Eq. 2.26, and is shown in Fig. 4.4b. A no-flux boundary condition (Eq. 2.68) is applied.
The simulated precipitate radius R is calculated from the interpolation field (Eq. 2.56) and is compared with the analytical solution in Fig. 4.4a. Relative errors of the slope $R(t)/\sqrt{t}$ between the phase-field result and the analytical solution (Eq. 2.27) is -0.0073% with the anti-trapping current $\mathbf{j}_{\mathrm{at}}$ and 0.046% without $\mathbf{j}_{\mathrm{at}}$. The comparison of composition profiles c is shown in Fig. 4.4b. In conclusion, the phase-field model can predict the diffusion behavior correctly.

Test case 2: capillary test. The equilibrium of a spherical solid particle in a finite-size box of the liquid phase (see Fig. 4.5a) is used to check if the phase-field model correctly captures the capillary effect. The domain size is

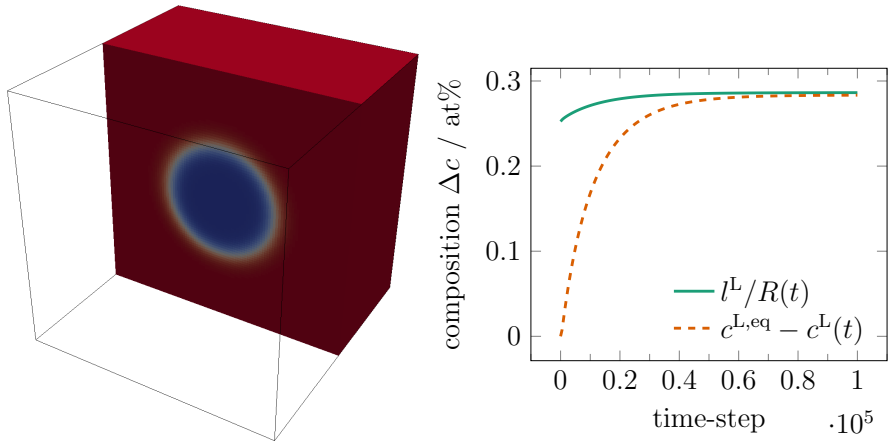

(a) Simulation geometry **(b)** Results

Figure 4.5: Test case 2: capillary test. (a) The simulation geometry is a spherical particle surrounded by a finite box of the liquid phase. (b) The composition difference $\Delta c = c^{\mathrm{L,eq}} - c^{\mathrm{L}}$ analytically predicted from the capillary effect in Eq. 2.25(b2) (solid line) is compared with the simulated one (dashed line). The spherical radius R is calculated from the interpolation field (Eq. 2.56) and c^{L} is the average of the simulated composition inside the liquid phase ($u^{\mathrm{L}} \geq 0.999$).

$10 \times 10 \times 10\ \mu m^3$, and the initial particle radius is 2.5 μm. Material parameters are given in Section 4.1.1 except that the capillary length is scaled by ten times to exaggerate the capillary effect. The grid size is $\Delta x = 0.1\ \mu m$, and the interface width is $7\Delta x$. The initial condition for the composition field is determined from the common tangent compositions $c^{\mathrm{S,eq}}$ and $c^{\mathrm{L,eq}}$. A no-flux boundary condition (Eq. 2.68) is prescribed on the outside of the box.

As a result of the capillary effect, a composition gradient is present at the interface and acts as a driving force for diffusion. As the system approaches equilibrium, the composition in the liquid phase should approach a value set by Gibbs-Thomson condition (Eq. 2.25(b2)). The phase-field result is compared with the analytical solution in Fig. 4.5b. The particle radius is determined from the interpolation field (Eq. 2.56), and is used to calculate the equilibrium composition of the liquid (solid line in Fig. 4.5b). The dashed line in Fig. 4.5b represents the average composition in the liquid phase, where the domain of the liquid phase is determined by $u^{\mathrm{L}} \geq 0.999$. As shown in Fig. 4.5b, the liquid composition (dashed line) approaches the one set by the capillary effect (solid line) as the system approaches equilibrium. The result means the phase-field model captures the capillary effect correctly.

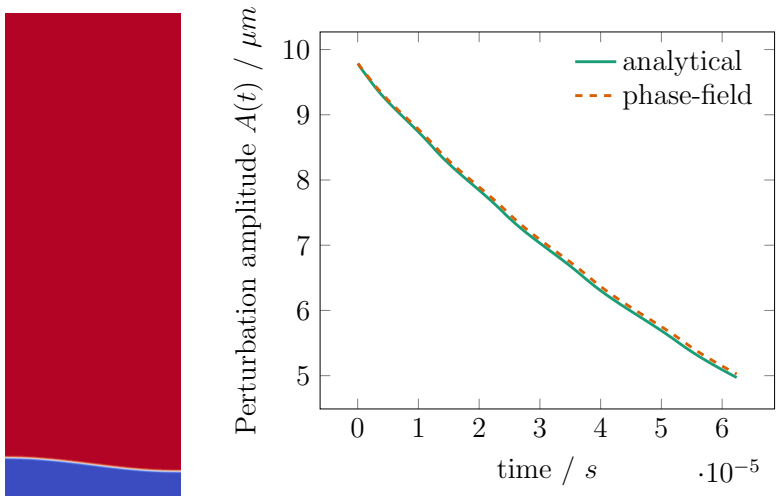

(a) Geometry **(b)** Results

Figure 4.6: Test case 3: the decay of a sinusoidal perturbation. The simulation geometry is shown in (a), where blue and red representing the solid and liquid phases, respectively. (b) The perturbation amplitude calculated from the phase-field simulation (dashed line) is compared with the analytical solution (Eq. 2.30).

Test case 3: perturbed sinusoidal interface. Different from above test cases where interface curvatures are constant, the purpose of this test case is to check the accuracy of the phase-field simulation with a non-constant interface curvature, as shown in Fig. 4.6a. The analytical solution of this test case was derived by Aagesen [70], assuming a small perturbation and an infinitely large liquid phase. The wavelength of the sinusoidal perturbation is $500\Delta x$. The initial amplitude of the perturbation is $A_0 = 10\Delta x$ and the height of the domain is chosen to be $750\Delta x$, which is much larger than the perturbation amplitude to mimic an infinitely large liquid phase. Material parameters are given in Section 4.1.1. The grid size is $\Delta x = 1\ nm$[3], and the interface width is $7\Delta x$. A no-flux boundary condition (Eq. 2.68) is applied on all sides of the domain. The initial condition of the phase-field variables is determined from the steady-state planar profile in Eq. 2.51. The initial condition of the composition is interpolated from the common tangent compositions: $c = h^{\mathrm{S}} c^{\mathrm{S,eq}} + h^{\mathrm{L}} c^{\mathrm{L,eq}}$. As this composition profile is not exactly accurate, the phase-field simulation is firstly performed to allow the system to relax until the amplitude reduces to $9.8\Delta x$, so the correct composition field can be determined. The phase-field

[3]This value is chosen to get a large capillary driving force. No atomic-scale physics is accounted here.

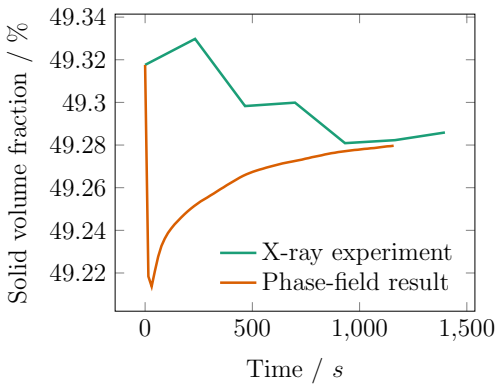

Figure 4.7: Solid volume fractions change with time in both the coarsening experiment and the phase-field simulation.

variable and the composition field from the initial run are used as the initial condition for the phase-field simulation.
The simulated interface positions on the left and right side of the domain are determined from the interpolation functions (Eq. 2.56), and the amplitude of the perturbation is calculated from the difference between these two positions. The simulated decay of the amplitude (dashed line) is compared with the analytical result (Eq. 2.30, solid line) in Fig. 4.6b. It can be seen that the phase-field result agrees well with the analytical solution with a maximum relative error of 1.28%. It should be noticed that the accuracy can be further improved with a larger domain (larger wavelength and domain height) to mimic better the assumptions used in deriving the analytical solution.

4.3.3 Initial condition

According to Eq. 2.57, initial values of both the phase-field variables ($u^{\mathrm{L}}(\mathbf{x},0)$ and $u^{\mathrm{S}}(\mathbf{x},0)$) and the composition field $c(\mathbf{x},0)$ are needed for the phase-field simulation. The initial condition of phase-field variables can be directly calculated from the experimentally measured signed distance function using Eq. 2.51. However, the composition field was not experimentally measured; thus it is assumed as $c = h^{\mathrm{S}}c^{\mathrm{S,eq}} + h^{\mathrm{L}}c^{\mathrm{L,eq}}$. Such composition field results in an initial relaxation at the beginning of the phase-field simulation. As shown in Fig. 4.7, this initial relaxation occurs in a short time at the beginning of the simulation and the change in solid volume fraction is very small (around 0.1%). Thus the influence of the initial relaxation on the fitting result is assumed to be minor.

4.4 Fitting material parameters

Based on the x-ray tomography experiment described in Section 4.2 and the verified phase-field model in Section 4.3, the fitting is applied to determine the liquid diffusion coefficient and the capillary length in an Al-Cu alloy.

4.4.1 Fitting the liquid diffusion coefficient

As a first step, the fitting approach is applied to determine the liquid diffusion coefficient only. The main results are given in the attached Paper I, and summary is provided here.

Paper I includes a survey of the optimal fitting domain Ω_{fit}. Two considerations apply, as illustrated in Fig. 3 of Paper I: (1) the fitting domain is restricted to a localized region near the interface as the interface is the primary focus in the fitting; (2) a sub-domain inside the simulation domain is used to reduce the influence from the applied artificial boundary condition. Moreover, large simulation error is observed in some regions with a thin liquid film, as illustrated in Fig. 4 of Paper I. Such regions are removed from the fitting domain.

The liquid diffusion coefficient is fitted according to Algorithm 1 (Section 3.2.3). The fitting approach is first demonstrated on a small patch (Section 3.4.1 in Paper I). With the help of the scaling property of the liquid diffusion coefficient derived in Section 3.2.2, the phase-field simulation only needs to run once. The phase-field simulation starts from experimental time-step 10 of the 4D coarsening dataset, and the comparison is performed at experimental time-steps 11 to 15. The results of two types of cost functions for comparison at different experimental time-steps are shown in Fig. 5 of Paper I. It can be seen that all cost functions have a similar unique minimum point. The simulated microstructures are further compared with the experiment in Fig. 6 of Paper I. It is concluded that the fitting approach provides the correct minimum.

The fitting approach is then applied to the case involving more interfaces. As shown in Fig. 4.8, the fitted value of the liquid diffusion coefficient D^{L} converges with increasing interface areas in the fitting. This result shows the importance of statistics on the accuracy of the fitting. Fig. 8 of Paper I shows the fitted D^{L} as a function of the sub-domain size. Two pieces of information can be obtained from this result: (1) the plateau in the figure shows a stable fitted value of D^{L} for different sub-domain sizes and different experimental time-steps. (2) the scatter at large sub-domain size is a result of the artificial boundary condition. The temporal variation of D^{L} is shown in Fig. 10 of Paper I. In this case, phase-

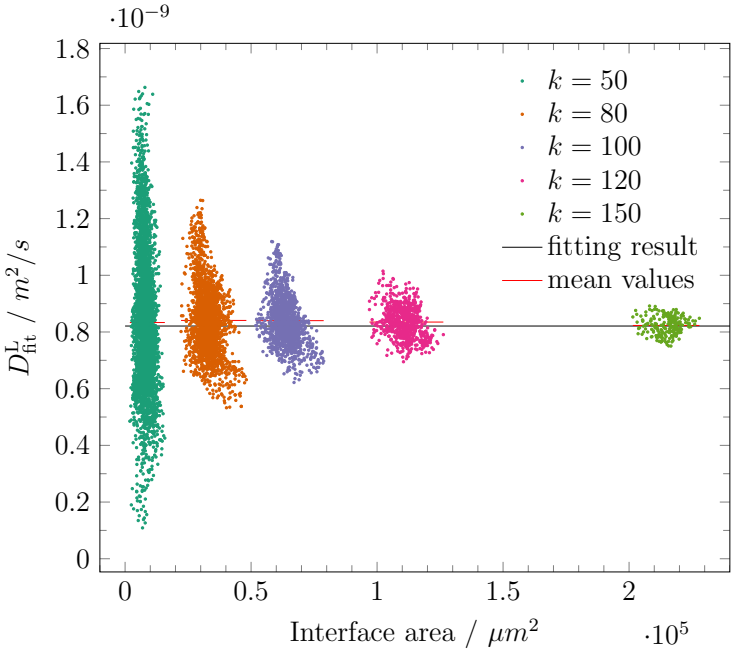

Figure 4.8: The best-fitted values of D^{L} as a function of the area of interfaces involved in the fitting. Different colors mean different fitting subdomain size k. The black line shows the fitting result with a representative subdomain and the red lines show the mean values for each subdomain size. The scatter in the fitted values reduces with increasing interface area. Reproduced from Fig. 9 of Paper I.

field simulations start from different experimental time-steps. The results show a small deviation in fitted values.

The liquid diffusion coefficient in hypoeutectic Al-Cu alloy determined from the one-parameter fitting has a value of $D^{\mathrm{L}} = 8.33 \pm 0.24 \times 10^{-10}\ m^2/s$. This value is believed to be better applied in materials design than previous values for two reasons: (1) the coarsening experiment is done in a condition mimics the engineering processing; (2) the characteristic length scale of the microstructure is small that convection effect on the measurement is negligible. Notice that this value is close to the one determined from an Al-15wt%Cu coarsening dataset ($8.3 \times 10^{-10}\ m^2/s$) [115].

In summary, the fitting approach is successfully applied to fit the liquid diffusion coefficient in Al-Cu from a 4D coarsening experiment. The results show that

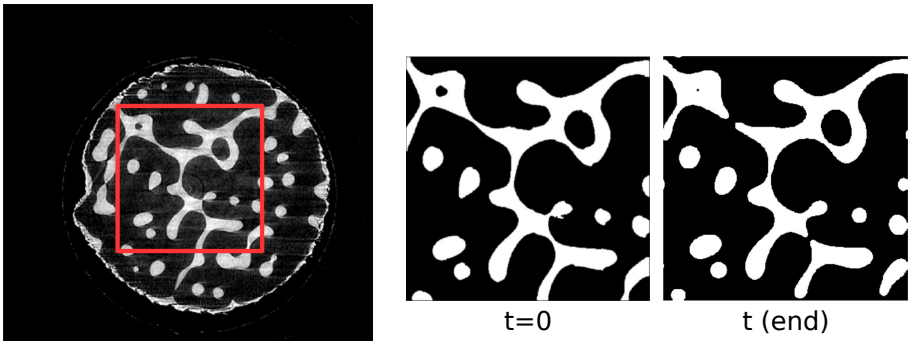

(a) experiment data (b) synthetic data using phase-field simulation

Figure 4.9: 2D synthetic dataset used for testing the two-parameter fitting algorithm.

the fitting approach is robust.

4.4.2 Fitting the capillary length

The one-parameter fitting in Section 4.4.1 from a method point of view is special, due to the scaling property. Here the fitting approach is applied to a two-parameter case. To verify its applicability further tests are performed on a 2D synthetic dataset.
To generate the synthetic dataset, a square region of one slice of the 3D coarsening dataset is chosen as the initial geometry of the phase-field simulation, as shown in Fig. 4.9a. The 2D phase-field simulation is carried out with material parameters $D^{\mathrm{L}} = 2.4 \times 10^{-9}\ m^2/s$ and $l^{\mathrm{L}} = 0.63\ nm$ to generate the synthetic dataset shown in Fig. 4.9b. The input material parameters are taken as ground truth to test the fitting. The norm-cost function surface of D^{L} and l^{L} is shown in Fig. 4.10a. For each l^{L} value, the fitted liquid diffusion coefficient $D^{\mathrm{L}}_{\mathrm{fit}}$ is found from Algorithm 1 (Section 3.2.3). The fitting results are shown by red crosses in Fig. 4.10a. It is observed that the fitted values of $D^{\mathrm{L}}_{\mathrm{fit}}$ and l^{L} present an inversely proportional relation. The capillary length is plotted as a function of $1/D^{\mathrm{L}}$ in Fig. 4.10b. A linear fit shows that data points $(1/D^{\mathrm{L}}_{\mathrm{fit}}, l^{\mathrm{L}})$ fall on a straight line: $D^{\mathrm{L}} l^{\mathrm{L}} = 1.5144\ \mu m^3/s$. This result is not surprising from both the coarsening theory [64] and the scaling properties derived in Section 3.2.2. However, this result, on the other side, verifies the fitting approach.

The fitting approach is further applied to the experimental data. The fitted liquid diffusion coefficient and the capillary length are shown in Fig. 11 of Paper

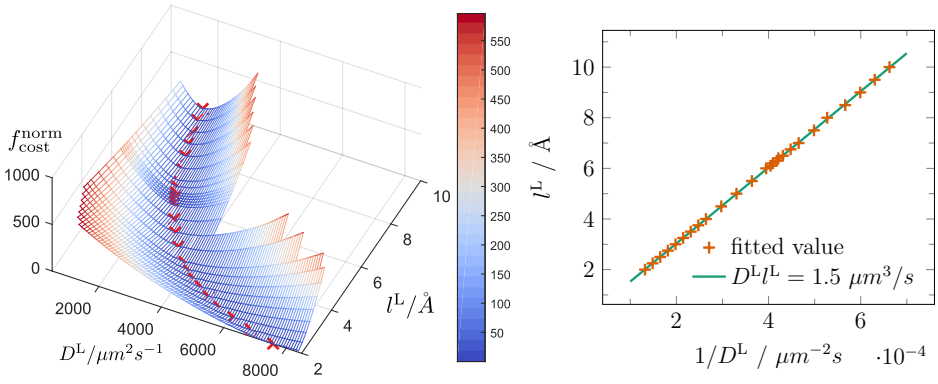

(a) Cost function surface **(b)** Fitted parameters

Figure 4.10: Two-parameter fitting of the synthetic dataset: (a) the cost function f_{cost} as a function of the liquid diffusion coefficient D^{L} and the capillary length l^{L}. For each l^{L}, the value of D^{L} that minimizes the cost function is found and marked by the red points. The best-fitted value of $1/D^{\text{L}}$ and l^{L} shown by the red points in (b) are fitted by a linear function (green line in (b)).

I. Similar to the fitting on the synthetic dataset, the optimal values are linearly related: $D^{\text{L}}l^{\text{L}} = 0.518 \pm 0.011\ \mu m^3/s$. This value is consistent with the one obtained in the one-parameter fitting in Section 4.4.1. Detailed information is given in Section 3.5 in Paper I.

4.4.3 Discussion on the fitting approach

The fitting methodology has been successfully applied to the coarsening of Al-Cu resulting in a fit of the liquid diffusion coefficient. The determined D^L is smaller than previously measured values (see Table 2.1), which is an indication of less influence from convection as it is known that convection in the measurement can lead to a larger measured value of the liquid diffusion coefficient. This result is believed to be more representative than previous results because the experiment is performed in a condition which mimics the engineering process. For the case of two-parameter fitting, it is found that D^L and l^L are coupled, and it is not possible to separate them solely from the coarsening experiment.

A proper cost function should help extract useful information from the experimental data while being insensitive to noise. The corr-cost function (Eq. 3.6) is easy to calculate, but when the geometry is represented by a limited number

of voxels, there will be discontinuities in the cost function. The norm-cost function (Eq. 3.5) is continuous, but an extra effort is needed to generate the signed distance function. Generally speaking, both cost functions work equally well in the case investigated here.

The initial condition of the composition field causes an initial relaxation in the phase-field simulation, as shown in Section 4.3.3. There are possible ways to suppress the initial relaxation: (1) experimentally measure the composition field (this is seen as very difficult considering the small composition gradient inside the liquid phase) and (2) estimate a better initial guess of the composition field, such as the steady-state solution of the diffusion equation. A possible way to get the solution is the smoothed boundary method [165].

The fitting approach is also a very powerful way to provide insight on the quality of the materials model. If the result of the optimization is a poor global match between experiment and optimized model, it may indicate that one or more mechanisms are absent from the model. If the simulation only deviates from the experiment in a local region, we may either attempt to improve the underlying model or exclude the problematic regions. Our work shows that in the case of coarsening we can get good results with the simplified model and a fitting domain excluding the problematic regions.

The coarsening phase-field model is implemented in C with Message Passing Interface (MPI) for parallelization among many cores. Compiler vectorization is considered to get a vectorized code for specific CPU architectures. The scaling of the code among many cores is good; however, it can be further improved by computer experts with the consideration of the CPU-specific and the high-performance computing (HPC) cluster-specific optimizations, *e.g.*, taking into account the cache size and hierarchy, and optimizing the communication pattern among many cores.

Applying the proposed method to fit more than one independent material parameters is straightforward by using multi-variable optimization algorithms. The main limitation of the fitting methodology is the heavy computational cost as generally phase-field simulations need to be performed many times. For the case investigated here, the phase-field simulations for one experimental time-step with a 300^3 domain took 22 hours on a Nehalem architecture machine with 16 cores and took 11 hours for simulations with a 400^3 domain on a Sandy Bridge architecture machine with 64 cores. However, speed up of the simulations can be achieved by massively parallel computing and fast convergence optimization algorithms, and a good initial guess of the material parameters will shorten the path to the global minimum.

Chapter 5

Application II: grain growth

In this chapter, the fitting approach proposed in Chapter 3 is applied to a complicated case with the aim to fit hundreds of reduced grain boundary mobilities of pure iron. A *grain growth* dataset acquired by *DCT* is chosen because DCT can provide 3D grain maps with high spatial resolution and grain growth can be simulated by the phase-field model accurately in 3D. In the phase-field simulation of grain growth, each grain boundary is assigned a mobility value. It is noted that the aim is not to fit *all* of the boundaries, but a statistically large portion of them.

In Section 5.1, the grain growth of pure iron is briefly introduced. The grain growth experiment and related data analysis are presented in Section 5.2, and the grain growth phase-field model is discussed in Section 5.3. Finally, the fitting approach is applied to synthetic datasets and the DCT dataset in Section 5.4.

5.1 Grain growth of pure iron

During plastic deformations, substantial energy is stored in metals. When the deformed material is annealed at an elevated temperature, the stored energy in it drives the change of microstructure to form dislocation free grains inside the

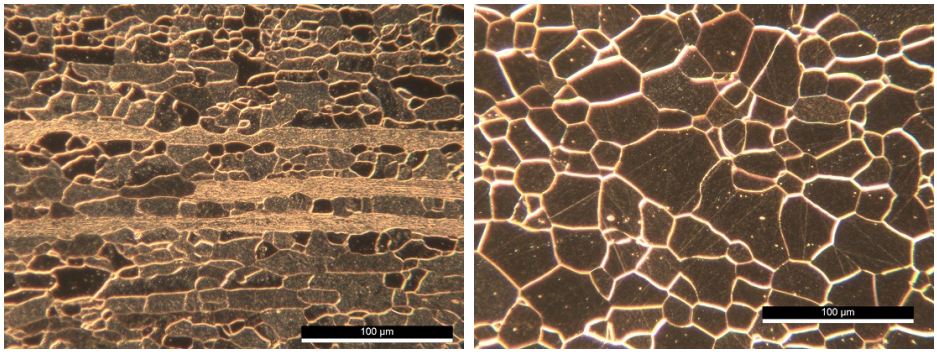

(a) Recrystallization **(b)** Grain growth

Figure 5.1: Typical microstructures appearing during annealing of deformed pure iron: (a) a partly recrystallized structure, and (b) a structure related to grain growth.

deformed structure. This process is called recrystallization. In Fig. 5.1a, a partly recrystallized microstructure is shown. The recrystallization continues until the deformed structure is fully consumed, *i.e.*, the sample is fully recrystallized. Grain growth refers to the further increase in grain size after full recrystallization under the curvature driving force. Depending on the annealing condition, grain growth can be normal or abnormal. In this thesis, I will only focus on the normal grain growth. A typical microstructure after grain growth is shown in Fig. 5.1b.

5.2 DCT experiment of grain growth

5.2.1 Sample preparation

The raw material is Armco iron with a purity of 99.9 wt% and several impurity elements. The chemical composition is measured by optical emission spectroscopy and listed in Table 5.1. Here iron is chosen for the grain growth study because there are no annealing twins and the grain size is well suited for DCT experiments.

The raw material is firstly cold rolled to a reduction in thickness of 50% and then recrystallized. The degree of recrystallization is quantified by Vickers hardness (HV) as a function of annealing temperature for a fixed annealing time, as shown in Fig. 5.2. It can be seen that annealing at a temperature of $700°C$ for 30

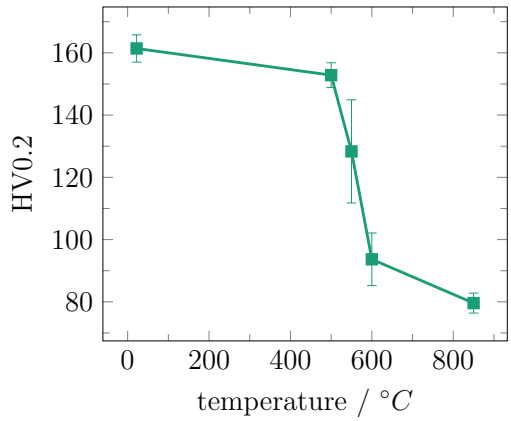

Figure 5.2: HV0.2 hardness measurements of a 50% cold rolled Armco iron sample as a function of the annealing temperature (30 minutes annealing).

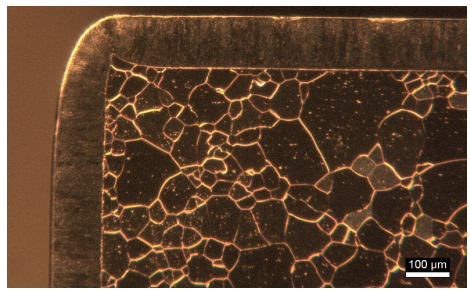

Figure 5.3: Optical microscope image of the oxidation layer in iron after annealing at $T = 850°C$ for 30 minutes in air.

Table 5.1: Chemical composition (wt%) of Armco iron.

Fe	C	Si	Mn	P	S	Ni
99.9%	0.002%	0.001%	0.041%	0.005%	0.002%	0.014%

minutes is proper to get fully recrystallized samples. This condition is further confirmed by microstructure analysis with a light optical microscope. After the pre-annealing, the specimen is cut by wire electrical discharge machining into rods of 1 mm diameter with the rolling direction (RD) along the cylinder axis. The rod is further electrochemically etched to a diameter of approximately 500 μm to remove the damage caused by the cutting.

Since iron oxidizes easily at high temperature, a study of the oxidation layer is carried out at a temperature of $850°C$ for 30 minutes in air. As shown in Fig. 5.3, the thickness of the oxidation layer is larger than 100 μm. Considering the typical sample size in a DCT experiment is several hundred micrometers, it is crucial to avoid sample oxidation during the experiment. In this work, the forming gas (Ar+2%H_2) is used to prevent sample oxidation.

5.2.2 DCT setup and data acquisition

The experimental setup of DCT on beamline ID11 at ESRF is shown in Fig. 5.4a. The sample with a diameter around 500 μm is adhered to a ceramic sample holder with a high-temperature glue, as shown in Fig. 5.4c. The sample holder is connected to the rotation stage which rotates continuously during exposure. An x-ray beam with energy 40 keV illuminates the sample, and the transmitted and diffracted beams are recorded on the detector. Usually, a beamstop is used to attenuate part of the transmitted beam to avoid saturation. A typical detector image in DCT is shown in Fig. 5.4b with four diffraction spots and the transmission image highlighted. Note that the extinction spots (black dots inside the bright transmitted beam) are visible as well. Diffraction spots are used to reconstruct the grains in 3D, and transmission images are used to reconstruct the sample shape (the absorption contrast tomography). A retractable tube furnace shown in Fig. 5.4d is used for annealing on the beamline with a forming gas (Ar+2%H_2) flowing through the furnace.

An image is recorded by the detector during every (continuous) rotation of $\Delta\omega = 0.1$ degrees with an exposure time of one second. During the DCT acquisition, 3600 images over 360° rotation are recorded. Diffraction spots are segmented and indexed as described in Section 2.1.2.2. For illustration, three (out of ∼50) projections from a grain are shown in Fig. 5.5a.

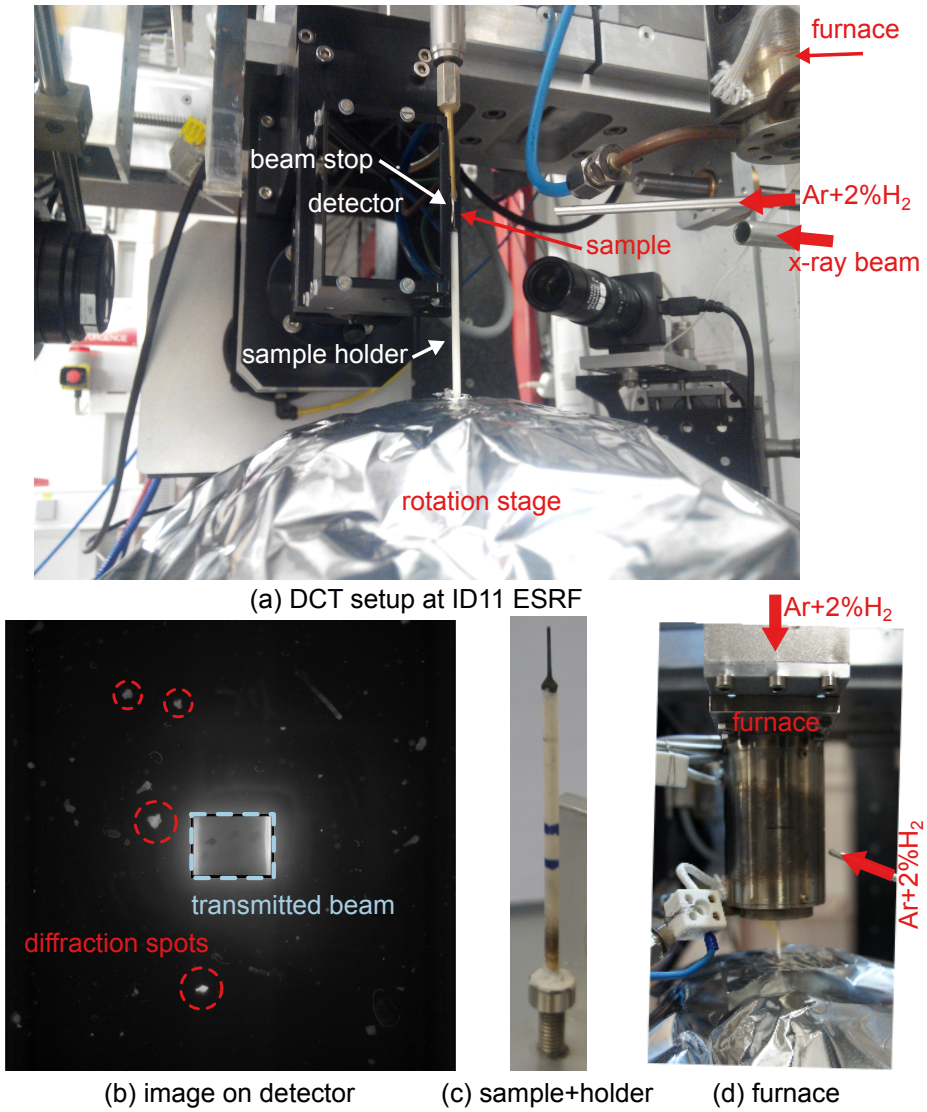

Figure 5.4: (a) The DCT setup at ESRF beamline ID11. (b) An example of the detector image. In the middle of the detector is the image of the transmitted beam. (c) Sample mounted on a ceramic holder. (d) The retractable furnace.

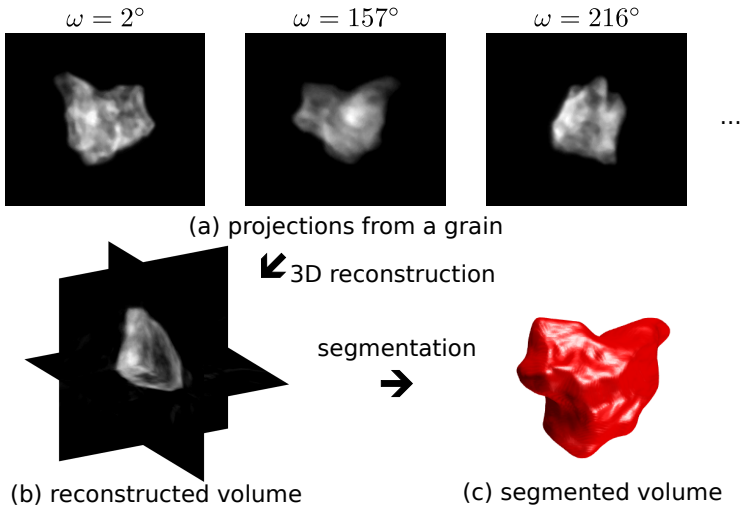

Figure 5.5: 3D-DCT reconstruction and segmentation. The projections (a) of a grain at different rotation angles ω are found from indexing. These projections are used to reconstruct the 3D grain volume (b). The gray-scale voxelized grain volume is segmented to get the grain volume (c) which can be binarized or represented by a level-set function.

5.2.3 DCT reconstruction

Based on the grouped projections from a grain (Fig. 5.5a), the 3D grain volume can be reconstructed by the ART/SIRT algorithm, as shown in Fig. 5.5b. The reconstruction algorithms for DCT are categorized into the 3D-DCT algorithm [44, 46] and the 6D-DCT algorithm [48, 49]. With 3D-DCT, only the 3D grain shape is reconstructed; while with 6D-DCT, the reconstruction is performed in a six-dimensional space (three-dimensional real space pluses three-dimensional orientation space). 3D-DCT neglects the presence of intragranular orientation spread and treats the grain as an object with constant (fixed) average orientation. 6D-DCT, on the other hand, allows for sub-domain and orientation gradients inside the grain volume and can therefore provide better reconstruction, especially in the case of plastically deformed materials. Both 3D-DCT and 6D-DCT reconstructions are used in this thesis. However, the 6D-DCT reconstruction only shows marginal improvement over the 3D-DCT reconstruction for the present sample. Since grains in a fully recrystallized microstructure only exhibit negligible intragranular orientation spread, the quality of the 3D-DCT and 6D-DCT are identical: the description of the grain as an object with constant lattice orientation is a valid one.

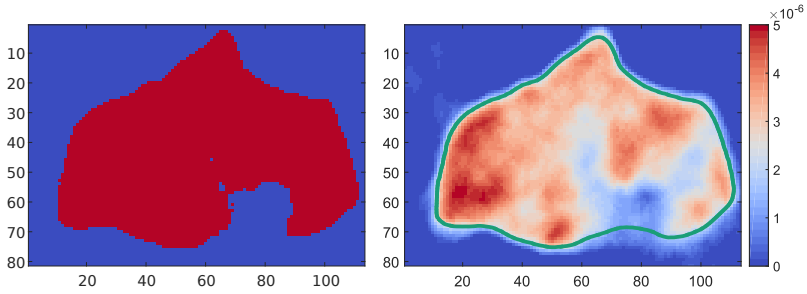

(a) Threshold segmentation **(b)** Level-set segmentation

Figure 5.6: Section plot of the segmentation of a 3D grain volume with (a) thresholding method and (b) level-set segmentation. The color in (b) represents the intensity, while the green curve is the boundary of the segmented grain. The unit of all axes is voxel size.

5.2.4 Segmentation of individual grains

As shown in Fig. 5.5b, the reconstructed grain volume (gray-scale voxelized volume) needs to be segmented to identify the grain shape (Fig. 5.5c). In traditional DCT, a thresholding method is used for the segmentation [46]. For the case studied here, extinction is observed in the reconstructed grain volume, as can be seen from the intensity field shown in Fig. 5.6b. With the thresholding method, the missing intensity makes it difficult to define a suitable threshold value and causes holes in the segmented volume, *c.f.* Fig. 5.6a. To deal with this problem caused by extinction, a level-set based segmentation [166] is used with a surface area penalty. With an appropriately chosen penalty term, the level-set segmentation handles the extinction successfully, as shown by the green contour line in Fig. 5.6b. A comparison between the assembled volumes in Fig. 5.7 also shows the improvement of the level-set segmentation. Moreover, the output of the level-set segmentation is a signed distance function for each grain, which is useful for the following data analysis and the proposed fitting approach, as we shall see below.

5.2.5 Assembly of sample volumes

The reconstruction and segmentation described above are applied to individual grains. These grain volumes need to be assembled to get the sample volume. The grain centroid determined by Friedel pairs is used to locate the position of a grain volume inside the sample volume. The result of assembly is shown in

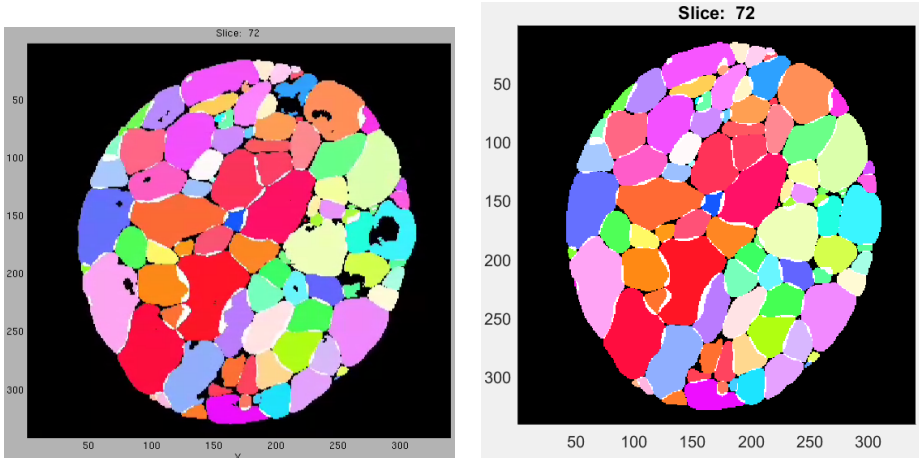

(a) Threshold segmentation **(b)** Level-set segmentation

Figure 5.7: Section plot of the assembled 3D sample volume to show the segmentation results of (a) the traditional threshold method and (b) the level-set method. The unit of axes is voxel size. Colors represent grain orientations (see Fig. 1 in Paper II for the inverse pole figure (IPF) color triangle).

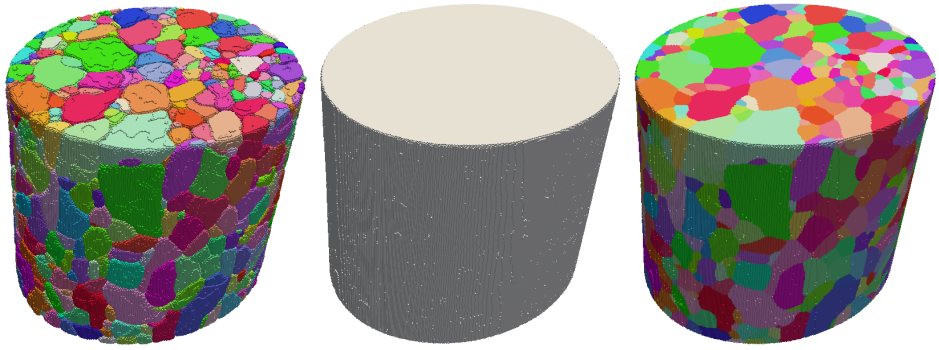

(a) Assembled volume **(b)** Absorption volume **(c)** Mask applied

Figure 5.8: Assembly of the sample volume at time-step 1: (a) individual grain volumes are gathered together; (b) the reconstructed absorption volume from the transmitted beam; and (c) the sample volume after applying the mask set by the absorption volume (dilation is applied before setting the mask). The colors in (a) and (c) represent grain orientations (IPF color).

Fig. 5.8a. The absorption volume (Fig. 5.8b) reconstructed from transmitted images is taken as a mask on the assembled grain volumes (assembled and then dilated) to define the exterior boundary of the sample volume, as shown in Fig. 5.8c.

5.2.6 Phase-field dilation

In the assembled sample volume, overlap or holes exist between neighboring grains, as shown in Fig. 5.9a. These ambiguities of where exact grain boundary is can, in principle, be solved by reconstructing all grains simultaneously, *e.g.*, using a cluster reconstruction [49] or a forward modeling approach similar to, *e.g.* [167, 168]. However, so far, both approaches are not ideal. The cluster reconstruction would need to treat all grains simultaneously (memory problem); otherwise, it can only improve a local neighborhood. The forward modeling approach takes long computational time and cannot reliably handle 2D illumination (extended beam). In traditional DCT data analysis, these ambiguities are removed by a morphological dilation process [46], and the output of the dilation is a voxelized volume, *c.f.* Fig. 5.9b.
In this thesis, a phase-field dilation algorithm [168] is used because the output is a smoothed field with sub-pixel accuracy which is preferable for the fitting approach. This phase-field dilation algorithm is described as follows:

1. Segmented grain volumes (signed distance functions) are used as the initial condition of the phase-field model (see Section 2.2.3.5).

2. Ambiguities are gradually removed as the phase-field variables evolve with time.

3. The phase-field simulation stops at a proper time when most ambiguities are removed.

It should be noticed that in the phase-field dilation process, the (bulk) driving force at ambiguous regions (overlap or holes) is very large; thus these regions are quickly removed after few simulation time-steps, see Fig. 5.9c for the result after 20 time-steps. The disadvantage of the phase-field dilation algorithm is that the (curvature) driving force for small grains is larger than big ones; it therefore causes a bias on small grains. This problem can potentially be solved by evolving small grains less than large grains (*e.g.*, using fewer phase-field time-steps) or adding a volume penalty term in the free energy functional in Eq. 2.40. The small grains disappear quickly in the experiment and the experimental error of small grains is relatively large, they are assumed to have less effect on the

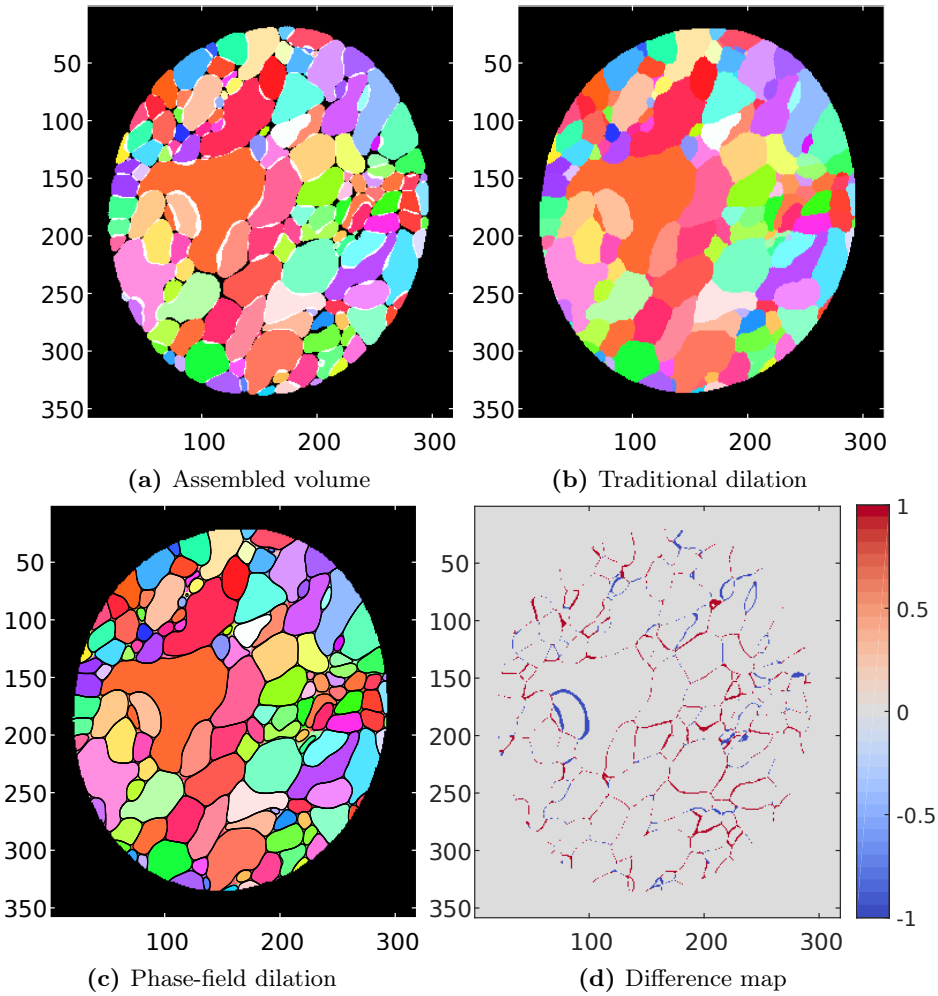

(a) Assembled volume **(b)** Traditional dilation

(c) Phase-field dilation **(d)** Difference map

Figure 5.9: Section plots to illustrate the phase-field dilation algorithm. The assembled sample volume (a) has overlaps (white region) or holes (black region) between neighboring grains. The results of the traditional dilation algorithm and the phase-field dilation algorithm are shown in (b) and (c), respectively. The contour lines in (c) are phase-field variables with a value 0.5. They are overlaid on the voxelized grain volumes determined from phase-field variables. The difference map between voxelized volumes in (b) and (c) is shown in (d). Notice that grain boundaries are also smoothed in the phase-field dilation. The unit of all axes is voxel size. The colors in (a), (b), and (c) represent grain orientations (IPF color).

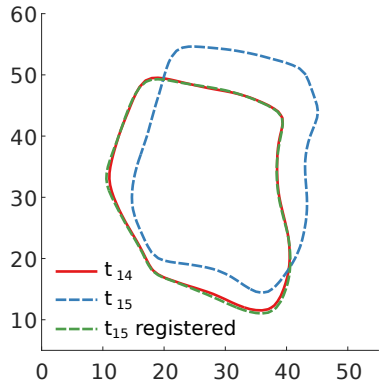

Figure 5.10: Section plot of a grain at time-step 14 (solid red line) overlaid with the uncorrected (dashed blue line) and corrected (dashed green line) section plot of the same grain at time-step 15. The unit of axes is voxel size.

comparison between simulation and experiment. Moreover, the bias on small grains is not so critical for the fitting as long as the grain boundaries of small grains are not considered in the fitting. In this thesis, 20 phase-field time-steps are found enough to remove most of the ambiguities without much effect on small grains, as shown in Fig. 5.9c. The difference map between the DCT dilation result and the phase-field dilation result is shown in Fig. 5.9d. Notice that the voxelized grain volumes in Fig. 5.9c are determined form phase-field variables ($u_\alpha \geq 0.5$). It is seen that the difference for most boundaries is less than one voxel size.

5.2.7 Registration of sample volumes

The 3D sample volumes acquired after different annealing steps need to be registered to have a 4D dataset. There may be small rigid body movements of the sample between two consecutive scans due to error motion in the mechanical system or thermal drifts. These misalignments between scans can cause a large error in the fitting and are corrected by a registration process. Grain centroids are used together with an iterative closest point algorithm[1] to get the transformation matrix that can be used to align two sample volumes. Notice that only grains appearing in both sample volumes are considered in the registration. The transformation matrix is then used to correct the signed distance function which represents the absorption volume and the phase-field variables of

[1] `https://www.mathworks.com/help/vision/ref/pcregrigid.html`

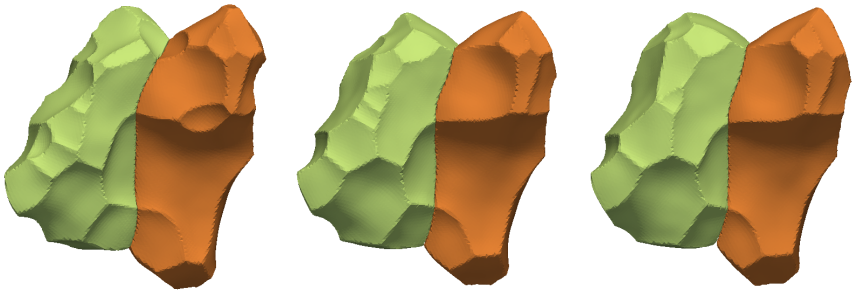

(a) Time-step 1 **(b)** Time-step 8 **(c)** Time-step 15

Figure 5.11: DCT dataset: evolution of two grains.

all grains volumes. As a smooth field is used in the correction, sub-pixel accurate representations of the absorption volume and grain volumes are maintained. An example of the registration of a grain is shown in Fig. 5.10.

5.2.8 Summary of the grain growth experiment

The DCT dataset acquired in this work includes 15 time-steps of the evolution of initially 1327 grains during annealing at $800°C$ for 75 minutes. An overview of grain growth during annealing is given in Table 1 of Paper II. The superior spatial resolution (1.54 μm) allows a detailed study on grain growth and precise fitting. An example of the evolution of two grains is given in Fig. 5.11. This dataset leads to a comprehensive statistical analysis on the grain level, including grain's geometrical and topological properties, as well as their evolution. Results of the statistical analysis are presented in the attached Paper II. This information on the grain level will complement the fitting results (on grain boundary level) for a multiscale understanding of grain growth. Moreover, these results can serve to determine initial guesses for the fitting procedure. For example, the growth analysis based on the MacPherson-Srolovitz equation (Eq. 2.33) can provide an estimation of reduced grain boundary mobilities, see for example Fig. 10b in Paper II.

5.3 Phase-field simulation of grain growth

5.3.1 Implementation of the phase-field method

Grain growth of pure iron is simulated based on the phase-field model presented in Section 2.2.3.5. The implementation of the phase-field model is briefly introduced in this part. Finite difference method is used to discretize the phase-field equation (Eq. 2.61). The 7-point stencil in Eq. 4.7 is used to discretize the Laplacian Δu_α. An explicit finite difference scheme (forward Euler method) is used for the temporal discretization. The time-step is set according to the CFL condition: $\Delta t \leq \Delta x^2/(2dL\kappa)$ to maintain numerical stability, where Δx is the grid size, L and κ are model parameters, and d is the dimension. Each grain is described by a phase-field variable. To reduce the memory and computational cost, a bounding box algorithm [110, 109] is used. The initial condition of phase-field variables is from the phase-field dilation described in Section 5.2.6. The phase-field model is implemented in MATLAB in order to combine with the DCT data analysis tool[2], which is written in MATLAB.

5.3.2 Verification of the phase-field model

The grain growth phase-field model (Section 2.2.3.5) and its implementation need to be tested before being applied in the fitting. In this part, various benchmark examples are proposed for verification. Phase-field simulation results are compared with analytical solutions presented in Section 2.2.2.2.

Test case 1: shrinking grain. The purpose of this test is to verify if the phase-field model can correctly predict the grain boundary migration. Geometries of test problems in 2D and 3D are shown in Figs. 5.12a and 5.12b, respectively. The domain sizes are $(100\Delta x)^2$ for the 2D case and $(100\Delta x)^3$ for the 3D case. The grid size is $\Delta x = 1$, and the grain boundary thickness is $l_{\mathrm{gb}} = 4\Delta x$. Initial radius of the circle and sphere are $30\Delta x$. In both cases, a sharp profile (Heaviside step function) is taken as the initial condition for the phase-field variables and a no-flux boundary condition (Eq. 2.68) is prescribed. The material parameters are $M_{\mathrm{gb}} = 1$ and $\sigma_{\mathrm{gb}} = 1$.
As there is only one grain boundary present, the scaling property of grain boundary mobilities M_{gb} derived in Section 3.3.4 is exact, which means changing M_{gb} is equivalent to a change of timescale. Moreover, for the case of isotropic energy studied here, changing σ_{gb} is also equivalent to a change of timescale, as

[2]DCT analysis code: `https://sourceforge.net/projects/dct/`

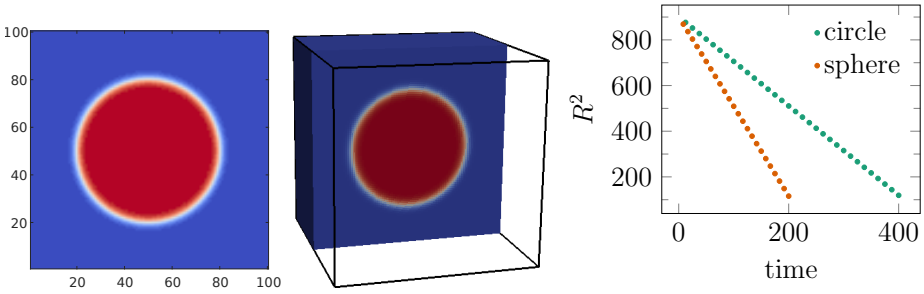

(a) Shrinking circle **(b)** Shrinking sphere **(c)** Simulation results

Figure 5.12: Test case 1: shrinking grain. Geometries (phase-field u_1) for the case of (a) 2D and (b) 3D. (c) The simulated R^2 as a function of time.

can be seen from Eqs. 2.61, 2.62, 2.66 and 2.67. Therefore, one set of material parameters is enough to verify the model and the implementation.
The evolutions of R^2 for 2D and 3D cases are shown in Fig. 5.12c. The data points are linearly fitted and compared with the analytical solution in Eqs. 2.35 and 2.34 (a slope of -2 in 2D and -4 in 3D). The relative error of the slope is -2.33% for the 2D case and -1.79% for the 3D case. To conclude, the phase-field model can correctly capture the grain boundary migration.

Test case 2: the growth of three grains. The purpose of this test is to verify if the triple-junction condition is correctly described by the phase-field model. Here the grain boundary energy is assumed isotropic; thus the triple-junction angles fulfill Young's law in Eq. 2.24. The domain size is $120\Delta x \times 150\Delta x$. The grid size is $\Delta x = 1$, and the grain boundary thickness is $l_{\mathrm{gb}} = 4\Delta x$. The initial microstructure is determined by the analytical solution in Eq. 2.36. An example is shown in Fig. 5.13a. Grain boundary energies are $\sigma_i = 1, i = 1, 2$, and 3. Grain boundary mobilities of Γ_1 and Γ_2 are 1 and 1.5, respectively. The mobility of Γ_3 is used to control the degree of anisotropy and listed in Table 5.2. A no-flux boundary condition (Eq. 2.68) is applied.
It is difficult to measure the triple-junction angle accurately [105] due to the curved grain boundary. In this work, the grain boundary position is used instead of measuring the triple-junction angle directly. If Young's law is applied correctly, the boundary movement should follow the analytical solution in Eq. 2.37. For the case of $M_3 = 3$, the simulated microstructure is shown in Fig. 5.13b. Boundary positions at the left and right end are measured and plotted in Fig. 5.13c as a function of time. The data points are linearly fitted to get the grain boundary velocity. The average value of velocities of Γ_1 and Γ_3 is listed and compared with the analytical solution (Eq. 2.37) in Table 5.2.

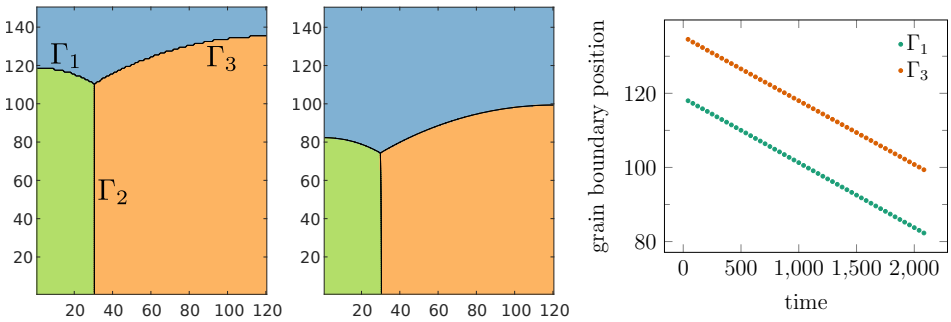

(a) Microstructure t_0 **(b)** Microstructure t_{end} **(c)** Grain boundary position

Figure 5.13: Test case 2: the growth of three grains. (a) Initial microstructure. (b) Simulated microstructure at t_{end}. (c) Positions of two curved boundaries Γ_1 and Γ_3 on the left and right side of the domain, respectively.

Table 5.2: Phase-field results of the growth of three grains.

M_1	M_3	v_{PF}	$v_{\text{analytical}}$	relative error
1	1	0.0085	0.0087	-2.09%
1	2	0.0129	0.0131	-1.60%
1	3	0.0174	0.0175	-0.59%
1	5	0.0268	0.0262	2.32%

Small relative errors indicate that the phase-field model provides the correct triple-junction condition.

5.3.3 Boundary condition

Boundary condition on the exterior surface of the sample volume is essential for the phase-field simulation. While the effect of oxidation is minimized by using the forming gas during the experiment, it is nevertheless observed that the grain boundaries at the exterior surface to some extent are pinned (grain boundaries close to the exterior surface move less than interior boundaries). Actually, the exact nature of the boundary condition is not known; thus we need to assume a boundary condition. Unlike the case with a regular domain, here the exterior sample surface has a complex shape as shown in Fig. 5.8c. In this thesis, the simulation domain is a box with the sample volume embedded, *c.f.* Fig. 5.9c. The boundary condition on the exterior sample surface is prescribed with the help of the signed distance function of the absorption volume. The idea is as

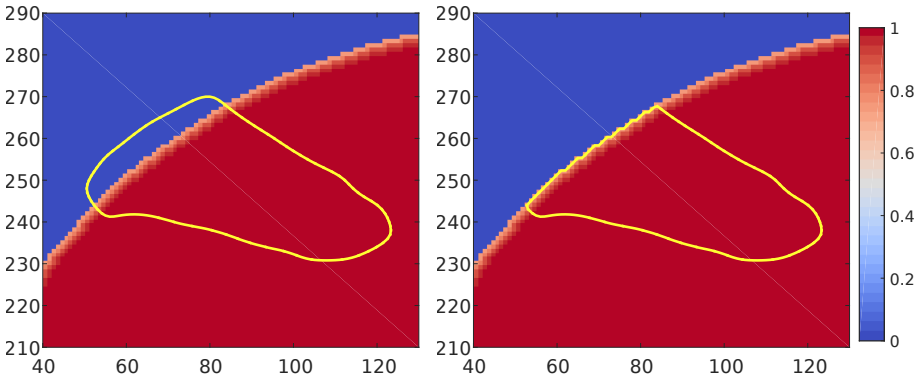

(a) Phase-field u_α evolves freely **(b)** Applied the boundary condition

Figure 5.14: Illustration of the application of boundary condition in the grain growth phase-field simulation. The color refers to u_{abs} in Eq. 5.1. The contour plot shows a surface grain. The boundary condition is applied in two steps: (a) the phase-field of the surface grain is allowed to evolve freely to the outside of the exterior surface. (b) u_{abs} confines the evolution of the surface grain within the sample volume as in Eq. 5.2. Notice (a) is an exaggeration of the growth (20 time-steps).

follows: firstly the phase-field variables of all grains are allowed to evolve freely in each simulation time-step. Phase-field variables of boundary grains thus can grow to the outside of the exterior surface, as shown in Fig. 5.14a. Then the absorption volume confines the evolution of phase-field variables, as shown in Fig. 5.14b.

The phase-field variable of the absorption volume u_{abs} is calculated from the signed distance function ϕ_{abs} according to Eq. 2.51 as

$$u_{\text{abs}} = \begin{cases} \frac{1}{2}\left(1 - \tanh\frac{2\phi_{\text{abs}}}{l_{\text{gb}}}\right) & \phi_{\text{abs}} \leq 0 \\ 0 & \phi_{\text{abs}} > 0, \end{cases} \tag{5.1}$$

where l_{gb} is the grain boundary thickness. A sharp cut at the exterior surface is used here to prevent numerical problems in the phase-field simulation. Unlike grain phase-field variables u_α, u_{abs} does not evolve with time (neglect oxidation) and is only used for prescribing the boundary condition. At the end of each phase-field time-step, all phase-field variables u_α are updated according to

$$u_\alpha = \min\{u_\alpha, u_{\text{abs}}\}. \tag{5.2}$$

The fact that this boundary condition may not be the same as reality can cause an error in the phase-field prediction near the exterior surface. To prevent the influence of this error on the fitting result, grain boundaries that touch the exterior surface should not be used in the fitting.

5.3.4 Thresholding parameter in the bounding box algorithm

In the bounding box algorithm [109, 110], a thresholding parameter ϵ_{bb} is used to control the memory cost and the simulation accuracy. Only a cuboid which contains the domain where the phase-field variable fulfills $u_\alpha \geq \epsilon_{\mathrm{bb}}$ is saved. A smaller value of ϵ_{bb} can provide a more accurate result, but need a larger bounding box, *i.e.*, require more memory. Bounding box algorithm with zero ϵ_{bb} is equivalent to the full field simulation where all phase-field variables are defined on the full simulation domain. A 2D test case shown in Fig. 5.15a is used to study the influence of the thresholding parameter ϵ_{bb} on the accuracy of phase-field simulations. Simulation results of the bounding box algorithm with various thresholding parameters are compared with the full field simulation result. The microstructure from bounding box algorithm with $\epsilon_{\mathrm{bb}} = 1 \times 10^{-3}$ (dashed green lines) is overlaid with the full field simulation result (solid red lines) at time-step 800 (Fig. 5.15a). The difference between two microstructures is invisible. To quantify the comparison, the following error is defined

$$\mathrm{err}^{\mathrm{bb}} := \sum_\alpha (u_\alpha^{\mathrm{ff}})^2 - \sum_\alpha (u_\alpha^{\mathrm{bb}})^2, \tag{5.3}$$

where u_α^{ff} and u_α^{bb} are results of the full field simulation and the bounding box algorithm simulation, respectively. The error map ($\epsilon_{\mathrm{bb}} = 10^{-3}$) at time-step 800 is shown in Fig. 5.15b. It can be seen that the largest error occurs at regions with small grains. In particular, the bounding box algorithm with a finite ϵ_{bb} slightly overestimates the small grain size. The convergence of the maximum absolute value of the error ($\max_{\mathbf{x}}\{|\mathrm{err}^{\mathrm{bb}}|\}$) at three time-steps are shown in Fig. 5.15c. It can be seen that the convergence behavior is approximately $\max_{\mathbf{x}}\{|\mathrm{err}^{\mathrm{bb}}|\} \propto \sqrt{\epsilon_{\mathrm{bb}}}$. Moreover, the error is observed to increase with time. Based on these analysis, a threshold value of $\epsilon_{\mathrm{bb}} = 10^{-4}$ is used to balance the memory cost and the accuracy in this thesis.

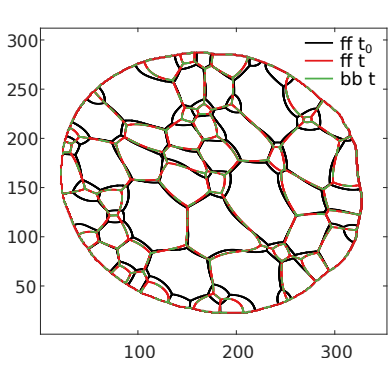

(a) Microstructures ($\epsilon_{\mathrm{bb}} = 10^{-3}$)

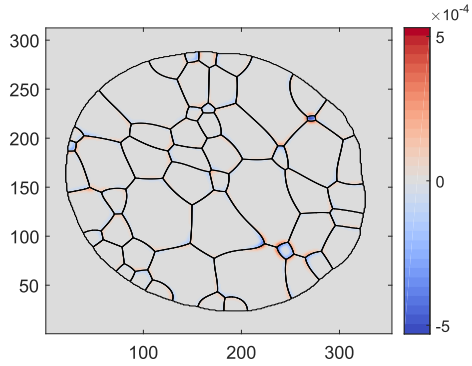

(b) Error map ($\epsilon_{\mathrm{bb}} = 10^{-3}$)

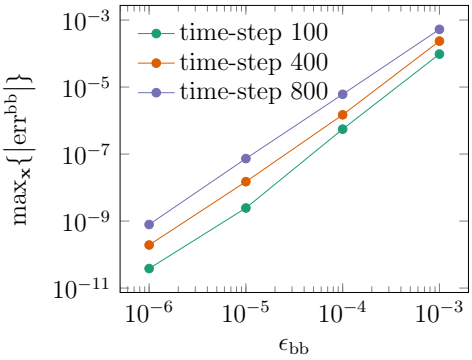

(c) Convergence of errors

Figure 5.15: Study of the threshold parameter ϵ_{bb} in the bounding box algorithm. (a) Simulated microstructure from the bounding box algorithm (bb) with a thresholding value $\epsilon_{\mathrm{bb}} = 10^{-3}$ is compared with the full field (ff) simulation result. The initial microstructure (at t_0) is shown as well. (b) The difference between the bounding box algorithm simulation and the full field simulation measured by the error defined in Eq. 5.3 at time-step 800. (c) Maximum errors as a function of ϵ_{bb} at various time-steps.

5.4 Fitting anisotropic reduced mobilities

In this part, the fitting approach discussed in Section 3.3 is applied to fit the anisotropic reduced grain boundary mobilities based on a grain growth dataset. In Section 5.4.2, the fitting approach is firstly studied based on two synthetic datasets. Then the fitting approach is applied to the DCT dataset to fit a 2D slice and the 3D volume in Section 5.4.3. As a first step, grain boundary energies are set to be one $\sigma_{\mathrm{gb}} = 1$; thus the fitting of reduced mobilities $m_{\mathrm{gb}} = M_{\mathrm{gb}}\sigma_{\mathrm{gb}}$ is essentially the same as the fitting of mobilities M_{gb} in this scenario. Employing a classical optimization algorithm to fit these mobility variables simultaneously requires a significant number of phase-field simulations for sensitivity calculation, which is currently unrealistic. The solution is an approximation of the original optimization problem in Eq. 3.27. The independence of parameters must fail near triple-junctions; therefore, triple-junction regions need to be removed from the fitting domain. Another reason to remove the triple-junction region is the approximation of the signed distance function from the phase-field given in Eq. 2.51 fails near triple-junctions.

5.4.1 Sets of grain boundaries

In phase-field simulations, each grain boundary is assigned a mobility value. The set of all grain boundaries is referred to as $\mathcal{S}^{\mathrm{all}}$. As some grain boundaries may disappear in the following experiment time-steps, only a subset of boundaries $\mathcal{S}^{\mathrm{fit}} \subset \mathcal{S}^{\mathrm{all}}$ can be fitted. Here $\mathcal{S}^{\mathrm{fit}}$ is called the set of fitted grain boundaries. Another set is called the set of 'good' grain boundaries $\mathcal{S}^{\mathrm{good}}$, which contains boundaries that provide most reliable fitted values. Generally speaking, there are several criteria to characterize a grain boundary as 'good':

1. The grain boundary must present at both experimental time-steps that are used for the fitting.

2. The grain boundary should not connect to the exterior sample surface, as discussed in Section 5.3.3.

3. The grain boundary should have a relatively large surface area.

4. The grain boundary should not be in a region with a large experimental error or less accuracy of phase-field simulations.

5.4.2 Testing on synthetic 2D datasets

Synthetic datasets are generated by phase-field simulations with initially given material parameters, which serve as the ground truth to verify the fitting approach.

5.4.2.1 Three-grain case

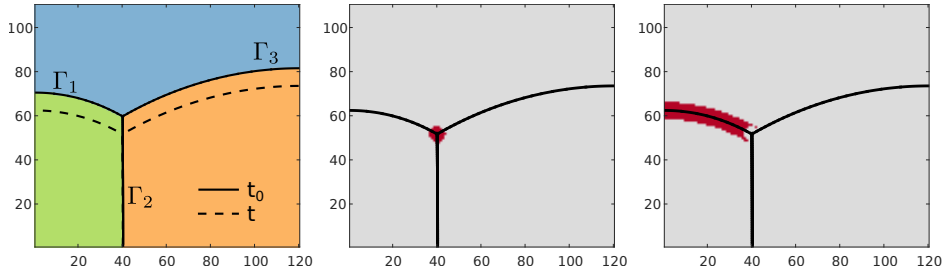

(a) Synthetic data **(b)** Triple-junction region **(c)** Fitting domain of Γ_1

Figure 5.16: Test of the fitting approach with a synthetic dataset of three grains: (a) Initial (t_0) and final (t) microstructures of the synthetic data. (b) The triple-junction region, which will be removed from the fitting domain. (c) The fitting domain of grain boundary Γ_1. The unit of all axes is Δx.

As shown in Fig. 5.16a, the microstructure composes three grains and three grain boundaries. The dimension of the simulation domain is $120\Delta x \times 110\Delta x$. Γ_2 is a straight grain boundary which does not move; thus the set of fitted grain boundaries is $\mathcal{S}^{\text{fit}} = \{\Gamma_1, \Gamma_3\}$. The synthetic dataset is generated by a phase-field simulation with grain boundary energies: $\sigma_i = 1, i = 1, 2$, and 3, grain boundary mobilities: $(M_1, M_2, M_3) = (1, 1, 2)$, and a no-flux boundary condition (Eq. 2.68). The initial and final microstructures of the synthetic dataset are shown by solid and dashed lines in Fig. 5.16a, respectively. The triple-junction region is shown in Fig. 5.16b. The fitting domain for each grain boundary is the boundary region subtracted by the triple-junction region, as shown in Fig. 5.16c.

In the fitting, grain boundary mobilities are assumed unknown, and an initial guess $(M_1, M_3) = (1.5, 1.5)$ is used. The fitting algorithm presented in Algorithm 2 (Section 3.3.5) is used to find the best-fitted values of M_1 and M_3. M_2 is set to be one throughout the whole fitting process. Contour lines of the norm-cost functions f_{cost} (Eq. 3.15) are plotted in Fig. 5.17a. Green crosses in

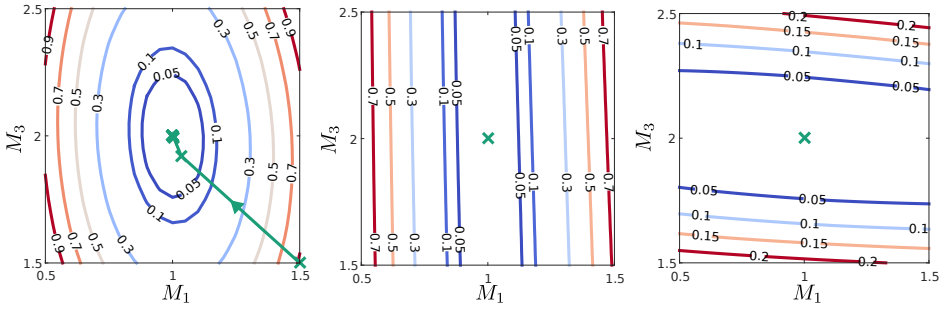

(a) Cost function f_{cost} **(b)** Cost function f^1_{cost} **(c)** Cost function f^3_{cost}

Figure 5.17: Cost function contours of the three-grain case. The initial guess of fitted parameters are $(M_1, M_3) = (1.5, 1.5)$. The green arrow in (a) indicates the direction of convergence and the crosses indicate the optimal value from each optimization iteration. Green crosses in (b) and (c) indicate the ground truth.

Fig. 5.17a shows the convergence (green arrow) of M_1 and M_3. It can be seen that the fitting approach finds the correct minimum of the cost function.
Moreover, the independence approximation in Eq. 3.26 is examined by contour lines of cost functions f^1_{cost} and f^3_{cost} for Γ_1 and Γ_3 in Figs. 5.17b and 5.17c, respectively. It can be seen that both contour lines are approximately straight, indicating that the independence approximation (Eq. 3.26) is valid.

5.4.2.2 Ten-grain case

The fitting algorithm is verified with a complicated case composing 10 grains and 30 grain boundaries, as shown in Fig. 5.18. The dimension of the simulation domain is $128\Delta x \times 128\Delta x$. The synthetic dataset is generated with material parameters $\sigma_i = 1, i \in \mathcal{S}^{\text{all}}$ and grain boundary mobilities with random values in a range of $[0.62, 1.07]$. A periodic boundary condition (Eq. 2.69) is applied in the phase-field simulation.
Grain boundaries $\Gamma_{3,9}$ and $\Gamma_{3,10}$ are excluded from the set of fitted grain boundaries $\mathcal{S}^{\text{fit}} = \mathcal{S}^{\text{all}} \setminus \{\Gamma_{3,9}, \Gamma_{3,10}\}$ because of their short boundary length. Thus, 28 out of 30 boundaries are fitted. The initial guess of mobilities is $M_i = 1, i \in \mathcal{S}^{\text{fit}}$. The two unfitted boundaries are assigned mobility values of 1. The purpose of assigning a mobility value of the unfitted boundary different from the ground truth is to mimic the experimental dataset as the mobility of the unfitted boundary is not known in practice.
Following Algorithm 2 in Section 3.3.5, best-fitted mobilities are found in 20 iterations, and convergence curves of 28 mobilities are shown in Fig. 5.19. The

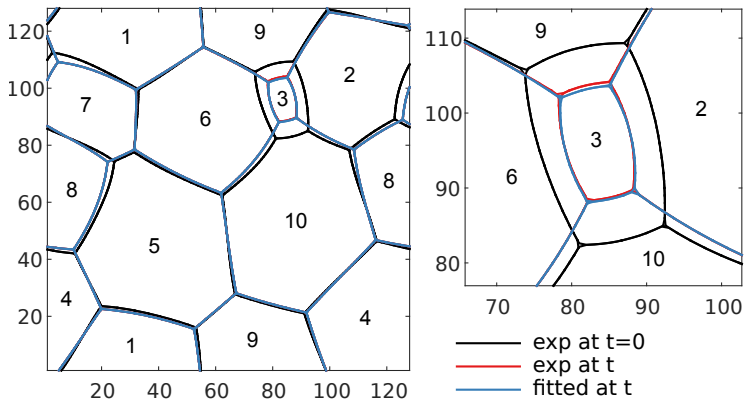

Figure 5.18: Test the fitting with a synthetic dataset of ten grains: synthetic microstructures and a zoom-in view. Grains are labeled with numbers. The unit of axes is grid size Δx.

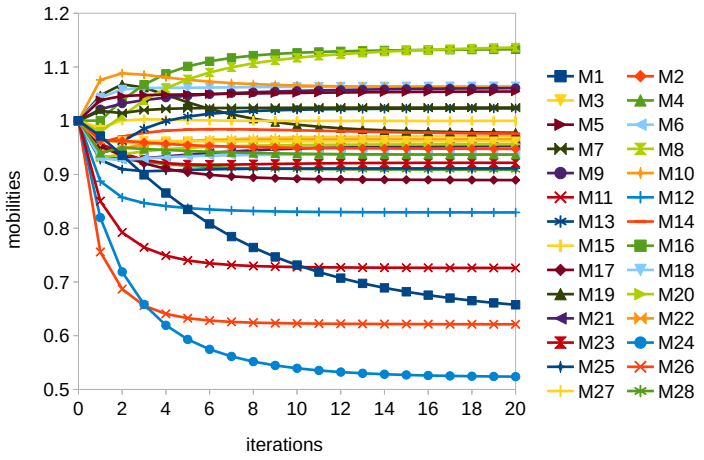

Figure 5.19: Convergence of the reduced grain boundary mobilities in the ten-grain case. Notice that most grain boundaries converge within few fitting iterations.

Table 5.3: Fitting results of the ten-grain case. The first column is the id of grain boundaries $\Gamma_{\alpha\beta}$. Fitted mobilities M^{fit} after 20 optimization iterations, the ground truth M^{real} and relative errors are listed. Grain boundaries $\Gamma_{3,9}$ and $\Gamma_{3,10}$ are not fitted. The two rows highlighted in gray are the fitting results with a large error.

Γ_i	α	β	M_i^{fit}	M_i^{real}	relative error
1	1	2	0.66	0.65	0.818%
2	1	4	0.95	0.96	-1.017%
3	1	5	0.96	0.96	-0.050%
4	1	6	0.94	0.96	-2.521%
5	1	7	1.05	1.05	-0.020%
6	1	9	0.94	0.92	1.566%
7	2	3	1.02	1.07	-4.406%
8	2	4	1.14	1.05	8.145%
9	2	7	1.06	1.06	-0.097%
10	2	8	1.06	1.06	0.350%
11	2	9	0.73	0.92	-21.261%
12	2	10	0.83	0.81	2.898%
13	3	6	1.02	1.07	-4.537%
–	3	9	1	0.74	–
–	3	10	1	1.05	–
14	4	5	0.98	0.97	0.327%
15	4	8	1.00	1.00	0.022%
16	4	9	1.13	1.07	5.934%
17	4	10	0.89	0.90	-1.217%
18	5	6	1.06	1.07	-0.137%
19	5	7	0.98	0.98	0.117%
20	5	8	0.96	0.96	-0.017%
21	5	9	0.95	0.97	-1.393%
22	5	10	0.97	0.96	0.036%
23	6	7	0.92	0.92	0.557%
24	6	9	0.52	0.90	-41.833%
25	6	10	0.91	0.90	0.964%
26	7	8	0.62	0.62	0.062%
27	8	10	0.97	0.98	-0.731%
28	9	10	0.91	0.91	-0.604%

fitted mobilities are compared with the ground truth in Table 5.3. Except for two boundaries ($\Gamma_{2,9}$ and $\Gamma_{6,9}$, the two rows highlighted in gray), relative errors of the fitted mobilities are all below 9%. The underestimation of mobilities of $\Gamma_{2,9}$ and $\Gamma_{6,9}$ is caused by the unfitted grain boundary $\Gamma_{3,9}$. A mobility value of $M_{3,9} = 0.74$ is used for generating the synthetic data, while a value of $M_{3,9} = 1$ is used in simulations in the fitting. The consequence is that grain boundary $\Gamma_{3,9}$ always moves faster in the fitting than it is in the synthetic dataset, as shown in the zoomed-in illustration in Fig. 5.18. The fast movement of $\Gamma_{3,9}$ causes a drag on the two connected grain boundaries, $\Gamma_{2,9}$ and $\Gamma_{6,9}$, to make them move faster than in the synthetic dataset. This drag, in turn, leads to smaller fitted mobility. This analysis concludes that grain boundaries connected to unfitted boundaries have a relatively large fitting error; thus should be removed from $\mathcal{S}^{\text{good}}$, according to the fourth criteria in Section 5.4.1. In summary, this result supports the validity of the fitting approach.

5.4.3 Fitting on the DCT dataset

In above cases, the fitting approach is verified on 'perfect' datasets. In this section, the fitting approach is further applied to the DCT experimental dataset, as presented in Section 5.2.

5.4.3.1 Fitting on a 2D slice of the DCT dataset

As a first step, the fitting approach is applied on a 2D slice of the DCT dataset as shown in Fig. 5.20a. A slice close to the middle of the sample volume at experimental time-step 2 ($t = 0$) is used as the initial microstructure for the phase-field simulation. The fitting is performed at experimental time-step 3 ($t = 300\ s$). For simplicity, the experimental time-step 2 and 3 are referred to as t_0 and t_1, respectively.

To use the signed distance $\phi^{\alpha}_{\text{exp}}$ (Eq. 2.50) in the fitting, the experimental data needs to be transferred from a 3D distance to a 2D distance. First, the 2D slice is extracted from the 3D phase-field variables obtained by the phase-field dilation (Section 5.2.6). Then extracted phase-field variables are corrected by a 2D phase-field code. It turns out that 20 phase-field time-steps are enough for the correction.

The dimension of the simulation domain is $350\Delta x \times 311\Delta x$. The initial grain number is 126 (at t_0), which reduces to 120 at t_1. The grain boundary number reduces from 301 at t_0 to 284 at t_1. In total, 269 grain boundaries are present

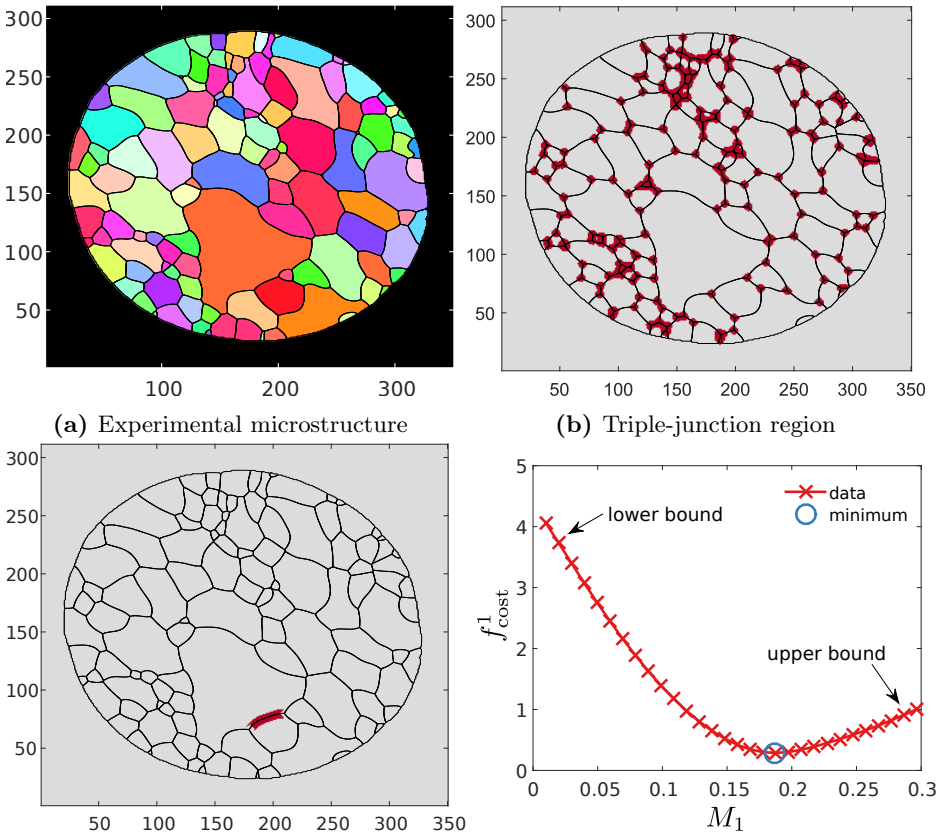

(a) Experimental microstructure

(b) Triple-junction region

(c) Fitting domain of boundary Γ_1

(d) Cost function of Γ_1 at iteration 1

Figure 5.20: Setup of the 2D fitting. (a) The experimental microstructure at t_0. (b) The triple-junction region. (c) The fitting domain of grain boundary Γ_1. (d) An example of the cost function. Data points used as upper and lower bounds are marked by arrows.

at both time-steps, so they are used as the fitted boundaries $\mathcal{S}^{\text{fit}}$. The grain boundary energies for all boundaries are set as 1. Based on the statistical analysis in Paper II, the initial guess of mobilities are $M_i = 0.1\ \mu m^2/s, i \in \mathcal{S}^{\text{fit}}$. Mobilities of unfitted grain boundaries are assigned as the average of all fitted mobilities. The grid size is $\Delta x = 1.54\ \mu m$, and the grain boundary width is $l_{\text{gb}} = 4\Delta x$. The simulation time-step is determined from $\Delta t \leq \Delta x^2/(4 \max\{M_i\}), i \in \mathcal{S}^{\text{all}}$ for numerical stability. The boundary condition proposed in Section 5.3.3 is used in the phase-field simulation.

The fitting is performed following Algorithm 2 (Section 3.3.5). Triple-junction

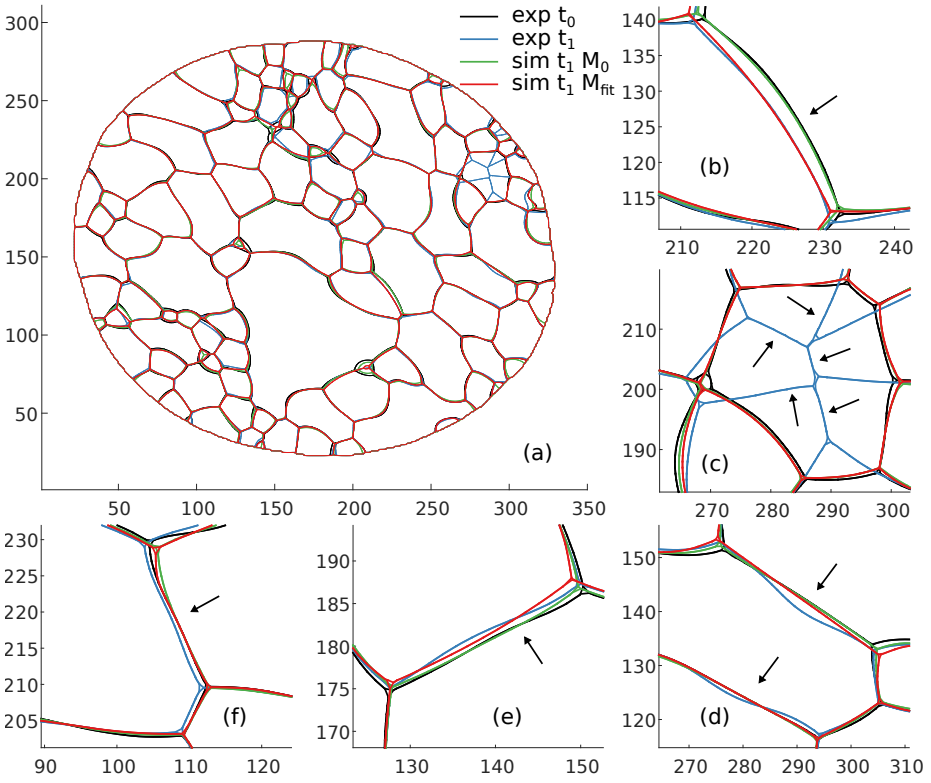

Figure 5.21: Comparison of microstructures. (a) The experimental microstructure at t_0 is shown by the black line. The simulated microstructures with the initial guess $\mathbf{M}_0$ (green line) and the best-fit values $\mathbf{M}_{\text{fit}}$ (red line) are compared with the experimental microstructure at t_1 (blue line). (b-f) zoom-in views to show detailed comparison.

regions (Fig. 5.20b) are removed from the fitting domain (Fig. 5.20c). An example of the cost function curve and the minimum point found with the fitting are shown in Fig. 5.20d. For each mobility variable, the lower and upper bounds are assigned dynamically using the second available data points as indicated by the two arrows in Fig. 5.20d.

In total four fitting iterations are performed. A comparison among microstructures is given in Fig. 5.21. The black and blue lines represent the experimental microstructures at t_0 and t_1, respectively. The green and red lines represent the simulated microstructure with the initial guess of the mobility variables M_0 and the fitted mobilities M_{fit}, respectively. It can be seen that for most grain boundaries the simulated microstructure with optimal mobilities (red lines) agrees well with the experimental one (blue lines). An example is shown in the zoom-in view (Fig. 5.21b). It is observed that the simulated microstructure with the initial guess $M_0 = 0.1\ \mu m^2/s$ (green lines) underestimates the mobility of this boundary. The convergence of this boundary is $M_{\text{fit}} = 0.1 \rightarrow 0.29 \rightarrow 0.85 \rightarrow 1.25 \rightarrow 1.29\ \mu m^2/s$. With the fitting approach, the simulation and the experiment match well. However, there are several boundaries where the simulation and the experiment do not match well:

- As shown in Fig. 5.21c, several new grains suddenly pop up at t_1. The reason is that one grain is accidentally forgotten to be selected at t_1. As only the common boundaries are fitted, this will not influence the fitting result.
- For the three boundaries pointed by arrows in Figs. 5.21d and 5.21e, grain boundaries grow from a flat shape to a curved shape, which cannot be captured by the 2D phase-field model. This may be a 3D phenomenon or due to the inclination dependence of grain boundary properties. For such cases, the fitting provides an average mobility value.
- As shown in Fig. 5.21f, the experimental microstructure moves in an opposite direction as the simulation (blue and red lines sit on the opposite side of the black line). This may because the curvature can have a different sign in 3D than viewed in 2D. For this boundary, the convergence is $M_{\text{fit}} = 0.1 \rightarrow 0.02 \rightarrow 1.3 \times 10^{-3} \rightarrow 3.2 \times 10^{-5} \rightarrow 2.5 \times 10^{-7}\ \mu m^2/s$. As the fitting cannot provide negative mobility, the lower bound is always reached. Based on this analysis, the fitted mobilities of such kind of boundaries are not reliable; thus they are not included in the final fitting result.

The fitted mobilities are plotted as a function of misorientation angle in Fig. 5.22. The set $\mathcal{S}^{\text{good}}$ is chosen according to following criteria: (1) grain boundaries

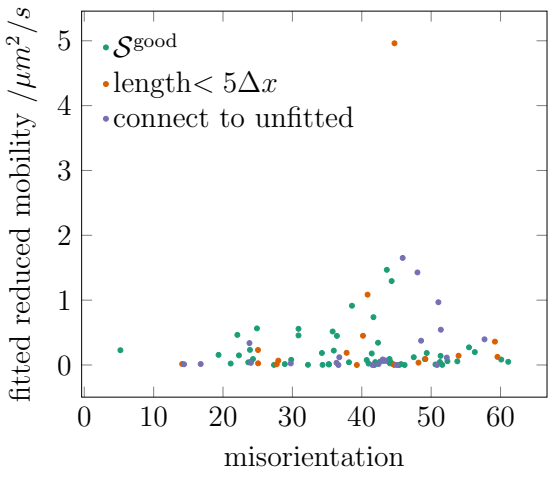

Figure 5.22: 2D fitting results of three classes of grain boundaries.

present at both time-steps. (2) the grain boundary is between interior grains at both time-steps. (3) the grain boundary length is greater than $5\Delta x$. (4) the grain boundary does not touch the unfitted boundaries. (5) the fitted mobilities should not be the upper or lower bound. There are 269 common boundaries in total, out of which 257 are fitted, because some boundaries are too small to calculate the cost function. 149 boundaries are between interior grains on both time-steps. There are 115 boundaries connected to the unfitted boundaries and 173 with a boundary length larger than $5\Delta x$. There are 68 boundaries reaching the lower bound and 7 reaching the upper bound. By applying all five criteria, 56 boundaries remain ($\mathcal{S}^{\text{good}}$), and the fitted mobilities are shown by green points in Fig. 5.22. For completeness, the fitted values of boundaries fulfill all other criteria except with a short length are also shown in Fig. 5.22 by red points. The fitted values of boundaries fulfill all other criteria except connect to the unfitted boundary are shown by blue points.

First observation of the results is that the reduced mobilities depend on misorientation angle. However, there is no simple pattern between the reduced mobility and the misorientation angle. For a fixed misorientation angle, a large variation (5 orders of magnitude) of reduced mobilities is seen between boundaries. This large scatter may be due to the misorientation axis dependence and the plane normal inclination dependence of the reduced mobilities. Moreover, a peak around 40-50 degree misorientation angles can be seen. A detailed interpretation of the fitting results will be performed shortly.

Table 5.4: An overview of the number of grains and grain boundaries (GB).

time-step	grain number	GB number	Common GB	Fitted GB
11	948	4782	-	-
12	943	4743	4412	523
13	933	4676	4361	565
14	841	4376	4150	103

5.4.3.2 Fit the 3D DCT dataset

From 2D to 3D, a major challenge is the computational time. The simulation of ∼1500 grains for 1000 phase-field time-steps takes about 14 hours on a workstation with a CPU of Xeon E5-2690v3 and MATLAB. In this part, I will present some preliminary results of the 3D fitting with one fitting iteration.

The sample volume of experimental time-step 11 is taken as the initial condition, and the fitting is performed at experimental time-steps 12 to 14. The simulation domain size is $312\Delta x \times 354\Delta x \times 306\Delta x$ with initially 948 grains. The grid size is $\Delta x = 1.54\ \mu m$ and the grain boundary width is $l_{\text{gb}} = 4\Delta x$. The grain boundary energies for all boundaries are $\sigma_{\text{gb}} = 1$. The initial guess of grain boundary mobilities is $M_i = 0.1\ \mu m^2/s$. An upper bound of $0.8\ \mu m^2/s$ and a lower bound of $0.01\ \mu m^2/s$ are set in the fitting. The boundary condition is described in Section 5.3.3.
The system has more than 4000 grain boundaries in total, with most of them are common boundaries among time-steps, as listed in Table 5.4. Applying following criteria: (a) boundary has an area larger than $100\Delta x^2$, (b) boundary between interior grains, and (c) upper or lower bounds are not reached in the fitting, several hundreds of boundaries are fitted.
Fitted mobilities at experimental time-steps 12-14 are shown in Figs. 5.23a-c. The results of 88 common fitted boundaries are shown in Fig. 5.23d for comparison. As only one fitting step is used, the accuracy of the fitted reduced mobilities is limited; nevertheless, some patterns of the reduced mobilities can still be observed. Similar to the 2D fitting results in Fig. 5.22, a large variation in the reduced mobilities and their dependence on the misorientation angle are seen. A similar peak around 40-50 degree misorientation angle is observed in all cases. A closer examination of data points in Fig. 5.23d suggests that a smaller mobility value is got with later time-steps. This is caused by the upper bound in the fitting and could potentially be solved with more fitting iterations. In the future, detailed fitting is needed to understand the reduced grain boundary mobilities.

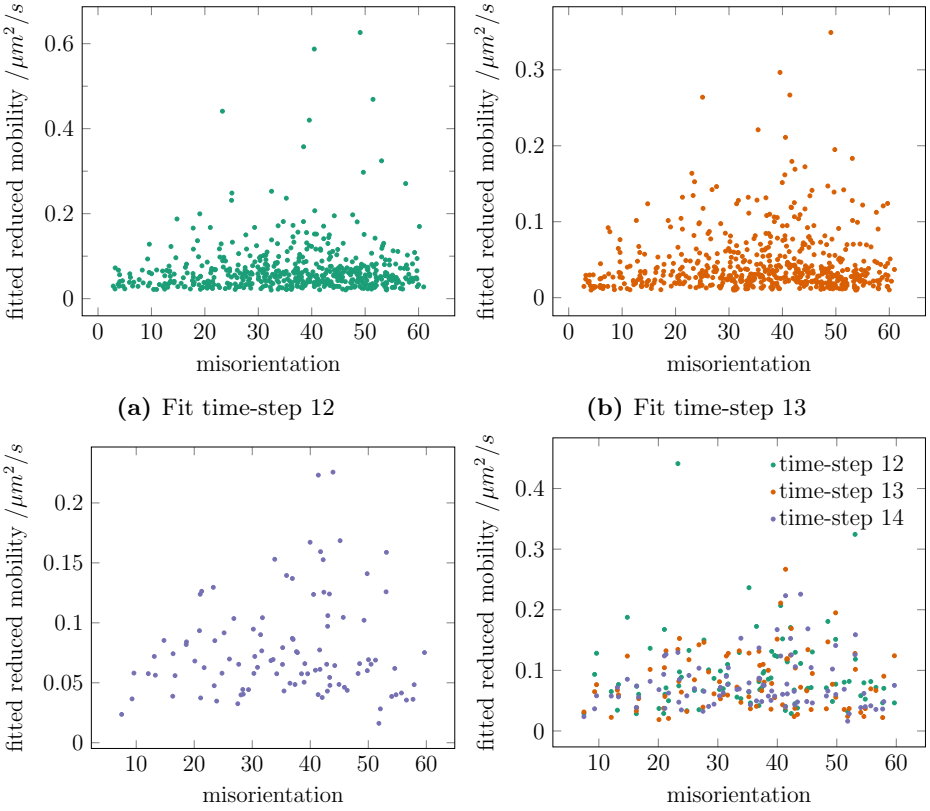

(a) Fit time-step 12

(b) Fit time-step 13

(c) Fit time-step 14

(d) Common fitted boundaries

Figure 5.23: Fitting results of reduced grain boundary mobilities on the 3D DCT dataset. (a-c) Fitted reduced grain boundary mobilities involving time-step 11 and time-steps 12-14, respectively. (d) The result of common fitted boundaries (data points presented in all fitting time-steps in (a-c)).

5.4.4 Discussion

Reduced grain boundary mobilities play a central role in the evolution of microstructures in polycrystalline materials and attribute to materials properties. They are known to live in a 5D parameter space. However, our understanding of the reduced mobilities is still limited due to lack of experimental measurements. In traditional ways of reduced mobilities measurements, such as the bi-crystal experiment, one mobility value is measured at a time. This makes it extremely time-consuming and costly to build a sufficiently large reduced mobility database.
In this chapter, the fitting approach is applied to determine hundreds of reduced mobility values simultaneously. The optimization problem involves hundreds and thousands of design variables (mobility values); thus it is difficult to be solved efficiently with a gradient-based optimization algorithm. To solve this problem, a fitting algorithm is constructed based on the independence approximation derived in Section 3.3.3. The fitting approach is verified based on synthetic datasets and then applied to a DCT dataset to fit the reduced mobilities in iron. 56 mobility values are determined from fitting a 2D section, and 1191 mobility values are determined from fitting the 3D DCT dataset. The results show that the fitting algorithm converges very fast and satisfying results can be obtained after few fitting iterations. Comparison between experimental microstructures and simulated ones with best-fitted mobilities further validates the fitting.

In the fitting, not all boundaries can be fitted. For those unfitted boundaries, a mobility value is still needed in the phase-field simulation. The test on synthetic dataset shows that assigning unfitted boundaries a mobility value differ from reality can cause a large fitting error in connected boundaries. To minimize the problem caused by unfitted boundaries, the strategy is to fit as many boundaries as possible. Then a relatively large number of the reliable fitted mobilities (in the set $\mathcal{S}^{\text{good}}$) can be obtained. Various criteria are proposed to characterize whether a boundary is 'good', so its mobility value is reliable.

In this work, I present the fitting result as a function of misorientation angles. Analysis on the misorientation axis dependence of reduced mobilities will be performed shortly. Moreover, further detailed analysis of the fitted reduced mobilities from a materials science point of view can help improve the understanding of grain boundary properties. Comparison of the fitted reduced mobilities, *e.g.*, Fig. 5.23, with those determined from molecular dynamics [142] can also be done in the future.

The phase-field model is implemented in MATLAB with the bounding box algorithm. The code is not optimized and only used as a prototype. In the future,

the computational speed can be improved by implementing in, *e.g.*, C/C++ and employing parallelization among many cores, *e.g.*, OpenMP.

Chapter 6

Conclusions and outlook

6.1 Conclusions

In this thesis, a fitting approach has been developed to extract material parameters from non-destructive three-dimensional (3D) experiments by optimizing the input material parameters of a 3D phase-field model. Compare to traditional ways of material parameter measurement, samples and sample environments representative of bulk properties and actual processing conditions can be used, and several parameters can be fitted simultaneously. The fitting methodology is presented with subsequent discussions on the cost functions, the fitting domain, and the way to reduce computational costs. The fitting approach is first applied to a simple problem of coarsening to fit two material parameters; then to the much more complex problem of grain growth to fit hundreds of material parameters.

Several conclusions from the materials science and the experiment point of view can be drawn based on these studies:

1. A liquid diffusion coefficient of value $D^{\mathrm{L}} = 8.33 \pm 0.24 \times 10^{-10}\ m^2/s$ is determined by fitting on a 4D coarsening dataset of Al-Cu alloy at a temperature just above the eutectic temperature with a composition of 20 wt%Cu.

2. If both the liquid diffusion coefficient D^{L} and the capillary length l^{L} in Al-Cu are fitted, it is observed that the best-fit values are not unique, but are found to fulfill $D^{\mathrm{L}} l^{\mathrm{L}} = 0.518 \pm 0.011\ \mu m^3/s$. This corroborates a basic hypothesis of the coarsening theory, and at the same time, this dependence indicates the high quality of the fitting approach.

3. A DCT experiment of grain growth has been performed at a synchrotron source. During annealing for 75 minutes at $800°C$, the evolution of initially 1327 grains is mapped in 3D as a function 15 time-steps with superior temporal and spatial resolution ($1.54\ \mu m$). The DCT data processing has been improved by introducing a level-set segmentation method and a phase-field dilation method for the present dataset. The segmentation problem caused by the extinction of intensities is alleviated.

4. As a first step, the inclination dependence of grain boundary mobilities and energies is neglected, and the energies are assumed isotropic in the grain growth phase-field simulation. In total, 56 reduced grain boundary mobilities are determined by fitting a 2D section, and 1191 reduced mobilities are determined from fitting a 3D DCT dataset. The reduced mobilities are observed to depend on misorientation angles and show large scatter.

Several conclusions from the fitting and the modeling point of view can be drawn:

1. Two phase-field models have been implemented for coarsening and grain growth, respectively. The phase-field model and the implementation have been verified carefully before applying in fitting the 4D experiments. For the verification, a range of numerical tests is designed to test different aspects of the phase-field models. The results show that the phase-field models can describe the underlying physics of the studied problems accurately.

2. Various scaling properties of material parameters have been derived to reduce the computational cost in the fitting. A scaling property of the liquid diffusion coefficient is applied to prevent running the phase-field simulation more than one time. An approximated scaling property of the capillary length is verified by the two-parameter fitting (liquid diffusion coefficient and capillary length). An approximated scaling property is utilized in fitting reduced grain boundary mobilities. The results show that the scaling properties can significantly reduce the number of phase-field simulations needs to be performed in the fitting.

3. For the case of fitting grain boundary mobilities, a new optimization algorithm is proposed and derived to approximate the original optimization

problem (fit all mobilities simultaneously) to sub-problems (fit the mobility of individual grain boundaries independently). The fitting results on synthetic datasets have shown that this approximation is valid, and the fitting algorithm converges fast.

6.2 Outlook

The fitting approach is foreseen to be broadly applied to many applications as 3D non-destructive experiments are becoming more and more available, and the phase-field model can be made for many relevant systems (*e.g.*, phase transformation in general). Based on the developments in this thesis, several relatively easy extensions can be:

1. Fitting of the liquid diffusion coefficient at different temperatures to determine the activation energies for diffusion.
2. Fitting the interdiffusion coefficient in materials systems with more components/phases. Both the experimental techniques [46] and phase-field models [92] are pretty mature.
3. Fitting grain boundary mobilities of iron samples with a different texture than the present one for a better understanding of the anisotropy of grain boundary mobilities.

For the last point, two extra grain growth datasets are captured during my PhD work: one with 5000 grains and 21 time-steps by DCT at ID11 ESRF and one with a different growth mode captured by 3DXRD at 1-ID APS. Samples have various textures, and experiments are performed at different temperatures. These datasets could be analyzed in the same way and be used to fit more material parameters or improve the statistics of the fitting, and therefore to obtain a better understanding of grain boundary properties.

However, in practice, several aspects can be improved in the future to improve the fitting approach:

1. Limited access to 4D experiments and a limited number of samples that can be scanned due to long scanning time (temporal resolution of techniques).
2. Phases or grains have to have sizes within a certain range to be studied experimentally. The spatial resolution of DCT today is at best 0.6 μm, which

is not optimal to precisely resolve grain boundary and triple-junction geometries.

3. The information obtained from the current 4D experiment is still not perfect, *e.g.*, the chemical information is missing.
4. This type of direct comparison with real data demands better materials models be developed.
5. The computing resources limit the number of phase-field time-steps and the number of phase-field simulations that could be performed in the fitting.

Regarding the first aspect, with the development of so-called ultimate storage ring light sources, it is foreseen that more than one order of magnitude in flux and consequently improvement in temporal and spatial resolution can be obtained in the near future. Already today the temporal resolution of absorption contrast tomography can be ten milliseconds [37]. Regarding DCT, if the acquisition time is ten times faster in the future, not only would this allow real *in situ* experiments, but also means that more samples can be handled in the same experimental time.
Recently, the DCT techniques have been migrated to laboratory sources, so-called laboratory DCT (labDCT) [153, 154], with a spatial resolution today at best 5 μm and a scanning time close to a day. With the continuous developments of new laboratory x-ray sources, the spatial resolution and scanning time is foreseen to be further improved, which will give more access to 4D experiments.

Regarding the second aspect, techniques which provide higher spatial resolution need to be developed. The dark field x-ray microscopy (DFXRM) [47, 169] is a technique that can offer grain maps with a much better resolution: about 80 nm today and could be improved to 25 nm with a multilayer Laue lens [170].

Regarding the third aspect, for example, to separate the liquid diffusion coefficient and the capillary length, more information need to be measured, *i.e.*, the composition profile is needed. This kind of measurement is very challenging as the composition change due to capillary is typically very small to be detected accurately. In the future, possible ways to solve this problem are (1) development of new techniques that can capture the small contrast difference, *e.g.*, by improving PCT, (2) reducing the characteristic length scale of the microstructure in order to have a larger capillary driving force, and (3) employing other driving forces, *e.g.* a temperature gradient.

One example regarding the fourth aspect, better phase-field models which can accurately capture the inclination dependence need to be developed and verified

to fit the 5D anisotropic grain boundary properties.
The anisotropic grain boundary energies can be determined by explicitly measuring the triple-junction geometry. With the help of the phase-field method, the triple-junction condition is implicitly implied in the phase-field equations. Therefore, in principle, it is possible to fit the energies without measuring the triple-junction geometries. However, a deep understanding of the behavior of the solution of phase-field equations near the triple-junction region is needed in order to build a fitting algorithm in the future.
Precise simulation of microstructure evolution needs correct boundary conditions. However, at the current stage, the actual boundary condition is difficult to be quantified accurately and is not straightforward to be included in the modeling. So far, the problem is solved by removing regions influenced by the artificial boundary condition from the fitting domain, however, at the expense of having fewer boundaries used for fitting. In the future, better ways to quantify the boundary condition have to be studied.

Regarding the last aspect, we can either speed up the phase-field simulation or reduce the number of fitting iterations. Generally speaking, there are four ways to reduce the computational time. (1) Solving the phase-field equations by massive parallel algorithms and advanced parallel hardware architectures, *e.g.*, general-purpose computing on graphics processing units (GPGPU) [171, 172, 173, 174, 175]. For example, the coarsening phase-field implementation can be heavily optimized and be used on a routine base to measure the liquid diffusion coefficients in other binary alloys. (2) Making a proper approximation of the phase-field model for the studied problems. For example, the parabolic approximation of the CALPHAD free energy used in the coarsening phase-field simulation can help reduce the simulation time. In the future, similar simplification of the model without losing much accuracy is highly demanded. (3) Preventing unnecessary phase-field simulations by investigating properties of the phase-field equation, such as the scaling properties used in this thesis. Notice that what kind of properties can be used depends on the scientific cases. (4) Providing a better initial guess of materials parameters can help reduce the number of fitting iterations. In the present fitting of the reduced grain boundary mobilities, I used an initial guess from the statistical analysis of the DCT dataset on the grain level (see Paper II). In the future, a better initial guess could be obtained by analyzing the experimental dataset on the grain boundary level. Such work is already planned.

Appendix A

Appendix

A.1 Cartesian tensors

In a Cartesian coordinate system of dimension n, the base vectors are denoted as $\mathbf{e}_i$ where $i = 1, \cdots, n$. A vector is defined as

$$\mathbf{a} := a_i \mathbf{e}_i.$$

The second order tensor can be written in index notation as

$$\mathbb{A} := A_{ij} \mathbf{e}_i \otimes \mathbf{e}_j,$$

where $\otimes$ is the tensor product. The transpose of a second order tensor is defined as

$$\mathbb{A}^T := A_{ij} \mathbf{e}_j \otimes \mathbf{e}_i = A_{ji} \mathbf{e}_i \otimes \mathbf{e}_j.$$

The second order identity tensor is defined as

$$\mathbb{I} := \delta_{ij} \mathbf{e}_i \otimes \mathbf{e}_j = \mathbf{e}_i \otimes \mathbf{e}_i.$$

The derivatives of tensor-valued functions are defined as

$$\mathbf{a}_{,j} := a_{i,j} \mathbf{e}_i,$$

$$\mathbb{A}_{,k} := A_{ij,k} \mathbf{e}_i \otimes \mathbf{e}_j.$$

where $_{,i}$ means the derivative to the ith coordinate.
Now let's define several useful operators. The gradient operators:

$$\nabla\phi := \phi_{,i}\mathbf{e}_i,$$

$$\nabla\mathbf{a} := \mathbf{e}_i \otimes \mathbf{a}_{,i} = a_{j,i}\mathbf{e}_i \otimes \mathbf{e}_j,$$

$$\nabla\mathbb{A} := \mathbf{e}_i \otimes \mathbb{A}_{,i} = A_{jk,i}\mathbf{e}_i \otimes \mathbf{e}_j \otimes \mathbf{e}_k,$$

The divergence operators:

$$\nabla \cdot \mathbf{a} := \mathbf{e}_i \cdot \mathbf{a}_{,i} = a_{i,i},$$

$$\nabla \cdot \mathbb{A} := \mathbf{e}_i \cdot \mathbf{A}_{,i} = A_{ij,i}\mathbf{e}_j,$$

The curl operators:

$$\nabla \times \mathbf{a} := \mathbf{e}_i \times \mathbf{a}_{,i} = a_{i,j}\mathbf{e}_j \times \mathbf{e}_i = \epsilon_{jik}a_{i,j}\mathbf{e}_k,$$

The Laplacian:

$$\Delta\mathbb{A} := \nabla^2\mathbb{A} = (\nabla \cdot \nabla)\mathbb{A}.$$

Based on these definitions, calculation rules can be derived. In the following I provide a list of useful relations:

$$\nabla(\phi\psi) = \phi\nabla\psi + \psi\nabla\phi,$$

$$\nabla(\phi\mathbf{a}) = \nabla\phi \otimes \mathbf{a} + \phi\nabla\mathbf{a},$$

$$\nabla(\mathbf{a} \cdot \mathbf{b}) = \nabla\mathbf{a} \cdot \mathbf{b} + \nabla\mathbf{b} \cdot \mathbf{a},$$

$$\nabla(\mathbb{A} \cdot \mathbf{a}) = \nabla\mathbb{A} \cdot \mathbf{a} + \mathbb{A} \cdot (\nabla\mathbf{a})^T = \nabla\mathbb{A} \cdot \mathbf{a} + \nabla\mathbf{a} \cdot \mathbb{A}^T,$$

$$\nabla \cdot (\phi\mathbf{a}) = \nabla\phi \cdot \mathbf{a} + \phi\nabla \cdot \mathbf{a},$$

$$\nabla \cdot (\mathbf{a} \otimes \mathbf{b}) = (\nabla \cdot \mathbf{a})\mathbf{b} + \mathbf{a} \cdot \nabla\mathbf{b},$$

$$\nabla \cdot (\mathbb{A} \cdot \mathbf{a}) = (\nabla \cdot \mathbb{A}) \cdot \mathbf{a} + (\nabla\mathbf{a}) : \mathbb{A}^T,$$

$$\nabla \cdot (\mathbb{A} \otimes \mathbf{a}) = (\nabla \cdot \mathbb{A}) \otimes \mathbf{a} + \mathbb{A}^T \cdot (\nabla\mathbf{a}),$$

$$\nabla \cdot (\mathbf{a} \otimes \mathbb{A}) = (\nabla \cdot \mathbf{a})\mathbb{A} + (\nabla \cdot \mathbb{A}^T) \otimes \mathbf{a},$$

$$\nabla \cdot (\mathbb{A} \cdot \mathbb{B}) = \nabla \cdot \mathbb{A} \otimes \mathbb{B} + \mathbb{A}^T \cdot \nabla\mathbb{B},$$

$$\nabla({}^n\mathbb{A}) = \nabla \cdot (\mathbb{I} \otimes {}^n\mathbb{A}),$$

where ${}^n\mathbb{A}$ is an n-th order tensor ($n \geq 1$).

The divergence theorem/Gauss's theorem expresses the translation between a volume integral and a surface integral.

$$\int_\Omega \nabla \cdot \mathbf{a}\,\mathrm{d}V = \int_{\partial\Omega} \hat{n} \cdot \mathbf{a}\,\mathrm{d}A,$$

where $\hat{n}$ is the outward unit normal of boundary $\partial\Omega$.
Some variations of the divergence theorem are

$$\int_\Omega \nabla \mathbf{a}\,\mathrm{d}V = \int_\Omega \nabla\cdot(\mathbb{I}\otimes\mathbf{a})\,\mathrm{d}V = \int_{\partial\Omega}\hat{n}\otimes\mathbf{a}\,\mathrm{d}A,$$

$$\int_\Omega \nabla\times\mathbf{a}\,\mathrm{d}V = \int_{\partial\Omega}\hat{n}\times\mathbf{a}\,\mathrm{d}V,$$

$$\int_\Omega \nabla\cdot\mathbb{A}\,\mathrm{d}V = \int_{\partial\Omega}\hat{n}\cdot\mathbb{A}\,\mathrm{d}A,$$

$$\int_\Omega \nabla\mathbb{A}\,\mathrm{d}V = \int_{\partial\Omega}\hat{n}\otimes\mathbb{A}\,\mathrm{d}A,$$

$$\int_\Omega \nabla\times\mathbb{A}\,\mathrm{d}V = \int_{\partial\Omega}\hat{n}\times\mathbb{A}\,\mathrm{d}A.$$

A.2 The delta function

The delta function $\delta(x)$ has the following property

$$\int_{-\infty}^{+\infty} f(x)\delta(x)\,\mathrm{d}x = f(0).$$

It can be extended to $\mathbb{R}^n$ as [34]

$$\int_{\mathbb{R}^n} f(\mathbf{x})\delta(\phi(\mathbf{x}))|\nabla\phi(\mathbf{x})|\,\mathrm{d}V = \int_{\phi=0} f(\mathbf{x})\,\mathrm{d}A,$$

where ϕ is a level-set function.

A.3 Functional derivatives

Let $F[\phi]$ be a functional $F : M \to \mathbb{R}$, where $M = \{\phi(x) : x \in \mathbb{R}\}$ is a Banach space. The object $\frac{\delta F[\phi]}{\delta\phi(x)}$ tells how the value of the functional changes if the function $\phi(x)$ is changed at the point x. The functional derivative (Fréchet derivative) is defined as [176]

$$\delta F[\phi] := \int \frac{\delta F[\phi]}{\delta\phi(x)}\delta\phi(x)\,\mathrm{d}x.$$

If we use

$$\delta\phi(x) = \epsilon\delta(x-y),$$

then

$$\delta F[\phi] = F[\phi + \epsilon\delta(x-y)] - F[\phi] = \int \frac{\delta F[\phi]}{\delta\phi(x)}\epsilon\delta(x-y)\,\mathrm{d}x = \epsilon\frac{\partial F[\phi]}{\partial\phi(y)}.$$

In the limit

$$\frac{\partial F[\phi]}{\partial\phi(y)} = \lim_{\epsilon\to 0}\frac{F[\phi+\epsilon\delta(x-y)] - F[\phi]}{\epsilon}.$$

Two examples of the functional derivative are

Example 1: $F = \int \phi(x)^n\,\mathrm{d}x$

$$\frac{\delta F[\phi]}{\delta\phi(y)} = n\phi(y)^{n-1}.$$

Example 2: $F = \int \left(\frac{\mathrm{d}\phi(x)}{\mathrm{d}x}\right)^n\,\mathrm{d}x$

$$\frac{\delta F[\phi]}{\delta\phi(y)} = -n\frac{\mathrm{d}}{\mathrm{d}x}\left[\left(\frac{\mathrm{d}\phi(x)}{\mathrm{d}x}\right)^{n-1}\right]_y.$$

A.4 Differential geometry

The mean curvature of a surface with unit normal $\hat{n}$ is calculated as

$$\mathcal{H} = \frac{1}{2}\nabla_\Gamma\cdot\hat{n} = \frac{1}{2}(\kappa_1+\kappa_2), \tag{A.1}$$

where κ_1 and κ_2 are the principal curvatures, and the operator ∇_Γ is the projection of the gradient operator ∇ on the surface Γ. It is defined as

$$\nabla_\Gamma = (\mathbb{I} - \hat{n}\otimes\hat{n})\cdot\nabla. \tag{A.2}$$

A.5 Asymptotic analysis of Allen-Cahn equation

The purpose here is not a comprehensive and rigorous derivation, but to show the fundamental idea of the asymptotic analysis of phase-field equations.

Suppose we have a two-phase system with domain $\mathcal{D}$, in which a domain of one phase Ω exists. The boundary of Ω is denoted as $\partial\Omega$.
Consider the Allen-Cahn equation of the form

$$\frac{\partial u}{\partial t} = \Delta u - \epsilon^{-2} W'(u). \tag{A.3}$$

The basic idea of the so-called matched asymptotic analysis is to expand the solution of Eq. A.3 in a power series of ϵ in two regions: near the interface (inner expansion) and far from the interface (outer expansion). Then the outer expansion and inner expansion is matched together to define the expansion coefficients [177, 178, 179, 82, 85, 86].
Let's define a stretched normal distance

$$z = \frac{\phi(\mathbf{x}, t)}{\epsilon},$$

where ϕ is the signed distance function of boundary $\partial\Omega$. Close to the boundary $\partial\Omega$, the solution of Eq. A.3 is inner expanded as

$$u(\mathbf{x}, t) = U(z; \mathbf{x}, t) = U_0(z; \mathbf{x}, t) + \epsilon U_1(z; \mathbf{x}, t) + \epsilon^2 U_2(z; \mathbf{x}, t) + \cdots . \tag{A.4}$$

With this, we have [179]

$$\begin{aligned} \nabla u &= \nabla_x U + \epsilon^{-1} \nabla\phi \partial_z U, \\ \Delta u &= \Delta_x U + \epsilon^{-1} \Delta\phi \partial_z U + \epsilon^{-2} \partial_{zz} U, \\ \partial_t u &= \partial_t U + \epsilon^{-1} \partial_t \phi \partial_z U. \end{aligned} \tag{A.5}$$

Similar to Eq. A.4, we expand the velocity field as

$$v = V_0 + \epsilon V_1 + \epsilon^2 V_2 + \cdots . \tag{A.6}$$

Substituting Eqs. A.5, A.4, and A.6 into Eq. A.3 and organizing terms with the same order of ϵ, we have to the lowest order ϵ^{-2}

$$\partial_{zz} U_0 + W'(U_0) = 0, \tag{A.7}$$

and to the order of ϵ^{-1}

$$(V_0 - 2\mathcal{H})\partial_z U_0 + W''(U_0) U_1 = 0. \tag{A.8}$$

Notice that $\partial_t \phi = v$ and $\Delta\phi = 2\mathcal{H}$ (Eq. A.1) are used.
Eq. A.7 is actually the Euler-Lagrange equation of Eq. A.3. By matching the outer expansion, the boundary condition for Eq. A.7 can be obtained. Then Eq. A.7 can be solved to get a steady-state profile $U_0 = q(z)$. As further shown by Fife [178], $U_1 = 0$; thus, we have the following equation from Eq. A.4.

$$u = q\left(\frac{x}{\epsilon}\right) + \mathcal{O}(\epsilon^2). \tag{A.9}$$

Similarly, Eq. A.8 can be written as (consider $U_1 = 0$)

$$V_0 = 2\mathcal{H}.$$

The velocity (Eq. A.6) is written as

$$v = 2\mathcal{H} + \mathcal{O}(\epsilon^2).$$

Bibliography

[1] OSTP. Materials genome initiative for global competitiveness. Technical report, Office of Science and Technology Policy, Washingtom, DC, 2011.

[2] S. Curtarolo et al. Fuelling discovery by sharing. *Nature Materials*, 12(3):173–173, 2013.

[3] Materials innovation case study: Questek's ferrium®M54®steel for hook shank application.

[4] J. Greeley, T. F. Jaramillo, J. Bonde, I. Chorkendorff, and J. K. Nørskov. Computational high-throughput screening of electrocatalytic materials for hydrogen evolution. *Nature materials*, 5(11):909–913, 2006.

[5] S. Curtarolo, G. L. Hart, M. B. Nardelli, N. Mingo, S. Sanvito, and O. Levy. The high-throughput highway to computational materials design. *Nature materials*, 12(3):191–201, 2013.

[6] M. L. Green, C. Choi, J. Hattrick-Simpers, A. Joshi, I. Takeuchi, S. Barron, E. Campo, T. Chiang, S. Empedocles, J. Gregoire, et al. Fulfilling the promise of the materials genome initiative with high-throughput experimental methodologies. *Applied Physics Reviews*, 4(1):011105, 2017.

[7] G. B. Olson and C. J. Kuehmann. Materials genomics: From CALPHAD to flight. *Scripta Materialia*, 70:25–30, 2014.

[8] G. B. Olson. Computational design of hierarchically structured materials. *Science*, 277(5330):1237–1242, 1997.

[9] J. Hemminger, G. Crabtree, and J. Sarrao. From quanta to the continuum: Opportunities for mesoscale science. Technical report, U.S. DOE Office of Science (SC)(United States), Sep 2012.

[10] A. Rollett, F. Humphreys, G. S. Rohrer, and M. Hatherly. *Recrystallization and related annealing phenomena*. Elsevier, 2004.

[11] G. Gottstein and L. S. Shvindlerman. *Grain boundary migration in metals: thermodynamics, kinetics, applications*. CRC press, December 2009.

[12] Z.-K. Liu. First-principles calculations and CALPHAD modeling of thermodynamics. *Journal of Phase Equilibria and Diffusion*, 30(5):517–534, 2009.

[13] M. Mantina, Y. Wang, R. Arroyave, L. Q. Chen, Z. K. Liu, and C. Wolverton. First-principles calculation of self-diffusion coefficients. *Physical Review Letters*, 100:215901, May 2008.

[14] M. Mantina, S. L. Shang, Y. Wang, L. Q. Chen, and Z. K. Liu. 3*d* transition metal impurities in aluminum: A first-principles study. *Physical Review B*, 80:184111, Nov 2009.

[15] W. Wang, H. Fang, S. Shang, H. Zhang, Y. Wang, X. Hui, S. Mathaudhu, and Z. Liu. Atomic structure and diffusivity in liquid $Al_{80}Ni_{20}$ by ab initio molecular dynamics simulations. *Physica B: Condensed Matter*, 406(15-16):3089 – 3097, 2011.

[16] B.-C. Zhou, S.-L. Shang, Y. Wang, and Z.-K. Liu. Diffusion coefficients of alloying elements in dilute Mg alloys: A comprehensive first-principles study. *Acta Materialia*, 103:573–586, 2016.

[17] P. Lazar and M. Otyepka. Accurate surface energies from first principles. *Physical Review B*, 91(11):115402, 2015.

[18] D. L. Olmsted, S. M. Foiles, and E. A. Holm. Survey of computed grain boundary properties in face-centered cubic metals: I. grain boundary energy. *Acta Materialia*, 57(13):3694 – 3703, 2009.

[19] D. L. Olmsted, E. A. Holm, and S. M. Foiles. Survey of computed grain boundary properties in face-centered cubic metals II: Grain boundary mobility. *Acta Materialia*, 57(13):3704 – 3713, 2009.

[20] H.-K. Kim, S. G. Kim, W. Dong, I. Steinbach, and B.-J. Lee. Phase-field modeling for 3D grain growth based on a grain boundary energy database. *Modelling and Simulation in Materials Science and Engineering*, 22(3):034004, 2014.

[21] S. Ratanaphan, D. L. Olmsted, V. V. Bulatov, E. A. Holm, A. D. Rollett, and G. S. Rohrer. Grain boundary energies in body-centered cubic metals. *Acta Materialia*, 88:346 – 354, 2015.

[22] J. Als-Nielsen and D. McMorrow. *Elements of modern X-ray physics*. John Wiley & Sons, 2011.

[23] H. E. Martz, C. M. Logan, D. J. Schneberk, and P. J. Shull. *X-ray imaging: Fundamentals, Industrial Techniques and Applications*. CRC Press, 2016.

[24] D. Rowenhorst, A. Lewis, and G. Spanos. Three-dimensional analysis of grain topology and interface curvature in a β-titanium alloy. *Acta Materialia*, 58(16):5511 – 5519, 2010.

[25] S. J. Dillon and G. S. Rohrer. Characterization of the grain-boundary character and energy distributions of yttria using automated serial sectioning and EBSD in the FIB. *Journal of the American Ceramic Society*, 92(7):1580–1585, 2009.

[26] P. Cloetens, M. Pateyron-Salomé, J. Buffiere, G. Peix, J. Baruchel, F. Peyrin, and M. Schlenker. Observation of microstructure and damage in materials by phase sensitive radiography and tomography. *Journal of Applied Physics*, 81(9):5878–5886, 1997.

[27] J. Radon. On the determination of functions from their integral values along certain manifolds. *IEEE transactions on medical imaging*, 5(4):170–176, 1986.

[28] R. Gordon, R. Bender, and G. T. Herman. Algebraic reconstruction techniques (ART) for three-dimensional electron microscopy and x-ray photography. *Journal of theoretical Biology*, 29(3):471IN1477–476IN2481, 1970.

[29] A. C. Kak and M. Slaney. *Principles of computerized tomographic imaging*. SIAM, 2001.

[30] N. Otsu. A threshold selection method from gray-level histograms. *IEEE transactions on systems, man, and cybernetics*, 9(1):62–66, 1979.

[31] S. Lloyd. Least squares quantization in PCM. *IEEE transactions on information theory*, 28(2):129–137, 1982.

[32] E. Forgy. Cluster analysis of multivariate data: efficiency versus interpretability models. *Biometrics*, 61(3):768–769, 1965.

[33] L. A. Vese and T. F. Chan. A multiphase level set framework for image segmentation using the mumford and shah model. *International journal of computer vision*, 50(3):271–293, 2002.

[34] S. Osher and R. Fedkiw. *Level set methods and dynamic implicit surfaces*, volume 153. Springer Science & Business Media, 2006.

[35] M. Beneš, V. Chalupeckỳ, and K. Mikula. Geometrical image segmentation by the Allen-Cahn equation. *Applied Numerical Mathematics*, 51(2-3):187–205, 2004.

[36] Y. Li and J. Kim. Multiphase image segmentation using a phase-field model. *Computers & Mathematics with Applications*, 62(2):737–745, 2011.

[37] E. Maire and P. J. Withers. Quantitative x-ray tomography. *International Materials Reviews*, 59(1):1–43, 2014.

[38] H. F. Poulsen and D. Juul Jensen. *Synchrotron radiation diffraction. A novel tool for recrystallization studies in bulk μm^3 sized local areas*, pages 503–508. Risø National Laboratory, 1995.

[39] H. F. Poulsen. *Three-dimensional X-ray diffraction microscopy: mapping polycrystals and their dynamics*, volume 205 of *Springer Tracts in Modern Physics*. Springer Berlin Heidelberg, 2004.

[40] S. Schmidt, S. F. Nielsen, C. Gundlach, L. Margulies, X. Huang, and D. J. Jensen. Watching the growth of bulk grains during recrystallization of deformed metals. *Science*, 305(5681):229–232, 2004.

[41] J. Oddershede, S. Schmidt, H. F. Poulsen, H. O. Sørensen, J. Wright, and W. Reimers. Determining grain resolved stresses in polycrystalline materials using three-dimensional x-ray diffraction. *Journal of Applied Crystallography*, 43(3):539–549, 2010.

[42] U. Lienert, S. Li, C. Hefferan, J. Lind, R. Suter, J. Bernier, N. Barton, M. Brandes, M. Mills, M. Miller, et al. High-energy diffraction microscopy at the advanced photon source. *JOM Journal of the Minerals, Metals and Materials Society*, 63(7):70–77, 2011.

[43] C. M. Hefferan, J. Lind, S. F. Li, U. Lienert, A. D. Rollett, and R. M. Suter. Observation of recovery and recrystallization in high-purity aluminum measured with forward modeling analysis of high-energy diffraction microscopy. *Acta Materialia*, 60(10):4311–4318, 2012.

[44] G. Johnson, A. King, M. G. Honnicke, J. Marrow, and W. Ludwig. X-ray diffraction contrast tomography: a novel technique for three-dimensional grain mapping of polycrystals. II. the combined case. *Journal of Applied Crystallography*, 41(2):310–318, Apr 2008.

[45] W. Ludwig, P. Reischig, A. King, M. Herbig, E. Lauridsen, G. Johnson, T. Marrow, and J.-Y. Buffiere. Three-dimensional grain mapping by x-ray diffraction contrast tomography and the use of friedel pairs in diffraction data analysis. *Review of Scientific Instruments*, 80(3), 2009.

[46] P. Reischig, A. King, L. Nervo, N. Viganó, Y. Guilhem, W. J. Palenstijn, K. J. Batenburg, M. Preuss, and W. Ludwig. Advances in x-ray diffraction contrast tomography: flexibility in the setup geometry and application to multiphase materials. *Journal of Applied Crystallography*, 46(2):297–311, Apr 2013.

[47] H. Simons, A. King, W. Ludwig, C. Detlefs, W. Pantleon, S. Schmidt, F. Stöhr, I. Snigireva, A. Snigirev, and H. F. Poulsen. Dark-field x-ray microscopy for multiscale structural characterization. *Nature communications*, 6, 2015.

[48] N. Viganò, W. Ludwig, and K. J. Batenburg. Reconstruction of local orientation in grains using a discrete representation of orientation space. *Journal of Applied Crystallography*, 47(6):1826–1840, Dec 2014.

[49] N. Viganò, A. Tanguy, S. Hallais, A. Dimanov, M. Bornert, K. J. Batenburg, and W. Ludwig. Three-dimensional full-field x-ray orientation microscopy. *Scientific reports*, 6, 2016.

[50] S. R. de Groot, P. Mazur, and A. L. King. Non-equilibrium thermodynamics. *American Journal of Physics*, 31(7):558–559, 1963.

[51] D. Chandler. *Introduction to modern statistical mechanics.* Oxford University Press, 1987.

[52] L. E. Reichl. *A modern course in statistical physics.* John Wiley & Sons, 2016.

[53] D. Jou, G. Lebon, and J. Casas-Vázquez. *Extended Irreversible Thermodynamics.* Springer, 4 edition, 2010.

[54] P. van der Schoot. Non-equilibrium thermodynamics and statistical mechanics. Lecture note for course 3CS02 Non-equilibrium Thermodynamics and Statistical Mechanics at Eindhoven University of Technology, 2014.

[55] J. W. Gibbs. *The collected works of J. Willard Gibbs.* Yale University Press, 1948.

[56] M. Upmanyu, G. Hassold, A. Kazaryan, E. Holm, Y. Wang, B. Patton, and D. Srolovitz. Boundary mobility and energy anisotropy effects on microstructural evolution during grain growth. *Interface Science*, 10(2):201–216, 2002.

[57] E. Brosh and R. Z. Shneck. Effect of strong anisotropy in grain-boundary energy on boundary mobility in abnormally grown grains. *Journal of the American Ceramic Society*, 87(4):640–643, 2004.

[58] G. S. Rohrer. Influence of interface anisotropy on grain growth and coarsening. *Annual Review of Materials Research*, 35(1):99–126, 2005.

[59] G. S. Rohrer. Grain boundary energy anisotropy: a review. *Journal of Materials Science*, 46(18):5881–5895, 2011.

[60] G. Gottstein, D. Molodov, L. Shvindlerman, D. Srolovitz, and M. Winning. Grain boundary migration: misorientation dependence. *Current Opinion in Solid State and Materials Science*, 5(1):9–14, 2001.

[61] A. Sutton, E. Banks, and A. Warwick. The five-dimensional parameter space of grain boundaries. *Proceedings of the Royal Society of London A: Mathematical, Physical and Engineering Sciences*, 471(2181):20150442, 2015.

[62] A. Morawiec. *Orientations and rotations*. Springer, 2003.

[63] O. Engler and V. Randle. *Introduction to texture analysis: macrotexture, microtexture, and orientation mapping*. CRC press, 2009.

[64] L. Ratke and P. W. Voorhees. *Growth and coarsening: Ostwald ripening in material processing*. Springer Science & Business Media, 2002.

[65] C. Herring. Surface tension as a motivation for sintering. In J. M. Ball, D. Kinderlehrer, P. Podio-Guidugli, and M. Slemrod, editors, *Fundamental Contributions to the Continuum Theory of Evolving Phase Interfaces in Solids*, pages 33–69. Springer Berlin Heidelberg, 1951.

[66] J. Cahn and D. Hoffman. A vector thermodlnamics for anisotropic surfaces: II. curved and faceted surfaces. *Acta Metallurgica*, 22(10):1205 – 1214, 1974.

[67] D. W. Hoffman and J. W. Cahn. A vector thermodynamics for anisotropic surfaces: I. fundamentals and application to plane surface junctions. *Surface Science*, 31:368 – 388, 1972.

[68] N. Provatas and K. Elder. *Phase-field methods in materials science and engineering*. John Wiley & Sons, 2011.

[69] C. Zener. Theory of growth of spherical precipitates from solid solution. *Journal of Applied Physics*, 20(10):950–953, 1949.

[70] L. K. Aagesen. *Phase-field simulation of solidification and coarsening in dendritic microstructures*. PhD thesis, Northwestern University, 2010.

[71] J. von Neumann. Discussion: Shape of metal grains metal interfaces. *American Society for Metals*, 1952.

[72] W. W. Mullins. Two-dimensional motion of idealized grain boundaries. *Journal of Applied Physics*, 27(8):900–904, 1956.

[73] R. D. MacPherson and D. J. Srolovitz. The von Neumann relation generalized to coarsening of three-dimensional microstructures. *Nature*, 446(7139):1053–1055, April 2007.

[74] S. Chen, B. Merriman, S. Osher, and P. Smereka. A simple level set method for solving Stefan problems. *Journal of Computational Physics*, 135(1):8 – 29, 1997.

[75] C. Mießen, M. Liesenjohann, L. Barrales-Mora, L. Shvindlerman, and G. Gottstein. An advanced level set approach to grain growth–accounting for grain boundary anisotropy and finite triple junction mobility. *Acta Materialia*, 99:39–48, 2015.

[76] S. A. Wright, S. J. Plimpton, and T. P. Swiler. Potts-model grain growth simulations: Parallel algorithms and applications. Technical report, Sandia National Labs., Albuquerque, NM (United States), 1997.

[77] D. Zöllner and P. Streitenberger. Three-dimensional normal grain growth: Monte Carlo Potts model simulation and analytical mean field theory. *Scripta Materialia*, 54(9):1697 – 1702, 2006.

[78] J. Langer. Models of pattern formation in first-order phase transitions. In G. Grinstein and G. Mazenko, editors, *Directions In Condensed Matter Physics*, volume 1, pages 165–186. World Scientific, aug 1986.

[79] G. J. Fix. Phase field models for free boundary problems. In A. Fasano and M. Primicerio, editors, *Free boundary problems*, volume 2. Piman, Boston, 1983.

[80] R. F. Sekerka. Morphology: from sharp interface to phase field models. *Journal of Crystal Growth*, 264(4):530–540, 2004.

[81] W. Böttinger, J. Warren, C. Beckermann, and A. Karma. Phase-field simulation of solidification. *Annual Review of Materials Research*, 32(1):163–194, 2002.

[82] G. Caginalp. An analysis of a phase field model of a free boundary. *Archive for Rational Mechanics and Analysis*, 92(3):205–245, 1986.

[83] G. Caginalp. Stefan and hele-shaw type models as asymptotic limits of the phase-field equations. *Physical Review A*, 39:5887–5896, Jun 1989.

[84] O. Penrose and P. C. Fife. Thermodynamically consistent models of phase-field type for the kinetic of phase transitions. *Physica D: Nonlinear Phenomena*, 43(1):44–62, May 1990.

[85] A. A. Wheeler, W. J. Böttinger, and G. B. McFadden. Phase-field model for isothermal phase transitions in binary alloys. *Physical Review A*, 45:7424–7439, May 1992.

[86] H. Garcke, B. Nestler, and B. Stoth. On anisotropic order parameter models for multi-phase systems and their sharp interface limits. *Physica D: Nonlinear Phenomena*, 115(1):87 – 108, 1998.

[87] L. Kaufman and H. Bernstein. *Computer calculation of phase diagrams. With special reference to refractory metals.* Academic Press, 1970.

[88] L. D. Landau, E. M. Lifshitz, and L. Pitaevskii. *Statistical physics, part I.* pergamon, Oxford, 1958.

[89] J. W. Cahn and J. E. Hilliard. Free energy of a nonuniform system. I. interfacial free energy. *The Journal of chemical physics*, 28(2):258–267, 1958.

[90] S. M. Allen and J. W. Cahn. A microscopic theory for antiphase boundary motion and its application to antiphase domain coarsening. *Acta Metallurgica*, 27(6):1085–1095, 1979.

[91] L. Modica. The gradient theory of phase transitions and the minimal interface criterion. *Archive for Rational Mechanics and Analysis*, 98(2):123–142, 1987.

[92] N. Moelans. A quantitative and thermodynamically consistent phase-field interpolation function for multi-phase systems. *Acta Materialia*, 59(3):1077–1086, 2011.

[93] L.-Q. Chen and W. Yang. Computer simulation of the domain dynamics of a quenched system with a large number of nonconserved order parameters: The grain-growth kinetics. *Physical Review B*, 50:15752–15756, Dec 1994.

[94] S. G. Kim. A phase-field model with antitrapping current for multicomponent alloys with arbitrary thermodynamic properties. *Acta Materialia*, 55(13):4391–4399, 2007.

[95] N. Moelans, B. Blanpain, and P. Wollants. Quantitative analysis of grain boundary properties in a generalized phase field model for grain growth in anisotropic systems. *Physical Review B*, 78(2):024113, July 2008.

[96] R. Folch and M. Plapp. Quantitative phase-field modeling of two-phase growth. *Physical Review E*, 72:011602, Jul 2005.

[97] I. Steinbach. Phase-field models in materials science. *Modelling and Simulation in Materials Science and Engineering*, 17(7):073001, 2009.

[98] J.-O. Andersson and J. Ågren. Models for numerical treatment of multicomponent diffusion in simple phases. *Journal of Applied Physics*, 72(4):1350–1355, 1992.

[99] G. I. Tóth, T. Pusztai, and L. Gránásy. Consistent multiphase-field theory for interface driven multidomain dynamics. *Physical Review B*, 92:184105, Nov 2015.

[100] C. E. Krill III and L.-Q. Chen. Computer simulation of 3-D grain growth using a phase-field model. *Acta Materialia*, 50(12):3059–3075, 2002.

[101] I. Steinbach and F. Pezzolla. A generalized field method for multiphase transformations using interface fields. *Physica D: Nonlinear Phenomena*, 134(4):385 – 393, 1999.

[102] S. G. Kim, D. I. Kim, W. T. Kim, and Y. B. Park. Computer simulations of two-dimensional and three-dimensional ideal grain growth. *Physical Review E*, 74:061605, Dec 2006.

[103] T. A. Abinandanan and F. Haider. An extended Cahn-Hilliard model for interfaces with cubic anisotropy. *Philosophical Magazine A*, 81(10):2457–2479, 2001.

[104] I. M. McKenna, M. P. Gururajan, and P. W. Voorhees. Phase field modeling of grain growth: effect of boundary thickness, triple junctions, misorientation, and anisotropy. *Journal of Materials Science*, 44(9):2206–2217, 2009.

[105] J. Hötzer, O. Tschukin, M. B. Said, M. Berghoff, M. Jainta, G. Barthelemy, N. Smorchkov, D. Schneider, M. Selzer, and B. Nestler. Calibration of a multi-phase field model with quantitative angle measurement. *Journal of Materials Science*, 51(4):1788–1797, 2016.

[106] E. Miyoshi and T. Takaki. Extended higher-order multi-phase-field model for three-dimensional anisotropic-grain-growth simulations. *Computational Materials Science*, 120:77–83, 2016.

[107] E. Miyoshi and T. Takaki. Validation of a novel higher-order multi-phase-field model for grain-growth simulations using anisotropic grain-boundary properties. *Computational Materials Science*, 112:44–51, 2016.

[108] J. Gruber, N. Ma, Y. Wang, A. D. Rollett, and G. S. Rohrer. Sparse data structure and algorithm for the phase field method. *Modelling and Simulation in Materials Science and Engineering*, 14(7):1189, 2006.

[109] L. Vanherpe, N. Moelans, B. Blanpain, and S. Vandewalle. Bounding box framework for efficient phase field simulation of grain growth in anisotropic systems. *Computational Materials Science*, 50(7):2221–2231, 2011.

[110] L. Vanherpe, N. Moelans, B. Blanpain, and S. Vandewalle. Bounding box algorithm for three-dimensional phase-field simulations of microstructural evolution in polycrystalline materials. *Physical Review E*, 76(5):056702, 2007.

[111] J.-H. Lee, S. Liu, H. Miyahara, and R. Trivedi. Diffusion-coefficient measurements in liquid metallic alloys. *Metallurgical and Materials Transactions B*, 35(5):909–917, 2004.

[112] B. Zhang, A. Griesche, and A. Meyer. Diffusion in Al-Cu melts studied by time-resolved x-ray radiography. *Physical Review Letters*, 104:035902, Jan 2010.

[113] M. Watson and J. Hunt. The measurement of liquid diffusion coefficients in the Al-Cu system using temperature gradient zone melting. *Metallurgical and Materials Transactions A*, 8(11):1793–1798, 1977.

[114] U. Dahlborg, M. Besser, M. Calvo-Dahlborg, S. Janssen, F. Juranyi, M. Kramer, J. Morris, and D. Sordelet. Diffusion of Cu in AlCu alloys of different composition by quasielastic neutron scattering. *Journal of Non-Crystalline Solids*, 353(32-40):3295–3299, 2007.

[115] L. K. Aagesen, J. L. Fife, E. M. Lauridsen, and P. W. Voorhees. The evolution of interfacial morphology during coarsening: A comparison between 4D experiments and phase-field simulations. *Scripta Materialia*, 64(5):394–397, 2011.

[116] J. B. Edwards, E. E. Hucke, and J. J. Martin. Diffusion in binary liquid-metal systems. *Metallurgical Reviews*, 13(1):1–28, 1968.

[117] R. Sharp and A. Hellawell. The microscopy and composition of quenched solid-liquid interfaces. *Journal of Crystal Growth*, 5(3):155–161, 1969.

[118] R. Jordan and J. Hunt. The growth of lamellar eutectic structures in the Pb- Sn and Al- $CuAl_2$ systems. *Metallurgical and Materials Transactions B*, 2(12):3401–3410, 1971.

[119] B. Bhat. Effect of thermotransport on directionally solidified aluminium-copper eutectic. *Journal of Crystal Growth*, 28(1):68–76, 1975.

[120] T. Sato and G. Ohira. Stability of a planar solid-liquid interface during unidirectional solidification of Al-0.1 wt%Cu alloy. *Journal of Crystal Growth*, 40(1):78–89, 1977.

[121] D. Froschhammer, H. Tensi, H. Zoller, and U. Feurer. Diffusion in the liquid near the moving solid-liquid interface of an aluminum-0.3 pct copper alloy. *Metallurgical Transactions B*, 11(1):169–171, 1980.

[122] T. Masaki, T. Fukazawa, S. Matsumoto, T. Itami, and S. Yoda. Measurements of diffusion coefficients of metallic melt under microgravity – current status of the development of shear cell technique towards JEM on ISS. *Measurement Science and Technology*, 16(2):327, 2005.

[123] Y. Sun, A. Cecen, J. W. Gibbs, S. R. Kalidindi, and P. W. Voorhees. Analytics on large microstructure datasets using two-point spatial correlations: Coarsening of dendritic structures. *Acta Materialia*, 132:374–388, 2017.

[124] N. Gjostein and F. Rhines. Absolute interfacial energies of [001] tilt and twist grain boundaries in copper. *Acta Metallurgica*, 7(5):319 – 330, 1959.

[125] B. L. Adams, S. Ta'Asan, D. Kinderlehrer, I. Livshits, D. Mason, C.-T. Wu, W. Mullins, G. Rohrer, A. Rollett, and D. Saylor. Extracting grain boundary and surface energy from measurement of triple junction geometry. *Interface Science*, 7(3):321–337, 1999.

[126] A. Morawiec. Method to calculate the grain boundary energy distribution over the space of macroscopic boundary parameters from the geometry of triple junctions. *Acta Materialia*, 48(13):3525 – 3532, 2000.

[127] D. J. Rowenhorst and P. W. Voorhees. Measurements of the grain boundary energy and anisotropy in tin. *Metallurgical and Materials Transactions A*, 36(8):2127–2135, 2005.

[128] C.-C. Yang, A. Rollett, and W. Mullins. Measuring relative grain boundary energies and mobilities in an aluminum foil from triple junction geometry. *Scripta Materialia*, 44(12):2735 – 2740, 2001.

[129] D. M. Saylor, A. Morawiec, and G. S. Rohrer. The relative free energies of grain boundaries in magnesia as a function of five macroscopic parameters. *Acta Materialia*, 51(13):3675 – 3686, 2003.

[130] J. Li, S. J. Dillon, and G. S. Rohrer. Relative grain boundary area and energy distributions in nickel. *Acta Materialia*, 57(14):4304 – 4311, 2009.

[131] H. Beladi and G. S. Rohrer. The relative grain boundary area and energy distributions in a ferritic steel determined from three-dimensional electron backscatter diffraction maps. *Acta materialia*, 61(4):1404–1412, 2013.

[132] K. Barmak, J. Kim, C.-S. Kim, W. Archibald, G. Rohrer, A. Rollett, D. Kinderlehrer, S. Ta'Asan, H. Zhang, and D. Srolovitz. Grain boundary energy and grain growth in Al films: Comparison of experiments and simulations. *Scripta Materialia*, 54(6):1059 – 1063, 2006. Viewpoint set no. 40: Grain boundary engineering.

[133] S. M. Foiles and J. Hoyt. Computation of grain boundary stiffness and mobility from boundary fluctuations. *Acta Materialia*, 54(12):3351–3357, 2006.

[134] G. S. Rohrer, E. A. Holm, A. D. Rollett, S. M. Foiles, J. Li, and D. L. Olmsted. Comparing calculated and measured grain boundary energies in nickel. *Acta Materialia*, 58(15):5063–5069, 2010.

[135] E. A. Holm, D. L. Olmsted, and S. M. Foiles. Comparing grain boundary energies in face-centered cubic metals: Al, Au, Cu and Ni. *Scripta Materialia*, 63(9):905–908, 2010.

[136] H.-K. Kim, W.-S. Ko, H.-J. Lee, S. G. Kim, and B.-J. Lee. An identification scheme of grain boundaries and construction of a grain boundary energy database. *Scripta Materialia*, 64(12):1152 – 1155, 2011.

[137] D. Scheiber, R. Pippan, P. Puschnig, and L. Romaner. Ab initio calculations of grain boundaries in bcc metals. *Modelling and Simulation in Materials Science and Engineering*, 24(3):035013, 2016.

[138] D. A. Molodov, C. Günster, G. Gottstein, and L. S. Shvindlerman. A novel experimental approach to determine the absolute grain boundary energy. *Philosophical Magazine*, 92(36):4588–4598, 2012.

[139] Y. Huang and F. Humphreys. Measurements of grain boundary mobility during recrystallization of a single-phase aluminium alloy. *Acta Materialia*, 47(7):2259–2268, 1999.

[140] I. Basu, M. Chen, M. Loeck, T. Al-Samman, and D. Molodov. Determination of grain boundary mobility during recrystallization by statistical evaluation of electron backscatter diffraction measurements. *Materials Characterization*, 117:99–112, 2016.

[141] Z. T. Trautt, M. Upmanyu, and A. Karma. Interface mobility from interface random walk. *Science*, 314(5799):632–635, 2006.

[142] K. G. Janssens, D. Olmsted, E. A. Holm, S. M. Foiles, S. J. Plimpton, and P. M. Derlet. Computing the mobility of grain boundaries. *Nature Materials*, 5(2), 2006.

[143] J. Zhou and V. Mohles. Towards realistic molecular dynamics simulations of grain boundary mobility. *Acta Materialia*, 59(15):5997–6006, 2011.

[144] M. Mendelev, C. Deng, C. Schuh, and D. Srolovitz. Comparison of molecular dynamics simulation methods for the study of grain boundary migration. *Modelling and Simulation in Materials Science and Engineering*, 21(4):045017, 2013.

[145] M. Rahman, H. Zurob, and J. Hoyt. A comprehensive molecular dynamics study of low-angle grain boundary mobility in a pure aluminum system. *Acta Materialia*, 74:39–48, 2014.

[146] S. Schmidt, U. L. Olsen, H. F. Poulsen, H. O. Sørensen, E. M. Lauridsen, L. Margulies, C. Maurice, and D. J. Jensen. Direct observation of 3-D grain growth in Al-0.1% Mn. *Scripta Materialia*, 59(5):491 – 494, 2008.

[147] S. F. F. Li. *Imaging of Orientation and Geometry in Microstructures: Development and Applications of High Energy X-ray Diffraction Microscopy.* Dissertation, Carnegie Mellon University, June 2011.

[148] M. Syha. *Microstructure evolution in strontium titanate Investigated by means of grain growth simulations and x-ray diffraction contrast tomography experiments.* PhD thesis, Karlsruhe Institute of Technology, 2014.

[149] I. M. McKenna, S. O. Poulsen, E. M. Lauridsen, W. Ludwig, and P. W. Voorhees. Grain growth in four dimensions: A comparison between simulation and experiment. *Acta Materialia*, 78:125–134, 2014.

[150] B. Lin, Y. Jin, C. M. Hefferan, S. F. Li, J. Lind, R. M. Suter, M. Bernacki, N. Bozzolo, A. D. Rollett, and G. S. Rohrer. Observation of annealing twin nucleation at triple lines in nickel during grain growth. *Acta Materialia*, 99:63–68, 2015.

[151] J. Sun, A. Lyckegaard, Y. Zhang, S. Catherine, B. Patterson, F. Bachmann, N. Gueninchault, H. Bale, C. Holzner, E. Lauridsen, et al. 4D study of grain growth in armco iron using laboratory x-ray diffraction contrast tomography. *IOP Conference Series: Materials Science and Engineering*, 219:012039, 2017.

[152] W. Ludwig, S. Schmidt, E. M. Lauridsen, and H. F. Poulsen. X-ray diffraction contrast tomography: a novel technique for three-dimensional grain mapping of polycrystals. I. direct beam case. *Journal of Applied Crystallography*, 41(2):302–309, 2008.

[153] A. King, P. Reischig, J. Adrien, and W. Ludwig. First laboratory X-ray diffraction contrast tomography for grain mapping of polycrystals. *Journal of Applied Crystallography*, 46(6):1734–1740, Dec 2013.

[154] S. McDonald, P. Reischig, C. Holzner, E. Lauridsen, P. Withers, A. Merkle, and M. Feser. Non-destructive mapping of grain orientations in 3D by laboratory x-ray microscopy. *Scientific reports*, 5:14665, 2015.

[155] J. W. Gibbs and P. W. Voorhees. Segmentation of four-dimensional, x-ray computed tomography data. *Integrating Materials and Manufacturing Innovation*, 3(1):1–12, 2014.

[156] J. Gruber, D. C. George, A. P. Kuprat, G. S. Rohrer, and A. D. Rollett. Effect of anisotropic grain boundary properties on grain boundary plane distributions during grain growth. *Scripta materialia*, 53(3):351–355, 2005.

[157] T. Massalski. The Al–Cu (Aluminum–Copper) system. *Bulletin of Alloy Phase Diagrams*, 1(1):27–33, 1980.

[158] I. Ansara, A. T. Dinsdale, and M. H. Rand, editors. *COST 507: Thermochemical Database for Light Metal Alloys*, volume 2. European Commission, Directorate-General XII, Science, Research and Development, 1998.

[159] J. Brillo, I. Egry, and J. Westphal. Density and thermal expansion of liquid binary Al–Ag and Al–Cu alloys. *International Journal of Materials Research*, 99(2):162–167, 2008.

[160] M. Gündüz and J. Hunt. The measurement of solid-liquid surface energies in the Al-Cu, Al-Si and Pb-Sn systems. *Acta Metallurgica*, 33(9):1651–1672, 1985.

[161] J. L. Fife. *Three-dimensional characterization and real-time interface dynamics of aluminum-copper dendritic microstructures*. PhD thesis, Northwestern University, June 2009.

[162] J. W. Gibbs. *Interfacial Dynamics in Liquid-Solid Mixtures: A Study of Solidification and Coarsening*. PhD thesis, Northwestern University, 2014.

[163] J. W. Gibbs, P. W. Voorhees, and J. L. Fife. Dataset for segmentation of four-dimensional, x-ray computed tomography data. http://dx.doi.org/doi:10.18126/M2CC73, February 2016.

[164] C. Guiffaut and K. Mahdjoubi. A parallel FDTD algorithm using the mpi library. *IEEE Antennas and Propagation Magazine*, 43(2):94–103, 2001.

[165] S. Poulsen and P. Voorhees. Smoothed boundary method for diffusion-related partial differential equations in complex geometries. *International Journal of Computational Methods*, page 1850014, 2017.

[166] C. Li, R. Huang, Z. Ding, J. C. Gatenby, D. N. Metaxas, and J. C. Gore. A level set method for image segmentation in the presence of intensity inhomogeneities with application to MRI. *IEEE Transactions on Image Processing*, 20(7):2007–2016, 2011.

[167] R. M. Suter, D. Hennessy, C. Xiao, and U. Lienert. Forward modeling method for microstructure reconstruction using x-ray diffraction microscopy: Single-crystal verification. *Review of Scientific Instruments*, 77(12), 2006.

[168] A. E. Johnson. *Four Dimensional Evolution of Grains and Interfaces in Materials*. PhD thesis, Northwestern University, 2013.

[169] H. Simons, A. C. Jakobsen, S. R. Ahl, C. Detlefs, and H. F. Poulsen. Multiscale 3D characterization with dark-field x-ray microscopy. *MRS Bulletin*, 41:454–459, 6 2016.

[170] A. J. Morgan, M. Prasciolu, A. Andrejczuk, J. Krzywinski, A. Meents, D. Pennicard, H. Graafsma, A. Barty, R. J. Bean, M. Barthelmess, et al. High numerical aperture multilayer laue lenses. *Scientific reports*, 5:9892, 2015.

[171] T. Shimokawabe, T. Takaki, T. Endo, A. Yamanaka, N. Maruyama, T. Aoki, A. Nukada, and S. Matsuoka. Peta-scale phase-field simulation for dendritic solidification on the TSUBAME 2.0 supercomputer. In *2011 International Conference for High Performance Computing, Networking, Storage and Analysis (SC)*, pages 1–11, Nov 2011.

[172] A. Vondrous. *Grain growth behavior and efficient large scale simulations of recrystallization with the phase-field method*. PhD thesis, Karlsruhe Institute of Technology, 2014.

[173] A. Yamanaka, M. Okamoto, and T. Shimokawabe. Multi-GPU computation of multi-phase field simulation of the evolution of metallic polycrystalline microstructure. *Tsubame ESJ. : e-science journal*, 13:18–22, nov 2014.

[174] J. Hötzer, M. Jainta, A. Vondrous, J. Ettrich, A. August, D. Stubenvoll, M. Reichardt, M. Selzer, and B. Nestler. Phase-field simulations of large-scale microstructures by integrated parallel algorithms. In *High Performance Computing in Science and Engineering '14*, pages 629–644. Springer, 2015.

[175] J. Hötzer, M. Kellner, P. Steinmetz, J. Dietze, and B. Nestler. Large-scale phase-field simulations of directional solidified ternary eutectics using high-performance computing. In *High Performance Computing in Science and Engineering 16*, pages 635–646. Springer, 2016.

[176] E. Engel and R. M. Dreizler. *Density Functional Theory*. Springer Berlin Heidelberg, 2011.

[177] J. Rubinstein, P. Sternberg, and J. B. Keller. Fast reaction, slow diffusion, and curve shortening. *SIAM Journal on Applied Mathematics*, 49(1):116–133, 1989.

[178] P. C. Fife. 1. Internal layers. In *Dynamics of Internal Layers and Diffusive Interfaces*, pages 1–16. Society for Industrial and Applied Mathematics, jan 1988.

[179] R. L. Pego. Front migration in the nonlinear Cahn-Hilliard equation. In *Proc. R. Soc. Lond. A*, volume 422, pages 261–278. The Royal Society, 1989.

Paper I

Acta Materialia 129 (2017) 229–238

Contents lists available at ScienceDirect

Acta Materialia

journal homepage: www.elsevier.com/locate/actamat

Full length article

Determining material parameters using phase-field simulations and experiments

Jin Zhang [a], Stefan O. Poulsen [b], John W. Gibbs [c], Peter W. Voorhees [b], Henning F. Poulsen [a, *]

[a] NEXMAP, Department of Physics, DTU, 2800, Kongens Lyngby, Denmark
[b] Department of Materials Science and Engineering, Northwestern University, Evanston, IL, 60208, USA
[c] Materials Science and Technology Division, Los Alamos National Laboratory, Los Alamos, USA

ARTICLE INFO

Article history:
Received 7 November 2016
Received in revised form
23 January 2017
Accepted 20 February 2017
Available online 22 February 2017

Keywords:
Phase-field method
X-ray tomography
Coarsening
Al alloys
Temporal evolution

ABSTRACT

A method to determine material parameters by comparing the evolution of experimentally determined 3D microstructures to simulated 3D microstructures is proposed. The temporal evolution of a dendritic solid-liquid mixture is acquired in situ using x-ray tomography. Using a time step from these data as an initial condition in a phase-field simulation, the computed structure is compared to that measured experimentally at a later time. An optimization technique is used to find the material parameters that yield the best match of the simulated microstructure to the measured microstructure in a global manner. The proposed method is used to determine the liquid diffusion coefficient in an isothermal Al-Cu alloy. However, the method developed is broadly applicable to other experiments in which the evolution of the three-dimensional microstructure is determined in situ. We also discuss methods to describe the local variation of the best-fit parameters and the fidelity of the fitting. We find a liquid diffusion coefficient that is different from that measured using directional solidification.

1. Introduction

Computational methods play an important role in accelerating the discovery and development of advanced materials [1]. One of the most promising areas in which computational methods are employed is in Integrated Computational Materials Engineering (ICME), which is receiving increased attention from both academia and industry [2,3]. The establishment of reliable and comprehensive materials databases - the main component of the Materials Genome Initiative (MGI) [3] - is a key to the success of ICME [2,4]. Traditionally, material parameters are measured one at a time by designing dedicated experiments using idealized specimens and specimen geometries (e.g. a planar interface in a diffusion couple experiment for measuring the diffusion coefficient). However, such procedures are often tedious, and typically parameters are measured only in a fraction of the relevant phase space, which may involve materials composition, temperature, pressure, etc. In addition, the idealized geometry may not be representative: industrially relevant microstructures are heterogeneous and artificial surfaces may introduce unwanted boundary effects. Furthermore, for hierarchically ordered materials, effects on different length scales compete and interact. Recently, researchers have begun to calculate material parameters from first-principles, such as the free energy [5] and the diffusion coefficients in the solid phase [6–8] and the liquid phase [9]. However, experimental verification of the calculated material parameters under realistic conditions is needed.

In this work, we propose to determine material parameters directly from structural studies of bulk samples acquired during synthesis or processing. To image material microstructure evolution, various techniques have been used, e.g. Computed Tomography (CT) [10,11], 3D X-Ray Diffraction (3DXRD) [12] and Diffraction Contrast Tomography (DCT) [13]. Using x-rays emitted from a synchrotron source, time-resolved high spatial resolution 3D images can be acquired using tomographic methods, for a review see Ref. [14]. In favorable cases, the temporal resolution may be on the sub-second scale [15]. Some of these techniques are increasingly becoming available in laboratory sources, such as the laboratory-based DCT (labDCT) [16]. At the same time, the rapid increase in computing power and the development of advanced modeling

* Corresponding author.
E-mail address: hfpo@fysik.dtu.dk (H.F. Poulsen).

http://dx.doi.org/10.1016/j.actamat.2017.02.056

techniques such as quantitative phase-field models [17–20], accurate simulations of microstructure evolution in 3D have become feasible. Therefore, we propose to determine material parameters by direct comparison between the 3D temporal evolution of microstructures determined through experiment and phase-field simulation. We claim that the parameter values that provide the best match between the experimental and the simulated microstructure in a global manner (both in 3D space and in time) correspond to the physically correct ones. The proposed method can be used to verify the calculated material parameters by first-principles and multiscale modeling simulations. Another advantage of this approach is that it permits the measurement of multiple - in some cases potentially all relevant - material parameters from one experiment in a realistic environment. Notice that though this paper focuses on the phase-field method, other modeling techniques relevant to the problem studied can also be used, such as Monte Carlo Potts model [21] and the vertex model [22] for grain growth and the level-set method for solidification [23].

In recent years, several direct comparisons between experiment and phase-field simulations have been performed [24–27], but the comparisons have mainly been qualitative or based on average quantities, such as the average particle size and the interface area per unit volume. Rigorous comparisons of the morphologies are rare. McKenna et al. [25] used a one-to-one comparison to test a grain growth phase-field model, but they did not use it for extracting material parameters. Demirel et al. [28] used a similar approach for grain growth in thin films. Aagesen et al. [24] estimated a value of the liquid diffusion coefficient using a comparison between phase-field simulations and tomography in a heuristic manner. We here introduce a general optimization formalism and discuss key aspects of this fitting approach, such as the cost functions to quantify the similarity between experiment and simulation, the accuracy, the initial and boundary conditions and the computational speed. To the best of our knowledge, this is the first systematic study where phase-field simulations and 3D tomography are combined to extract material properties. Though in general the optimization relies on performing phase-field simulations many times, we predict that one may only need to consider a small fraction of space-time in a given step of the optimization for many relevant problems.

We demonstrate the approach by fitting the liquid diffusion coefficient D^{L} and the capillary length l^{L} in the context of the isothermal coarsening of dendrites in a liquid of composition nearly equal to that of the eutectic composition in the Al-Cu system. It is a well-studied system, and relevant material parameters have been extensively measured by traditional means, e.g. the free energy [29,30], the solid/liquid interfacial energy [31,32] and the liquid diffusion coefficient [33–35]. However, the values determined from the liquid diffusion coefficient measurements display a large scatter in value, argued to be mainly due to convection [33]. Moreover, an existing temperature gradient during directional solidification may alter the measured liquid diffusion coefficient. In section 2, the fitting methodology is presented in detail. In section 3, the results of the demonstration on the Al-Cu system are provided. We discuss limitations and potential applications in section 4 and conclude the paper in section 5.

2. Optimization approach

Initially, we present the mathematical model and the associated terminology and notations. Then two types of cost functions and several ways to define the fitting domain are proposed and compared. Finally, the statistics of the fitting method is discussed. Throughout, for reasons of simplicity, we shall assume a two-phase problem, where the microstructure is characterized by a moving boundary between the two phases.

2.1. The mathematical model

The fitting approach is shown schematically in Fig. 1. Here the symbol $\mathscr{G}$ represents the geometry of the material microstructure. The x-ray experiment provides a series of 3D material microstructures $\mathscr{G}^{\mathrm{exp}}(t)$ evolving with time (shown in the upper solid box in Fig. 1). With one frame of the experimental microstructure (time t_0) as input ($\mathscr{G}^{\mathrm{sim}}(t_0) = \mathscr{G}^{\mathrm{exp}}(t_0)$) and a guess of material parameters $\mathbf{p}$, the simulation method [19] can produce a series of evolving microstructures $\mathscr{G}^{\mathrm{sim}}(t, \mathbf{p})$ (shown in the lower dashed box in Fig. 1). For time $t > t_0$, a cost function f_{cost} is used to measure the dissimilarity between the two microstructures. We claim the real material parameters $\mathbf{p}^{\mathrm{real}}$ should give the least dissimilarity between the experimental and simulated microstructures, i.e. f_{cost} reaches a minimum as shown in Fig. 1 (right).

This fitting process can be described by the following optimization problem:

$$\begin{aligned} &\text{find} && \mathbf{p} \\ &\text{minimize} && f_{\mathrm{cost}}(t, \mathbf{p}) = f_{\mathrm{cost}}\left(\mathscr{G}^{\mathrm{exp}}(t), \mathscr{G}^{\mathrm{sim}}(t, \mathbf{p})\right) \\ &\text{such that} && \mathscr{G}^{\mathrm{sim}}(t, \mathbf{p}) \text{ fulfills phase-field equation} \\ & && \mathscr{G}^{\mathrm{sim}}(t_0, \mathbf{p}) = \mathscr{G}^{\mathrm{exp}}(t_0) \\ & && \mathscr{G}^{\mathrm{sim}}(t, \mathbf{p}) \text{ fulfills boundary condition} \end{aligned} \tag{1}$$

The optimization problem can be solved by any appropriate optimization algorithm. Notice here the optimization approach is independent of the geometric representation $\mathscr{G}$, which may thus be discretized like a binary image or be continuous like NURBS (explicit) [36] and level-set methods (implicit) [37]. The flowchart of the fitting algorithm is shown in Fig. 2.

2.2. The cost function

Two types of cost functions are proposed based on the representation of the microstructure geometry. If these microstructures are represented by binary images ($\mathscr{G}^{\mathrm{exp}} = \mathrm{Img}^{\mathrm{exp}}$, $\mathscr{G}^{\mathrm{sim}} = \mathrm{Img}^{\mathrm{sim}}$), the correlation function can be used to construct the cost function (the corr-cost function)

$$f_{\mathrm{cost}}(t, \mathbf{p}) = 1 - \operatorname*{corr}_{\Omega_{\mathrm{fit}}}\left(\mathrm{Img}^{\mathrm{exp}}(t), \mathrm{Img}^{\mathrm{sim}}(t, \mathbf{p})\right) \tag{2}$$

where Ω_{fit} is the fitting domain. If a continuous geometry representation like the signed distance function as known from the level-set method is used ($\mathscr{G}^{\mathrm{exp}} = \phi^{\mathrm{exp}}$, $\mathscr{G}^{\mathrm{sim}} = \phi^{\mathrm{sim}}$), the squared 2-norm function can be used:

$$f_{\mathrm{cost}}(t, \mathbf{p}) = \frac{\left\|\phi^{\mathrm{sim}}(t, \mathbf{p}) - \phi^{\mathrm{exp}}(t)\right\|^2_{2,\Omega_{\mathrm{fit}}}}{\left\|\phi^{\mathrm{exp}}(t) - \phi^{\mathrm{exp}}(t_0)\right\|^2_{2,\Omega_{\mathrm{fit}}}} \tag{3}$$

Here, the normalization is used to make the cost function independent of the fitting domain size. By this definition, $\sqrt{f_{\mathrm{cost}}}$ has a physical meaning, namely representing the root mean square migration distance of the simulated interfaces relative to the experimentally determined interfaces if no topological change occurs. As the segmentation applied to the tomographic data in the example case given in the current work is based on the signed distance function [38], ϕ^{exp} is available. However, ϕ^{sim} is not directly available from the phase-field simulation. In this work, the equilibrium profile of a planar interface is used to provide an approximation of the signed distance function from the interpolation function in the phase-field model, and then a reinitialization

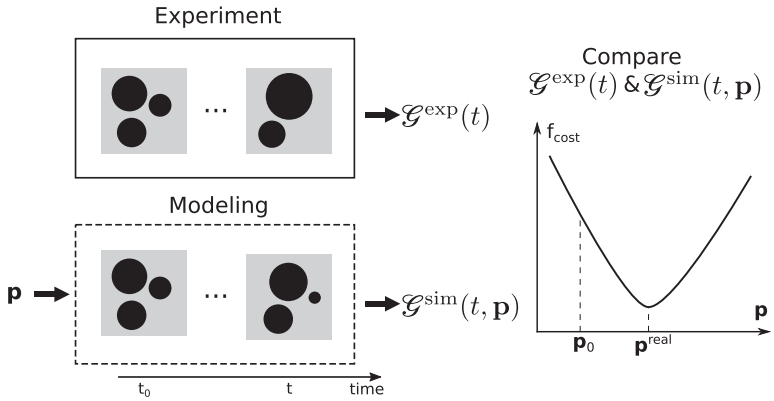

Fig. 1. Schematic diagram of the fitting method.

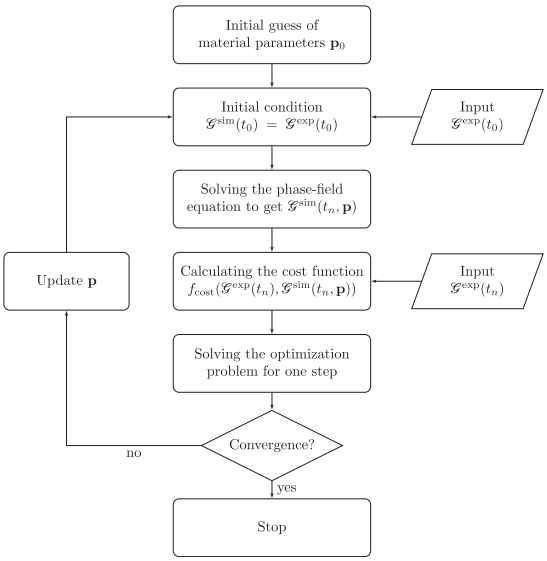

Fig. 2. Flowchart of the fitting algorithm.

algorithm [39] is used to calculate the signed distance function while leaving the interface position unchanged.

2.3. The fitting domain

We anticipate that a proper fitting domain Ω_{fit} often will be critical for the fitting. In particular, we need to remove regions which provide noisy or even wrong information on the underlying interfacial evolution due to known limitations of the applied model, such as missing physics or violated assumptions.

In the current work, we use an implicit representation of the microstructure. As the comparison of microstructures is only needed at the interfaces, regions far from the interface are removed from fitting. This also helps to reduce the computational cost. In this work, we restrict the fitting to an interfacial domain $\Omega_{\text{interface}}$; see the region between two dashed lines in Fig. 3. The interfacial domain with width w is defined as

$$\Omega_{\text{interface}=w} = \left\{\mathbf{x} : |\phi^{\exp}(\mathbf{x})| \leqslant \frac{w}{2}\right\} \tag{4}$$

where $\phi^{\exp}$ is the signed distance function of the experimental interface. We find that the cost function is insensitive to the width w when w is small, so in the current work $w = 5$ grid points will be used throughout.

A region near the boundary of the simulation domain is removed from the fitting domain. To reduce the computational cost, the simulation domain Ω^{sim} is usually chosen to be a subset of the sample. Artificial boundary conditions are imposed on the boundary of Ω^{sim}. In the region close to the external boundary of Ω^{sim}, we will not expect simulation to match experiment because of the assumed boundary condition. To overcome this problem, the fitting is constrained to a smaller subdomain Ω_{sub}, with size k, defined as

$$\Omega_{\text{sub}=k} = \left\{\mathbf{x} : |x_i - x_i^c| \leqslant \frac{k}{2}, i = 1,2,3\right\} \tag{5}$$

where $\mathbf{x}^c$ is the center of Ω^{sim} (see Fig. 3). The subdomain size k plays an important role in the fitting and will be discussed in detail

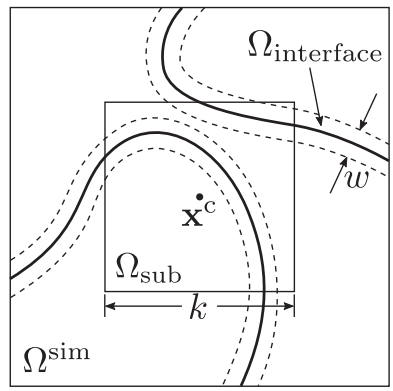

Fig. 3. Schematic diagram of the fitting domain. The thick lines show the interfaces; the simulation domain Ω^{sim} is where the phase-field simulation is performed; the subdomain Ω_{sub} is a smaller domain inside Ω^{sim} with size k; the interfacial domain $\Omega_{\text{interface}}$ is a narrow region with width w near the interface.

in section 3.4.2.

In some applications, there are regions with small features which are difficult to capture by simulation with a reasonable computational cost. In relation to the coarsening study below, there are regions where solid particles are separated by thin liquid films, as shown in Fig. 4. These films are too thin be resolved using the interface thickness employed in the phase-field simulation, so solid particles in close vicinity tend to coalesce in the simulations, which leads to a high local interface velocity. We can either reduce the grid size or exclude these regions. As these regions are not necessary for determining the liquid diffusion coefficient and it is more efficient to look at larger volumes that do not contain these small features than it is to refine the mesh significantly, these high-velocity regions will be removed from the fitting domain.

2.4. Statistics

Differences between experiment and simulation may arise from numerous sources, such as temperature gradients in the experiment, reconstruction and segmentation error, local fluctuation in the material parameters and discretization error in the simulation. These errors are often stochastic in nature. We hypothesize that one can reduce these errors by using a large number of interface patches in the fitting. Below we test this hypothesis as part of a systematic study of the importance of varying a number of settings of relevance to the fitting: the number of interface patches used, the size and position of the simulation domain Ω^{sim} and various combinations of starting time t_0 and fitting time t_n.

3. Application: coarsening of a hypo-eutectic Al-Cu system

In this section, the fitting methodology proposed in section 2 is applied to the coarsening of a hypo-eutectic Al-Cu system with a composition of 20 wt% Cu (calculated from the measured phase volume fraction). Firstly, the x-ray experiment, the setup of simulations and the fitting algorithm specific to this system are presented. Then we make a one-parameter fit to the liquid diffusion coefficient only, as it is the simplest case for fitting and easy for visualization and analysis. Finally, to demonstrate the generality of the fitting method, a two-parameters fit to both the liquid diffusion coefficient and the capillary length is given in section 3.5.

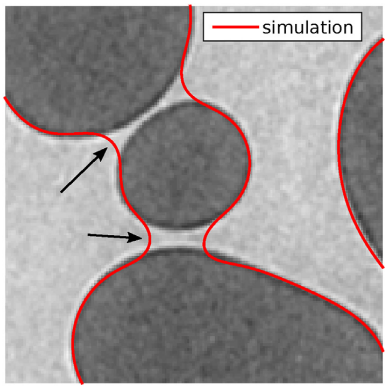

Fig. 4. Illustration of thin liquid films that are present in the microstructure. The simulation result (red curve) overlaid on the experimental data. The arrows show the regions of thin liquid films where coalescence occurs in the simulation. (For interpretation of the references to colour in this figure legend, the reader is referred to the web version of this article.)

3.1. X-ray tomography experiment

The experimental data used in this paper are phase contrast tomography data collected at the beamline TOMCAT at the Swiss Light Source. An isothermal coarsening experiment was performed for 362 min at a fixed temperature of $558\,^{\circ}C$, $5\,^{\circ}C$ above the eutectic temperature. The tomography data were reconstructed and segmented to provide a 3D movie of the microstructure evolution. The spatial and temporal resolutions are $\Delta x = 1.44\ \mu m$ and $\Delta t^{\text{exp}} = 231\ s$, respectively. Details about the experiment, reconstruction and segmentation can be found in Refs. [40–42].

3.2. Setup of phase-field simulation

To model coarsening of the Al-Cu system, multiorder-parameter models [43] or multiphase-field models [44] can be used. In the current work, the multiorder-parameter model presented in Refs. [43,45–47] with the interpolation function introduced in Ref. [19] is used. The total free energy of the system is expressed as a functional of phase-field variables (η_S and η_L) and Cu compositions (c_S and c_L) for each phase

$$F = \int_{\Omega^{\text{sim}}} \left(m \left[\sum_{i=\text{S,L}} \left(\frac{\eta_i^4}{4} - \frac{\eta_i^2}{2} \right) + \gamma \eta_S^2 \eta_L^2 + \frac{1}{4} \right] + \frac{\kappa}{2} \sum_{i=\text{S,L}} \left(\vec{\nabla} \eta_i \right)^2 + h^S f^S + h^L f^L \right) \mathrm{d}V \tag{6}$$

The evolution of the system is governed by the phase-field equations

$$\frac{\partial \eta_i}{\partial t} = -L \frac{\delta F}{\delta \eta_i}, \quad i = \text{S, L} \tag{7}$$

$$\frac{\partial c_i}{\partial t} = \vec{\nabla} \cdot \left(M_i \vec{\nabla} \frac{\delta F}{\delta c_i} \right), \quad i = \text{S, L} \tag{8}$$

Furthermore, appropriate initial conditions for $\eta_i(t=0,\mathbf{x})$ and $c_i(t=0,\mathbf{x})$ and boundary conditions for $\eta_i\left(t,\mathbf{x}\big|_{\partial\Omega^{\text{sim}}}\right)$ and $c_i\left(t,\mathbf{x}\big|_{\partial\Omega^{\text{sim}}}\right)$ are needed to guarantee a well-posed problem. The last two terms in Eq. (6) represent the bulk free energy density, which is constructed by interpolating the free energy densities of different phases (f^S and f^L) with the interpolation functions (h^S and h^L) of the form

$$h^S = \frac{\eta_S^2}{\eta_S^2 + \eta_L^2}, \quad h^L = \frac{\eta_L^2}{\eta_S^2 + \eta_L^2} \tag{9}$$

The mobilities (M_S and M_L) are related to the diffusion coefficients (D^S and D^L) by

$$M_S = \frac{D^S}{\frac{\partial^2 f^S}{\partial c_S^2}}, \quad M_L = \frac{D^L}{\frac{\partial^2 f^L}{\partial c_L^2}} \tag{10}$$

For further details on the model parameters (m,γ,κ and L) and their connection to the material parameters, and the calculation of functional derivatives in Eqs. (7) and (8), the reader can refer to [19].

The simulation domain size is chosen to provide a sufficient amount of interface patches for accurate fitting while keeping an affordable computational cost. In the one-parameter fitting in section 3.4, a simulation domain of $300 \times 300 \times 300$ voxels is used.

In the two-parameters fitting in section 3.5, a simulation domain of $400 \times 400 \times 400$ voxels is used. To discretize the phase-field equations, the second-order finite difference is used for the spatial discretization and the forward Euler method is used for the temporal discretization. For details on solving the phase-field equations with the finite difference method, the reader can refer to e.g. Ref. [48] for more information. The interface width l is chosen to be seven grid points, where the width of one voxel is equal to the grid spacing. The code is written in C and uses MPI to parallelize over multiple nodes. At the beginning of the experiment, there are features with high curvatures and the spatial resolution is not high enough to capture them; therefore the very first time steps are not used. Unless otherwise mentioned, the simulations are started with the experimental time step $t_0 = 10$ and the fitting is performed at later time steps, e.g. $t_n = 11, 12, \cdots, 15$.

3.2.1. Material parameters

In the current work, a parabolic free energy density function is used by fitting to the CALPHAD free energy [29]: $f^S = 2.78(c^S - 0.78)^2 - 4.61\, J/m^3$ and $f^L = 5.10(c^L - 0.57)^2 - 4.45\ J/m^3$. The capillary length of the liquid phase is $l^L = 0.63\ nm$, which is calculated from the Gibbs-Thomson coefficient measured in Ref. [31]. The initial guess of the diffusion coefficient is $D_0^L = 1 \times 10^{-9}\ m^2/s$. The anisotropy of the solid-liquid interfacial energy in Al-Cu is 0.0098 [49], which is small for coarsening, so we assume isotropic interfacial energy in this work. The diffusion coefficient in the solid is estimated to be four orders of magnitude less than in the liquid [50] and is therefore taken to be zero: $D^S = 0$. The anti-trapping current [18,51] is neglected in this work because the solute trapping effect of the problem studied is negligible: $Vl/D^L \sim \mathcal{O}(10^{-5}) \ll 1$, where V is the interface velocity and l is the interface width in the phase-field calculation, which is around $10\mu m$ in this work. The phase-field method is known to only reproduce the accepted sharp interface predictions when the product of the interface width and the mean curvature is small, $l\varkappa \ll 1$ [52], so regions where this assumption is invalidated should be removed from the fitting domain. Regions of high curvature occur, for example, at topological singularities where there is pinching or merging of solid domains. However, in this case the high-curvature region is always related to the high-velocity region. In this work, the high-velocity region is removed, and the high curvature regions are not considered explicitly.

3.2.2. Initial condition

The initial condition for the phase-field variables (η_S and η_L) is input directly from experiment (use ϕ^{exp}), but the initial condition for the diffusion fields (c_S and c_L) is unknown as the small variations in liquid composition occurring during coarsening are undetectable with the current experimental method. Thus, the phase compositions are initially set to their equilibrium values. Numerical simulation shows that the initial relaxation caused by this artificial initial condition is fast and the change of volume fraction is much smaller than that in the experiment; therefore we assume the uncertainty related to the initial diffusion field will not influence the results of the fitting.

3.2.3. Boundary conditions

In the current work, a no-flux boundary condition is used in the one-parameter fitting in section 3.4 and a periodic boundary condition is used in the two-parameters fitting in section 3.5. As expected, both types of boundary conditions give rise to problems near the simulation domain boundary. The influence of the boundary condition will be studied in section 3.4.2 by varying the subdomain size.

3.3. Fitting method

As shown in Fig. 2, the phase-field equations need to be solved in each iteration, which makes the fitting process quite time-consuming. However, for the case of determining the diffusion coefficient only, the fitting can be done with only one phase-field simulation. This is based on the scaling property of the governing phase-field equations [19]:

$$\mathscr{G}^{\mathrm{sim}}\left(t, \alpha D^L\right) = \mathscr{G}^{\mathrm{sim}}\left(\alpha t, D^L\right) \tag{11}$$

where α is an arbitrary positive constant. So we only need to run the simulation once with an arbitrary value of the diffusion coefficient to determine the cost function for other values of the diffusion coefficient through above scaling to the simulation time. A spline interpolation is used to interpolate the curve of f_{cost} over D^L since the simulations only produce output at discrete times. A standard nonlinear optimization algorithm is used to find the optimal D^L. The convergence criteria is that the derivative of the cost function is less than 1×10^{-6} in the current work.

3.4. One-parameter fitting: liquid diffusion coefficient

In this first case, all material parameters except the liquid diffusion coefficient are assumed to be known. Thus the only fitting variable is $\mathbf{p} = \{D^L\}$.

3.4.1. Test of the fitting with a small interface patch

To demonstrate the proposed fitting method, the subdomain is restricted to a domain of size $49 \times 36 \times 51$ voxels to include only one interface patch. Both types of cost functions are calculated at various experimental time steps t_n and are shown in Fig. 5. Notice here $\sqrt{f_{\mathrm{cost}}}$ of the norm-cost function is shown as it has a clear physical meaning. The norm-cost function (Eq. (3)) shows a smaller difference between fitting time steps t_n than the corr-cost function (Eq. (2)), as a result of the normalization. There is a well-defined minimum in all cases. At various time steps, the experimental microstructures and the simulated microstructures with three values of D^L represented by the three vertical lines in Fig. 5 are shown in Fig. 6. For visualization purposes, two slices are shown. We can see that when a small diffusion coefficient $D^L = 6 \times 10^{-10}\ m^2/s$ is used, the simulated interfaces move slower than the experimental ones. When a large diffusion coefficient $D^L = 1.8 \times 10^{-9}\ m^2/s$ is used, the opposite is observed. Only when the diffusion coefficient is near the optimal point $D^L = 1.3 \times 10^{-9}\ m^2/s$, we see a better match between experiment and simulation. Notice that the optimal value determined from the interface patch is a local fit and it can be different from a global fit. This will be discussed in section 3.4.2 and section 3.4.3.

3.4.2. Subdomain size study

To determine the size of a representative subdomain and study the influence of the external boundary, the fitting is performed using subdomains with an increasing size. Examples of cubic subdomains with different edge length k in units of grid points are shown in Fig. 7. The regions subject to the coalescence problem are removed from the fitting domain, see Appendix A for details. The resulting diffusion coefficients and the cost functions at the best fit are shown in Fig. 8. It is seen, that as more interface patches are included in the fitting domain, the fitted material parameter reaches a stable value for all four experimental time steps after $k = 160$. We interpret this to mean that interface area becomes statistically sufficient when $k > 160$. As the subdomain size continues to increase ($k > 250$), the influence of the boundary condition

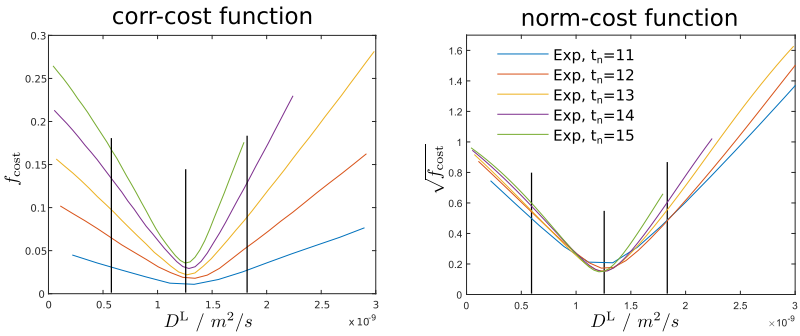

Fig. 5. The variation of the cost functions with D^L for the small interface patch at different experimental time steps t_n.

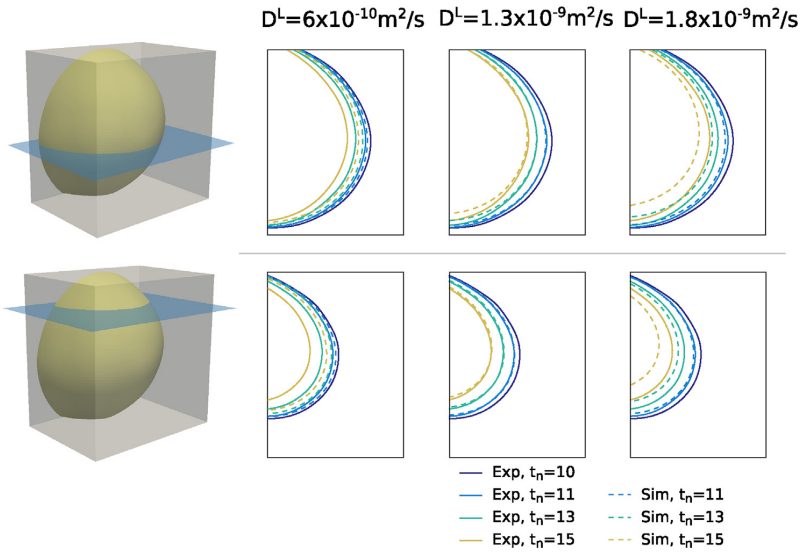

Fig. 6. Comparison between experimental and simulated microstructures of the small interface patch at different experimental time steps t_n.

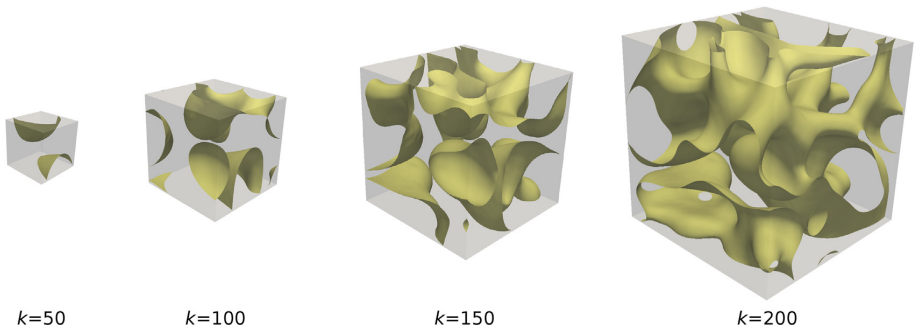

Fig. 7. Examples of subdomains with different sizes k.

starts to alter the fitted values. Simultaneously, as shown in Fig. 8(b), the cost functions start to increase near the boundary ($k > 250$), which means that the resulting diffusion coefficients are not correct. In summary, the influence of the boundary condition is around 25 to 50 grid points from the boundary. For the current problem, a subdomain with a size between $k = 160$ and $k = 210$ is

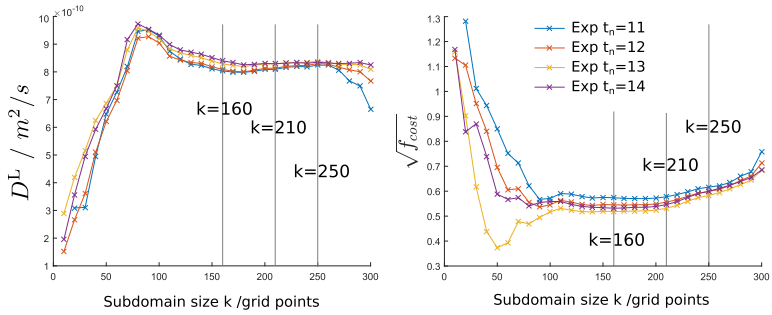

(a) The best-fit liquid diffusion coefficient (b) The cost function at the best fit

Fig. 8. Subdomain size study. Different curves are the fitting with different experimental time steps t_n.

called a representative subdomain. Here the values of time steps $t_n = 12, 13, 14$ are used (the time step 11 is not used to be consistent with section 3.4.4). The average of the 3×6 (three time steps and six representative subdomains) best-fit liquid diffusion coefficients is $8.21 \pm 0.12 \times 10^{-10}$ m^2/s with the indicated interval being the standard error.

3.4.3. Spatial variation of the fitted diffusion coefficients

In this section, subdomains with a fixed size but different locations within the simulation domain are studied. Using five subdomain sizes varying from $k = 50$ to $k = 150$, fitting is performed as the center of the subdomain sweeps through the entire simulation domain with a step of 10 grid points. The domain within 50 grid points from the simulation domain boundary is excluded because of the boundary condition (see section 3.4.2). The area of the interface within each subdomain is calculated and is plotted together with the fitted liquid diffusion coefficient in Fig. 9. As the surface area increases, there is a smaller spread of the points while the mean values of the distributions are similar for all subdomain sizes. As a result of the small step size, there will be overlap regions between subdomains; however, removing the overlapping regions reduces the density of points but does not change the overall trend in Fig. 9. Possible reasons for the spread of points include the influence of convection, temperature gradients in the sample, local impurity, reconstruction and segmentation errors and simulation errors. The convergence shown in Fig. 9 implies that the variation caused by these systematic errors is averaged out with increasing interface area. Hence we conclude that in the current system a large interface area is essential to average out local heterogeneity while fitting a limited number of representative subdomains is sufficient to get a high precision value of the material parameter.

3.4.4. Temporal variation of the fitted diffusion coefficients

As shown in Fig. 8, if we compare the resulting fitted diffusion coefficients of the representative subdomains at different fitting time steps t_n, they show a very small deviation.

Starting from different experimental time steps t_0, several phase-field simulations are performed, and the liquid diffusion coefficient D^L is fitted by comparing with three later experimental time steps $t^{exp} = t_0 + 2, 3, 4$ (the immediately followed time step $t_0 + 1$ is not used because the interfaces need time to move a sufficient distance). The six representative subdomains determined in section 3.4.2 are used for fitting. In total, 3×6 (three time steps and six representative subdomains) best-fit values of D^L are determined from the fitting. The mean value and standard deviation of these are shown as a function of t_0 in Fig. 10. We observe that the best-fit diffusion coefficient is nearly constant in time. Taking into account the variation in t_0, the fitted liquid diffusion coefficient is

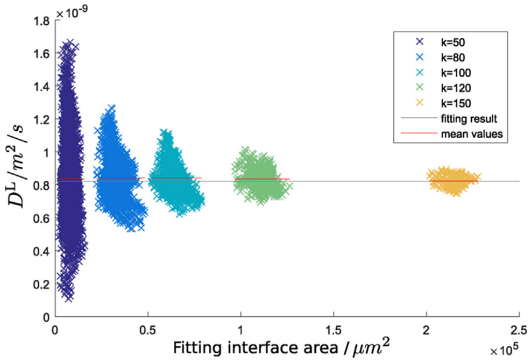

Fig. 9. Correlation between best-fit values of D^L and the fitting interface area for different subdomain size (fitting time $t_n = 12$). Points with the same color are results from the same subdomain size. The gray line shows the result of the fitting from the representative subdomains (section 3.4.2). The red lines show the mean value for each subdomain size. The scatter in the best-fit D^L decreases as the surface area increases. (For interpretation of the references to colour in this figure legend, the reader is referred to the web version of this article.)

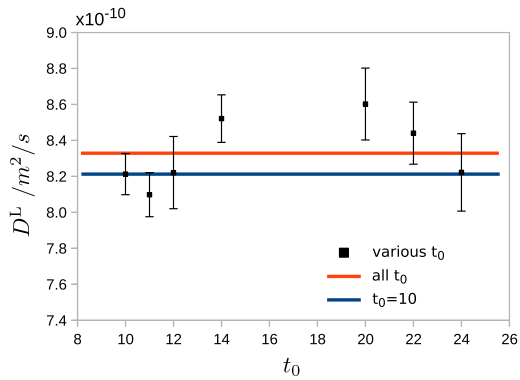

Fig. 10. Fitting results of different starting time steps t_0. The orange line shows the mean value determined from all t_0. The blue line shows the result determined from $t_0 = 10$, as given in section 3.4.2. (For interpretation of the references to colour in this figure legend, the reader is referred to the web version of this article.)

$8.33 \pm 0.24 \times 10^{-10}\ m^2/s$.

3.5. Two-parameters fitting: diffusion coefficient and capillary length

The fitting parameters are now the liquid diffusion coefficient and the capillary length $\mathbf{p} = \{D^L, l^L\}$. As the approach to determine the diffusion coefficient given in section 3.3 does not work for the capillary length, we need to perform a full phase-field simulation for each trial value of the capillary length. To reduce the computational cost, we here perform six phase-field simulations with six values of the capillary length. The liquid diffusion coefficient is fitted in a similar manner as in section 3.4 for each capillary length. The starting time step is $t_0 = 10$ and the fitting time step is $t_n = 12, 13, 14$. The size of representative subdomains is found to be between $k = 150$ and $k = 250$. The mean value and the standard deviation of the fitted liquid diffusion coefficients for each capillary length are determined with the representative subdomains. A linear fit as shown in Fig. 11 reveals that the best-fit values of D^L and l^L are not unique, but rather fulfill the relationship $D^L l^L = 0.518 \pm 0.011\ \mu m^3/s$ to good approximation. This is further substantiated by the values of the cost function at best-fit being indistinguishable within the fitting error. The observed relationship between the best-fit values of D^L and l^L is consistent with coarsening theory [53], and therefore indicates that the assumptions of the theory are correct.

4. Discussion

4.1. The fitting methodology

The results show that a consideration of statistics is important to get reliable fitted values of material parameters. Various error sources in experiment, simulation, and fitting may cause a large scatter of the locally fitted values. This, on the one hand, indicates that the local measurement of material parameters, which traditional techniques rely on, can be questionable. On the other hand, the amount of interface involved in the fitting methodology introduced here needs to be statistically sufficient to make sure the local variation is averaged out.

A good cost function should help extract useful information from the experimental data while being insensitive to noise. The corr-cost function (Eq. (2)) is easy to calculate, but when the geometry is represented by a limited number of voxels, there will be discontinuities in the cost function. The norm-cost function (Eq. (3)) is continuous, but an extra effort is needed to generate the signed distance function. Generally speaking, both cost functions work equally well in the case investigated here.

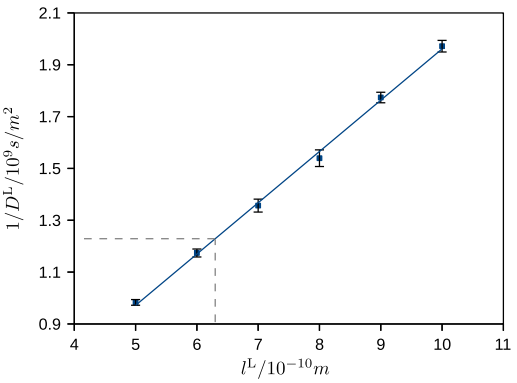

Fig. 11. The optimal values of the liquid diffusion coefficient D^L and the capillary length l^L. The blue line shows a linear fit to the points. The error bar is calculated from the representative subdomains. The dotted lines show l^L used in the one-parameter fitting and the corresponding D^L.

Though in this paper we apply the proposed fitting methodology to coarsening of a binary system, we foresee it can be applied to more complex material systems and physical processes, for example:

1. Systems with more than two phases and/or components: measure e.g. the interdiffusion coefficients in a multicomponent system and the anisotropic grain boundary energies/mobilities and the triple junction mobilities of a polycrystalline material.
2. Processes other than coarsening: measure e.g. the mobilities of domain walls in ferroelectric/piezoelectric materials and the dislocation mobility in crystalline materials.
3. Materials with structural hierarchy: determine material parameters which have an influence across scales with the help of multiscale experimental and modeling techniques.

The fitting methodology is also a very powerful way to provide insight on the quality of the materials model. If the result of the optimization is a poor global match between experiment and optimized model, it may indicate that one or more mechanisms are absent from the model. If the simulation only deviates from the experiment in a local region, we may either attempt to improve the underlying model or exclude the problematic regions. Our work shows that in the case of coarsening we can get good results with the simplified model and a fitting domain excluding the problematic regions.

Applying the proposed method to fitting more than one independent material parameters is straightforward by using multivariable optimization algorithms. The main limitation of the fitting methodology is the heavy computational cost as generally the phase-field simulation need to be performed many times. For the case investigated here, the phase-field simulations for one experimental time step with a 300^3 domain took 22 h on a Nehalem architecture machine with 16 cores and took 11 h for simulations with a 400^3 domain on a Sandy Bridge architecture machine with 64 cores. However, the simulations may be speeded up by massively parallel computing and fast convergence optimization algorithms, and a good initial guess of the material parameters will shorten the path to the global minimum. Furthermore, we anticipate that in many cases it will be sufficient to base the fitting of some of the parameters on small regions in space-time.

4.2. The Al-Cu alloy

The liquid diffusion coefficient of the hypo-eutectic Al-Cu has been experimentally measured several times [24,33–35], resulting in a large scatter of values between $\sim 8 \times 10^{-10}\ m^2/s$ and $\sim 6 \times 10^{-9}\ m^2/s$. Except for the value determined by Aagesen et al. [24]: $D^L = 8.3 \times 10^{-10}\ m^2/s$, the previously reported values are larger than the one determined in this paper. The most popular technique to measure the liquid diffusion coefficient employs a capillary tube. As shown by Lee et al. [33], convection in the liquid is not negligible in a capillary tube experiment if the diameter of the tube is large and this will result in a larger measured liquid diffusion coefficient. In that work, the liquid diffusion coefficient is measured during directional solidification, and the capillary tube diameter is chosen to be small ($< 0.8\ mm$) to minimize the effect of convection, but it is not clear that convection had been eliminated as a source of bias. In Aagesen et al. [24] and in the current study, the features of the microstructures are at a micrometer scale so the

Rayleigh number is very small; hence convection can be neglected. The experiment is also isothermal, unlike experiments that determine diffusion coefficients by composition measurements on quenched samples following directional solidification where a large temperature gradient is present, e.g. 10 K/mm in Ref. [33]. This can result in an uncertainty in the temperature and composition at which the liquid diffusion coefficient is determined. Moreover, microstructure evolution during quench may alter the composition profile, which is prevented in the present study since the measurements are in situ. Compared to the liquid diffusion coefficient, the measured values of the capillary length show small scatter [31,32]. The capillary length used in the one-parameter fitting is calculated from the Gibbs-Thomson coefficient measured by Gündüz and Hunt [31] in the grain boundary groove experiments. Given this value of the capillary length, the measured liquid diffusion coefficient from the one-parameter fitting has a value of $D^{\mathrm{L}} = 8.33\pm0.24 \times 10^{-10}\ m^2/s$. Taking into account the uncertainty in the measurement of the Gibbs-Thomson coefficient (5% ∼ 7%) [31,32], we have $D^{\mathrm{L}} = 8.3\pm0.9 \times 10^{-10}\ m^2/s$ by assuming linear error propagation.

5. Conclusion

We have developed a methodology of fitting material parameters by comparison between time-resolved 3D experimental measurements of microstructure and simulations. Compared to traditional ways of material parameter measurement, samples and sample environments representative of bulk properties and actual processing conditions can be used and several parameters can be fitted simultaneously. The fitting methodology was presented with subsequent discussions on the cost functions, the fitting domain, and the statistics. As a demonstration, our methodology is applied to a hypo-eutectic Al-Cu system to determine the liquid diffusion coefficient and the capillary length. A detailed analysis of the fitting is given, including the convergence over subdomain size/interface area and the temporal and the spatial variation of the fitted values. From simulations varying both diffusion coefficient and liquid capillary length, it is found that the best-fit values are not unique, but are found to fulfill $D^{\mathrm{L}}l^{\mathrm{L}} = 0.518\pm0.011\ \mu m^3/s$ which corroborates a basic hypothesis of the coarsening theory. Given the value of the capillary length, the measured liquid diffusion coefficient from the one-parameter fitting has a value of $D^{\mathrm{L}} = 8.33\pm0.24 \times 10^{-10}\ m^2/s$. The proposed fitting methodology provides a way to measure microstructure material parameters which are difficult to be measured by traditional methods.

Acknowledgment

JZ and HFP acknowledge the financial support of the CINEMA project. SOP acknowledges financial assistance award 70NANB14H012 from U.S. Department of Commerce, National Institute of Standards and Technology as part of the Center for Hierarchical Materials Design (CHiMaD). HFP acknowledges the ERC advanced grant d-TXM. The usage of supercomputers Quest at Northwestern University and Niflheim at Technical University of Denmark is acknowledged. JZ thanks Yue Sun and Matthew Peters at Northwestern University for helpful discussion.

Appendix A. Elimination of the coalescence regions

As the thin liquid films sometimes observed separating solid particles in the experiment, see Fig. 4, are too thin to be resolved in the phase-field simulation, interfaces close to each other in the simulations will tend to coalesce. Regions where this happens should be removed from the fitting domain to get a reliable fitted value of material parameters. A common feature of those regions is that the interface has very high velocity. Here the high-velocity domains are selected and then removed from Ω_{fit} with a given velocity threshold v_{min} by

$$\Omega_{\mathrm{highv}} = \{\mathbf{x} : |\mathbf{v}(\mathbf{x})| \geqslant v_{\mathrm{min}}\} \tag{A.1}$$

The coalescence may influence the evolution of interfaces nearby, so a dilation of the high-velocity region is performed to include nearby regions. The velocity threshold and the extent of dilation are chosen to ensure that the influence on the fitting result is minimized.

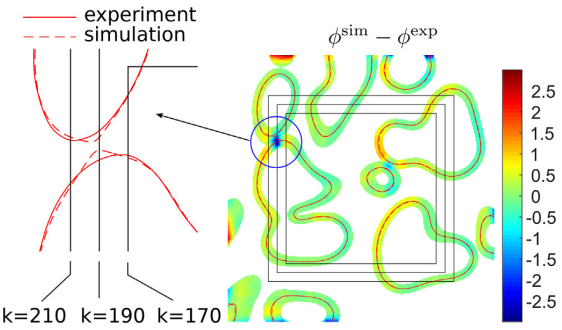

Fig. A.12. In coalescence regions, there is a large difference between ϕ^{exp} and ϕ^{sim}, indicating a large velocity. The square boxes show the subdomains with different sizes k.

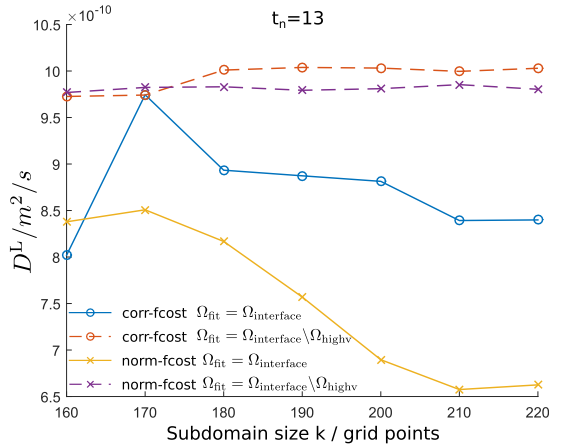

Fig. A.13. Influence of the high-velocity region Ω_{highv}. Solid and dashed lines are fitting results with and without Ω_{highv}, respectively. Lines with circular and cross symbols are fitting results using the corr-cost function (Eq. (2)) and the norm-cost function (Eq. (3)), respectively.

The influence of the high-velocity regions on the fitting results is shown by a simplified problem. For visualization purposes, the fitting domain is a 2D slice of a 3D simulation domain. We can see a coalescence event inside subdomain of size $k = 210$ but not $k = 170$. The value $(\phi^{\mathrm{sim}} - \phi^{\mathrm{exp}})/\Delta t$ can be regarded as the interfacial velocity and is shown in Fig. A.12 (right). For simplicity, here Δt is set to be one and the signed distance functions have a unit of grid points. The magnitude of $\phi^{\mathrm{sim}} - \phi^{\mathrm{exp}}$ is very large in the coalescence region compare to the other regions. The fitted values of the liquid diffusion coefficient are plotted with the subdomain sizes in Fig. A.13. When the fitting is performed with the high-velocity regions, the best-fit D^{L} will be underestimated as the high-

velocity interfaces tend to dominate the fitting result. So as more high-velocity regions are included in fitting, the best-fit values decrease, as shown by the solid lines in Fig. A.13. The fitted values with a fitting domain eliminating the high-velocity region (dashed lines) show a smaller scatter than the ones with the high-velocity region (solid lines) and show a similar best-fit value for both cost functions. We conclude that the proposed process excludes regions of the simulations where coalescence occurs without biasing the global fit.

References

[1] G.B. Olson, Computational design of hierarchically structured materials, Science 277 (1997) 1237–1242.

[2] National Research Council, Integrated Computational Materials Engineering: a Transformational Discipline for Improved Competitiveness and National Security, The National Academies Press, Washington, DC, 2008, http://dx.doi.org/10.17226/12199.

[3] OSTP, Materials Genome Initiative for Global Competitiveness, Technical Report, Office of Science and Technology Policy, Washingtom, DC, 2011. URL: https://www.whitehouse.gov/sites/default/files/microsites/ostp/materials_genome_initiative-final.pdf.

[4] G. Olson, C. Kuehmann, Materials genomics: from CALPHAD to flight, Scr. Mater 70 (2014) 25–30.

[5] Z.-K. Liu, First-principles calculations and CALPHAD modeling of thermodynamics, J. Phase Equilib. Diffus. 30 (2009) 517–534.

[6] M. Mantina, Y. Wang, R. Arroyave, L.Q. Chen, Z.K. Liu, C. Wolverton, First-principles calculation of self-diffusion coefficients, Phys. Rev. Lett. 100 (2008) 215901.

[7] M. Mantina, S.L. Shang, Y. Wang, L.Q. Chen, Z.K. Liu, 3*d* transition metal impurities in aluminum: a first-principles study, Phys. Rev. B 80 (2009) 184111.

[8] B.-C. Zhou, S.-L. Shang, Y. Wang, Z.-K. Liu, Diffusion coefficients of alloying elements in dilute Mg alloys: a comprehensive first-principles study, Acta Mater 103 (2016) 573–586.

[9] W. Wang, H. Fang, S. Shang, H. Zhang, Y. Wang, X. Hui, S. Mathaudhu, Z. Liu, Atomic structure and diffusivity in liquid Al_{80} Ni_{20} by ab initio molecular dynamics simulations, Phys. B 406 (2011) 3089–3097.

[10] M. Strobl, I. Manke, N. Kardjilov, A. Hilger, M. Dawson, J. Banhart, Advances in neutron radiography and tomography, J. Phys. D. Appl. Phys. 42 (2009) 243001.

[11] E. Maire, P.J. Withers, Quantitative x-ray tomography, Int. Mater. Rev. 59 (2014) 1–43.

[12] H.F. Poulsen, Three-dimensional X-ray Diffraction Microscopy: Mapping Polycrystals and Their Dynamics, Volume 205 of Springer Tracts in Modern Physics, Springer Berlin Heidelberg, 2004, http://dx.doi.org/10.1007/b97884.

[13] W. Ludwig, S. Schmidt, E.M. Lauridsen, H.F. Poulsen, X-ray diffraction contrast tomography: a novel technique for three-dimensional grain mapping of polycrystals. I. direct beam case, J. Appl. Crystallogr. 41 (2008) 302–309.

[14] D.J. Rowenhorst, P.W. Voorhees, Measurement of interfacial evolution in three dimensions, Annu. Rev. Mater. Res. 42 (2012) 105–124.

[15] C. Raufaste, B. Dollet, K. Mader, S. Santucci, R. Mokso, Three-dimensional foam flow resolved by fast x-ray tomographic microscopy, Europhys. Lett. 111 (2015) 38004.

[16] S. McDonald, P. Reischig, C. Holzner, E. Lauridsen, P. Withers, A. Merkle, M. Feser, Non-destructive mapping of grain orientations in 3D by laboratory x-ray microscopy, Sci. Rep. 5 (2015) 14665.

[17] A. Karma, W.-J. Rappel, Quantitative phase-field modeling of dendritic growth in two and three dimensions, Phys. Rev. E 57 (1998) 4323–4349.

[18] A. Karma, Phase-field formulation for quantitative modeling of alloy solidification, Phys. Rev. Lett. 87 (2001) 115701.

[19] N. Moelans, A quantitative and thermodynamically consistent phase-field interpolation function for multi-phase systems, Acta Mater 59 (2011) 1077–1086.

[20] I. Steinbach, Phase-field model for microstructure evolution at the mesoscopic scale, Annu. Rev. Mater. Res. 43 (2013) 89–107.

[21] D. Zöllner, P. Streitenberger, Three-dimensional normal grain growth: Monte Carlo Potts model simulation and analytical mean field theory, Scr. Mater 54 (2006) 1697–1702.

[22] M. Syha, D. Weygand, A generalized vertex dynamics model for grain growth in three dimensions, Modell. Simul. Mater. Sci. Eng. 18 (2010) 015010.

[23] S. Chen, B. Merriman, S. Osher, P. Smereka, A simple level set method for solving stefan problems, J. Comput. Phys. 135 (1997) 8–29.

[24] L.K. Aagesen, J.L. Fife, E.M. Lauridsen, P.W. Voorhees, The evolution of interfacial morphology during coarsening: a comparison between 4D experiments and phase-field simulations, Scr. Mater 64 (2011) 394–397.

[25] I.M. McKenna, S.O. Poulsen, E.M. Lauridsen, W. Ludwig, P.W. Voorhees, Grain growth in four dimensions: a comparison between simulation and experiment, Acta Mater 78 (2014) 125–134.

[26] M. Wang, Y. Xu, Q. Zheng, S. Wu, T. Jing, N. Chawla, Dendritic growth in Mg-based alloys: phase-field simulations and experimental verification by x-ray synchrotron tomography, Metall. Mater. Trans. A 45 (2014) 2562–2574.

[27] P. Steinmetz, Y.C. Yabansu, J. Hötzer, M. Jainta, B. Nestler, S.R. Kalidindi, Analytics for microstructure datasets produced by phase-field simulations, Acta Mater 103 (2016) 192–203.

[28] M.C. Demirel, A.P. Kuprat, D.C. George, A.D. Rollett, Bridging simulations and experiments in microstructure evolution, Phys. Rev. Lett. 90 (2003) 016106.

[29] I. Ansara, A.T. Dinsdale, M.H. Rand (Eds.), COST 507: Thermochemical Database for Light Metal Alloys, vol. 2, European Commission, Directorate-General XII, Science, Research and Development, 1998.

[30] V. Witusiewicz, U. Hecht, S. Fries, S. Rex, The Ag-Al-Cu system: Part I: reassessment of the constituent binaries on the basis of new experimental data, J. Alloys Compd. 385 (2004) 133–143.

[31] M. Gündüz, J. Hunt, The measurement of solid-liquid surface energies in the Al-Cu, Al-Si and Pb-Sn systems, Acta Metall. 33 (1985) 1651–1672.

[32] N. Maraşli, J. Hunt, Solid-liquid surface energies in the Al-$CuAl_2$, Al-$NiAl_3$ and Al-Ti systems, Acta Mater 44 (1996) 1085–1096.

[33] J.-H. Lee, S. Liu, H. Miyahara, R. Trivedi, Diffusion-coefficient measurements in liquid metallic alloys, Metall. Mater. Trans. B 35 (2004) 909–917.

[34] U. Dahlborg, M. Besser, M. Calvo-Dahlborg, S. Janssen, F. Juranyi, M. Kramer, J. Morris, D. Sordelet, Diffusion of Cu in AlCu alloys of different composition by quasielastic neutron scattering, J. Non-Cryst. Solids 353 (2007) 3295–3299.

[35] B. Zhang, A. Griesche, A. Meyer, Diffusion in Al-Cu melts studied by time-resolved x-ray radiography, Phys. Rev. Lett. 104 (2010) 035902.

[36] L. Piegl, W. Tiller, The NURBS Book, Springer-Verlag Berlin Heidelberg, 1995, http://dx.doi.org/10.1007/978-3-642-97385-7.

[37] J.A. Sethian, Level Set Methods and Fast Marching Methods: Evolving Interfaces in Computational Geometry, Fluid Mechanics, Computer Vision, and Materials Science, vol. 3, Cambridge University Press, 1999.

[38] J.W. Gibbs, P.W. Voorhees, Segmentation of four-dimensional, x-ray computed tomography data, Integr. Mater. Manuf. Innov. 3 (2014) 1–12.

[39] G. Russo, P. Smereka, A remark on computing distance functions, J. Comput. Phys. 163 (2000) 51–67.

[40] J.W. Gibbs, Interfacial Dynamics in Liquid-solid Mixtures: a Study of Solidification and Coarsening, Ph.D. thesis, Northwestern University, 2014.

[41] J.L. Fife, Three-dimensional Characterization and Real-time Interface Dynamics of Aluminum-copper Dendritic Microstructures, Ph.D. thesis, Northwestern University, 2009.

[42] J.W. Gibbs, P.W. Voorhees, J.L. Fife, Dataset for Segmentation of Four-dimensional, X-ray Computed Tomography Data, 2016, http://dx.doi.org/10.18126/M2CC73.

[43] L.-Q. Chen, W. Yang, Computer simulation of the domain dynamics of a quenched system with a large number of nonconserved order parameters: the grain-growth kinetics, Phys. Rev. B 50 (1994) 15752–15756.

[44] I. Steinbach, F. Pezzolla, B. Nestler, M. Seeßelberg, R. Prieler, G. Schmitz, J. Rezende, A phase field concept for multiphase systems, Phys. D. 94 (1996) 135–147.

[45] S.G. Kim, W.T. Kim, T. Suzuki, Interfacial compositions of solid and liquid in a phase-field model with finite interface thickness for isothermal solidification in binary alloys, Phys. Rev. E 58 (1998) 3316–3323.

[46] S.G. Kim, A phase-field model with antitrapping current for multicomponent alloys with arbitrary thermodynamic properties, Acta Mater 55 (2007) 4391–4399.

[47] N. Moelans, B. Blanpain, P. Wollants, Quantitative analysis of grain boundary properties in a generalized phase field model for grain growth in anisotropic systems, Phys. Rev. B 78 (2008) 024113.

[48] N. Provatas, K. Elder, Phase-field Methods in Materials Science and Engineering, John Wiley & Sons, 2011, http://dx.doi.org/10.1002/9783527631520.

[49] S. Liu, R. Napolitano, R. Trivedi, Measurement of anisotropy of crystal-melt interfacial energy for a binary Al-Cu alloy, Acta Mater 49 (2001) 4271–4276.

[50] L.K. Aagesen, Phase-field Simulation of Solidification and Coarsening in Dendritic Microstructures, Ph.D. thesis, Northwestern University, 2010.

[51] B. Echebarria, R. Folch, A. Karma, M. Plapp, Quantitative phase-field model of alloy solidification, Phys. Rev. E 70 (2004) 061604.

[52] A. Karma, W.-J. Rappel, Phase-field method for computationally efficient modeling of solidification with arbitrary interface kinetics, Phys. Rev. E 53 (1996) R3017–R3020.

[53] L. Ratke, P.W. Voorhees, Growth and Coarsening: Ostwald Ripening in Material Processing, Springer Science & Business Media, 2002.

Paper II

Three-dimensional grain growth in pure iron. Part I. statistics on the grain level

Jin Zhang[a], Yubin Zhang[b,*], Wolfgang Ludwig[c], David Rowenhorst[d], Peter W. Voorhees[e], Henning F. Poulsen[a,**]

[a] *NEXMAP, Department of Physics, DTU, 2800 Kongens Lyngby, Denmark*
[b] *Department of Mechanical Engineering, DTU, 2800 Kongens Lyngby, Denmark*
[c] *European Synchrotron Radiation Facility, 38043 Grenoble, France*
[d] *Materials Science and Technology Division, The US Naval Research Laboratory, Washington, D.C. 20735, USA*
[e] *Department of Materials Science and Engineering, Northwestern University, Evanston, IL, 60208, USA*

Abstract

Grain evolution in pure iron is determined in three dimensions using diffraction contrast tomography at a synchrotron source. During annealing for 75 minutes at $800°C$, the evolution of initially 1327 grains is quantified as a function of 15 time-steps. A comprehensive statistical analysis is provided based on the equivalent radius, the number of faces and the mean width parameters of the grains. We introduce analytical relations between these parameters, validate them, and discuss their physical meaning. While the sample is fully recrystallized, the growth is found not to be self-similar, as evidenced in changes in the distributions of normalized grain size and number of faces per grain. More importantly, a strong decrease in the slope of the growth rate over the mean width of grain faces is observed, indicating a slowdown of grain growth. The data is used to determine the applicability of the isotropic MacPherson-Srolovitz theory to an anisotropic material such as iron. Geometrical properties that are averaged over the entire grain ensemble are well described by the model, but the properties and evolution of the individual grains exhibit substantial scatter.

Keywords: Diffraction contrast tomography (DCT), Ferrite, Microstructure, X-ray synchrotron radiation, Temporal evolution

1. Introduction

Grain growth is an integral part of the thermal processing of most polycrystalline materials. It is a complicated process, involving crystallographic,

*Corresponding author
**Principal corresponding author
Email addresses: yubz@dtu.dk (Yubin Zhang), hfpo@fysik.dtu.dk (Henning F. Poulsen)

geometrical, and topological changes of the microstructure [1] under various driving forces [2]. The fact that mobilities and grain boundary energies depend on misorientations and boundary plane inclinations [2, 3] further complicates the situation. In the past 70 years, a great variety of grain growth models have been introduced, including analytical theories in 2D [4, 5] and in 3D [6, 7], and simulations using Monte Carlo Potts models [8], vertex models [9, 10], level-set based methods [11, 12], and phase-field methods [13–16]. Generally speaking, these models make the assumption of isotropic energies and mobilities of the interfaces, thus they only directly apply to idealized situations.
As an example, for one class of models, the growth rate of a grain with anisotropic grain boundary mobility M and energy γ is determined from differential geometry and Herring's relation [17]

$$\frac{\mathrm{d}V}{\mathrm{d}t} = -\int_{\Gamma_{\mathrm{face}}} 2M\gamma\mathcal{H} + M\left(\frac{\partial^2\gamma}{\partial n_1^2}\kappa_1 + \frac{\partial^2\gamma}{\partial n_2^2}\kappa_2\right)\mathrm{d}A, \tag{1}$$

where Γ_{face} is the set of all faces of the grain, V is the grain volume, κ_1 and κ_2 are the principle curvatures, $2\mathcal{H} = \kappa_1 + \kappa_2$ is the local mean curvature, n_i are the components of the normal along the principle coordinate directions. The exact integral for 2D grain growth was obtained by von Neumann and Mullins [4, 5] in the 1950s. In 2007, MacPherson and Srolovitz [6] derived an exact solution in 3D for an isotropic material (*i.e.*, the reduced mobility $m = M\gamma$ is identical for all grain boundaries and there is no inclination dependence of the energy, that is the second term in Eq. 1 is 0):

$$\frac{\mathrm{d}V}{\mathrm{d}t} = -2\pi m\left(\mathcal{L}_{\mathrm{grain}} - \frac{1}{6}\mathcal{M}\right). \tag{2}$$

Here $\mathcal{L}_{\mathrm{grain}}$ is the mean width of a grain [6], and $\mathcal{M}$ is the total triple-line length of the grain. Despite the elegant mathematics, to our knowledge, this relationship has not tested experimentally, and it is not clear to what extent this theory applies to grain growth in crystalline materials, which typically show anisotropy.

The lack of validation reflects a lack of experimental methods that can provide time resolved 3D measurements of grain growth, representing both a statistically relevant set of grains and the required time and spatial resolution. The development of nondestructive 3D grain mapping techniques such as three-dimensional x-ray diffraction (3DXRD) [18] and diffraction contrast tomography (DCT) [19, 20], provides a possible remedy to the situation. The first 3DXRD results on the growth of 480 Al-Mn grains by Schmidt *et al.* [21], involved six time-steps and a resolution of about $5 - 8\ \mu m$. Li [22] later used 3DXRD to measure the growth of about 2000 pure nickel grains with a slightly improved resolution. Concerning DCT, Syha [23] measured two steps of grain growth in strontium titanate sample with 849 grains and with a voxel size of $0.7\ \mu m$. Recently, Sun *et al.* [24] studied three steps of grain growth of more than 300 grains using a laboratory-based DCT [25, 26] with a voxel size of $5\ \mu m$. However, in all cases, the experimental settings were not ideal for a detailed test of

the above grain growth models. Phase contrast tomography (PCT) using decoration of the grain boundaries as a contrast is an alternative method exhibiting a superior spatial resolution [27]. However, the process is not representative of classical grain growth and PCT does not provide crystallographic information.

In this work, we present a high-resolution time resolved 3D measurements of grain growth of pure Fe, a material with anisotropic grain boundary energies [28] and mobilities [29]. Using DCT, 3D grain maps were acquired with a voxel size of 1.54 μm during annealing at 800°C for a total of 15 time-steps. The 1327 initial grains reduced to 776 in the last time-step. Based on this dataset, a comprehensive and statistically-sound analysis of crystallographic, geometrical and topological evolution during grain growth can be conducted. In this paper (part I), we present a statistical analysis of grain-based quantities, including the growth kinetics for the individual grains. To ease the discussion, the MacPherson-Srolovitz (MS) model [6] is used to rationalize our results. Local analysis of specific grain boundaries and topological analysis will be the focus of upcoming papers.

2. Methods

2.1. Experimental details

The sample material is 99.9% pure polycrystalline iron. The raw material was cold rolled to a reduction in thickness of 50% and subsequently annealed at a temperature of 700°C for 30 minutes to become fully recrystallized with an average grain radius of ∼20 μm. Cylindrical samples were cut with the rolling direction (RD) along the cylinder axis and subsequently electrochemically etched to a diameter of approximately 500 μm to remove the damage caused by the cutting.

The DCT experiment took place at beamline ID11 at the European Synchrotron Radiation Facility (ESRF) using a monochromatic x-ray beam with an energy of 40 keV. The sample was mounted on an ω rotation stage with RD parallel to the vertical rotation axis. A uniform beam illuminated the cylinder with a height of 400 μm. Both the diffracted and the transmitted beam were recorded using a near-field detector (comprising a transparent luminescent screen, with the emerging light optically coupled to a CCD) with 2048×2048 pixels and an effective pixel size of 1.54 μm. The detector was placed at ∼4.65 mm from the sample, implying that diffraction spots from individual grains from the first 5 hkl families were recorded. A continuous scan was made in ω with a range of 360°, in intervals of 0.1° and with exposure times of 1 s. Detailed information about the DCT set-up can be found in [30]. Nearly all diffraction spots were found to be distinct, appearing in one or at most two rotation step(s), indicating that the mosaic spread of all grains was below 0.2° and for most below 0.1°.

During the experiment, the sample was alternately mapped in air at room temperature and annealed on the beamline. For the annealing, a retractable tube furnace was used, operated at a constant temperature of 800°C and with a flow of a forming gas (Ar+2%H_2) to prevent sample oxidation. After annealing,

the sample was cooled by a jet of the forming gas and allowed to stabilize for 5 minutes before starting a new DCT acquisition. In total, the sample was annealed 14 times with annealing times of either ∼10 or 5 minutes (see Table 1). Notably, the time duration of the first annealing step was less accurately determined, so this time-step will be discarded when comparing with analytical models of time evolution.

The data was analyzed using a DCT analysis package at ID11 using the Networked Interactive Computing Environment (NICE) cluster [31]. The spatial resolution of the DCT reconstruction is $1-2$ voxels (*i.e.* $1.5-3$ μm), as demonstrated previously by Ludwig *et al.* [30] by comparison to PCT, and by Lenthe *et al.* [32] by comparison with TriBeam.

2.2. Determining mean width parameters

As we will use the MS model to interpret our results, relevant parameters in this model are calculated based on the DCT dataset. We define the mean width of a grain, $\mathcal{L}_{\text{grain}}$, and the mean width of the set of all faces of this grain, $\mathcal{L}_{\text{face}}$, as

$$\mathcal{L}_{\text{grain}} := \frac{1}{\pi}\int_{\partial\Omega_{\text{grain}}} \mathcal{H}\,\mathrm{d}A, \quad \mathcal{L}_{\text{face}} := \frac{1}{\pi}\int_{\Gamma_{\text{face}}} \mathcal{H}\,\mathrm{d}A,$$

where the integral over Γ_{face} does not take into account the turning angle at the triple-lines/edges while the integral over $\partial\Omega_{\text{grain}}$ does. We also define the mean width of the set of triple-lines/edges of the grain

$$\mathcal{L}_{\text{edge}} := \mathcal{L}_{\text{grain}} - \mathcal{L}_{\text{face}}. \tag{3}$$

For isotropic materials, Eq. 1 can be written as:

$$\frac{\mathrm{d}V}{\mathrm{d}t} = -2\pi m\left(\mathcal{L}_{\text{grain}} - \mathcal{L}_{\text{edge}}\right) = -2\pi m\mathcal{L}_{\text{face}}. \tag{4}$$

Comparing Eq. 4 with Eq. 2, for isotropic materials $\mathcal{L}_{\text{edge}}$ equals $\mathcal{M}/6$.

To determine the mean width parameters, the measured voxelized 3D grain volumes were firstly reconstructed into surface meshes using the multiple material marching cubes algorithm [33]. Then the mesh was smoothed using a two-step Laplacian smoothing algorithm. In Laplacian surface mesh smoothing, the location of the vertex point $\boldsymbol{v}_i$ of the surface mesh, in the $n+1$ iteration is described by:

$$\boldsymbol{v}_{i_{n+1}} = \boldsymbol{v}_{i_n} + \frac{\lambda}{C}\sum_{j=0}^{C}\left(\boldsymbol{v}_{j_n} - \boldsymbol{v}_{i_n}\right), \tag{5}$$

where λ is a scalar that describes the rate of smoothing for each iteration, $\boldsymbol{v}_j$ is the location of a vertex point j that is connected to vertex point i, and C is the number of vertex points connected to i. This then is repeated for N iterations until the desired amount of smoothing is achieved. The value of λ was chosen to keep the evolution of the mesh stable: $\lambda = 0.05$. In a two-step process, first the mesh points that describe the triple-lines and quad-points were extracted and

smoothed for $N = 200$ iterations. These smoothed triple-line points were then placed back into the surface mesh and held constant while the vertex points that constitute the grain faces were smoothed for $N = 200$ iterations. The reasoning for choosing the number of iterations and the effect of the number of smoothing iterations on the measured properties is provided in Section S1. From this smoothed surface mesh the mean width parameters $\mathcal{L}_{\text{face}}$ and $\mathcal{L}_{\text{grain}}$, as well as the total triple-line length of the grain, $\mathcal{M}$, were calculated, see [34] for details. $\mathcal{L}_{\text{edge}}$ was then calculated from Eq. 3.

2.3. Correlation between parameters

We derive relationships between the mean width parameters and two commonly used parameters: the equivalent radius R ($R = (3V/4\pi)^{1/3}$, where V is the grain volume) and the number of faces F of a grain.

For isotropic materials, according to Hillert [35], the growth of a grain with radius R follows

$$\frac{\mathrm{d}R}{\mathrm{d}t} = \alpha m \left(\frac{1}{R_{\text{cr}}} - \frac{1}{R} \right), \tag{6}$$

where R_{cr} is a critical radius and α is a geometry parameter. Substituting Eq. 6 into Eq. 2, we derive an analytical relationship between $\mathcal{L}_{\text{face}}$ and R:

$$\mathcal{L}_{\text{face}} = 2\alpha \left(R - \frac{1}{R_{\text{cr}}} R^2 \right). \tag{7}$$

Notably, $\mathcal{L}_{\text{face}}$ equals zero for $R = 0$ and $R = R_{\text{cr}}$. Next, as the mean width of grain $\mathcal{L}_{\text{grain}}$ is a linear measure of grain size, we assume a phenomenological expression:

$$\mathcal{L}_{\text{grain}} = k_1 R, \tag{8}$$

where k_1 is a dimensionless coefficient. From Eqs. 3, 7 and 8, it then follows that $\mathcal{L}_{\text{edge}}$ is a quadratic function of R.

For the correlation between R and F, we note that according to the MS theory [6], $\mathcal{L}_{\text{edge}}/\mathcal{L}_{\text{grain}}$ is proportional to the square root of F. Using Eqs. 3, 7 and 8, we have

$$\sqrt{F} = k \frac{R}{\langle R \rangle} + \sqrt{F_0}, \tag{9}$$

where k and F_0 are dimensionless constants, and $\langle R \rangle$ is the average equivalent spherical radius. We interpret F_0 as the face number of a shrinking grain just before it disappears, here named the disappearing face number. Substituting Eq. 9 into Eq. 7, and using $R_{\text{cr}} = \langle R^2 \rangle / \langle R \rangle$ [36], we have

$$\frac{\mathcal{L}_{\text{face}}}{\langle R \rangle} = -c_0 (\sqrt{F} - \sqrt{F_0})(\sqrt{F} - \sqrt{F_{\text{cr}}}), \tag{10}$$

where $c_0 = 2\alpha/k^2$, F_0, and $F_{\text{cr}} = (k + \sqrt{F_0})^2$ are dimensionless constants. This equation exhibits two zero points corresponding to the disappearing face number F_0 and the critical face number F_{cr}, respectively. A grain with face number F_{cr}

will neither grow nor shrink. Similarly, we can derive an expression between $\mathcal{L}_{\text{grain}}$ and F

$$\frac{\mathcal{L}_{\text{grain}}}{\langle R \rangle} = -c_1(\sqrt{F} - \sqrt{F_0}), \tag{11}$$

where $c_1 = k_1/k$ is a dimensionless constant.

3. Results

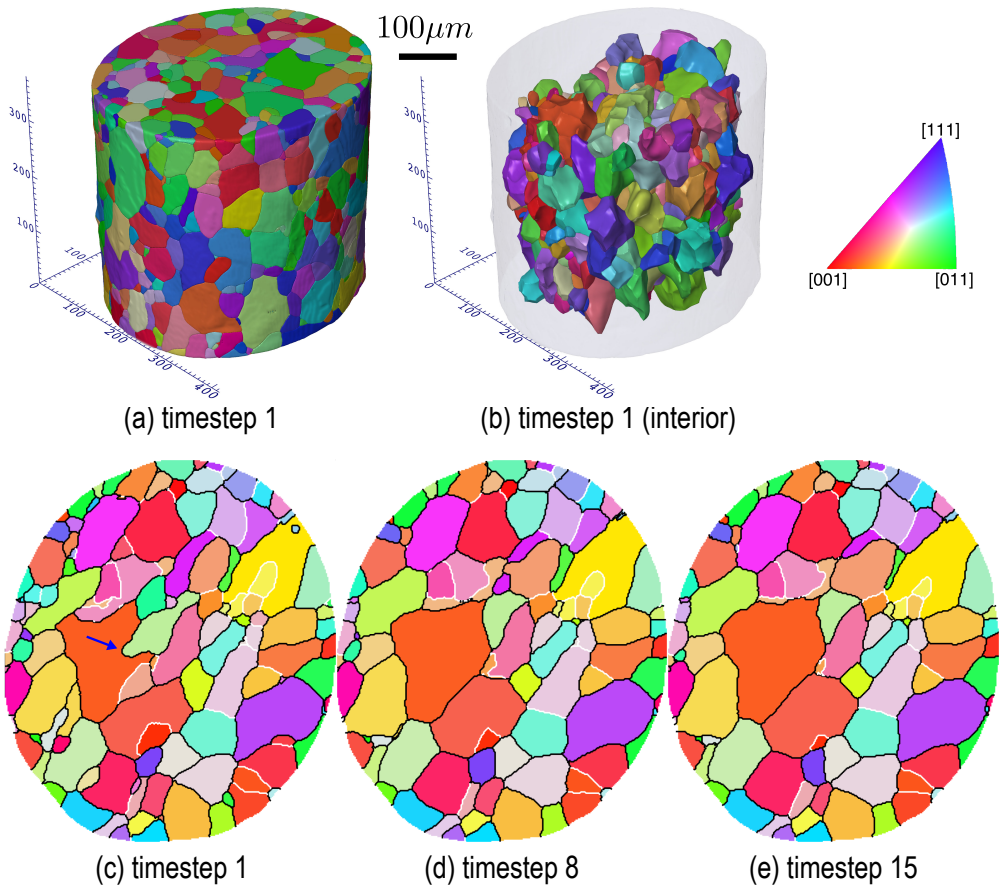

Figure 1: Experimental results. Above: 3D grain maps for time-step 1, displaying (a) all grains and (b) only interior grains. Below: one section of the 3D grain map for time-step 1 (c), 8 (d), and 15 (e). The color represents the grain orientation along sample RD (see the insert triangle), while black and white lines in (c)-(e) represent boundaries with misorientations above and below 15°, respectively.

The reconstructed 3D grain map of time-step 1 is shown in Fig. 1a. A 3D movie of the growth of one grain is given in the supplementary materials. During annealing, a significant amount of grain growth occurs, as evidenced in the evolution of one slice close to the center of the illuminated volume, cf. Fig. 1c-e.

3.1. Basic grain growth analysis

As a first step in the analysis chain, sample boundary effects were removed by discarding all "surface grains." Similar to previous work [34], this sorting of grains can be done in an unbiased way by setting two criteria:

1. grains directly touching the sample surface and surface of the top and bottom of the illuminated cylinder are removed,
2. grains whose center are within a given distance to the sample surface are removed. This distance is determined to be 46 μm, valid for all time-steps (see Section S2 in supplementary materials).

The interior grains at time-step 1 are shown in Fig. 1b. These represent less than 1/3 of the total number of grains (see Table 1). The analysis of this paper is based only on the interior grains.

Table 1: Overview of grain statistics. The average equivalent spherical radius $\langle R \rangle$ and the average number of faces $\langle F \rangle$ represent the average over interior grains.

Time-step	Time/min	Number of grains	Number of interior grains	$\langle R \rangle / \mu m$	$\langle F \rangle$
1	0	1327	387	19.30	13.49
2	10	1174	330	20.96	13.65
3	15	1069	286	22.32	13.71
4	20	1019	269	22.93	13.65
5	25	956	253	23.70	13.81
6	30	950	244	23.78	13.73
7	35	933	237	23.90	13.70
8	40	903	223	24.55	13.72
9	45	841	212	25.34	13.95
10	50	837	208	25.42	13.93
11	55	847	204	25.65	13.84
12	60	834	201	25.81	13.85
13	65	833	200	25.73	13.75
14	70	783	193	26.23	13.89
15	75	776	189	26.45	13.94

Table 1 provides statistics on basic grain parameters as a function of time: the number of total/interior grains, $\langle R \rangle$ and $\langle F \rangle$. Here R is calculated by counting the number of voxels belonging to a particular grain, while F is based on nearest neighbors.

The average number of faces is seen to be almost constant during the grain growth. Taking into account all 15 steps, the average number of faces is $\langle F \rangle = 13.77 \pm 0.13$. This value is very close to previous results from computer simulations: 13.7 [13] and 13.769 [10], and from experiment: 13.7 [34].

During the 14 annealing steps, the number of interior grains reduces by about one half. At the same time, the average radius of the grains grows about

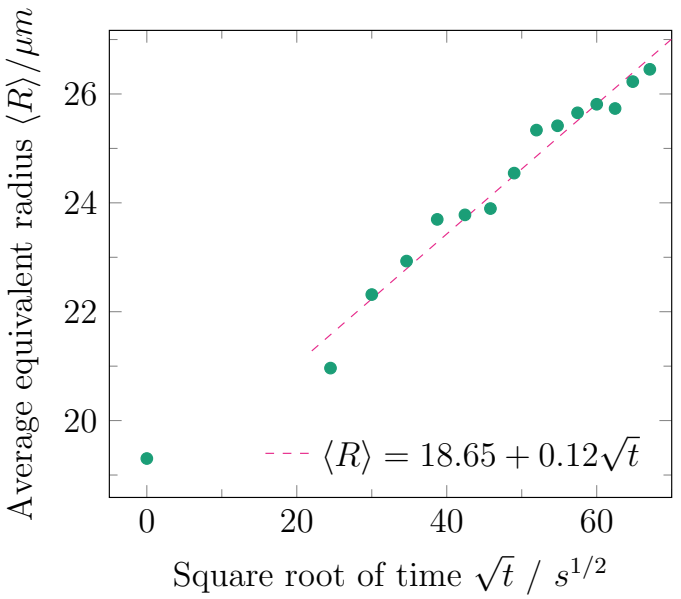

Figure 2: The average grain size $\langle R \rangle$ as a function of the square root of time $\sqrt{t}$. The dashed line shows the linear regression of the data. The first data point ($t = 0$) is not used in the fitting.

40%. This amount of growth is, however, insufficient to determine precisely the growth exponent. In Fig. 2 the average radius $\langle R \rangle$ is plotted as a function of the square root of time. Within the experimental uncertainty, the evolution of $\langle R \rangle$ is consistent with the parabolic growth. Detailed analysis of the growth will be given in Section 3.3.

3.2. Evolution in texture, geometry and topology

At the beginning of the experiment the sample has a weak texture, which is inherited from recrystallization. The texture of the sample is slightly strengthened during the annealing (see Fig. S4 in supplementary materials). The distribution of misorientation angles at time-steps 1, 8 and 15 are shown in Fig. 3. The initial distribution is relatively close to that of a sample with a random texture, except for a relatively higher fraction of low angle boundaries ($< 15°$). This is likely to be related to the texture of the sample. During the annealing, the fraction of low angle boundaries decreases by about 2.4%.

3.2.1. Distributions

The distribution of R and F, with averages listed in Table 1, are shown in Fig. 4a and 4b, respectively, for time-steps 1, 8 and 15 approximately the same change in $\langle R \rangle$ between each of the noted time-steps. The normalized grain size distribution (Fig. 4a) exhibits a peak shift from $R/\langle R \rangle = 0.6$ to 0.8 during the annealing, and the fraction of the small grains reduces markedly with time, indicating that the growth is not fully self-similar. Likewise, the distribution of

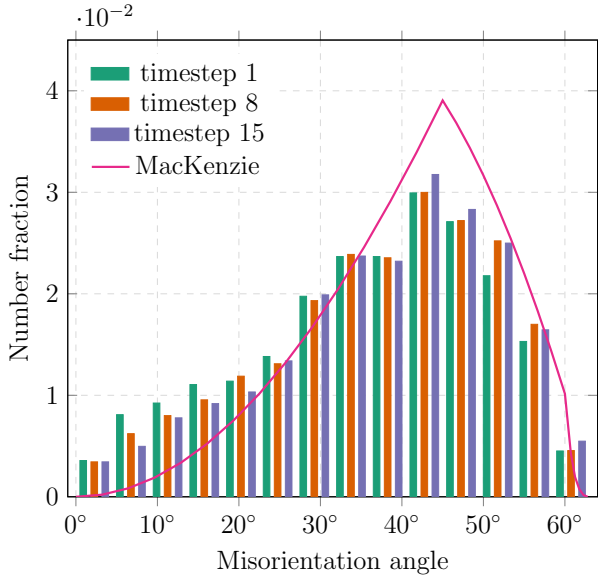

Figure 3: The misorientation distribution for three time-steps in bins of 4.5°. Overlaid is the theoretical distribution of a random texture (MacKenzie) [37].

the number of faces per grain (Fig. 4b) exhibits a peak shift, and, again, the tail of the distribution on the lower side decreases during the grain growth. This is consistent with Fig. 4a since small grains tend to have a small number of faces.

The distributions of two of the mean width parameters are shown in Fig. 4c and 4d. $\mathcal{L}_{\text{grain}}$ (Fig. 4c) is a linear measure of grain size, exhibiting a similar shape and evolution as the normalized grain size distribution in Fig. 4a. The distribution of $\mathcal{L}_{\text{face}}$ is shown in Fig. 4d. At all times, there is a peak near zero, and an asymmetric distribution with the tail of negative $\mathcal{L}_{\text{face}}$ (growing grains according to Eq. 4) much broader than that of positive $\mathcal{L}_{\text{face}}$ (shrinking grains according to Eq. 4). This is reasonable as growing grains are generally large with complex geometries, thus causing a large scatter in the values.

3.2.2. Correlation between geometrical and topological quantities

For each time-step, the mean width parameters are plotted against the grain size R to examine their correlation. As an example, the plot for time-step 8 is shown in Fig. 5. Small grains tend to have a positive $\mathcal{L}_{\text{face}}$, and vice versa. Despite some scatter, the relations proposed in Section 2.3 (Eq. 7 and Eq. 8) fit the mean width data well. The quality of fit is very similar for all 15 time-steps, and the fitted values of α and k_1 are nearly identical (see Table S1 in supplementary materials). Taking into account all 15 time-steps, on average $\alpha = 1.18 \pm 0.12$ (all errors represent standard deviations of the data in this paper). This value is similar to results from phase-field simulations ($\alpha = 1.1$ [38] and $\alpha \approx 1.25$ [39]), but slightly higher than the heuristic assumption in the Hillert theory ($\alpha = 1$) for 3D growth [35]. Theoretically, the critical radius R_{cr} is predicted to be $R_{\text{cr}}^{\text{H}} = 1.125\langle R \rangle$ by Hillert [35], and $R_{\text{cr}}^{\text{R}} = \langle R^2 \rangle / \langle R \rangle$

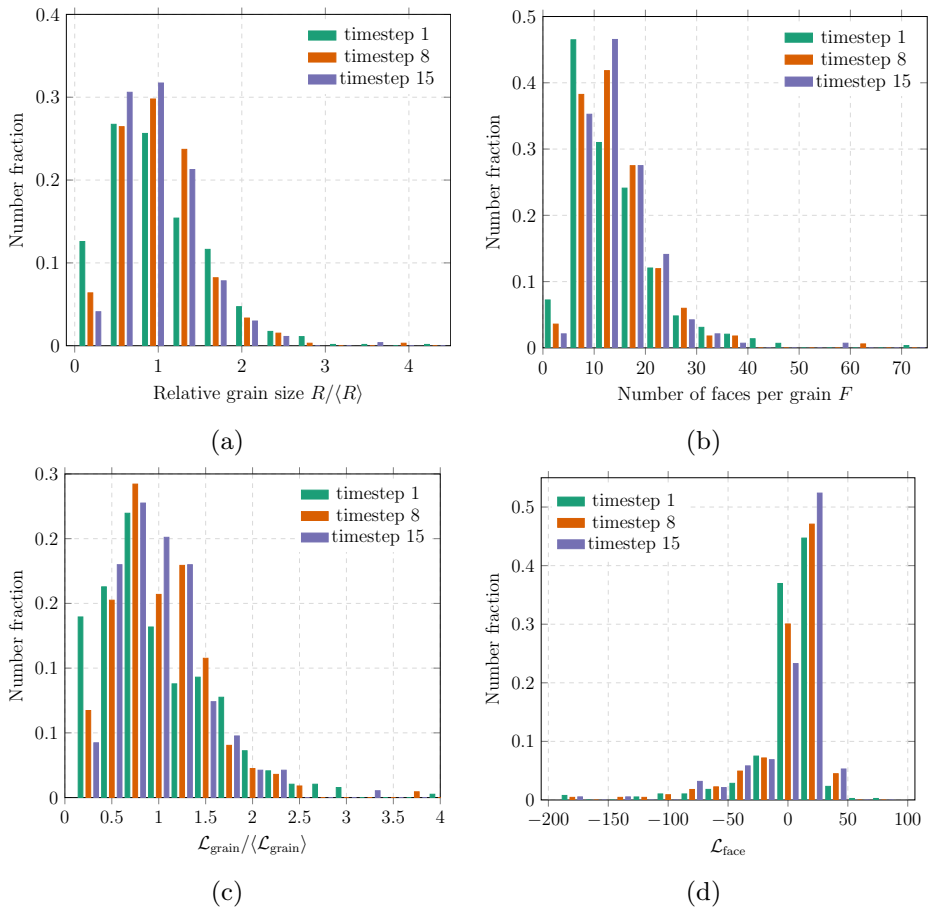

Figure 4: Distributions of four geometrical and topological parameters for three time-steps 1, 8 and 15: (a) normalized grain size $R/\langle R\rangle$, (b) number of faces per grain F, (c) normalized $\mathcal{L}_{\text{grain}}$, and (d) $\mathcal{L}_{\text{face}}$. The bins are 0.375 (a), 5 (b), 0.25 (c) and 20 (d), respectively.

by Rios [36]. Comparing to these theories, the fitted R_{cr} has a similar value: $R_{\text{cr}} = (1.12 \pm 0.05)R_{\text{cr}}^{\text{H}} = (1.04 \pm 0.02)R_{\text{cr}}^{\text{R}}$. Also evident from Fig. 5 is that a linear fit to the $\mathcal{L}_{\text{grain}}$ data and a quadratic fit to the $\mathcal{L}_{\text{edge}}$ data both show good agreement, cf. Fig. 5.

This analysis suggests a way to estimate the abstract and difficult-to-measure mean width parameters from the conventional parameter, grain size R, which is more readily available from a 3D dataset. However, the applicability of the values of the fitting parameters, *e.g.* α and $R_{\text{cr}}/\langle R\rangle$, for other materials systems has to be tested.

Then, we consider the correlation between R and F as given in Eq. 9. The data of three different time-steps are shown in Fig. 6. The dashed lines represent linear regressions of the data. Though the data display significant scatter, as a result of neglecting the underlying geometry, a linear relationship between R and $\sqrt{F}$ is in all cases seen. The fitted values of the disappearing face number

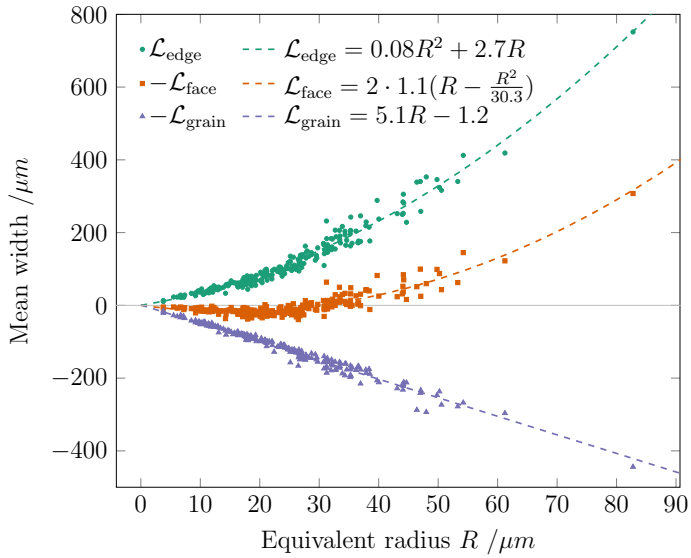

Figure 5: $\mathcal{L}_{\text{edge}}$, $-\mathcal{L}_{\text{face}}$ and $-\mathcal{L}_{\text{grain}}$ as functions of the equivalent radius R for time-step 8. The dashed lines show the results of quadratic fits to the $\mathcal{L}_{\text{face}}$ and $\mathcal{L}_{\text{edge}}$ data, and a linear fit to $\mathcal{L}_{\text{grain}}$.

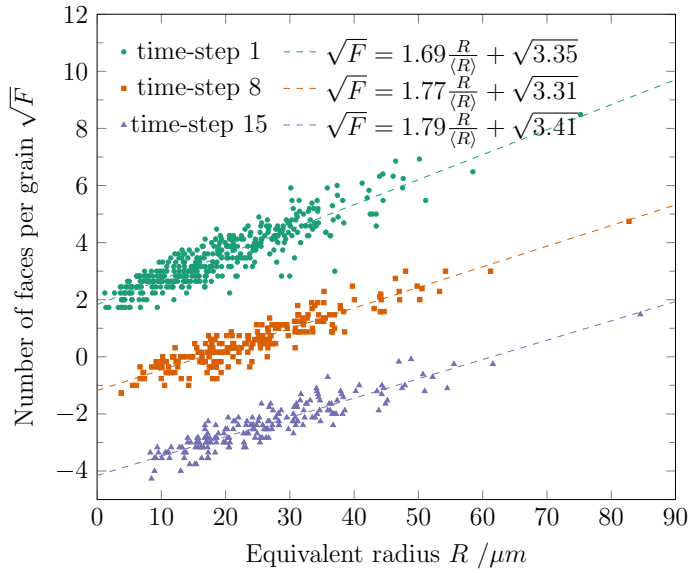

Figure 6: The equivalent radius R vs. the number of grain faces F for time-steps 1, 8 and 15. To ease visualization, the data of time-step 8 and time-step 15 are shifted downward by 3 and 6 units, respectively.

are on average $F_0 = 3.33 \pm 0.10$, which is consistent with the argument of Smith [1]: a shrinking grain has three faces before disappearing: $F_0 = 3$. The slope is nearly identical for the various time-steps: on average $k = 1.77 \pm 0.03$. The fitted

values for the 15 time-steps are listed in Table S1 in supplementary materials.

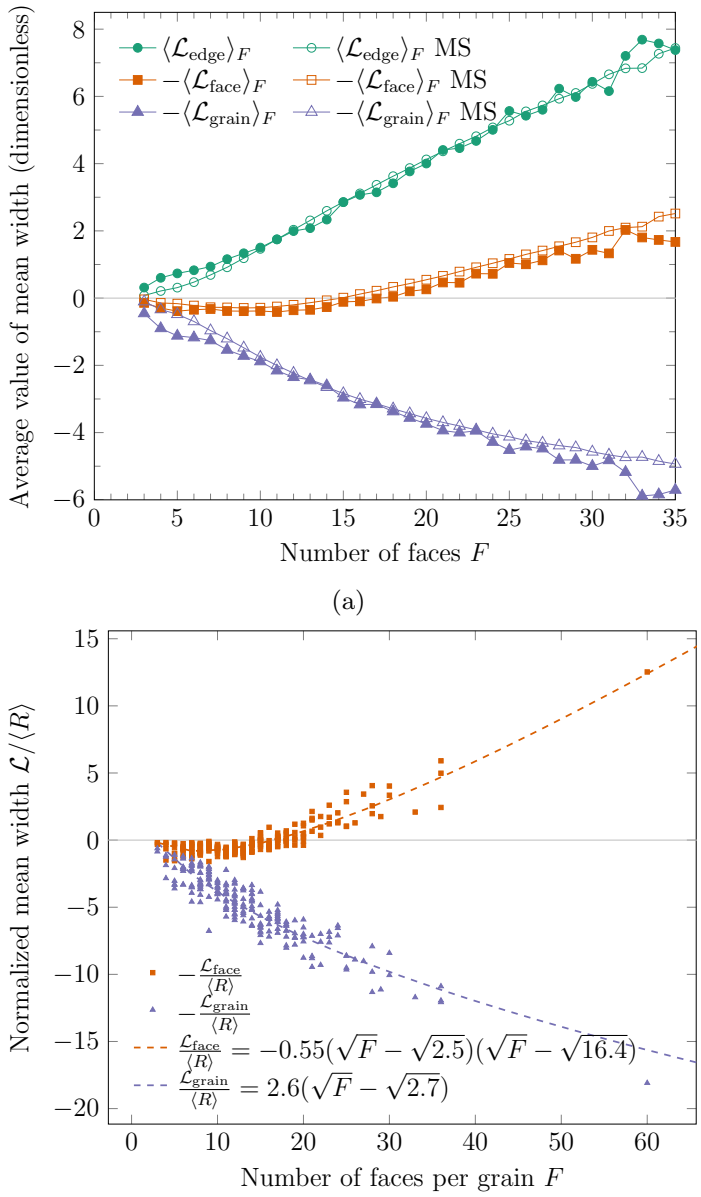

Figure 7: (a) The average values $\langle\mathcal{L}_{\text{edge}}\rangle_F$, $-\langle\mathcal{L}_{\text{face}}\rangle_F$ and $-\langle\mathcal{L}_{\text{grain}}\rangle_F$ as a function of F, using data from all 15 time-steps. Here $\langle\cdot\rangle_F$ is the topological class average (to be distinguished with the average over grain ensemble $\langle\cdot\rangle$). The measured values are scaled using $\langle V\rangle^{1/3} = 40.03\ \mu m$ (an average value representing all interior grains and all 15 time-steps). The results of a simulation based on the MacPherson-Srolovitz theory (MS) are superposed [40]. No fitting is involved in these results. (b) $-\mathcal{L}_{\text{face}}$ and $-\mathcal{L}_{\text{grain}}$ as a function of the number of grain faces F for time-step 8 (dots). Also shown are fits to analytical models (dashed lines).

Next, the correlation between mean width parameters and the number of faces is compared with simulations based on the MS theory and with the analytical expression proposed in Section 2.2.
First we consider the topological class average behavior, *i.e.* averaged for different classes of number of faces. Shown in Fig. 7a is a comparison with a MS simulation [10, 40] comprising about 200,000 grains. There is good correspondence with the simulations. Note that there are no fitting parameters in this comparison. The correspondence indicates that the topological class average mean width parameters are insensitive to the anisotropy in the grain boundary properties. Insufficient amount of data (see Fig. 7b) may cause the minor disagreement at small and large F. Moreover, errors in the mean width calculation for small grains may also contribute to the disagreement at small F as these small grains have the fewest number of voxels describing their shape, and thus the largest uncertainty in their measured morphology [41].
Then, we consider the behavior of the individual grains. As shown in Fig. 7b, fits of Eqs. 10 and 11 to the experimental data show reasonably good agreement. We attribute the scatter to anisotropy and to ignoring the underlying geometry. The fitted results of Eq. 10 are $c_0 = 0.56 \pm 0.05$, $F_0 = 2.73 \pm 0.37$ and $F_{\text{cr}} = 16.91 \pm 0.64$, and the fitted results of Eq. 11 are $c_1 = 2.58 \pm 0.11$ and $F_0 = 2.73 \pm 0.09$ (see Table S1 in supplementary materials for the fitted value of each time-step). The F_0 values are slightly smaller than the fitted values obtained in Fig. 6. The critical face number F_{cr} is slightly larger than literature values $F_{\text{cr}} = 15.5$ [34] and $F_{\text{cr}} = 15$ [40]. Notice that the fitted critical face number F_{cr} is consistent with that calculated using Eq. 9 and the critical radius R_{cr} fitted in Fig. 5.

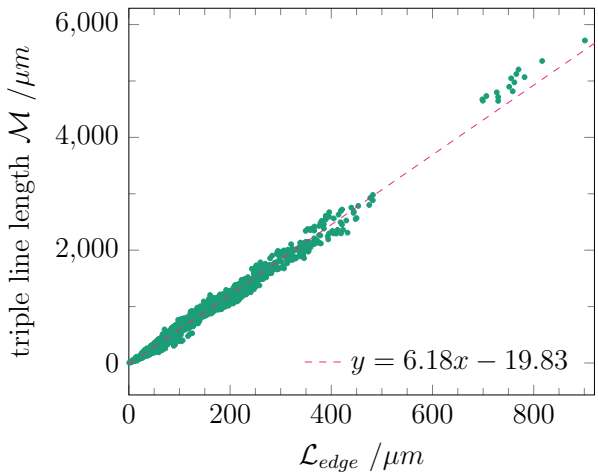

Figure 8: The total triple-line length $\mathcal{M}$ vs. $\mathcal{L}_{\text{edge}}$ (green dots) for all 15 time-steps. Overlaid is a best fit to a linear relationship.

Finally, we consider the correlation between $\mathcal{L}_{\text{edge}}$ and the total triple-line length $\mathcal{M}$. In our work, the mean width of edges $\mathcal{L}_{\text{edge}}$ is calculated from Eq. 3, so the triple-junction angle is not fixed to be the isotropic value of $2\pi/3$. In

the isotropic MS theory, $\mathcal{L}_{\text{edge}}$ is related to $\mathcal{M}$: $\mathcal{M} = 6\mathcal{L}_{\text{edge}}$. In Fig. 8, the correlation between $\mathcal{M}$ and $\mathcal{L}_{\text{edge}}$ is shown. The data are consistent with a linear relationship and a fit gives a slope of 6.16 ± 0.08. This is close to the prediction of 6 from the MS theory. As $\mathcal{M}$ and $\mathcal{L}_{\text{edge}}$ are quantities attributed to an entire grain, they may not be very sensitive to anisotropies in the individual grain boundary energies. For example, it is possible to change the grain shape significantly (as a result of grain boundary energy anisotropy) without the triple-line length $\mathcal{M}$ changing at all. Alternatively or simultaneously the anisotropy itself may be weak.

3.3. Growth rate of individual grains

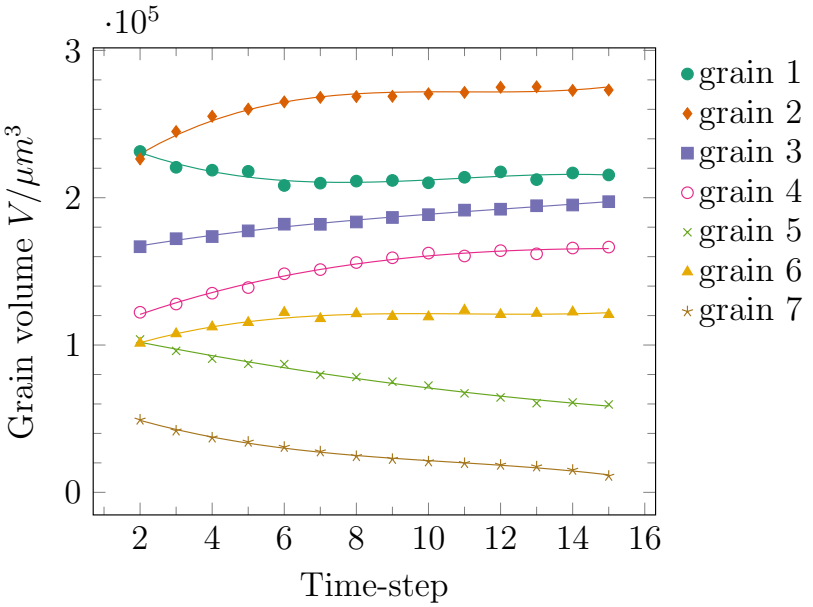

Figure 9: Examples of experimental growth curves for individual grains without (dots) and with smoothing by a third order polynomial (lines).

The growth of the individual grains were tracked through time.The evolution of the grain volume for seven randomly selected grains that survived throughout the experiment (time-step 2 to 15) are shown in Fig. 9. As illustrated, to obtain a robust measure of the growth rate $\mathrm{d}V/\mathrm{d}t$, the data are smoothed using a third-order polynomial. As one might expect, most of the large grains are growing while small grains typically are shrinking during annealing. However, there are examples of large grains that shrink (grain 1) and smaller grains that grow (grain 6), thus there is no universal value of grain volume that separates growing and shrinking grains and it is clear that whether a grain grows or shrinks depends on the local environment of the grain in contrast to the Hillert mean field theory.

The growth rates as a function of $\mathcal{L}_{\text{face}}$ is plotted for a statistically significant number of individual grains in Fig. 10a. For each time-step, despite some scatters, on average $\mathrm{d}V/\mathrm{d}t$ shows a linear correlation with $-2\pi\mathcal{L}_{\text{face}}$. Interestingly,

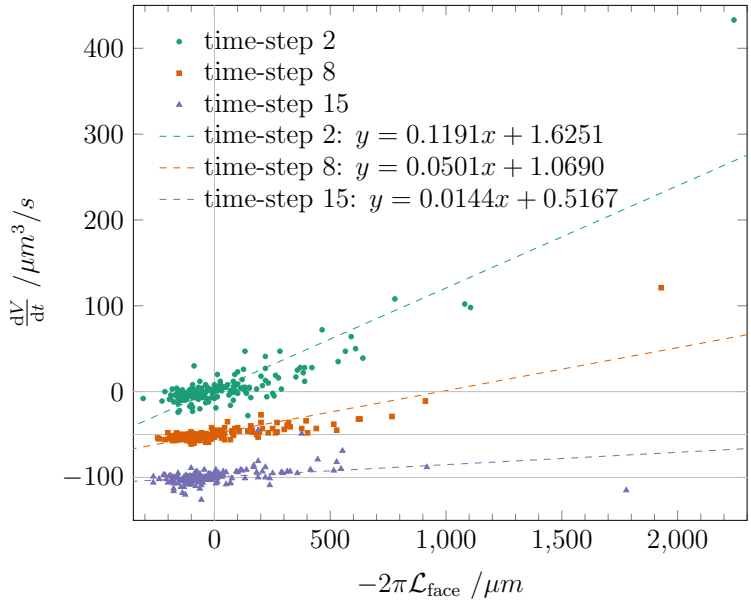

(a)

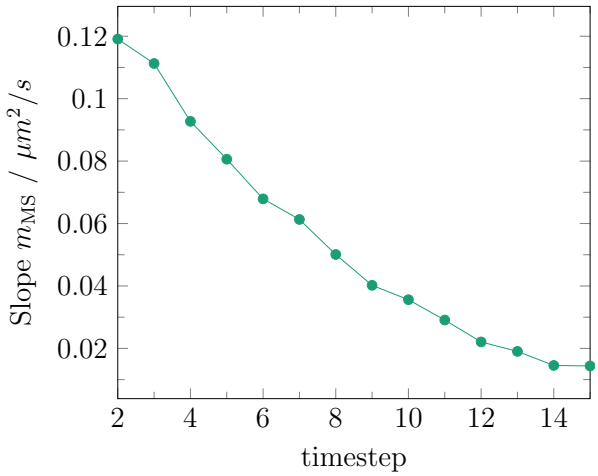

(b)

Figure 10: (a) The growth rate dV/dt is plotted versus $-\mathcal{L}_{\text{face}}$ for all grains at three time-steps. To ease visualization, the data of time-step 8 and time-step 15 have been shifted downward by 50 and 100 units, respectively. The dashed lines represent linear regressions of the data. (b) the fitted slope in (a) as a function of time.

the fitted slope ($m_{\text{MS}} = dV/dt/(-2\pi\mathcal{L}_{\text{face}})$), decreases as a function of annealing time (see Fig. 10b). Within the total annealing period, the slope decreases by a factor of 8.

4. Discussion

Over a century, a significant amount of work has been devoted to develop models that can predict the growth behavior of individual grains based on their geometry or topology, including the two outstanding models by Hillert [35], and MacPherson-Srolovitz (MS) [6] discussed above. The MS model is more elaborate as it takes into account the grain's morphology and neighbor relationships (reflected in parameter $\mathcal{L}_{\text{face}}$), while in the Hillert's model, all grains are assumed to be spheres growing in a mean field. So far none of these models have been empirically validated. The present dataset offers a unique possibility to address this issue. We can make this comparison for grain averages or by examining the results for all individual grains. Alternatively we can use the scatter in Figs. 5, 6, 7b, 8 and 10a to quantify to what extent the models are applicable on the individual grain level for anisotropic materials like iron. Below we comment and further analyze the results on first the macro scale (averaged over a grain ensembles), then the local scale (individual grains).

4.1. Macro scale grain growth

Our results in Section 3.2.2 and 3.3 demonstrate that on this scale MS theory is a good approximation for pure iron. Notably, the fitted value of the critical grain size R_{cr} from the MS model (see Fig. 5) is close to the prediction from Hillert's theory for our material. The changes in the distributions in Figs. 3 and 4 indicate that the grain growth of pure iron was not in a stationary self-similar regime during the experiment where the average grain size increases by 40 %. In particular, as shown in Fig. 4a, the shape of the grain size distribution changed. The grain size distribution is close to the log-normal distribution (see Fig. S5a in supplementary materials). During the growth, the grain size distribution becomes narrower and a peak shift is observed, c.f. Fig. S5b. The change in grain size distribution may be caused by a transition of microstructure [42] or materials anisotropy [43]. Computer simulations can be used to understand the causality of the change of distributions.

Another remarkable result on the macro scale is the fast decrease in the fitted slope m_{MS}, as shown in Fig. 10b, indicating a slowdown of grain growth. This slope decrease strongly suggests that the overall boundary characteristics have changed. From Eq. 1, the slope m_{MS} of individual grain is:

$$m_{\text{MS}} = \frac{\mathrm{d}V/\mathrm{d}t}{-2\pi\mathcal{L}_{\text{face}}} = \frac{\displaystyle\int_{\Gamma_{\text{face}}} M\gamma(\kappa_1+\kappa_2)\,\mathrm{d}A}{\displaystyle\int_{\Gamma_{\text{face}}} (\kappa_1+\kappa_2)\,\mathrm{d}A} + \frac{\displaystyle\int_{\Gamma_{\text{face}}} M\left(\frac{\partial^2\gamma}{\partial n_1^2}\kappa_1 + \frac{\partial^2\gamma}{\partial n_2^2}\kappa_2\right)\mathrm{d}A}{\displaystyle\int_{\Gamma_{\text{face}}} (\kappa_1+\kappa_2)\,\mathrm{d}A}. \tag{12}$$

Notice that for the isotropic case, the reduced grain boundary mobility, $m_{\text{MS}} = M\gamma$, must be a constant for all grains and independent of time. For anisotropic materials, both terms in Eq. 12 can change during grain growth and affect the slope m_{MS}. In the following, we discuss potential causes for the observed decrease of slope m_{MS}.

1. A decrease in the population frequency of certain grain boundaries with very high mobilities M, up to $10^3 - 10^4$ higher than low mobility ones [2, 44]. We also emphasize that the fraction of high angle boundaries *increases* (see Fig. 3), which is surprising given the fact that high angle boundaries are generally believed to have higher mobilities and energies than low angle boundaries [45]. A detailed characterization of the changes in boundary characteristics will be conducted in an upcoming paper.
2. Molecular dynamics simulations have shown that during grain growth, the boundary roughness at the atomic scale can reduce, therefore causing a decrease in boundary mobility M [46]. At the same time, local atomic scale elastic strains have recently been suggested to be a reason for a slowdown of grain growth [47]. However, to verify these mechanisms, 3D grain growth studies with atomic resolution is required, which is not possible in the near future.
3. The material contains a small amount of Mn and Ni. It is known that the solute tends to segregate at the grain boundaries during annealing [45, 48]. As the boundaries migrate, the solute accumulates, which in turn reduces the boundary mobilities [49]. To quantify this effect, some chemical analysis on individual grains boundaries using, *e.g.* atom probe [50], are required.
4. A decrease in the population of grain boundaries with large grain boundary energies γ. However is unlikely to cause the strong decrease in the slope m_{MS}, as the energies of different high angle boundaries at most vary by a factor of 2-3 [28]. Likewise, it is very unlikely that the fraction of special boundaries with significantly low energy (*e.g.* twin boundaries) increases during growth in iron [28].
5. The starting microstructure comprises some large grains with large concave retrusions at the boundaries, see the boundary marked by the blue arrow in Fig. 1c. These features are presumably inherited from recrystallization process; although significant grain growth has already occurred prior to the current experiments (the average grain radius after recrystallization is about 12 μm). These features typically lead to fast boundary migration, and the fraction of such features decreases during grain growth. As can be seen in Eq. 12, the change in curvature may lead to a change in m_{MS}. As mentioned above, a detailed characterization of the changes in boundary characteristics will be conducted in an upcoming paper.

Although the specific reason for the decrease in the fitted slope m_{MS} is not clarified, we speculate that this decrease is a general phenomenon, which is applicable to many engineering materials that contain a certain amount of impurities and with anisotropic material properties. Moreover, as the possible causes for the lack of self-similarity and the decresing slope is similar, there can be a connection between two.

4.2. Local scale grain growth

Considering now the validity of the MS model for the individual grains, we test the MS prediction that grains with a positive $\mathcal{L}_{\mathrm{face}}$ shrinks and those with

a negative $\mathcal{L}_{\text{face}}$ grows. Based on the data represented in Fig. 10a, we find that the majority ($> 70\%$) of the grains fulfill this criterion for all annealing steps. Next, we test the quantitative prediction of the growth rate $\mathrm{d}V/\mathrm{d}t$ based on $\mathcal{L}_{\text{face}}$. If the grain properties are isotropic, all the data of Fig. 10a should be on a straight line with a slope equal to the reduced mobility. The scatter in the values of the growth rates indicates that Eq. 4 does not predict the experimentally measured grain growth rates. The slopes m_{MS} from individual grains show a broad distribution (see Fig. S6) with the majority of the data concentrated around the fitted m_{MS}. This broad distribution may be partly caused by small measurement error in $\mathcal{L}_{\text{face}}$ when $\mathcal{L}_{\text{face}}$ is around zero. However, only 13% of the grains have m_{MS} within a range $\pm 25\%$ of the fitted m_{MS}. This implies that even on the grain scale where boundary properties are averaged over the number of faces F, the behavior is quite anisotropic.

Comparing different annealing times, the applicability of the model is even worse, as evidenced by the significant decrease in the slope of the linear fit as grain growth proceeds. As the slowdown from a decreasing curvature driving force is already considered in the model, this decrease in the slope arises from other mechanisms, of which candidates were presented in Section 4.1. These mechanisms are rather generic and will apply to many other polycrystalline materials. Therefore, at a certain stage of grain growth, it is a challenging task to predict how much a given grain will grow or shrink, based solely on $\mathcal{L}_{\text{face}}$ and the MS model, even with 50% uncertainty. This difficulty is mainly related to the fact that different boundaries around the same grains move differently, even taken the curvature into account. For example, some boundaries did not move much during the whole annealing period, while other boundaries move more than 30 μm. To better predict the growth rates of individual grains, the mobilities and energies for the individual boundaries have to be taken into account, as given in Eq. 1. This is the topic of a subsequent paper.

5. Conclusion

In this work, we demonstrate that DCT can provide 3D time-series of sufficient quality for advancing our current understandings of grain growth and for comprehensive tests of grain growth models. Several conclusions can be drawn based on the quantitative analysis:

- The grain growth of the iron material studied is not self-similar during the monitored interval in time and temperature. The distributions of normalized grain size, number of faces per grain, and mean width parameters exhibit shape changes during the annealing. The starting weak texture has slightly strengthened after the final annealing step, while the fraction of the low angle boundaries ($< 15°$) decreases by about 2.4%.

- Within the framework of isotropic materials, analytical expressions correlating the mean width parameters, the grain size and the number of faces are derived and validated based on the 3D dataset at individual time-steps. The results show that when averaging over the grain ensemble -

and within short time intervals - these analytical expressions describe the experimental data well.

- The growth rates for the individual grains are determined. Evidence is provided for an overall slowdown of the growth, associated with a decrease of the slope m_{MS} by a factor of 8. Several possible reasons for this decrease are discussed.

- Based on the correlation between $\mathcal{L}_{\mathrm{face}}$ and growth rate, the MacPherson-Srolovitz model correctly predicts whether a grain grows or shrinks for $> 70\%$ (range between 70% and 85% for 15 time-steps) of the grains. However, it fails to predict the exact growth rate. This is not surprising as the MS model is based on an isotropic assumption while iron is known to be anisotropic. To accurately predict the growth behavior of individual grains, Eq. 1 needs to be calculated either analytically or numerically. This requires the determination of the anisotropic grain boundary mobilities and energies.

Acknowledgments

JZ and HFP acknowledge funding from the CINEMA alliance. ESRF is acknowledged for beamtime, and the instrument center Danscatt for travel refund. JZ and YZ thank Mr. Lars Lorentzen at DTU Wind Energy for help with preparation of the sample. DJR acknowledges funding from the Office of Naval Research (ONR) under their Structural Materials Program.

References

[1] C. S. Smith, Grain shapes and other metallurgical applications of topology, Metallography, Microstructure, and Analysis 4 (1952) 543–567.

[2] G. Gottstein, L. S. Shvindlerman, Grain boundary migration in metals: thermodynamics, kinetics, applications, CRC press, 2009.

[3] G. S. Rohrer, Grain boundary energy anisotropy: a review, J. Mater. Sci. 46 (2011) 5881.

[4] J. von Neumann, Discussion: Shape of metal grains metal interfaces, American Society for Metals (1952).

[5] W. W. Mullins, Two-dimensional motion of idealized grain boundaries, J. Appl. Phys. 27 (1956) 900–904.

[6] R. D. MacPherson, D. J. Srolovitz, The von Neumann relation generalized to coarsening of three-dimensional microstructures, Nature 446 (2007) 1053–1055.

[7] T. Le, Q. Du, A generalization of the three-dimensional MacPherson-Srolovitz formula, Communications in Mathematical Sciences 7 (2009) 511–520.

[8] D. Zöllner, P. Streitenberger, Three-dimensional normal grain growth: Monte Carlo Potts model simulation and analytical mean field theory, Scr. Mater. 54 (2006) 1697–1702.

[9] M. Syha, D. Weygand, A generalized vertex dynamics model for grain growth in three dimensions, Modell. Simul. Mater. Sci. Eng. 18 (2010) 015010.

[10] E. A. Lazar, J. K. Mason, R. D. MacPherson, D. J. Srolovitz, A more accurate three-dimensional grain growth algorithm, Acta Mater. 59 (2011) 6837 – 6847.

[11] H.-K. Zhao, T. Chan, B. Merriman, S. Osher, A variational level set approach to multiphase motion, J. Comput. Phys. 127 (1996) 179–195.

[12] C. Mießen, M. Liesenjohann, L. Barrales-Mora, L. Shvindlerman, G. Gottstein, An advanced level set approach to grain growth - accounting for grain boundary anisotropy and finite triple junction mobility, Acta Mater. 99 (2015) 39 – 48.

[13] C. E. Krill III, L.-Q. Chen, Computer simulation of 3-d grain growth using a phase-field model, Acta Mater. 50 (2002) 3059–3075.

[14] N. Moelans, B. Blanpain, P. Wollants, Quantitative analysis of grain boundary properties in a generalized phase field model for grain growth in anisotropic systems, Phys. Rev. B 78 (2008) 024113.

[15] H.-K. Kim, S. G. Kim, W. Dong, I. Steinbach, B.-J. Lee, Phase-field modeling for 3d grain growth based on a grain boundary energy database, Modell. Simul. Mater. Sci. Eng. 22 (2014) 034004.

[16] G. I. Tóth, T. Pusztai, L. Gránásy, Consistent multiphase-field theory for interface driven multidomain dynamics, Phys. Rev. B 92 (2015) 184105.

[17] C. Herring, Surface tension as a motivation for sintering, in: J. M. Ball, D. Kinderlehrer, P. Podio-Guidugli, M. Slemrod (Eds.), Fundamental Contributions to the Continuum Theory of Evolving Phase Interfaces in Solids: A Collection of Reprints of 14 Seminal Papers, Springer Berlin Heidelberg, Berlin, Heidelberg, 1951, pp. 33–69. doi:10.1007/978-3-642-59938-5_2.

[18] H. F. Poulsen, Three-dimensional X-ray diffraction microscopy: mapping polycrystals and their dynamics, volume 205 of *Springer Tracts in Modern Physics*, Springer Berlin Heidelberg, 2004. doi:10.1007/b97884.

[19] W. Ludwig, S. Schmidt, E. M. Lauridsen, H. F. Poulsen, X-ray diffraction contrast tomography: a novel technique for three-dimensional grain mapping of polycrystals. I. direct beam case, J. Appl. Crystallogr. 41 (2008) 302–309.

[20] G. Johnson, A. King, M. G. Honnicke, J. Marrow, W. Ludwig, X-ray diffraction contrast tomography: a novel technique for three-dimensional grain mapping of polycrystals. ii. the combined case, J. Appl. Crystallogr. 41 (2008) 310–318.

[21] S. Schmidt, U. L. Olsen, H. F. Poulsen, H. O. Sørensen, E. M. Lauridsen, L. Margulies, C. Maurice, D. J. Jensen, Direct observation of 3-d grain growth in Al-0.1%Mn, Scr. Mater. 59 (2008) 491 – 494.

[22] S. F. F. Li, Imaging of Orientation and Geometry in Microstructures: Development and Applications of High Energy X-ray Diffraction Microscopy, Dissertation, Carnegie Mellon University, 2011. URL: `http://repository.cmu.edu/dissertations/59`.

[23] M. Syha, Microstructure evolution in strontium titanate Investigated by means of grain growth simulations and x-ray diffraction contrast tomography experiments, Ph.D. thesis, Karlsruhe Institute of Technology, 2014. URL: `https://publikationen.bibliothek.kit.edu/1000042175`. doi:`10.5445/KSP/1000042175`.

[24] J. Sun, A. Lyckegaard, Y. Zhang, S. Catherine, B. Patterson, F. Bachmann, N. Gueninchault, H. Bale, C. Holzner, E. Lauridsen, et al., 4D study of grain growth in Armco iron using laboratory x-ray diffraction contrast tomography, IOP Conference Series: Materials Science and Engineering 219 (2017) 012039.

[25] A. King, P. Reischig, J. Adrien, W. Ludwig, First laboratory X-ray diffraction contrast tomography for grain mapping of polycrystals, J. Appl. Crystallogr. 46 (2013) 1734–1740.

[26] S. McDonald, P. Reischig, C. Holzner, E. Lauridsen, P. Withers, A. Merkle, M. Feser, Non-destructive mapping of grain orientations in 3d by laboratory x-ray microscopy, Sci. Rep. 5 (2015) 14665.

[27] I. M. McKenna, S. O. Poulsen, E. M. Lauridsen, W. Ludwig, P. W. Voorhees, Grain growth in four dimensions: A comparison between simulation and experiment, Acta Mater. 78 (2014) 125–134.

[28] S. Ratanaphan, D. L. Olmsted, V. V. Bulatov, E. A. Holm, A. D. Rollett, G. S. Rohrer, Grain boundary energies in body-centered cubic metals, Acta Mater. 88 (2015) 346 – 354.

[29] Z. Zhang, Y. Zhang, O. V. Mishin, N. Tao, W. Pantleon, D. J. Jensen, Microstructural analysis of orientation-dependent recovery and recrystallization in a modified 9Cr-1Mo steel deformed by compression at a high

strain rate, Metallurgical and Materials Transactions A 47 (2016) 4682–4693.

[30] W. Ludwig, P. Reischig, A. King, M. Herbig, E. M. Lauridsen, G. Johnson, T. J. Marrow, J. Y. Buffire, Three-dimensional grain mapping by x-ray diffraction contrast tomography and the use of Friedel pairs in diffraction data analysis, Rev. Sci. Instrum. 80 (2009).

[31] P. Reischig, A. King, L. Nervo, N. Viganó, Y. Guilhem, W. J. Palenstijn, K. J. Batenburg, M. Preuss, W. Ludwig, Advances in x-ray diffraction contrast tomography: flexibility in the setup geometry and application to multiphase materials, J. Appl. Crystallogr. 46 (2013) 297–311.

[32] W. C. Lenthe, M. P. Echlin, A. Trenkle, M. Syha, P. Gumbsch, T. M. Pollock, Quantitative voxel-to-voxel comparison of TriBeam and DCT strontium titanate three-dimensional data sets, J. Appl. Crystallogr. 48 (2015) 1034–1046.

[33] Z. Wu, J. M. Sullivan, Multiple material marching cubes algorithm, Int. J. Numer. Methods Eng. 58 (2003) 189–207.

[34] D. Rowenhorst, A. Lewis, G. Spanos, Three-dimensional analysis of grain topology and interface curvature in a β-titanium alloy, Acta Mater. 58 (2010) 5511 – 5519.

[35] M. Hillert, On the theory of normal and abnormal grain growth, Acta Metall. 13 (1965) 227 – 238.

[36] P. Rios, Comparison between a computer simulated and an analytical grain size distribution, Scr. Mater. 40 (1999) 665–668.

[37] J. Mackenzie, Second paper on statistics associated with the random disorientation of cubes, Biometrika 45 (1958) 229–240.

[38] Y. Suwa, Y. Saito, H. Onodera, Parallel computer simulation of three-dimensional grain growth using the multi-phase-field model, Mater. Trans. 49 (2008) 704–709.

[39] R. D. Kamachali, I. Steinbach, 3-d phase-field simulation of grain growth: topological analysis versus mean-field approximations, Acta Mater. 60 (2012) 2719–2728.

[40] E. A. Lazar, The evolution of cellular structures via curvature flow, Ph.D. thesis, Princeton University, Applied and Computational Mathematics Department, 2011. URL: `http://arks.princeton.edu/ark:/88435/dsp01sx61dm30d`, advisor: MacPherson, Robert D; Srolovitz, David J.

[41] X. Zhong, D. J. Rowenhorst, H. Beladi, G. S. Rohrer, The five-parameter grain boundary curvature distribution in an austenitic and ferritic steel, Acta Mater. 123 (2017) 136–145.

[42] P. Rios, T. Dalpian, V. Brandao, J. Castro, A. Oliveira, Comparison of analytical grain size distributions with three-dimensional computer simulations and experimental data, Scr. Mater. 54 (2006) 1633–1637.

[43] W. Mullins, Grain growth of uniform boundaries with scaling, Acta Mater. 46 (1998) 6219–6226.

[44] D. L. Olmsted, E. A. Holm, S. M. Foiles, Survey of computed grain boundary properties in face-centered cubic metals ii: Grain boundary mobility, Acta Mater. 57 (2009) 3704 – 3713.

[45] A. Rollett, F. Humphreys, G. S. Rohrer, M. Hatherly, Recrystallization and related annealing phenomena, Elsevier, 2004.

[46] E. A. Holm, S. M. Foiles, How grain growth stops: a mechanism for grain-growth stagnation in pure materials, Science 328 (2010) 1138–1141.

[47] S. L. Thomas, K. Chen, J. Han, P. K. Purohit, D. J. Srolovitz, Reconciling grain growth and shear-coupled grain boundary migration, Nat. Commun. 8 (2017) 1764.

[48] A. Rollett, G. Gottstein, L. Shvindlerman, D. Molodov, Grain boundary mobility–a brief review, Zeitschrift für Metallkunde 95 (2004) 226–229.

[49] M. Mendelev, D. Srolovitz, Impurity effects on grain boundary migration, Modell. Simul. Mater. Sci. Eng. 10 (2002) R79.

[50] M. Herbig, D. Raabe, Y. J. Li, P. Choi, S. Zaefferer, S. Goto, Atomic-scale quantification of grain boundary segregation in nanocrystalline material, Phys. Rev. Lett. 112 (2014) 126103.

Supplementary materials

S1. Smoothing in the surface mesh reconstruction

Analyzing the geometry of the interface of data described by discrete voxels can be problematic. Using the original voxel edges will grossly overestimate the surface areas and local curvatures, thus surface smoothing methods are employed. However, there is no clear threshold for when there has been too much or too little smoothing applied. It is assumed that the grain interfaces, at these length scales, are described by smooth continuous surfaces, thus the high curvature, stair-step like artifacts of the voxel edges should be removed. But using Laplacian smoothing, it is clear that with infinite numbers of iterations, the grain faces will eventually remove all long-range curvature as well. In this section, the effect on various geometrical measurements as a function of the amount of Laplacian smoothing is considered. As outlined in Section 2.2, a two-step smoothing process is implemented, first independently smoothing the triple-lines in the mesh, then constraining the smoothed triple-lines and smoothing the grain faces. In both steps, a value of $\lambda = 0.05$ is used, and the number of smoothing iterations, N is varied. Here, only the surface mesh of the first time-step is considered, as it has the fewest number of voxels per grain on average, and thus should be the most sensitive to the surface-smoothing process. We also introduce the smoothing metric f_{vox} which is defined as the fraction of surface mesh vertex points that have moved more than the distance of a voxel dimension from the original position. In an ideal surface mesh construction, the smooth interface points should remain within the voxel that they originated within. However, it is expected that with experimental data, not all voxels, and thus not all surface mesh points will be properly labeled, and thus it is reasonable that some fraction of the surface mesh points travel further than a voxel distance from its original position.

The values of f_{vox}, average value of the spherical equivalent radius $\langle R \rangle$, average surface area per grain $\langle S_A \rangle$, average triple-line length per grain L_{TL}, the average mean width of the grain faces $\langle \mathcal{L}_{\mathrm{face}} \rangle$ and mean width of the triple-lines $\langle \mathcal{L}_{\mathrm{TL}} \rangle$ were evaluated for $N = 0, 50, 100, 150, 200, 250, 300, 500, 1000$, and the results are plotted in Fig. S1. Fig S1a shows that f_{vox}, continuously increases, although at a slower rate with increasing iterations. The rate of change of the average radius shown in Fig S1b shows an overall decrease in the average radius with iteration, but note that the total change in the mean grain size is 0.01% for $N = 1000$, a negligible change.

The average surface area of the grains as a function of smoothing iteration, Fig. S1c shows the more characteristic behavior, initially with no smoothing the value of the surface area is very high and even moderate amount of smoothing leads to a dramatic reduction in the value. But as smoothing continues, the reduction in the surface area slows. The inset graph shows that the variation in $\langle S_A \rangle$from $N = 100$ to $N = 300$ is only 0.9%. The values of $\langle L_{\mathrm{TL}} \rangle$ and $\langle \mathcal{L}_{\mathrm{TL}} \rangle$ shown in Fig. S1d and e, show a similar trend although the values continue to see a decrease in value with more iterations, but still at a slower rate than the initial changes from no smoothing. This is most likely because in the two-step

smoothing nothing constrains the triple-lines during the smoothing, thus in the limit of very high iterations the triple-lines would remove all curvatures and assume straight lines between the quad-points. Nonetheless, the total variation in the measurement of $\langle L_{\mathrm{TL}} \rangle$ and $\langle \mathcal{L}_{\mathrm{TL}} \rangle$ between $N = 100$ to 300 is 3% and 6% respectively. The higher variation for $\langle \mathcal{L}_{\mathrm{TL}} \rangle$ is not surprising, given that the variation in length, and line curvature are both represented here.

Fig. S1f shows the change in the average mean width of the grain faces, which shows the initial reduction in value which is directly related to the reduction in surface area. The value passes through a minima near $N = 150 - 200$, then it slowly starts increasing again. It is not immediately clear what causes this increase, since the surface area is relatively constant over the domain of $N > 150$. Since most of the measured mesh is conformal, a reduction in the negative curvature in one grain would be matched by the reduction in curvature of the positive curvature in the neighboring grain. Thus this increase in the curvature must be related to interfaces that would be contacting the outside touching grains which are not included in the average. Thus we have chosen that $N = 200$ provides the best compromise of reducing the number of artifacts from the original voxel faces, while not reducing the long-range curvature of the grain boundaries.

S2. Convergence study of unbiased selection

As most grain growth theories assume that grains grow in an infinite medium, grains close to the free surface should not be used in the analysis to compare with these theories. Grains whose center are within a given distance to the free surface are removed. The distance is found by a convergence study of time-steps 1 and 15 to ensure average grain size $\langle R \rangle$ and average face number $\langle F \rangle$ of the interior grains reach a stable value, see Fig. S2. The convergence is seen to be achieved around 30 voxels, equivalent to about 46 μm. This value is applied to all time-steps to remove surface grains.

S3. Reproducibility of the DCT scan

In order to estimate spatial resolution and test reproducibility, the last time-step was repeated with slightly different experimental parameters: the sample was translated upward by 5 μm and the detector to sample distance was increased by 10 μm. The result is shown in Fig. S3. The average shift in position is 0.305 voxels, corresponding to $0.47 \mu m$.

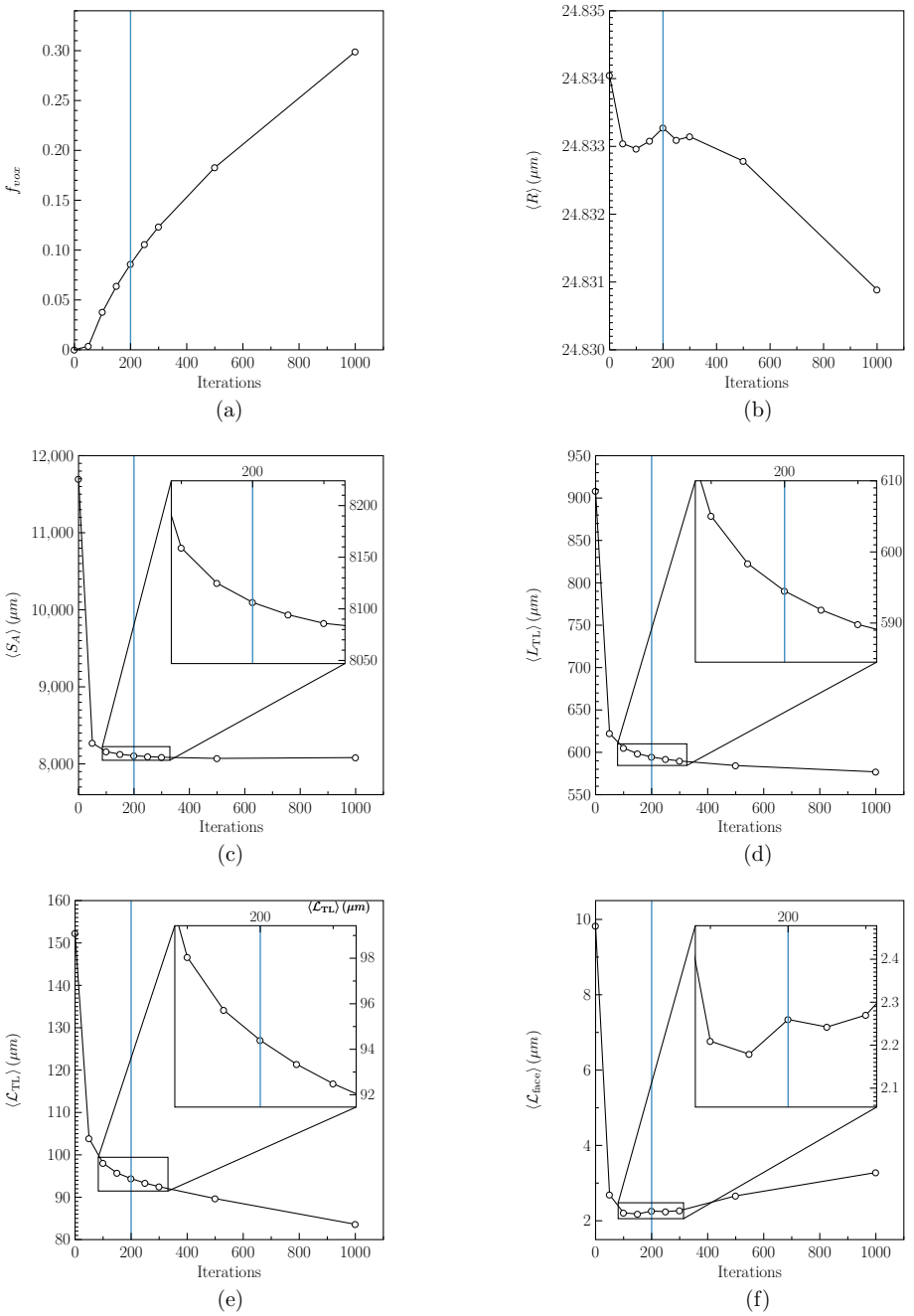

Figure S1: Effect of the extent of smoothing on the measurement of geometry parameters.

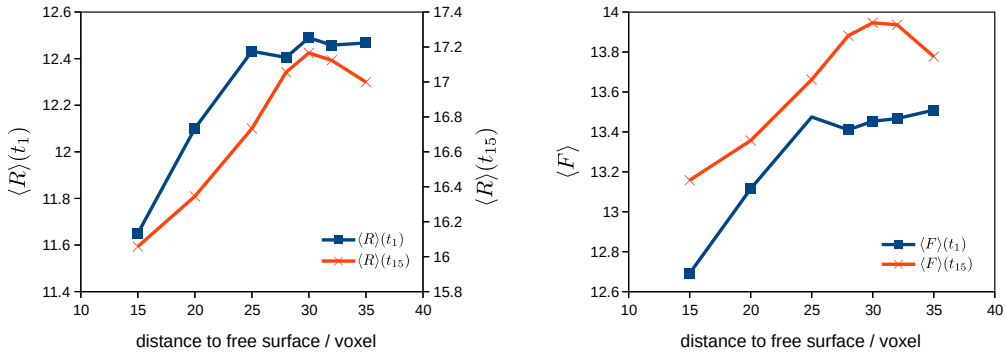

Figure S2: Unbiased selection: convergence of average radius $\langle R\rangle$ and average face number $\langle F\rangle$ calculated using interior grains as a function of distance to the free surface.

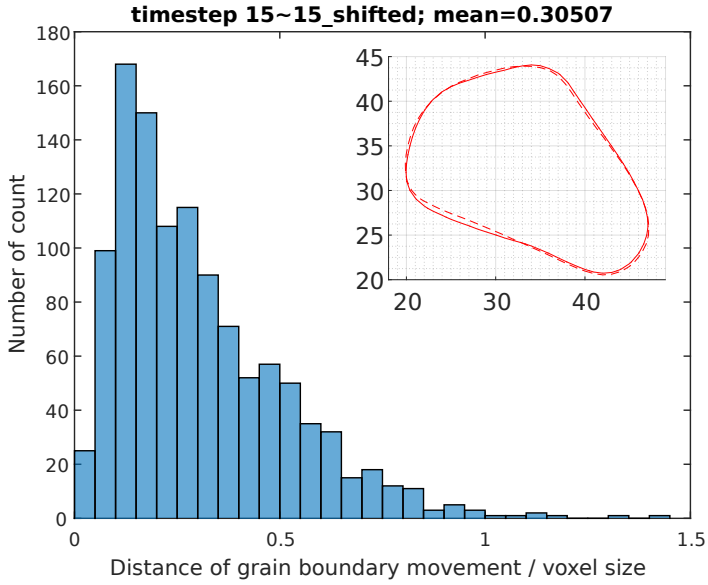

Figure S3: Test of reproducibility. A histogram is provided of the difference in position of the reconstructed grain boundary between two scans with minor changes in detector position. An example of the change in morphology of one grain boundary is shown in the insert with units of μm. The solid line represents the grain morphology of time-step 15 and the dashed line the additional scan.

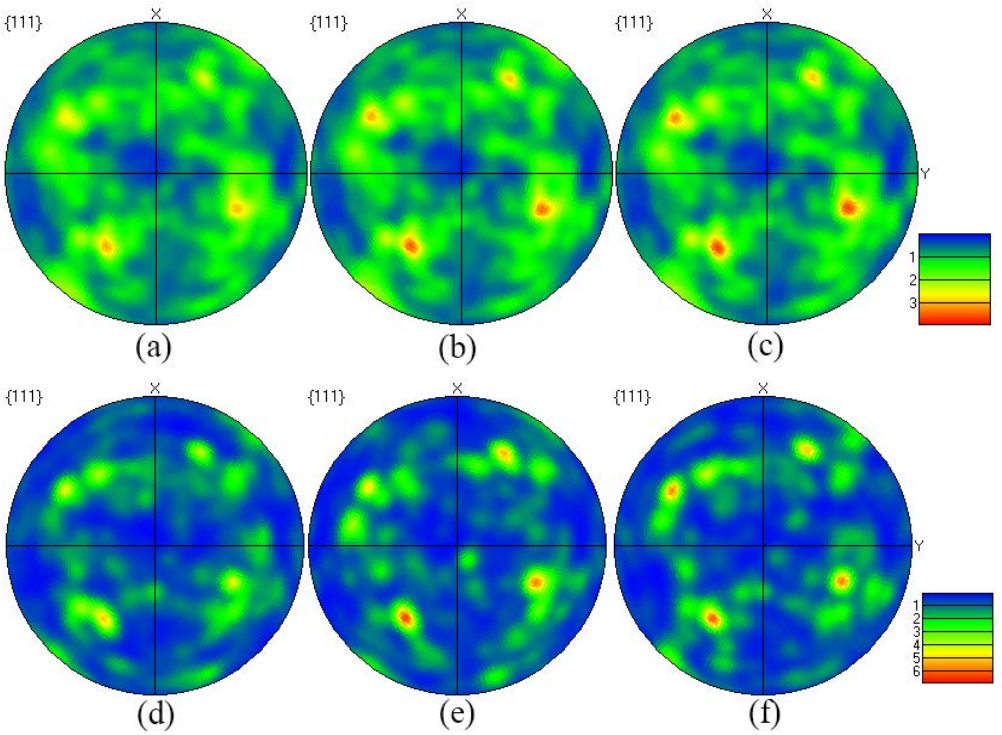

Figure S4: Texture of all and the interior grains in the gauge volume. (a)-(c) for the whole sample volume at time-steps 1, 8 and 15; (d)-(f) for interior grains at time-steps 1, 8 and 15. The texture of the whole gauge volume strengthens slightly during annealing, while the texture of the interior grains strengthens first and then weakens afterward. Notice that the statistics for interior grains are relatively poor, especially in the late stage of the growth.

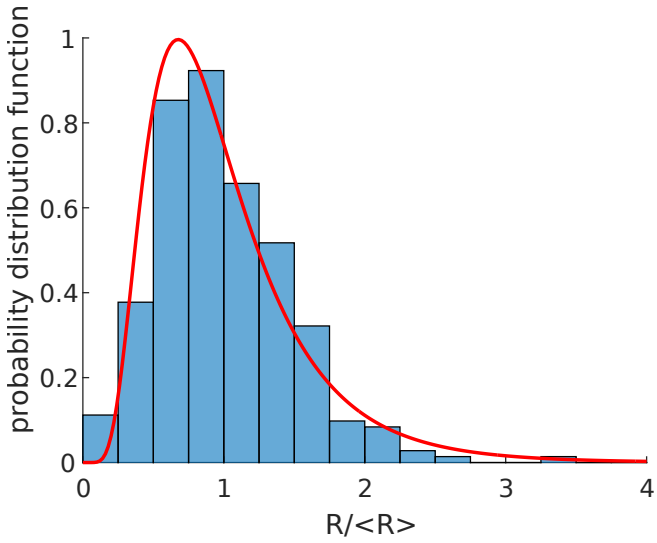

(a)

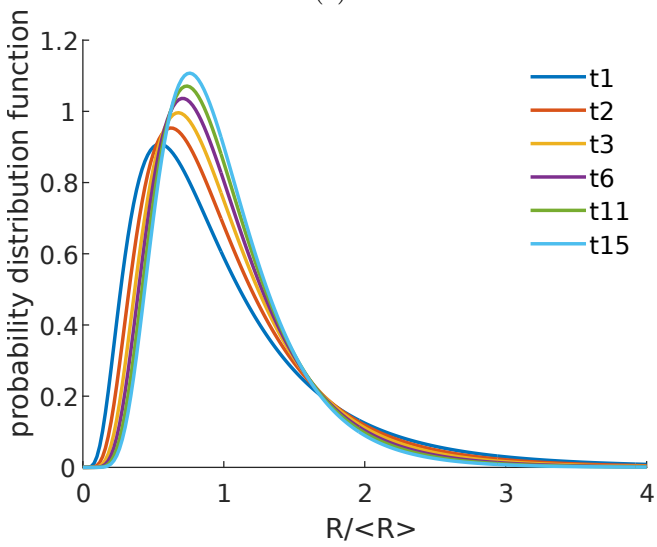

(b)

Figure S5: Log-normal fit of the grain size distribution. (a) is the log-normal fit of time-step 3. (b) is the change of fitted log-normal distributions with time. Notice here the probability distribution function differs from the number fraction used in Fig. 4a by a constant scale.

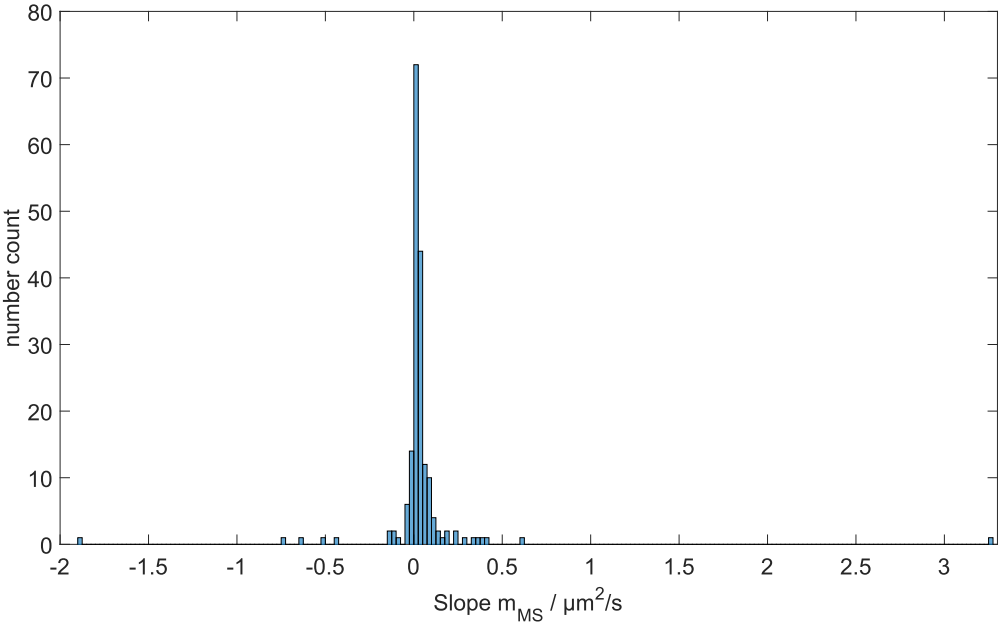

Figure S6: The distribution of the apparent reduced mobilities calculated from individual grains for time-step 8. Bin size is 0.025 $\mu m^2/s$.

Table S1: List of fitted values of parameters in Section 2.3 for each time-step

Time-step	Eq. 7		Eq. 8	Eq. 9		Eq. 10			Eq. 11	
	α	R_{cr}	k_1	k	F_0	c_0	F_0	F_{cr}	c_1	F_0
1	1.41	27.15	5.77	1.69	3.35	0.66	3.57	18.55	2.88	2.93
2	1.35	27.94	5.60	1.76	3.23	0.62	3.30	17.88	2.70	2.73
3	1.24	28.73	5.52	1.79	3.20	0.55	2.88	17.33	2.61	2.67
4	1.28	29.54	5.47	1.80	3.15	0.58	2.67	17.11	2.60	2.64
5	1.25	29.96	5.42	1.82	3.19	0.57	2.81	16.98	2.55	2.66
6	1.24	30.11	5.28	1.76	3.35	0.58	2.83	16.83	2.61	2.84
7	1.16	30.65	5.18	1.75	3.36	0.58	2.97	17.16	2.62	2.83
8	1.10	30.27	5.10	1.77	3.31	0.55	2.51	16.44	2.57	2.74
9	1.21	31.62	5.31	1.80	3.38	0.58	2.80	16.89	2.54	2.79
10	1.03	31.14	5.10	1.79	3.39	0.49	2.30	16.46	2.51	2.74
11	1.03	31.33	5.08	1.78	3.38	0.49	2.24	16.25	2.49	2.68
12	1.08	31.65	5.13	1.77	3.43	0.53	2.59	16.36	2.50	2.71
13	0.99	31.26	5.00	1.78	3.33	0.51	2.45	16.34	2.49	2.62
14	1.17	32.57	5.23	1.77	3.47	0.56	2.71	16.70	2.51	2.73
15	1.11	32.37	5.18	1.79	3.41	0.51	2.26	16.33	2.45	2.64

Fysikvej, building 307
2800 Kgs. Lyngby, Denmark

fysik.dtu.dk